M. E.

AERONAUTICAL ENGINEERING
LIBRARY

JOURNAL OF THE
AERO/SPACE SCIENCES

VOLUME 27 MARCH, 1960 NUMBER 3

PURDUE UNIVERSITY
LIBRARY

CONTENTS

Sloshing of Liquids in Circular Canals and Spherical Tanks ... BERNARD BUDIANSKY 161

Viscous Aerodynamic Characteristics in Hypersonic Rarefied Gas Flow ... RONALD F. PROBSTEIN AND NELSON H. KEMP 174

A Study of Vortex Cancellation ... ALLAN SCHAFFER 193

Optimization of the Flight-Control, Airframe System ... I. L. ASHKENAS AND D. T. MCRUER 197

Heat Conduction in a Melting Slab ... STEPHEN J. CITRON 219

Electrogasdynamic Motion of a Charged Body in a Plasma ... L. KRAUS AND H. YOSHIHARA 229

Readers' Forum ... 234

Published by
INSTITUTE OF THE AERONAUTICAL SCIENCES, INC.

JOURNAL OF THE AERO/SPACE SCIENCES

Editor: W. R. SEARS
Director, Graduate School of Aeronautical Engineering, Cornell University

Associate Editor: ROBERT R. DEXTER *Managing Editor:* RITA J. TURINO
Editorial Assistant: CAROLINE TAYLOR

Editorial Committee

Aerodynamics and Fluid Mechanics
H. Julian Allen
Holt Ashley
Dean R. Chapman
Francis H. Clauser
Hugh L. Dryden
John C. Evvard
Antonio Ferri
Alexander Flax
Wallace D. Hayes
R. T. Jones
Carl Kaplan
H. W. Liepmann
C. C. Lin
H. F. Ludloff
Harold Luskin
Clark B. Millikan
Henry T. Nagamatsu
H. J. E. Reid
George S. Schairer
G. B. Schubauer
John Stack
Theodore Theodorsen
Arthur N. Tifford
Th. von Kármán

Flight Testing
R. R. Gilruth
Melvin N. Gough
W. L. Howland
W. F. Milliken, Jr.

Rotating Wing Aircraft
F. B. Gustafson
K. H. Hohenemser
Bartram Kelley
R. B. Maloy
Ralph McClarren
R. H. Miller
R. H. Prewitt
Igor I. Sikorsky

Structures
John E. Duberg
R. R. Heldenfels
N. J. Hoff
Samuel Levy
J. F. McBrearty
W. Ramberg
E. E. Sechler
F. R. Shanley
C. R. Strang
S. Timoshenko

Vibration and Flutter
Lee Arnold
M. A. Biot
R. L. Bisplinghoff
Harold A. Cheilek
I. E. Garrick
Martin Goland

Aircraft Design
W. E. Beall
E. H. Heinemann
Hall L. Hibbard
Richard Hutton
C. L. Johnson
A. A. Kartveli
F. K. Teichmann

Electronics
K. C. Black
M. V. Kiebert, Jr.
David S. Little
Paul Rosenberg
Giles J. Strickroth

Physiologic Problems
H. G. Armstrong
Louis H. Bauer
Robert J. Benford
W. Randolph Lovelace, II
Ross A. MacFarland

Flight Propulsion
William Bollay
George W. Brady
R. P. Kroon
Frank E. Marble
Abe Silverstein
E. S. Taylor

Instruments
Alan G. Binnie
Charles H. Colvin
Frank R. Cook
C. S. Draper
S. G. Eskin
C. F. Savage
R. C. Sylvander

SUBSCRIPTION RATES

JOURNAL OF THE AERO/SPACE SCIENCES (formerly Journal of the Aeronautical Sciences), Published Monthly. United States and Possessions: 1 Year, $15.00; Single Copies, $1.50. Foreign Countries Including Canada (American Currency Rates): 1 Year, $16.00; Single Copies, $1.50.

AERO/SPACE ENGINEERING, Published Monthly. United States and Possessions: 1 Year, $5.00; Single Copies, $0.50. Foreign Countries Including Canada (American Currency Rates): 1 Year, $6.00; Single Copies, $0.50.

Notices of change of address should be sent to the Institute at least 30 days prior to actual change of address.

Manuscripts for publication, proofs, and all correspondence should be addressed to the Editorial Office of the JOURNAL.

Publication Office, 20th and Northampton Sts., Easton, Pa. Correspondence regarding subscriptions may be addressed to the Editorial Office of the JOURNAL OF THE AERO/SPACE SCIENCES, 2 East 64th Street, New York 21, N.Y.

© *Copyright, 1960, by the Institute of the Aeronautical Sciences, Inc.*

Second-Class Mail Privileges Authorized at Easton, Pa. Acceptance for mailing at a special rate of postage provided for in Section 1103, Act of October 3, 1917, authorized April 29, 1937.

JOURNAL OF THE AERO/SPACE SCIENCES

VOLUME 27 MARCH, 1960 NUMBER 3

Sloshing of Liquids in Circular Canals and Spherical Tanks†

BERNARD BUDIANSKY*

Harvard University

Summary

Theoretical calculations are made of the natural modes and frequencies of small-amplitude sloshing of liquids in partially filled circular canals and spherical tanks. An integral-equation approach is used to analyze the circular canal for arbitrary depth of liquid. A similar approach for the spherical tank provides modes and frequencies for the nearly full and half full cases. These results, together with the known behavior of the nearly empty tank, are used in conjunction with the trends established for the circular canal as a basis for estimating frequencies for arbitrary depth of liquid in the spherical tank. The dynamic analysis of the container-fluid system by means of the mode-superposition approach is discussed, and modal parameters required in such analyses are presented.

Symbols

x, y, z	= geometrical coordinates (see Fig. 1.)
$\xi, \bar{\xi}, \eta$	= nondimensional coordinates
R	= canal or sphere radius
a, e, β	= geometrical parameters related to liquid depth
v_x, v_y, v_z	= velocity distributions in x, y, and z directions, respectively
ω	= oscillation frequency
t	= time
ϕ, Φ, Ω	= velocity potentials
Ψ	= displacement potential
g	= acceleration of free fall relative to container wall
λ	= frequency parameter: $\lambda = \omega^2 R/g$
h	= liquid depth (variable)
z, f	= complex variables
F	= complex potential
G	= kernel function (circular canal)
H	= kernel function (spherical tank)
w_n	= mode shape for circular canal
f_n	= mode shape for spherical tank
$g(\rho)$	= $\sqrt{\rho f(\rho)}$
r, y, θ	= cylindrical coordinate system
$\rho, \bar{\rho}$	= nondimensional coordinates
m	= $\rho/\bar{\rho}$
s	= $\rho\bar{\rho}$
K, E	= complete elliptic integrals of first and second kind, respectively
N	= Neumann function for sphere
α_n, β_n	= modal parameters
$A_nB_nC_nD_n$	= nondimensional modal parameters
M_e	= mass of container
ρ_L	= density of liquid
M_L	= mass of liquid
X	= external transverse force acting on container
F_S	= sloshing force acting on container
U	= transverse displacement of container
A	= square matrix
T	= integrating matrix
$\{\ \}$	= column matrix
$[\ ]$	= row matrix
m, n, j, k, N	= integers
Δ	= interval of subdivision ($\Delta = 1/N$)

Received February 2, 1959.

† This paper was prepared under Air Force Contract No. AF-04(647)-181 during the summer of 1958 while the author was a consultant to the Missile Systems Division of the Lockheed Aircraft Corporation.

* Associate Professor of Structural Mechanics.

(1) Introduction

For sufficiently small amplitudes of motion, the dynamic effects of the sloshing of a liquid in a partially filled container can be analyzed in terms of the natural modes and frequencies of the small, free-surface oscillations of the liquid. This paper is concerned with the calculation of the modes and frequencies of partially filled circular canals and spherical tanks, with attention restricted to the modes that would be induced by lateral accelerations of the containers. The usual assumptions of inviscid, incompressible flow are made, and the container is considered to be rigid. The dynamic analysis of the container-fluid system by means of the mode-superposition approach is discussed, and modal parameters required in such analyses are presented.

The case of the half full circular canal was considered by Rayleigh (see reference 1, p. 444), who carried out

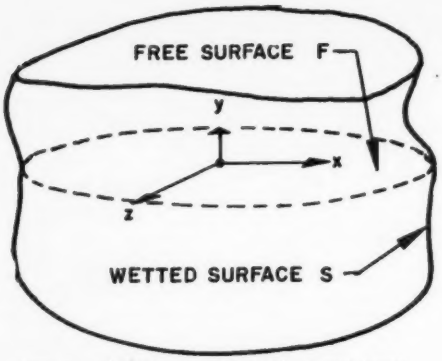

FIG. 1. Container partially filled with liquid.

an approximate energy solution for the fundamental frequency. Graham[2] estimated the fundamental frequency of the half full sphere by conceptually dividing the liquid into a collection of half-discs and then using Rayleigh's result in an unspecified averaging process.

The frequency and mode calculations of this paper are based on a rigorous integral equation approach. In the case of the circular canal, the appropriate integral equation is formulated explicitly for an arbitrary depth of liquid, and numerical calculations of the first three pertinent modes and frequencies are performed for a range of depths by means of a matrix approximation to the integral equation. For the spherical tank, rigorous analyses are made for only the nearly empty, half full, and nearly full tanks; results for the intermediate depths are estimated by interpolation and by means of the trends established for the circular canal.

The results for the fundamental frequency for the spherical tank are compared with available experimental data.

(2) Sloshing Modes and Frequencies

(2.1) *Basic Differential Equations*

The differential equation and boundary conditions governing free-surface oscillations (reference 1, p. 363) will be displayed.

The liquid is supposed to be bounded by a horizontal free surface F and a rigid wetted surface S (see Fig. 1), and small, harmonic oscillations are assumed. The velocities in the x, y, z directions, respectively, are then

$$\begin{aligned} &v_x(x, y, z) \sin \omega t \\ &v_y(x, y, z) \sin \omega t \\ &v_z(x, y, z) \sin \omega t \end{aligned} \tag{1}$$

where ω is the circular frequency.

Since the flow is irrotational, there exists a velocity potential

$$\phi(x, y, z) \sin \omega t$$

such that

$$v_x = \partial\phi/\partial x, \quad v_y = \partial\phi/\partial y, \quad v_z = \partial\phi/\partial z \tag{2}$$

The continuity equation for incompressible flow is

$$\nabla^2\phi = 0 \tag{3}$$

The condition of tangential flow at the rigid surface requires that

$$\Delta\phi \cdot \mathbf{n} \equiv \partial\phi/\partial n = 0 \text{ on } S \tag{4}$$

where $\mathbf{n}$ is the unit normal vector to S.

Finally, the condition of constant pressure at the free surface together with the linearized Bernoulli equation leads to the condition

$$\partial\phi/\partial y = (\omega^2/g)\phi \text{ on } F \tag{5}$$

where g is the acceleration of free fall relative to the container.

Eqs. (3), (4), and (5) govern the eigenvalue problem for the frequency ω. Note that Eqs. (1), (2), and (5) imply that the shape of the vertically displaced free surface during oscillation is given by $\phi(x, 0, z)$.

The analogous two-dimensional problem of transverse sloshing in a uniform channel is formulated in an obvious fashion by suppressing the z coordinate.

(2.2) *Circular Canal*

The geometrical parameters for the partially filled circular canal are shown in Fig. 2; the depth of liquid is measured by e, which varies from -1 for the empty canal to 1 for the full vessel.

It is clear that, because of geometrical symmetry, the natural modes involve free-surface vertical displacements that are either symmetrical or antisymmetrical about the origin. Since the symmetrical modes would not be induced by transverse motion of the canal, attention is restricted to the antisymmetrical modes.

It is convenient to nondimensionalize the problem by introducing

$$\xi = x/aR, \quad \eta = y/aR \tag{6}$$

The normalized geometry is shown in Fig. 3; the free-surface condition becomes

$$\partial\phi/\partial\eta = (\lambda a)\phi \tag{7}$$

where $\lambda = \omega^2 R/g$. The angle β shown in Fig. 3 is given by

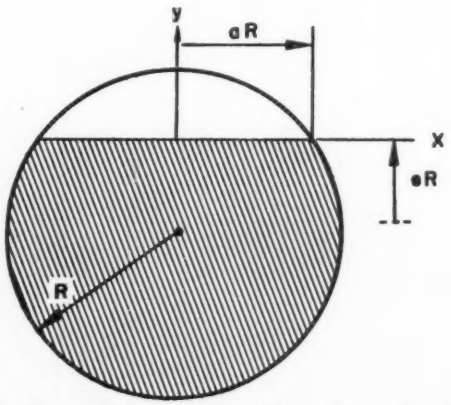

FIG. 2. Geometrical parameters and coordinates for circular canal and spherical tank.

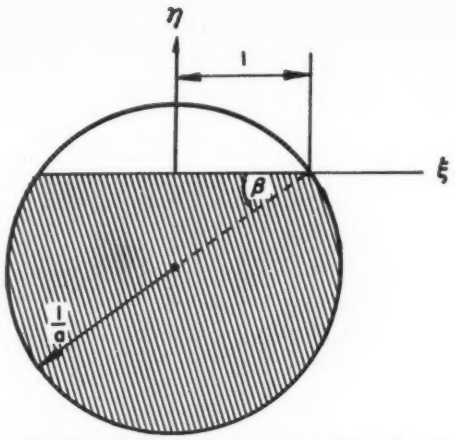

FIG. 3. Nondimensional geometrical parameters and coordinates for circular canal and spherical tank.

$$\beta = \arcsin e \tag{8}$$

and varies from $\pi/2$ for the full canal to $-\pi/2$ for the empty canal.

The procedure for setting up an integral equation governing the antisymmetrical modes follows.

Consider the fluid-filled container consisting of the original wetted boundary plus its reflection about the ξ axis (Fig. 4). Place a two-dimensional sink of strength $2w(\bar{\xi})d\bar{\xi}$ at $\bar{\xi}$ and a source of equal strength at $-\bar{\xi}$ and smear out both over a strip of length $d\bar{\xi}$. Denote the resulting velocity potential for the internal flow by

$$w(\bar{\xi})\Phi(\xi, \eta; \bar{\xi})d\bar{\xi}$$

Since the velocity potential is arbitrary to within a constant, it will be assumed that $\Phi(0, \eta; \bar{\xi}) = 0$ and, hence, $\Phi(\xi, \eta; \bar{\xi}) = -\Phi(-\xi, \eta; \bar{\xi})$. By symmetry, the vertical velocities along $\eta = 0$ vanish everywhere except on the strips of length $d\bar{\xi}$ at $\bar{\xi}$ and $-\xi$, where just below the ξ axis they are $w(\bar{\xi})$ and $-w(\bar{\xi})$, respectively. It is now possible to construct the velocity potential for the free-surface oscillation of the configuration of Fig. 3 by means of a distribution of sources and sinks along the ξ axis. It is necessary only to satisfy the free-surface condition, Eq. (7), relating the vertical velocities along the ξ axis to the velocity potential along the ξ axis. Thus, we require that

$$w(\xi) = (\lambda a)\int_0^1 \Phi(\xi, 0; \bar{\xi})w(\bar{\xi})d\bar{\xi} \tag{9}$$

for $0 \leq \xi \leq 1$; since $\Phi(-\xi, 0; \bar{\xi}) = -\Phi(\xi, 0; \bar{\xi})$, Eq. (9) is automatically satisfied for negative ξ, with $w(-\xi) = -w(\xi)$.

The problem now is to find the kernel function

$$G(\xi, \bar{\xi}) \equiv \Phi(\xi, 0; \bar{\xi}) \tag{10}$$

and this is readily accomplished by conformal mapping.

The successive transformations shown in Fig. 5 map the region of Fig. 4 into the entire f plane; the resultant transformation is

$$f = \{(1/2)[(1 - z)/(1 + z)]\}^{\gamma} \tag{11}$$

where $\gamma = 2/[(1 + 2\beta)/\pi]$. Now let f_1 and f_2 correspond to $z = \bar{\xi}$ and $-\bar{\xi}$, respectively. The complex potential of a sink at f_1 and a source at f_2, each of strength 2, is

$$F = -(1/\pi)\log[(f - f_1)/(f - f_2)] + g(\bar{\xi}) \tag{12}$$

where g is an arbitrary function of $\bar{\xi}$.

Substituting Eq. (11) into Eq. (12) gives, in the z plane, the corresponding potential

$$F = -\frac{1}{\pi}\log \left\{\frac{[(1 - z)/(1 + z)]^{\gamma} - [(1 - \bar{\xi})/(1 + \bar{\xi})]^{\gamma}}{[(1 - z)/(1 + z)]^{\gamma} - [(1 + \bar{\xi})/(1 - \bar{\xi})]^{\gamma}}\right\} + g(\bar{\xi})$$

Now choose g so that $F(0) = 0$; then

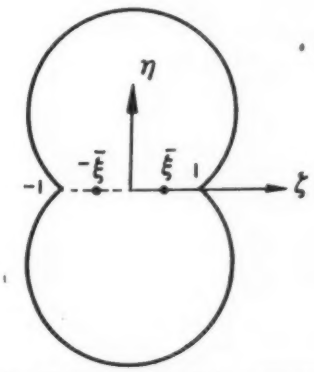

FIG. 4. Location of source-sink pair in symmetrized domain.

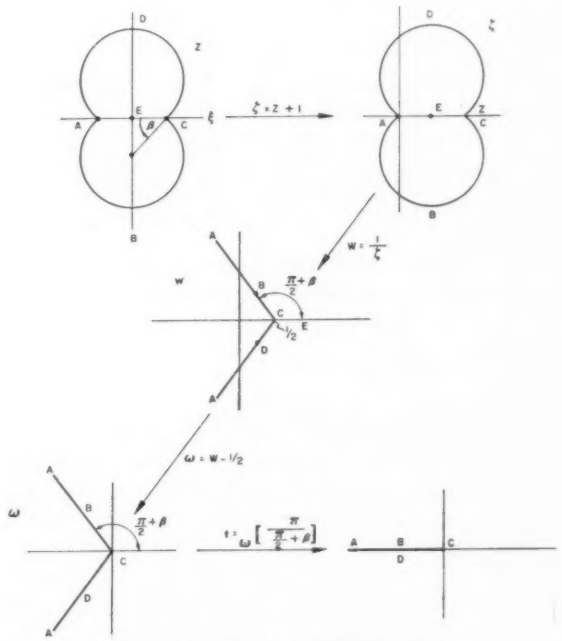

FIG. 5. Conformal mapping sequence.

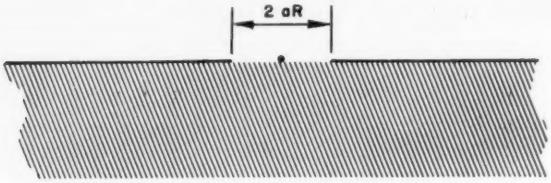

FIG. 6. Limiting case of nearly full container.

$$F(z) = -\frac{1}{\pi}\log \left\{\frac{[(1-z)/(1+z)]^{\gamma} - [(1-\bar{\xi})/(1+\bar{\xi})]^{\gamma}}{[(1-z)/(1+z)]^{\gamma} - [(1+\bar{\xi})/(1-\bar{\xi})]^{\gamma}}\right\} \times \left\{\frac{1-[(1+\bar{\xi})/(1-\bar{\xi})]^{\gamma}}{1-[(1-\bar{\xi})/(1+\bar{\xi})]^{\gamma}}\right\}$$

$$= -\frac{1}{\pi}\log \left\{\frac{(1-z)^{\gamma}(1+\bar{\xi})^{\gamma} - (1+z)^{\gamma}(1-\bar{\xi})^{\gamma}}{(1+z)^{\gamma}(1+\bar{\xi})^{\gamma} - (1-z)^{\gamma}(1-\bar{\xi})^{\gamma}}\right\}$$

Finally, $G(\xi, \bar{\xi}) = Re\, F(z)$ is

$$G(\xi, \bar{\xi}) = -\frac{1}{\pi}\log \left|\frac{(1+\xi)^{\gamma}(1-\bar{\xi})^{\gamma} - (1-\xi)^{\gamma}(1+\bar{\xi})^{\gamma}}{(1+\xi)^{\gamma}(1+\bar{\xi})^{\gamma} - (1-\xi)^{\gamma}(1-\bar{\xi})^{\gamma}}\right| \quad (13)$$

Note that G has a logarithmic singularity at $\xi = \bar{\xi}$. Note also that

$$G(\xi, \bar{\xi}) = G(\bar{\xi}, \xi) = -G(-\xi, \bar{\xi})$$

To recapitulate, then, the solutions of the homogeneous (singular) integral equation

$$w(\xi) = (\lambda a)\int_0^1 G(\xi, \bar{\xi}) w(\bar{\xi}) d\bar{\xi} \quad (14)$$

with $G(\xi, \bar{\xi})$ given by Eq. (13), provide the characteristic free-surface shapes $w(\xi)$, and the associated eigenvalues of (λa) yield the natural frequencies.

The numerical solution of the integral equation, Eq. (14), has been performed for various depths on the basis of the matrix formulation described in the Appendix. The results are presented in Section (4).

Special Cases—Several special cases for which approximate solutions can easily be obtained are of particular interest. For the half full canal ($e = 0$), the kernel becomes

$$G(\xi, \bar{\xi}) = -\frac{1}{\pi}\log \left|\frac{(\xi - \bar{\xi})(1 - \xi\bar{\xi})}{(\xi + \bar{\xi})(1 + \xi\bar{\xi})}\right|$$

A one-term Galerkin-type solution for the lowest frequency can be carried out without difficulty for this case.

From Eq. (14),

$$\int_0^1 [w(\xi)]^2 d\xi = (\lambda a)\int_0^1\int_0^1 G(\xi, \bar{\xi})\, w(\bar{\xi})\, w(\xi)\, d\xi d\bar{\xi} \quad (15)$$

Introducing the approximate mode shape $w = \xi$ into Eq. (15) and carrying out the integrations give, for $e = 0$, $(a = 1)$, the approximate fundamental eigenvalue

$$\lambda_1 \approx 1/3[(2/\pi) - (\pi/8)] = 1.367 \quad (16)$$

or

$$\omega_1 \approx 1.169\,(g/R)^{1/2}$$

This is precisely the result found by Rayleigh in an entirely different way. The result is necessarily an upper bound to the exact frequency. Rayleigh also obtained an improved approximation $\omega \approx 1.1644\,(g/R)^{1/2}$.

Also of special interest is the limiting case of the nearly full canal, where $\beta \to \pi/2$ and $\gamma \to 1$. The integral equation becomes simply

$$w(\xi) = -(\lambda a)\int_0^1 \frac{1}{\pi}\log\left|\frac{\xi - \bar{\xi}}{\xi + \bar{\xi}}\right| w(\bar{\xi})\, d\bar{\xi} \quad (17)$$

Denote the critical values of (λa) by c_n $(n = 1, 2, \ldots)$; then, for e sufficiently close to 1,

$$\lambda_n \approx c_n/a$$
$$= c_n/\sqrt{1 - e^2}$$

Thus, the frequencies tend to infinity as the full condition is approached. This result, as well as the form of the integral equation, Eq. (17), could have been anticipated by consideration of the sloshing of liquid in a half plane with a rigid boundary having an aperture of length $(2aR)$. (See Fig. 6.) The kernel function for this case can be written directly in terms of a source-sink pair, without the need for conformal transformations. A one-term Galerkin solution of Eq. (17), again with $w = \xi$, gives the approximate result

$$c_1 \approx 2\pi/3 = 2.094$$

so that

$$\lambda_1 \approx 2.094/\sqrt{1 - e^2} \quad (18)$$

for $e \to 1$.

For the nearly empty canal ($e \to -1$), γ becomes infinite. The asymptotic results for this case are most readily found by abandoning the integral equation and exploiting shallow-water theory (see reference 1, p. 291). The differential equation for the velocity potential may be conveniently deduced from the variational principle given by Lawrence, Wang, and Reddy.[3] The variational equation is

$$\delta\left[\int_V (1/2)|\nabla\phi|^2\, dV - (\omega^2/2g)\int_F \phi^2\, dF\right] = 0 \quad (19)$$

where V denotes the volume of fluid in Fig. 1.

As shown in reference 3, Eqs. (3), (4), and (5) constitute the Euler equation and natural boundary conditions of Eq. (19).

For the two-dimensional canal of *shallow* depth variation $h(x)$, it is assumed that ϕ may be taken independent of y. Then Eq. (19) becomes

$$\delta\left[(1/2)\int_F h(x)(d\phi/dx)^2\,dx - (\omega^2/2g)\int_F \phi^2\,dx\right] = 0$$

The Euler equation is

$$(d/dx)[h(d\phi/dx)] + (\omega^2/g)\phi = 0 \qquad (20)$$

For the nearly empty circular canal, the depth has approximately the parabolic variation

$$h(x) = (1/2R)[(aR)^2 - x^2]$$

so that Eq. (20) becomes

$$(1/2)(d/dx)[(aR)^2 - x^2(d\phi/dx)] + (\omega^2 R/g)\phi = 0$$

or, in terms of $\xi = x/aR$,

$$(1/2)(d/d\xi)[(\xi^2 - 1)(d\phi/d\xi)] - \lambda\phi = 0$$

whence

$$(\xi^2 - 1)\phi'' + 2\xi\phi' - 2\lambda\phi = 0 \qquad (21)$$

This is essentially Legendre's differential equation. For the antisymmetrical modes, $\phi(0) = 0$; in addition, the condition of finiteness at $\xi = 1$ is imposed. The solutions of Eq. (21) are then the odd-order Legendre polynomials of the first kind

$$P_{2n-1}(\xi) \qquad n = 1, 2, 3, \ldots \qquad (22)$$

with the corresponding eigenvalues

$$\lambda_n = 2n^2 - n \qquad n = 1, 2, 3, \ldots \qquad (23)$$

The polynomials [Eq. (22)] represent the limiting free-surface shapes of the natural modes as the depth approaches zero.

The first eigenvalue is $\lambda_1 = 1$; and so the fundamental frequency

$$\omega_1 = \sqrt{g/R}$$

is, as could be expected, simply the frequency of a pendulum of length R.

(2.3) *Spherical Tank*

The geometrical parameters of Figs. 2 and 3 may be considered to apply to the spherical tank. A rigorous analysis was executed for only the nearly full and half full cases; rigorous results for the nearly empty case, given by Lamb (reference 1, p. 291), are also available.

Introduce the cylindrical coordinate system (r, y, θ), where $x = r\cos\theta$, $z = r\sin\theta$. The appropriate nondimensional system becomes (ρ, η, θ), where $\rho = r/aR$, and, as before, $\eta = y/aR$. In these nondimensional coordinates, the governing differential equation is:

$$(\partial^2\phi/\partial\rho^2) + (1/\rho)(\partial\phi/\partial\rho) + (\partial^2\phi/\partial\eta^2) + (1/\rho^2)(\partial^2\phi/\partial\theta^2) = 0 \qquad (24)$$

and the free-surface boundary condition remains that given in Eq. (7). It is evident that solutions for the modes may be written in the form

$$\phi = \psi(\rho, \eta)\cos k\theta, \quad (k = 1, 2, \ldots) \qquad (25)$$

It will be shown later that only the modes with $k = 1$ are induced by lateral accelerations in the ξ direction.

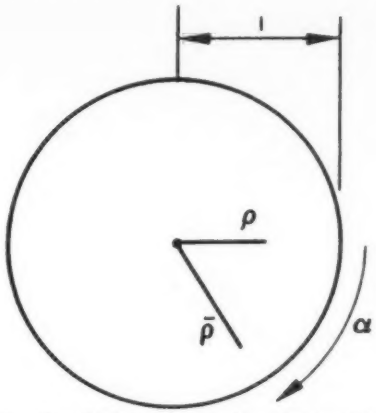

FIG. 7. Coordinates in free surface of spherical tank.

Consequently, attention will be restricted to these cases.

The procedure for setting up an integral equation analogous to Eq. (14) is as follows. Consider the volume of fluid enclosed by the wetted surface and its reflection about the originally free surface $\eta = 0$. (See Fig. 4.) Now, in the plane $\eta = 0$ (Fig. 7), place a distribution of three-dimensional sinks along the annulus $(\bar\rho, \bar\rho + d\bar\rho)$ of strengths $2f(\bar\rho)\cos\alpha$ per unit area. Let $f(\bar\rho)\Omega(\rho, \eta, \theta; \bar\rho)\bar\rho d\bar\rho$ be the resulting velocity potential. Then, since the vertical velocity just below the plane $\eta = 0$ is, because of this potential, zero everywhere except in the annulus, where it is $f(\bar\rho)\cos\theta$, the imposition of the boundary condition Eq. (7) at $\theta = 0$ requires that

$$f(\rho) = (\lambda a)\int_0^1 \Omega(\rho, 0, 0; \bar\rho)\bar\rho f(\bar\rho)\,d\bar\rho \qquad (26)$$

It is convenient to let $g(\rho) = \sqrt{\rho}\,f(\rho)$; then,

$$g(\rho) = (\lambda a)\int_0^1 H(\rho, \bar\rho)g(\bar\rho)d\bar\rho \qquad (27)$$

where

$$H(\rho, \bar\rho) = \sqrt{\rho\bar\rho}\,\Omega(\rho, 0, 0; \bar\rho) \qquad (28)$$

The problem now is to determine $H(\rho, \bar\rho)$.

(2.3.1) Nearly Full Tank—For the nearly full case, the symmetrized region is the entire space (Fig. 6), and the potential of a sink in the plane $\eta = 0$ is unmodified by the presence of a rigid boundary in this plane. The potential of a sink of strength 2 at $(\bar\rho, 0, \alpha)$ is

$$\frac{1}{2\pi} \times \frac{1}{[(\rho\cos\theta - \bar\rho\cos\alpha)^2 + (\rho\sin\theta - \bar\rho\sin\alpha)^2 + \eta^2]^{1/2}}$$

and so

$$\Omega(\rho, 0, 0; \bar\rho) = \frac{1}{2\pi}\int_0^{2\pi} \frac{\cos\alpha\,d\alpha}{[\rho^2 + \bar\rho^2 - 2\rho\bar\rho\cos\alpha]^{1/2}}$$

Then,

$$H(\rho, \bar\rho) = \left(\frac{1}{\pi}\right)\sqrt{\rho\bar\rho}\int_0^{\pi} \frac{\cos\alpha d\alpha}{[\rho^2 + \bar\rho^2 - 2\rho\bar\rho\cos\alpha]^{1/2}}$$

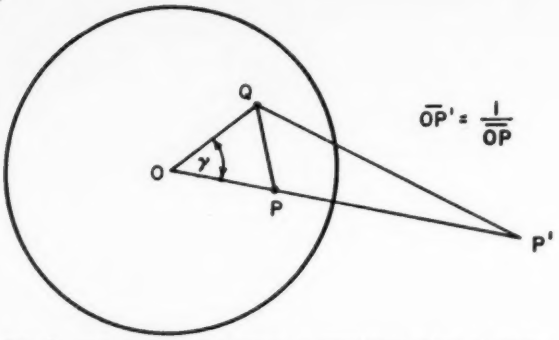

FIG. 8. Geometrical parameters in equatorial plane of sphere.

Clearly, $H(\rho, \bar{\rho}) = H(\bar{\rho}, \rho)$. Consider $\rho < \bar{\rho}$, and let $m = (\rho/\bar{\rho})$. Then,

$$H = \frac{\sqrt{m}}{\pi} \int_0^{\pi} \frac{\cos \alpha \, d\alpha}{[m^2 - 2m \cos \alpha + 1]^{1/2}} \tag{29}$$

Letting $\beta = \alpha/2$ yields

$$H = \frac{q}{\pi} \int_0^{\pi/2} \frac{(2 \sin^2 \beta - 1) d\beta}{[1 - q^2 \sin^2 \beta]^{1/2}} \tag{30}$$

where $q = 2\sqrt{m}/(m + 1)$.

This may be evaluated in terms of complete elliptic integrals (reference 4, p. 73) to give

$$H = (1/\pi)\{[(2/q) - q] \, K(q) - (2/q)E(q)\} \tag{31}$$

where

$$K(q) = \int_0^{\pi/2} \frac{d\theta}{[1 - q^2 \sin^2 \theta]^{1/2}}$$

and

$$E(q) = \int_0^{\pi/2} [1 - q^2 \sin^2 \theta]^2 \, d\theta$$

are the complete elliptic integrals of the first and second kind, respectively.

The result [Eq. (31)] for $H(\rho, \bar{\rho})$ may be put into a much more convenient form by exploiting the Landen transformations[5]

$$K(m) = [1/(1 + m)]K(q)$$

$$E(m) = [(1 + m)/2]E(q) + [(1 - m)/2]K(q)$$

to give, as a final result

$$H(\rho, \bar{\rho}) = 2/\sqrt{\pi \rho/\bar{\rho}}[K(\rho/\bar{\rho}) - E(\rho/\bar{\rho})] \tag{32}$$

for $\rho < \bar{\rho}$. Since $H(\rho, \bar{\rho}) = H(\bar{\rho}, \rho)$, the kernel is completely defined. This kernel, like the ones for the circular canal, also has a logarithmic singularity at $\rho = \bar{\rho}$.

(2.3.2) Half Full Tank—For the half full case, the symmetrized volume is a complete sphere, and so the kernel function can be evaluated on the basis of the known Neumann function (or Dirichlet function of the second kind) for the sphere. Thus,[6] the function of the position Q (Fig. 8) given by

$$N(Q) = \frac{1}{2\pi}\left\{\frac{1}{\overline{PQ}} + \frac{1}{(\overline{OP})(\overline{QP'})} + \log \frac{2}{1 - (\overline{OQ})(\overline{OP}) \cos \gamma + (\overline{OP})(\overline{QP'})}\right\} \tag{33}$$

satisfies the following conditions in the unit sphere:

(*i*) $N(Q)$ is harmonic.
(*ii*) $N(Q)$ has a sink of strength 2 at P.
(*iii*) The normal derivative of $N(Q)$ has the constant value $-(1/2\pi)$ at the surface of the sphere.

Now, let Q be the point $(\rho, 0, 0)$ in the equatorial plane of the sphere (Fig. 7), and let P be the point $(\bar{\rho}, 0, \alpha)$. Then,

$$N(\rho, 0, 0) = \frac{1}{2\pi}\left\{\frac{1}{[\rho^2 + \bar{\rho}^2 - 2\rho\bar{\rho} \cos \alpha]^{1/2}} + \frac{1}{[(\rho\bar{\rho})^2 + 1 - 2\rho\bar{\rho} \cos \alpha]^{1/2}} + \log \frac{2}{1 - \rho\bar{\rho} \cos \alpha + [(\rho\bar{\rho})^2 + 1 - 2\rho\bar{\rho} \cos \alpha]^{1/2}}\right\}$$

and, therefore,

$$H(\rho, \bar{\rho}) = \frac{\sqrt{\rho\bar{\rho}}}{\pi} \int_0^{\pi} \frac{\cos \alpha d\alpha}{[\rho^2 + \bar{\rho}^2 - 2\rho\bar{\rho} \cos \alpha]^{1/2}} + \frac{\sqrt{\rho\bar{\rho}}}{\pi} \times \int_0^{\pi} \frac{\cos \alpha d\alpha}{[(\rho\bar{\rho})^2 + 1 - 2\rho\bar{\rho} \cos \alpha]^{1/2}} + \frac{\sqrt{\rho\bar{\rho}}}{\pi} \int_0^{\pi} \cos \alpha \times \left[\log \frac{2}{1 - \rho\bar{\rho} \cos \alpha + [(\rho\bar{\rho})^2 + 1 - 2\rho\bar{\rho} \cos \alpha]^{1/2}}\right] d\alpha \tag{34}$$

Note that, because of the cosine variation of local sink strength at the radius $\bar{\rho}$, the normal flow at the spherical surface vanishes, as it should, despite the fact that the Neumann function [Eq. (33)] for a *single* sink produces a *constant* flux at the surface.

The evaluation of the first two integrals in Eq. (34) follows immediately from the results for the nearly full case; the last integral may be evaluated as follows. Let $s = (\rho\bar{\rho})$, and let

$$I(s) = \int_0^{\pi} \cos \alpha \times \log \left\{\frac{2}{[1 - s \cos \alpha + (s^2 + 1 - 2s \cos \alpha)]^{1/2}}\right\} d\alpha$$

$$= -\int_0^{\pi} \cos \alpha \times \log [(1 - s \cos \alpha) + (s^2 + 1 - 2s \cos \alpha)^{1/2}] d\alpha \tag{35}$$

Note that $I(0) = 0$; subtract the zero quantity $\int_0^{\pi} (\cos \alpha) \log s d\alpha$ from Eq. (35), giving

$$I(s) = -\int_0^{\pi} \cos \alpha \log \{(1/s) - \cos \alpha + [1 + (1/s^2) - (2 \cos \alpha/s)]^{1/2}\} d\alpha$$

Then, by differentiation under the integral sign, it is

found that

$$I'(s) = \frac{1}{s}\int_0^{\pi} \frac{\cos \alpha d\alpha}{[s^2 + 1 - 2s\cos\alpha]^{1/2}}$$

which [see Eqs. (29) and (32)] is

$$I(s) = (2/s^2)[K(s) - E(s)]$$

Hence,

$$I(s) = \int_0^s (2/s^2)[K(s) - E(s)]ds$$

which gives (reference 7, p. 273)

$$I(s) = (2/s)[E(s) - (1 - s^2)K(s)]$$

Then, with $m = (\rho/\bar{\rho})(\rho < \bar{\rho})$, evaluation of the three integrals in Eq. (34) gives:

$$H(\rho, \bar{\rho}) = (1/\pi)\{(2/\sqrt{m}) \times [K(m) - E(m)] + (2/\sqrt{s})[K(s) - E(s)] + (2/\sqrt{s})[E(s) - (1 - s^2)K(s)]\}$$

or, finally,

$$H(\rho, \bar{\rho}) = (1/\pi) \times \{(2/\sqrt{\rho/\bar{\rho}})[K(\rho/\bar{\rho}) - E(\rho/\bar{\rho})] + 2(\rho\bar{\rho})^{3/2} K(\rho\bar{\rho})\} \quad (36)$$

for $\rho < \bar{\rho}$. Again, the additional fact that $H(\rho, \bar{\rho}) = H(\bar{\rho}, \rho)$ [see Eq. (34)] completely defines $H(\rho, \bar{\rho})$.

As in the case of the circular canal, the solutions of the integral equation with the kernels Eqs. (32) and (36), were performed on the basis of the matrix setup discussed in the Appendix. The results are given in Section (4).

(2.3.3) Nearly Empty Tank—The nearly empty tank may be analyzed in a fashion analogous to the treatment of the nearly empty circular canal by approximating the wetted surface with the paraboloid of revolution having the depth variation

$$h(r) = (1/2R)[(aR)^2 - r^2]$$

and using shallow-water theory. The problem of oscillation in such a container has been solved by Lamb (reference 1, p. 291); the pertinent parts of the solution are repeated here in a convenient form. By assuming $\phi = f(\rho)\cos\theta$ (independent of η), the governing differential equation for f can be found from the variational principle [Eq. (19)] to be

$$\rho^2(\rho^2 - 1)f'' + \rho(3\rho^2 - 1)f' + [1 - (2\lambda + 1)\rho^2]f = 0 \quad (37)$$

or

$$[\rho(\rho^2 - 1)f] + [(1/\rho) - (2\lambda + 1)\rho]f = 0 \quad (38)$$

Then, appropriate boundary conditions are that $f = 0$ at $\rho = 0$, and f is finite at $\rho = 1$. Note, then, for future use, that Eq. (38) implies that the orthogonality condition

$$\int_0^1 \rho f_m(\rho) f_n(\rho) = 0 \quad (39)$$

holds for eigenfunctions f_m and f_n associated with distinct eigenvalues λ_m and λ_n.

The solution of Eq. (38) for the antisymmetrical modes is

$$f_n = \sum_{j=1}^{n} a_j \rho^{2j-1}, \quad n = 1, 2, \ldots \quad (40)$$

where

$$a_1 = 1$$
$$a_{j+1} = -[(n^2 - j^2)/j(j + 1)]a_j$$

and the corresponding eigenvalues are

$$\lambda_n = 2n^2 - 1, \quad n = 1, 2, \ldots \quad (41)$$

The first three eigenfunctions, normalized to give $f_n(1) = 1$, are:

$$f_1 = \rho$$
$$f_2 = 3\rho^3 - 2\rho$$
$$f_3 = 10\rho^5 - 12\rho^3 + 3\rho \quad (42)$$

As in the case of the circular canal, the lowest eigenvalue is $\lambda_1 = 1$, corresponding to the frequency of a pendulum of length R. It is interesting to compare the eigenvalues for the nearly empty canal and spherical tank; from Eqs. (41) and (23),

$$(\lambda_n)_{\text{sphere}} = (\lambda_n)_{\text{canal}} + (n - 1)$$

(3) Sloshing Forces and Motion

Suppose that the rigid container shown in Fig. 1 is subjected to a displacement $U(t)$ in the x direction; tank displacements in the y and z direction, as well as rotations of the tank about all axes, are assumed to be fully constrained. Define a *displacement* potential Ψ for the resulting fluid displacement *relative to the tank*, such that the relative displacements are given by

$$[\partial\Psi/\partial x, \partial\Psi/\partial y, \partial\Psi/\partial z]$$

and assume Ψ in the form

$$\Psi = \sum a_n(t)\phi_n(x, y, z)$$

where the ϕ_n's are the potentials associated with the natural modes of liquid oscillation in a stationary, rigid tank. Lagrange's equations will be the basis for establishing differential equations relating the generalized coordinates $U(t)$ and $a_n(t)$ to the external force X on the tank. The results will be used to calculate the "sloshing" forces of the liquid on the container wall.

The potential energy during motion is

$$\text{P.E.} = (1/2)\int_F \rho_L g(\partial\Psi/\partial y)^2\, dF$$

$$= (1/2)\int_F \rho_L g[\sum a_n(\partial\phi_n/\partial y)]^2\, dF$$

where ρ_L is the density. But [see Eq. (5)]

$$\partial\phi_n/\partial y = (\omega_n^2/g)\phi_n$$

so that

$$\text{P.E.} = (1/2)\int_F \rho_L g[\sum(a_n\omega_n^2/g)\phi_n]^2\,dF \qquad (43)$$

Note, however, that if ϕ_m and ϕ_n are modes corresponding to the distinct frequencies ω_m and ω_n,

$$\int_V \nabla\phi_m\cdot\nabla\phi_n dV = -\int_V \phi_m\nabla^2\phi_n dV + \int_S \phi_m\nabla\phi\cdot\mathbf{n}dS + \int \phi_m(\partial\phi_n/\partial y)\,dF \qquad (44)$$

Also, by Eqs. (3) and (4), the first two integrals on the right-hand side vanish; and so, by Eq. (5), the right-hand side becomes

$$\int_F (\omega_n^2/g)\phi_m\phi_n dF \qquad (45)$$

But then the left-hand side of Eq. (44) is also given by

$$\int_F (\omega_m^2/g)\phi_m\phi_n dF \qquad (46)$$

and so, for $\omega_m \neq \omega_n$, the equality of Eqs. (45) and (46) implies that

$$\int_F \phi_m\phi_n dF = 0 \qquad (47)$$

and also

$$\int_V \nabla\phi_m\cdot\nabla\phi_n dV = 0 \qquad (48)$$

Hence, the potential energy [Eq. (42)] becomes

$$\text{P.E.} = (\rho_L/2g)\int_F \sum a_n^2\omega_n^4\phi_n^2 dF$$

or, letting $\alpha_n = \int_F \phi_n^2\,dF$,

$$\text{P.E.} = (\rho_L/2g)\sum \alpha_n a_n^2 w_n^4 \qquad (49)$$

The kinetic energy of the container-liquid system is

$$\text{K.E.} = (1/2)M_c(\dot{U})^2 + (\rho_L/2)\times \int_V \{[\dot{U} + \sum \dot{a}_n(\partial\phi_n/\partial x)]^2 + [\sum \dot{a}_n(\partial\phi_n/\partial y)]^2 + [\sum a_n(\partial\phi_n/\partial z)]^2\}\,dV$$

where M_c is the container mass.

Using Eq. (48), together with the energy relation for a single mode [see Eqs. (44) and (45)].

$$(1/2)\int_V |\nabla\phi_n|^2\,dV = (\omega_n^2/2g)\int_F \phi_n^2\,dF$$

gives

$$\text{K.E.} = (1/2)(M_c + M_L)(\dot{U})^2 + (\rho_L/2g)\sum \alpha_n\omega_n^2(\dot{a}_n)^2 + \rho_L\,\dot{U}\sum \beta_n\dot{a}_n \qquad (50)$$

where

$$\beta_n = \int_V (\partial\phi_n/\partial x)dV \qquad (51)$$

and M_L is the total mass of liquid.

The expression for β_n may be transformed as follows:

$$\beta_n = \int_V \{(\partial/\partial x)[x(\partial\phi_n/\partial x)] + (\partial/\partial y)[x(\partial\phi_n/\partial y)] + (\partial/\partial z)[x(\partial\phi_n/\partial z)]\}\times dV - \int_V x\nabla^2\phi_n dV = \int_F x(\partial\phi_n/\partial y)dF + \int_S x\nabla\phi\cdot\mathbf{n}dS$$

Finally,
$$\beta_n = (\omega_n^2/g)\cdot\int_F x\phi_n dF \qquad (52)$$

With the Lagrangian L = (K.E. − P.E.) determined by Eqs. (50) and (49), Lagrange's equations

$$(d/dt)(\partial L/\partial\dot{U}) - (\partial L/\partial U) = X$$
$$(d/dt)(\partial L/\partial\dot{a}_n) - (\partial L/\partial a_n) = 0$$

yield the differential equations

$$\ddot{a}_n + \omega_n^2 a_n = -(g/\omega_n^2)(\beta_n/\alpha_n)\dot{U} \qquad (53)$$

$$(M_c + M_L)\dot{U} + \rho_L\sum \beta_n\ddot{a}_n = X \qquad (54)$$

The sloshing force F_S of the *liquid acting on the container in the positive x direction* is

$$F_S = M_c\dot{U} - X$$

Therefore, from Eq. (54),

$$F_S = -M_L\dot{U} - \rho_L\sum \beta_n\ddot{a}_n \qquad (55)$$

These results will be cast in convenient forms for the circular canal and the spherical tank.

(3.1) *Circular Canal*

The quantities α_n and β_n in Eqs. (53)–(55) involve only the values of ϕ_n at the surface, which are proportional to the eigenfunctions w_n of the integral equation, Eq. (14). For convenience, choose $w_n(1) = 1$; then

$$\beta_n = (2\omega_n^2/g)(aR)^2\int_0^1 \xi w(\xi)\,d\xi$$

$$\alpha_n = 2(aR)\int_0^1 [w(\xi)]^2\,d\xi$$

Introduce, now, the slosh height ζ_n at the right-hand side of the canal associated with the nth mode.

$$\zeta_n = a_n(\partial\phi_n/\partial y)(aR) = (a_n)(\omega_n^2/g)\,w_n(1) = a_n\omega_n^2/g$$

The total height of slosh at the wall is then $\sum \zeta_n$. Eqs. (52)–(54) may then be modified to

$$\ddot{\zeta}_n + \omega_n^2\zeta_n = -(\lambda_n A)(B_n/A_n)\dot{U} \qquad (56)$$

$$(M_c + M_L)\dot{U} + 2\rho_L(aR)^2\sum B_n\ddot{\zeta}_n = X \qquad (57)$$

$$F_S = -M_L\dot{U} - 2\rho_L(aR)^2\sum B_n\ddot{\zeta}_n \qquad (58)$$

TABLE 1
Eigenvalues for Circular Canal

e	a	$\lambda_1 a$	$\lambda_2 a$	$\lambda_3 a$	λ_1	λ_2	λ_3
−1.0	0.0	0.0	0.0	0.0	1.0	6.0	15.0
−0.8	0.6	0.627	3.23	6.51	1.045	5.38	10.85
−0.6	0.8	0.879	3.98	7.30	1.099	4.97	9.13
−0.4	0.917	1.068	4.34	7.63	1.165	4.74	8.33
−0.2	0.980	1.224	4.56	7.82	1.249	4.65	7.99
0.0	1.0	1.360	4.70	7.96	1.360	4.70	7.96
0.2	0.980	1.482	4.81	8.06	1.513	4.91	8.23
0.4	0.917	1.596	4.89	8.15	1.742	5.34	8.89
0.6	0.8	1.706	4.97	8 22	2.13	6.22	10.28
0.8	0.6	1.822	5.05	8.30	3.04	8.42	13.84
1.0	0.0	2.018	5.20	8.44	∞	∞	∞

where

$$A_n = \int_0^1 [w_n(\xi)]^2 \, d\xi \tag{59}$$

and

$$B_n = \int_0^1 \xi w_n(\xi) \, d\xi \tag{60}$$

Here, of course, all forces and masses are understood to be per unit length of the canal.

It is important to note that for the circular canal these results are valid without the restriction imposed in the general development that only rectilinear motion of the tank in the x direction was permitted. Rotation of the canal about its center produces no sloshing, nor, by symmetry, does vertical tank motion produce horizontal sloshing force. (In fact, it can be shown that vertical motion produces no sloshing at all in the circular canal.) Since all pressures are in a radial direction, the resultant horizontal slosh force F_S always passes through the center of the canal.

(3.2) *Spherical Tank*

In terms of the sloshing natural modes

$$\phi_n = \psi_n(r, y) \cos k\theta$$

the parameter β_n is

$$\beta_n = (\omega_n^2/g) \int_0^{aR} \int_0^{2\pi} r(r \cos\theta) \psi_n(r, 0) \cos k\theta \, dr \, d\theta$$

Thus, it follows that β_n vanishes for all $k \neq 1$, justifying the restriction previously made to consideration of only the case $k = 1$. The values of ψ_n at the free surface are proportional to $f_n(\rho)$, where $f_n(\rho) = (1/\sqrt{\rho}) g_n(\rho)$, and $g_n(\rho)$ is an eigenfunction of the integral equation, Eq. (28). Normalize $f_n(\rho)$ so that $f_n(1) = 1$. Then, as in the circular canal case, the slosh height ζ_n at the wall is $a_n \omega_n^2/g$, and

$$\beta_n = (aR)^3(\omega_n^2/g) \int_0^1 \int_0^{2\pi} \rho^2 f(\rho) \cos^2\theta \, d\rho$$

$$= \pi(aR)^3(\omega_n^2/g) \int_0^1 \rho^2 f(\rho) \, d\rho$$

$$\alpha_n = (aR)^2 \int_0^1 \int_0^{2\pi} \rho [f(\rho)]^2 \cos^2\theta \, d\rho$$

$$= \pi(aR)^2 \int_0^1 \rho [f(\rho)]^2 \, d\rho$$

Hence, from Eqs. (53)–(55),

$$\ddot{\xi}_n + \omega_n^2 \xi_n = -(\lambda_n a)(D_n/C_n) \ddot{U} \tag{61}$$

$$(M_c + M_L)\ddot{U} + \pi\rho_L(aR)^3 \sum D_n \xi_n = X \tag{62}$$

$$F_S = -M_L \ddot{U} - \pi\rho_L(aR)^3 \sum D_n \xi_n \tag{63}$$

where

$$C_n = \int_0^1 \rho [f_n(\rho)]^2 \, d\rho = \int_0^1 [g_n(\rho)]^2 \, d\rho \tag{64}$$

and

$$D_n = \int_0^1 \rho^2 f_n(\rho) \, d\rho \tag{65}$$

The force F_S, again, passes through the center of the sphere.

(4) Numerical Results

(4.1) *Circular Canal*

The first three modes and frequencies for the circular canal were found for the values $e = 1$, 0.8, 0.6, 0.4, 0.2, 0, −0.2, −0.4, −0.6, and −0.8, from the 20-by-20 matrix formulation described in the Appendix. The values of $(\lambda_n a)$ and λ_n $(n = 1, 2, 3)$ thus obtained, together with those found analytically for $e = -1$, are given in Table 1.

The solid curves in Fig. 9 show the variation with e of $\sqrt{\lambda}$ (which is proportional to frequency) for the first three modes. Worthy of note is the fact that the variation with e of the higher frequencies is not monotonic; the minimum frequency of a given higher mode appears to occur slightly below the half full condition, whereas the fundamental mode has its lowest frequency in the nearly empty state. This situation is

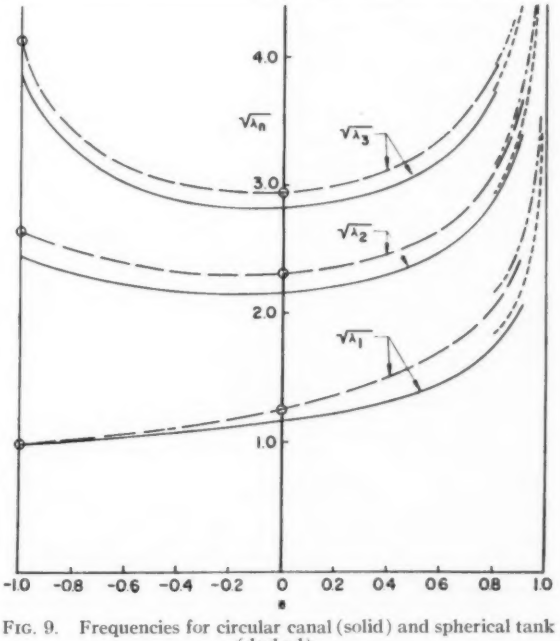

FIG. 9. Frequencies for circular canal (solid) and spherical tank (dashed).

at least partially associated with the fact that, in general, as depth increases, frequencies of free-surface oscillation tend to shift to more closely packed spectra. Thus, for example, the ratio λ_2/λ_1 decreases monotonically with increasing e.

For the nearly full case ($e = 1$), the matrix calculation provided the result $(\lambda_1 a) = 2.018$, as compared with the upper bound of 2.094 obtained from the one-term Galerkin solution. The corresponding asymptotic behavior

$$\sqrt{\lambda_1} \approx [(2.018)^{1/2}/(1 - e^2)^{1/4}] \text{ for } e \to 1$$

is shown as the dotted curve in Fig. 9; the asymptotic behaviors for $\sqrt{\lambda_2}$ and $\sqrt{\lambda_3}$ are similarly indicated.

TABLE 2
Eigenvalues for Spherical Tank

e	a	$\lambda_1 a$	$\lambda_2 a$	$\lambda_3 a$	λ_1	λ_2	λ_3
−1	0.0	0.0	0.0	0.0	1.0	7.0	17.0
0	1.0	1.565	5.34	8.66	1.565	5.34	8.66
1	0.0	2.78	5.99	9.25	∞	∞	∞

It may be noted that the upper bound $\lambda_1 = 1.367$ obtained by Rayleigh (or by the one-term Galerkin solution of this paper) for the half full canal is very close to the value $\lambda_1 = 1.360$ found from the matrix calculation. Rayleigh's improved upper bound, corresponding to $\lambda_1 = 1.356$, is actually more accurate, but there is little doubt that the results obtained from the matrix setup are entirely satisfactory for practical application.

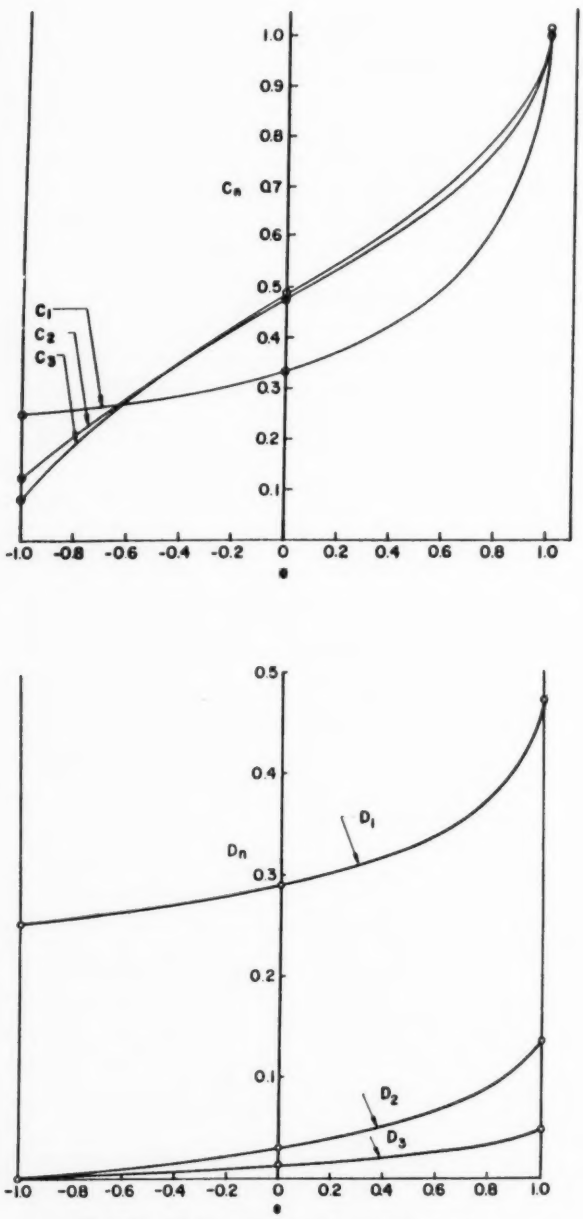

FIG. 10. Modal parameters for circular canal.

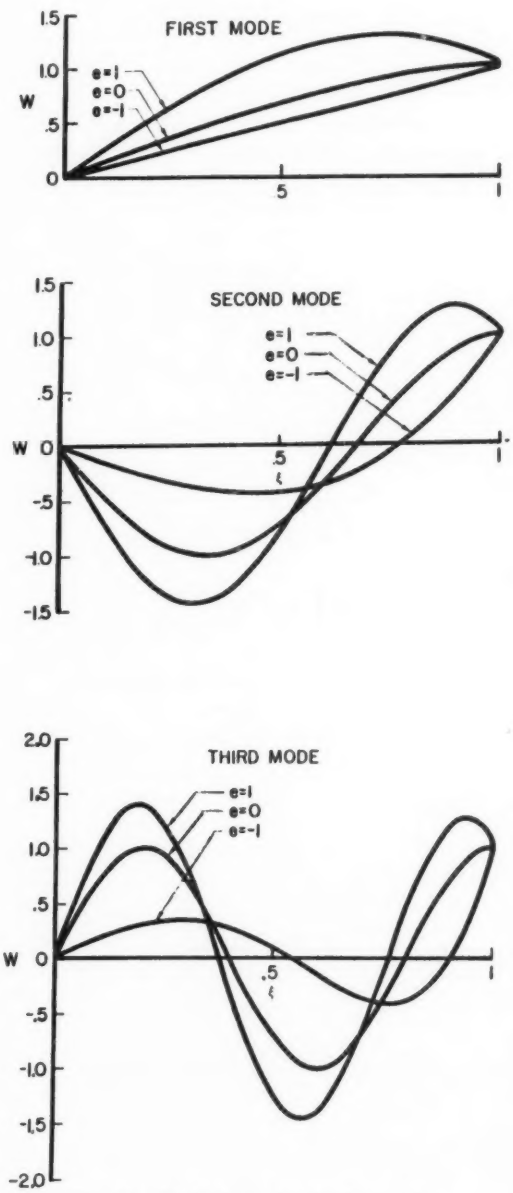

FIG. 11. Mode shapes for circular canal.

The modal parameters A_n and B_n defined by Eqs. (58) and (59) are plotted against e in Fig. 10. Except for the nearly empty case ($e = -1$), these parameters were found by numerical integration. For $e = -1$, the result [Eq. (22)] for the natural mode shapes provides:

$$A_n = 1/(4n - 1)$$
$$B_n = 1/3 \text{ for } n = 1$$
$$= 0 \text{ for } n > 1$$

The modal parameter B_n is closely related to the amount of nth mode induced by lateral acceleration. The low values of B_n for $n > 1$ indicate that, in general, the higher modes would not have a major influence on sloshing forces.

The mode shapes $w_n(\xi)$ are shown in Fig. 11 for $e = 1$, 0, and -1. A point of minor theoretical interest in connection with the mode shapes is that the slope at $\xi = 1$ can be shown to be given by

$$w_n'(1) = -\lambda_n e$$

Thus, the slope is negative for $e > 0$ and positive for $e < 0$; for $e = 1$, the slope is infinite. The nature of these slopes is a direct consequence of the inclination of the container wall at the free surface.

(4.2) *Spherical Tank*

The values of $(\lambda_n a)$ and λ_n for the nearly full ($e = 1$) and half full ($e = 0$) spherical tank were found, for $n = 1$, 2, and 3, from the matrix formulation described in the Appendix and are given in Table 2. Also presented in this table are the values found analytically for the nearly empty tank ($e = -1$). From the values of $(\lambda_n a)$ for $e = 1$, the asymptotic behavior of $\sqrt{\lambda_n}$ near $e = 1$ is shown as the dot-dash curves in Fig. 10, and the values of $\sqrt{\lambda_n}$ for $e = 0$ and $e = 1$ are shown as the circles in this figure. The dashed curves represent estimates of the variation of λ_n in the intermediate ranges, based on the presumably analogous trends for the circular canal.

The modal parameters C_n and D_n were calculated (by numerical integration for $e = 1$ and $e = 0$, and analytically from Eq. (42) for $e = -1$) and are shown in Fig. 12. The curves connecting the calculated points in this figure were estimated, with the results of Fig. 9 for the canal as a guide.

Finally, the mode shapes $f_n(\rho) = (1/\sqrt{\rho})g_n(\rho)$ for the three calculated cases are given in Fig. 13.

(5) Comparison With Experiment

Resonance tests (unpublished) conducted by the Lockheed Missile Systems Division on partially filled spherical tanks provided the experimental results for $\sqrt{\lambda_1}$, which are shown as crosses in Fig. 14. The estimated curve for $\sqrt{\lambda_1}$ given in Fig. 10 is reproduced in Fig. 14 for comparison. The agreement is generally good, and the agreement of experiment with the rigorously calculated frequency for the half full case is excellent.

(6) Conclusions

The results for the circular canal are sufficiently complete to be used in the dynamic analysis of such canals filled to arbitrary depth. Some degree of caution is evidently required, however, in the use of the estimated results for the spherical tank in the ranges intermediate to the nearly empty, half full, and nearly full cases.

Appendix—Numerical Solution of Integral Equations

The general kernel function [Eq. (13)] for the circular canal has a logarithmic singularity at $\xi = \bar{\xi} > 0$. For

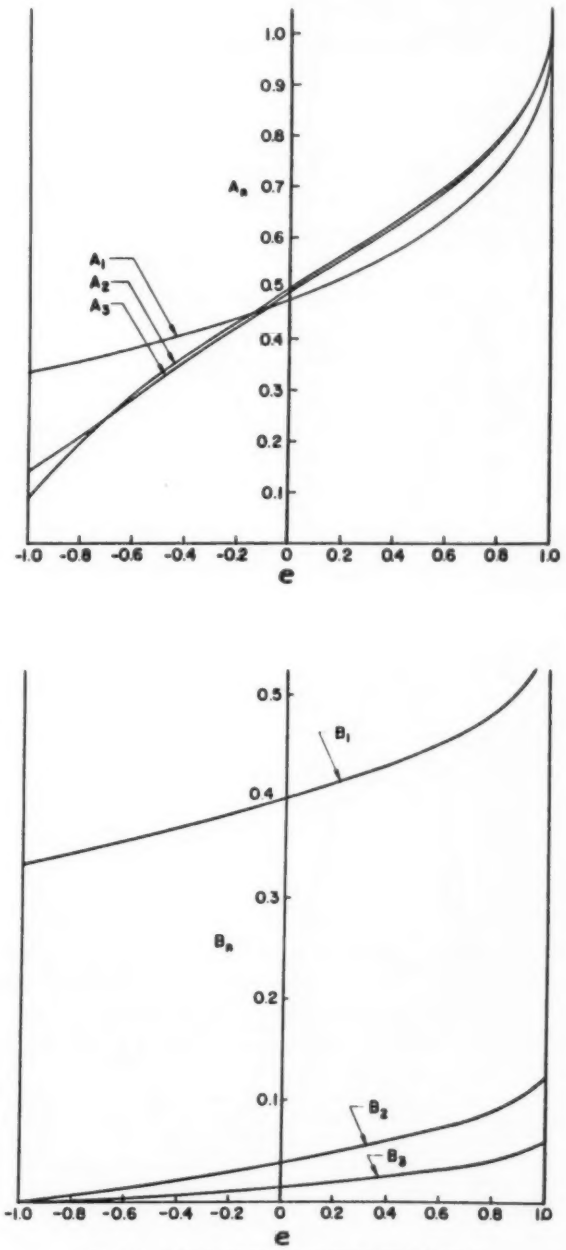

FIG. 12. Modal parameters for spherical tank.

ξ near $\bar{\xi}$, with $\xi \neq 1$,

$$G(\xi, \bar{\xi}) \approx -(1/\pi) \log |\xi - \bar{\xi}| + \rho(\xi) \quad \text{(A-1)}$$

where

$$\rho(\xi) = -\frac{1}{\pi} \log \left\{ \frac{2\gamma (1 - \xi^2)^{\gamma - 1}}{(1 + \xi)^{2\gamma} - (1 - \xi)^{2\gamma}} \right\} \quad \text{(A-2)}$$

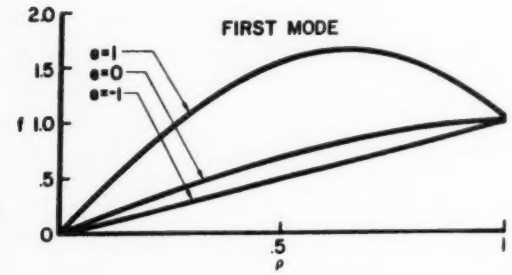

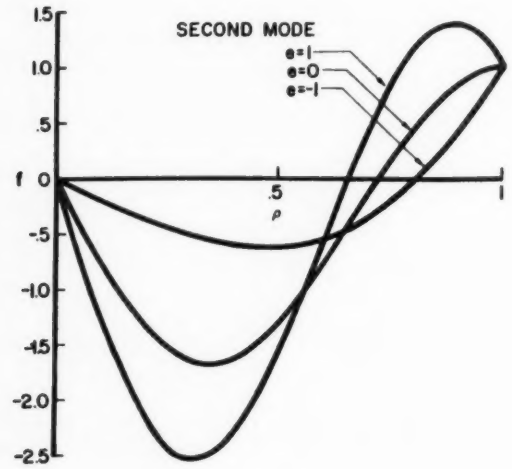

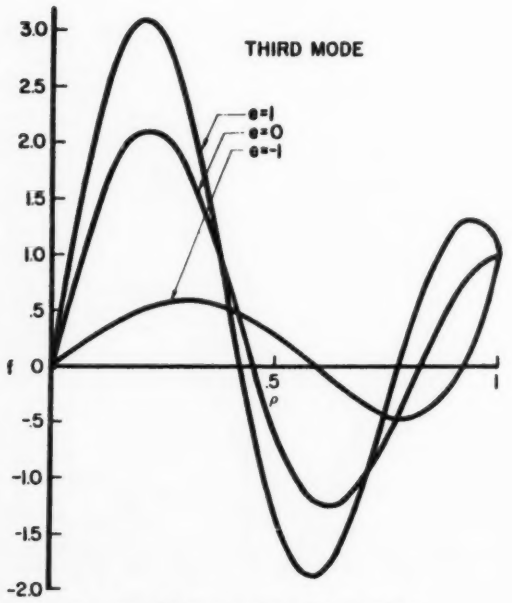

FIG. 13. Mode shapes for spherical tank.

Near $\xi = 1$,

$$G(1, \bar{\xi}) \approx -(\gamma/\pi) \log |1 - \xi| + \gamma \log 2 \quad \text{(A-3)}$$

Note, however, that $G(0, \bar{\xi}) = G(\xi, 0) = 0$ and recall that $w(0) = 0$. Then, the integral

$$\int_0^1 G(\xi, \bar{\xi})\, w(\bar{\xi})\, d\bar{\xi}$$

may be approximated by

$$\sum_{i=1}^{N-1} \omega(i\Delta) \int_{i\Delta - (\Delta/2)}^{i\Delta + (\Delta/2)} G(\xi, \bar{\xi})\, d\bar{\xi} + w(1) \int_{1 - \Delta/2}^{1} G(\xi, \bar{\xi})\, d\bar{\xi} \quad \text{(A-4)}$$

where $\Delta = 1/N$. Suppose $\xi = j\Delta$; then,

$$\int_{i\Delta - (\Delta/2)}^{i\Delta + (\Delta/2)} G(\xi, \bar{\xi})\, d\bar{\xi} \approx \Delta G(j\Delta, i\Delta) \quad i \neq j \neq N$$

$$\int_{1 - (\Delta/2)}^{1} G(\xi, \bar{\xi})\, d\bar{\xi} \approx (\Delta/2) G(j\Delta, 1) \quad j \neq N$$

$$\int_{j\Delta - (\Delta/2)}^{j\Delta + (\Delta/2)} G(\xi, \bar{\xi})\, d\bar{\xi} \approx \Delta p(j\Delta) + \int_{-(\Delta/2)}^{(\Delta/2)} -(1/\pi) \log |t|\, dt = \Delta \{ p(j\Delta) + (1/\pi)[1 - \log (\Delta/2)] \} \quad j \neq N$$

$$\int_{1 - (\Delta/2)}^{1} G(1, \bar{\xi})\, d\bar{\xi} \approx (\Delta/2) \{ [(\gamma/\pi) \log 2] + (\gamma/\pi)[1 - \log(\Delta/2)] \}$$

Hence, the integral equation, Eq. (14), is approximated by the matrix equation

$$AT \{w\} = (N/\lambda a) \{w\} \quad \text{(A-5)}$$

where $\{w\}$ is the column vector with elements $w(j\Delta)$ $(j = 1, 2, \ldots N)$, T is the "integrating" diagonal matrix

$$\begin{bmatrix} 1 & & & & \\ & 1 & & & \\ & & 1 & & \\ & & & \ddots & \\ & & & & 1/2 \end{bmatrix}$$

and A is the symmetrical square matrix with the general element A_{ij} defined by:

$$\begin{aligned} A_{ij} &= G(i\Delta, j\Delta) && i \neq j \neq N \\ &= p(j\Delta) + (1/\pi)[1 - \log(\Delta/2)] && i = j \neq N \\ &= (\gamma/\pi)\log 2 + (\gamma/\pi)[1 - \log(\Delta/2)] && i = j \neq N \end{aligned}$$

Note that, in the absence of a logarithmic singularity, the integration scheme would reduce precisely to the conventional trapezoidal rule.

The orthogonality condition for distinct eigenfunctions w_m and w_n

$$\int_0^1 w_m(\xi) w_n(\xi) d\xi = 0$$

is approximated, according to trapezoidal rule, by

$$[w_m]\,T\{w_n\} = 0 \qquad \text{(A-6)}$$

where $[w_m]$ is a row matrix and $\{w_n\}$ is a column matrix.

The orthogonality condition [Eq. (A-6)] is satisfied exactly by the eigenvectors of the matrix equation, Eq. (A-5), and, for this reason, the present integration scheme is considered to be a reasonably appropriate one.

An entirely analogous scheme is adaptable to the integral equation, Eq. (22), for the spherical tank. In the case of the nearly full tank, the behavior of $H(\rho, \bar{\rho})$ near $\bar{\rho} = \rho$ is

$$H(\rho, \bar{\rho}) \approx (1/\pi)\log|\rho - \bar{\rho}| + (1/\pi)(\log \rho + \log 8 - 2) \qquad \text{(A-7)}$$

including the case $\rho = 1$.

For the half full tank, for $\bar{\rho}$ near ρ, with $\rho \neq 1$,

$$H(\rho, \bar{\rho}) \approx -(1/\pi)\log|\rho - \bar{\rho}| + (1/\pi)[\log \rho + 2\rho^3 K(\rho^2) + \log 8 - 2] \qquad \text{(A-8)}$$

On the other hand, $H(1, \bar{\rho})$ near $\bar{\rho} = 1$ is

$$H(1, \bar{\rho}) \approx -(2/\pi)\log(1 - \bar{\rho}) + (1/\pi)(2\log 8 - 2) \qquad \text{(A-9)}$$

Hence, the matrix formulations for the spherical tank may be made in a fashion similar to those for the circular canal; the eigenvectors are then proportional to $\sqrt{\rho f_n(\rho)}$.

Eigenvalues and eigenvectors of the matrix $C = AT$ [Eq. (A-5)] were found by using a Remington Rand 1103AF computer on the basis of 20-by-20 matrix approximation—i.e., $N = 20$. The highest eigenvalue of C (and, hence, the lowest value of λ) and the corresponding eigenvector were found by matrix iteration. The second mode was found from the modified ("swept") matrix

$$C' = C - C\{w_1\}\,[w_1]\,T$$

where w_1 is the previously determined first eigenvector, normalized according to

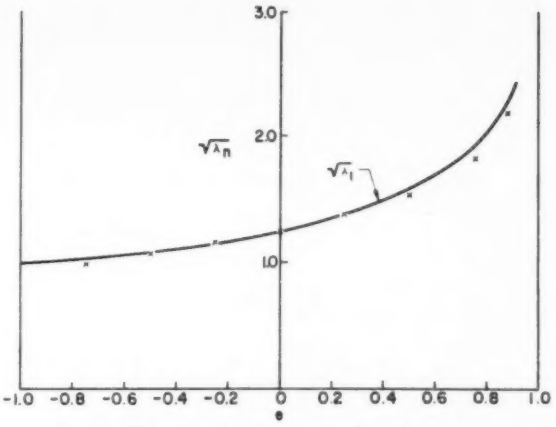

FIG. 14. Experimental frequencies for spherical tank.

$$[w_1]\,T\{w_1\} = 1$$

After determining the second eigenvalue and eigenvector, again by iteration, C' was similarly swept to provide a matrix C'', direct iteration of which gave the third eigenvalue and eigenvector.

References

[1] Lamb, Sir Horace, *Hydrodynamics*, 6th Ed., Dover Publications, New York, 1945.

[2] Graham, E. W., *The Forces Produced by Fuel Oscillation in a Rectangular Tank*, Douglas Aircraft Co., SM-13748, April, 1951.

[3] Lawrence, H. R., Wang, C. T., and Reddy, R. B., *Variational Solution of Fuel Sloshing Modes*, Jet Propulsion, Vol. 28, No. 11, November, 1958.

[4] Jahnke, E., and Emde, F., *Tables of Functions*, 4th Ed., Dover Publications, New York, 1945.

[5] Grobner, W., and Hofreiter, N., *Integraltafel, Zweiter Teil, Bestimmte Integrale*, p. 40, Springer-Verlag, Vienna, 1950.

[6] Kellogg, O. D., *Foundations of Potential Theory*, p. 247, Ungar Publishing Co., New York.

[7] Byrd, Paul F., and Friedman, Morris D., *Handbook of Elliptic Integrals*, Springer-Verlag, Berlin, 1954.

Notice to Contributors

To expedite review, an additional copy of both the manuscript and figures should be submitted. The manuscript submitted for publication *must* be a double- or triple-spaced original. There should be wide margins on all sides of the sheets and triple spacing around formulas to allow for the marking of directions to the printer.

Original drawings (jet black India ink on white paper or tracing cloth) should accompany the manuscript. *(Blueprints are not acceptable.)* Photographs *must* be on glossy white paper. The smallest lettering on 8- by 10-in. figures should be no less than 1/4 in. high.

Formulas should be typewritten or carefully written in pen and ink. The difference between capital and lower-case letters and Greek symbols should be clearly distinguished.

See Inside Back Cover of this issue for further details

Viscous Aerodynamic Characteristics in Hypersonic Rarefied Gas Flow†

RONALD F. PROBSTEIN* AND NELSON H. KEMP**

Avco-Everett Research Laboratory

Summary

This paper considers the problem of calculating viscous aerodynamic characteristics of blunt bodies at hypersonic speeds and at sufficiently high altitudes where the appropriate mean free path becomes too large for the use of familiar boundary-layer theory but not so large that free molecule concepts apply.

Results of an order-of-magnitude analysis are presented to define the regimes of rarefied gas flow and the limits of continuum theory. Based on theoretical and experimental evidence, the complete Navier-Stokes equations are used as a model, except "very close" to the free molecule condition. This model may not necessarily give the shock wave structure in detail but satisfies overall conservation laws and should give a reasonably accurate picture of all mean aerodynamic quantities.

In this "intermediate" regime there are two fundamental classes of problems: a "viscous layer" class and a "merged layer" class, the latter corresponding to a larger degree of rarefaction. For the viscous layer class there is a thin shock wave, but the shock layer region between the shock and the body is fully viscous, although the viscous stresses and conductive heat transfer are small at the shock wave boundary. Here, the use of the Navier-Stokes equations with outer boundary conditions given by the Hugoniot relations is justified. For the merged layer class, the shock wave is no longer thin, and the Navier-Stokes equations can be used to give a solution which includes the shock structure and has free-stream conditions as outer boundary conditions. A simpler procedure is presented for "incipient merged" conditions where the shock may no longer be considered an infinitesimally thin discontinuity but where it has not thickened sufficiently to entail the "fully merged layer" analysis. In this case we approximate the shock by a discontinuity obeying conservation laws which include curvature effects, viscous stresses, and heat conduction.

For a sphere and cylinder it is shown that the Navier-Stokes equations can be reduced to ordinary differential equations for both the viscous and merged layer class of problems. Solutions of these equations, when used in connection with hypersonic flow problems, are in general only valid in the stagnation region. To illustrate the viscous layer solutions, numerical calculations have been performed for a sphere and cylinder with the assumption of constant density in the shock layer, which is a useful approximation at hypersonic speeds. To illustrate the merged layer solution, calculations have been carried out for a sphere using the incipient merged layer approximation.

Results are presented for detachment distance, surface shear, and heat-transfer rate in the stagnation region of a highly cooled sphere flying at hypersonic speed. With decreasing Reynolds number, the shear and heat transfer are shown to increase above the extrapolated boundary-layer values in the viscous layer regime and then to begin falling in the incipient merged regime. As the Reynolds number decreases in the incipient merged regime, the density in the shock layer increases, and the static and stagnation enthalpy behind the shock decrease.

Calculations performed for an insulated sphere show that, with decreasing Reynolds number in the incipient merged regime, the density in the shock layer decreases; the total enthalpy behind the shock and at the stagnation point increase so that they are higher than the free-stream total enthalpy; and the stagnation-point pressure behaves like the total enthalpy.

For the highly cooled cylinder in the viscous layer regime, the same quantities are presented as for the sphere. The increase found in shear and heat transfer above extrapolated boundary-layer theory is small, in agreement with vorticity interaction theory.

A discussion is given of the behavior of available experimental data for viscous flow quantities in the intermediate regime and the behavior predicted by the results of the present calculations. Qualitative agreement is indicated.

Symbols

A, B	=	constants in specified surface enthalpy, Eq. (4-13)
c_p	=	specific heat at constant pressure
$e_{\alpha\beta}$	=	component of strain tensor
f''	=	boundary-layer constant in shear stress, Eq. (5-20)
G	=	vorticity divided by sin θ, Eq. (5-4)
$(g_b')_{Pr=1}$	=	boundary-layer constant in heat-transfer rate, Eq. (5-21)
h	=	specific enthalpy
h_0, h_2	=	enthalpy functions, Eq. (4-1g)
$\tilde{h}_2$	=	$h_2 - h_0$
j	=	integer specifying number of dimensions, = 0 for two-dimensional case, = 1 for axisymmetric case
k	=	thermal conductivity
M_∞	=	free-stream Mach number
p	=	pressure
p_0, p_2	=	pressure functions, Eq. (4-1f)
Pr	=	Prandtl number, $c_p\mu/k$
q_R, q_θ	=	radial and tangential velocity components
$-q_0$	=	stagnation-point surface heat-transfer rate
R	=	radial polar coordinate
R_b	=	radius of curvature of body
R_s	=	radius of curvature of shock
Re_∞	=	Reynolds number, $\rho_\infty U R_b/\mu_\infty$
Re_b	=	Reynolds number, $\rho_\infty U R_b/\tilde{\mu}_0$
Re_s	=	Reynolds number, $\rho_\infty U R_s/\mu_{0_s}$
T	=	absolute temperature
U	=	free-stream velocity
V	=	$U(\gamma - 1)/(\gamma + 1)$

Presented at the Aerodynamics—IV Session, IAS 27th Annual Meeting, N.Y., January 26–29, 1959. Resubmitted March 2, 1959.

† This work was supported by the Ballistic Missile Division, Air Research and Development Command, USAF, under Contract AF 04(645)-18 and AF 04(647)-278. The authors thank Professors Wallace D. Hayes of Princeton University and James A. Fay of the Massachusetts Institute of Technology for many suggestions and stimulating discussions during the course of the present work. Grateful acknowledgment is also made to Miss Patricia Jackson and Mr. Al Amoling of the Avco-Everett Research Laboratory for their competent and patient handling of the numerical calculations.

* Consultant; also Professor of Engineering, Brown University, Providence, Rhode Island.

** Principal Research Scientist.

u, v = velocity functions, Eqs. (4-1b) and (4-1c)
x = distance along body surface measured from stagnation point
γ = isentropic exponent
Δ = shock layer thickness (detachment or stand-off distance of shock from stagnation point)
δ_s = shock-wave thickness
ϵ = density ratio across shock, ρ_∞ / ρ_s
θ = polar angle
λ = mean free path
μ = ordinary viscosity coefficient
μ^* = dilational or bulk viscosity coefficient
μ_0 = ordinary viscosity function Eq. (4-1d)
$\mu_0{}^*$ = dilational viscosity function, Eq. (4-1e)
$\tilde{\mu}_0$ = ordinary viscosity function evaluated at an enthalpy of $U^2/2$
ν_s = kinematic viscosity constant, μ_{0_s}/ρ_{0_s}
ρ = mass density
ρ_0 = density function, Eq. (4-1a)
τ = shear stress at body
$\tau_{\alpha\beta}$ = components of shear tensor
Φ = dissipation function in energy equation
ψ = stream function, Eq. (5-1)
Ψ = R-dependent part of stream function, Eq. (5-2)
Ω = vorticity interaction parameter, Eq. (5-24)
Ω_η = vorticity component normal to flow plane, Eq. (5-4)

Subscripts

b = conditions at body surface (or wall)
FM = free molecule value
R, θ, n = radial, tangential, and normal directions, respectively
s = conditions immediately behind (downstream of) shock wave
stag = conditions at stagnation point
∞ = conditions in free stream
$( )'$ = differentiation with respect to R
$\sim$ = same order of magnitude (requires dimensional consistency)

(1) Introduction

AN INCREASINGLY important problem in aeronautical engineering is that of predicting aerodynamic characteristics of bodies flying at very high speeds and high altitudes. Under these conditions, the flow about a given aerodynamic configuration may be sufficiently rarefied so that the appropriate mean free path becomes too large for the use of classical boundary-layer theory but not large enough for free molecule concepts to apply. In such an "intermediate" rarefied gas regime, any complete calculation of the flow field would in general require the full formulation of kinetic theory. At the present time such an approach is not satisfactory for obtaining mean aerodynamic characteristics such as skin friction and surface heat-transfer rate.

An alternative procedure for making reasonably accurate estimates of the mean flow variables at hypersonic speeds is to postulate the Navier-Stokes equations as a model for this intermediate regime. In so doing we assume that the flow is not so close to the free molecule condition that it is in the first-order molecular collision regime, to be defined later. Such a "continuum" approach was suggested by Adams and Probstein,[1] and the ideas were modified and further amplified in Sections 10.1 and 10.2 of Hayes and Probstein,[2] and in reference 3. The assumption that the Navier-Stokes model should be a satisfactory one for determining mean flow quantities, even when continuum concepts may no longer be theoretically justified, is empirically based upon certain known experimental and analytical results which are briefly outlined in reference 2.

Most earlier analytical treatments of the intermediate regime have dealt principally with the effect of the introduction of slip and temperature jump into the flow. This approach to the problem is most adequately described in Schaaf and Chambré.[4] The present treatment is not meant to imply that slip does not exist as an identifiable phenomenon, but only that its effect on mean aerodynamic quantities is generally not large at hypersonic speeds where our Navier-Stokes model is applicable, although, if the body is insulated, it will have to be considered in certain cases.

(2) Rarefied Gas Flow Regimes

Rarefied gas flow regimes may be classified according to the degree of rarefaction as measured by the value of the Knudsen number, defined as the ratio of the mean free path λ to a characteristic flow length L. In references 1–3, it was emphasized that the concept of the Knudsen number must be applied in context, in connection with the particular characteristic scale used and the particular phenomenon of interest. For example, if we are interested in the flow behind a strong shock wave, we must consider the mean free path behind the shock, whereas if we are studying the structure of a strong shock wave, we must consider the characteristic length to be its thickness. It is as a result of this point of view that we find differences arising in our classification of rarefied gas flow regimes when compared with the original classification of Tsien.[5]

We shall summarize, for hypersonic flight speeds, a possible classification for the regimes of rarefied gas flow. This classification is discussed in greater detail in reference 2, Section 10.1. It is based principally on consideration of a blunt body, but it is general enough so that its main features are applicable to slender configurations as well, with appropriately redefined characteristic lengths.

In assessing the limits of continuum theory, we shall assume that the local mean free path must be small compared to the characteristic length of interest for continuum theory to be valid. Therefore, we take as the basic criterion for continuum flow on an axisymmetric blunt body

$$\lambda_s/\Delta \ll 1 \qquad (2\text{-}1)$$

Here, the subscript s denotes conditions in the shock layer behind a shock wave which may not be sharply defined, and Δ is the shock layer thickness (see Fig. 1). With R_b, the body radius of curvature, the order of Δ is given by (cf. references 1–3)

$$\Delta/R_b \sim \epsilon \tag{2-2}$$

where

$$\epsilon \equiv \rho_\infty/\rho_s \tag{2-3}$$

is the density ratio across the shock, taken to be approximately constant along the shock and small compared to one. For air behaving as a perfect gas at hypersonic speeds, $\epsilon \to 1/6$, while for atmospheric hypersonic flight, because of the elevated temperatures and resultant activation of more degrees of freedom, such as dissociation, ϵ is of the order of 0.1 to 0.07 or less. At hypersonic speeds the corresponding order of magnitude of the pressure p_s is $\rho_\infty U^2$ and of the enthalpy, h_s is $(1/2)U^2$, where U is the free-stream velocity. In the shock layer the tangential velocity component q_θ is of the order of Ux/R_b with x the distance along the surface measured from the stagnation point, while the magnitude of the radial velocity component q_R varies from ϵU to U depending on the degree of rarefaction.

Since we are primarily interested in hypersonic flight conditions where the temperatures of interest in the flow field are high, we may for simplicity assume that the viscosity μ is proportional to the square root of the absolute temperature T. This corresponds to the rigid sphere model of kinetic theory for which $\lambda\rho$ is a constant. With this assumption, it follows from our previous estimates that

$$\lambda_s/\Delta \sim \lambda_\infty/R_b \sim M_\infty/Re_\infty \tag{2-4}$$

where the subscript ∞ denotes free-stream conditions, M_∞ is the free-stream Mach number, and Re_∞ is the free-stream Reynolds number

$$Re_\infty \equiv \rho_\infty U R_b/\mu_\infty \tag{2-5}$$

We should point out that, with a two-dimensional blunt body, these order-of-magnitude estimates would have to be somewhat revised since, with ϵ small, the shock layer thickness is much larger than on the corresponding axisymmetric blunt body. Furthermore, although as a result of the assumption of hypersonic speeds, certain of our free-stream criteria may appear similar to those of Tsien,[5] we point out that these free-stream criteria would change with lower speeds and different body shapes.

The preceding order-of-magnitude estimates are used to define in a rough quantitative manner the intermediate regime. We may consider as one limit of this intermediate regime the boundary-layer regime which exists at Reynolds numbers sufficiently high that viscous effects can be taken into account by classical boundary-layer theory. The other limit at the very low density end is the free molecule regime where intermolecular collisions are neglected and the mean free path is everywhere much larger than the characteristic length. Based on the classification given in reference 2, we subdivide the intermediate regime from high to very low Reynolds numbers as follows:

(1) *Vorticity Interaction Regime*

The vorticity in the inviscid part of the shock layer is sufficiently high that boundary-layer concepts must be modified. Without external vorticity, the velocity at the outer edge of the boundary layer equals the velocity at the inner edge of the inviscid flow obtained by ignoring the boundary layer. With external vorticity, the velocity at the outer edge of the boundary layer must equal the velocity in the inviscid flow at the same value of the stream function. A parameter characterizing the importance of vorticity interaction may be defined as the ratio of the external inviscid vorticity to the average vorticity in the boundary layer (roughly the velocity at the edge of the boundary layer divided by the boundary layer thickness). In the case of a blunt axisymmetric body, the inviscid velocity profile is approximately linear and the vorticity interaction parameter is of the order of one. From this condition the above order-of-magnitude estimates lead to the following rough quantitative limit for this regime:

$$\lambda_\infty/R_b \ll \epsilon \tag{2-6}$$

(2) *Viscous Layer Regime*

Here the Reynolds numbers are less than required for the validity of the vorticity interaction approach; the shock layer is a fully viscous continuum amenable to treatment with the complete Navier-Stokes equations; and the shock wave may be treated as a discontinuity across which the Hugoniot (shock) relations apply. Expressing this condition by requiring the shear at the shock $(\mu\partial q_\theta/\partial R)_s$ to be small compared with the tangential momentum transport at the shock $(\rho q_\theta q_R)_s$, we can show that we may use the viscous layer concept when

$$\lambda_\infty/R_b \ll \epsilon^{1/2} \tag{2-7}$$

(3) *Incipient Merged Layer Regime*

Here we consider the shock layer still to be a continuum but may no longer consider the shock as a discontinuity satisfying the classical Hugoniot relations. In one approach to this regime, we determine conditions behind the shock by treating it as thin but introducing the effects of curvature, viscous stresses, and heat conduction into the integrated conservation equations. In this case the density ratio is not given by the usual shock-wave relations nor is the tangential velocity component constant through the shock wave. This regime is delimited by Eq. (2-1), that is,

$$\lambda_\infty/R_b \ll 1 \tag{2-8}$$

(4) *Fully Merged Layer Regime*

For this regime the shock layer is taken to be in an almost continuum state, and the shock wave is no longer thin. A strict treatment of this regime requires the full formulation of kinetic theory. We may delimit its range roughly by the condition that

$$\lambda_\infty/R_b < 1 \tag{2-9}$$

(5) Transitional Layer Regime

The merged shock layer is taken to be in an almost first-order collision regime defined below. It is delimited by the inequality

$$\lambda_\infty / R_b > 1 \qquad (2\text{-}10)$$

(6) First-Order Collision Regime

In this regime the appropriate local Knudsen number is large but not large enough to ensure the full validity of the free molecule concept. Here an analysis can be carried out by taking into account only collisions between a free-stream molecule and a molecule re-emitted by the surface. We shall not consider this regime any further but instead refer the reader to Lunc and Lubonski,[6] Baker and Charwat,[7] Hammerling and Kivel,[8] Liu,[9] and Willis.[10]

From our definitions, the flow within the shock layer down to and including the incipient merged layer regime is a continuum and is properly described by the compressible Navier-Stokes equations. Although neither the fully merged layer regime nor the transitional layer regime is a continuum regime, we may for purposes of obtaining estimates of skin friction, heat transfer, and other mean aerodynamic quantities postulate the complete Navier-Stokes equations as a model for these regimes. This point of view was discussed in the Introduction.

Excluding the first-order collision regime, with the Navier-Stokes model there are essentially two classes of problems in the whole intermediate regime. In the one class we have a discontinuous shock with negligible viscous stresses and heat conduction immediately behind the shock wave, and the Navier-Stokes equations are used in the shock layer with outer boundary conditions given by the Hugoniot shock relations. This class of problems we term a "viscous layer" class, and it includes both the viscous layer and vorticity interaction regimes. (See Fig. 1a.) In the other class of problems the Navier-Stokes equations are used with outer boundary conditions given by free-stream conditions. Here, if we choose to include the shock structure in the incipient merged layer regime, we can treat this regime together with the fully merged layer and transitional layer regimes in one class of problems we term a "merged layer" class. (See Fig. 1b). We note that, if the body is insulated, slip and temperature jump will have to be considered in the fully merged layer and transitional layer regimes; however, if the body is cooled, these factors will not be important in affecting the mean flow variables.[2]

(3) Coordinate Systems and Basic Equations

The approach we shall adopt to solve the viscous and merged layer problems allows us, at least for a cylinder and a sphere, to reduce the Navier-Stokes equations to ordinary differential equations. Solutions of the resulting equations, when applied to hypersonic flow past a sphere or cylinder, are in general only

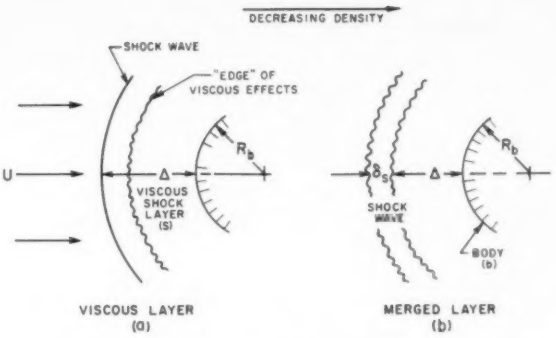

FIG. 1. Sketch of stagnation region flow field in intermediate regime.

applicable to the stagnation region because of the unrealistic behavior which is required of such quantities as the viscosity, enthalpy, and thermal conductivity away from the stagnation region. The procedure for obtaining these solutions is to use cylindrical or spherical coordinates, respectively, and to seek cylindrically or spherically symmetric solutions. Such a procedure is analogous to that employed by Lighthill[11] in obtaining his inviscid constant density spherical solution and that used by Whitham[12] and Hayes and Probstein[2] in obtaining the analogous cylindrical solution. These treatments made the assumptions of a discontinuous shock wave, an inviscid shock layer, a constant density ratio across the shock, and constant density in the shock layer. Although the approach described in this paper is related to the one used by these authors, it is more general, particularly for the merged layer class of problems.

An alternative approach to the present one, described in references 1 and 2, is to employ a coordinate system of the boundary-layer type and to simplify the Navier-Stokes equations, based on an analysis in which the shock layer thickness is assumed to be small in comparison to the body radius (or radii) of curvature. The actual analysis of the orders of magnitude is identical with the classical one for the boundary-layer equations. The magnitudes of most of the flow variables were given in the preceding section. The results of such an analysis show that the tangential momentum equation is the same as the boundary-layer momentum equation with a curvature term added. The principal difference is that the usual boundary-layer assumption that the normal pressure gradient may be neglected cannot generally be made, as for example within a shock wave. The analysis which is carried out to determine the appropriate normal momentum equation is, however, the same as in the usual boundary-layer theory. Solution of this system of equations in the stagnation region of blunt bodies makes use of local similarity and takes advantage of the fact that for local similarity to apply the shock layer must be thin.

Both the thin layer approach and the present approach employing a complete solution with cylindrical or spherical symmetry are in general compatible. As just noted, it will be seen that sufficiently far from the

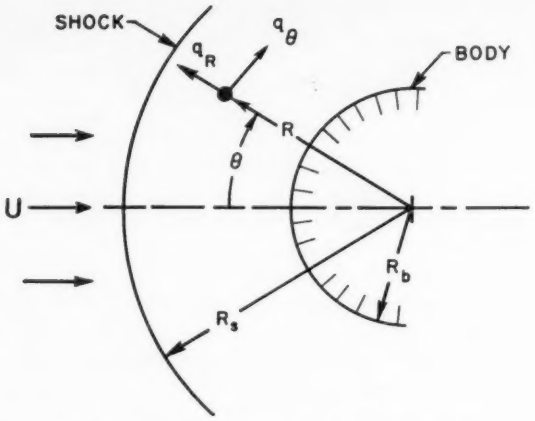

FIG. 2. Coordinate system for cylinder and sphere.

stagnation region, that is, for sufficiently large ray angles θ (Fig. 2), the complete symmetric solutions are in general unjustifiable and may be anomalous. On the other hand, for a blunt body the thin layer approach is only valid near the stagnation region. A closer examination shows that for application to hypersonic flight problems the validity of both approaches is roughly the same and both require the hypersonic condition that the shock layer be thin. However, apart from this question, the complete solutions of the present paper do afford new solutions of the Navier-Stokes equations which may in themselves be of interest.

The basic equations for our problem are the compressible, heat-conducting Navier-Stokes equations written in cylindrical polar or spherical polar coordinates R and θ with the axis $\theta = 0$ directed upstream and with respective velocity components q_R and q_θ. (See Fig. 2.) These equations for a flow in thermodynamic quasi-equilibrium are given in Appendix (A).

For both the merged and viscous layers with no slip or temperature jump, the boundary conditions at the body surface $R = R_b$ are

$$q_\theta(R_b) = 0, \quad q_R(R_b) = 0 \tag{3-1a}$$

$$h(R_b) = h_b(\theta) \text{ or } \partial h(R_b)/\partial R = \text{function of } \theta \tag{3-1b}$$

Here h is the specific enthalpy; the subscript b denotes conditions at the body surface; and function of θ in Eq. (3-1b) is zero for an insulated surface.

For the merged layer we have free-stream conditions as outer boundary conditions:

$$q_\theta \to U \sin\theta, \quad q_R \to -U\cos\theta, \quad \text{as } R \to \infty \tag{3-2a}$$

$$\rho \to \rho_\infty, \quad p \to p_\infty, \quad h \to h_\infty, \quad \text{as } R \to \infty \tag{3-2b}$$

Because of the equation of state, only two of the three conditions in Eq. (3-2b) are independent.

For the viscous layer the outer boundary conditions are those existing behind a discontinuous circular or spherical shock of radius R_s:

$$q_\theta(R_s) = U\sin\theta, \quad q_R(R_s) = -\epsilon U\cos\theta \tag{3-3a}$$

$$p(R_s) = p_\infty + \rho_\infty U^2\cos^2\theta(1-\epsilon) \tag{3-3b}$$

$$h(R_s) = h_\infty + (1/2)U^2\cos^2\theta(1-\epsilon^2) \tag{3-3c}$$

where

$$\rho(R_s) \equiv \rho_\infty/\epsilon \tag{3-3d}$$

Eqs. (3-3) are just the Hugoniot relations for an infinitesimally thin shock. We note that ϵ as written here is purely a definition, and, to specify the density, we must introduce an equation of state between the thermodynamic variables ρ, h, and p. In the present paper we shall be concerned with shocks sufficiently strong that the density ratio takes on its limiting value, which depends only on the thermodynamic state behind the shock. For purposes of numerical calculation, we will use the perfect gas law

$$p = \rho h[(\gamma-1)/\gamma] \tag{3-4}$$

behind the shock, with γ the isentropic exponent there. This, combined with the Hugoniot relations, then gives for the limiting density ratio

$$\epsilon = (\gamma-1)/(\gamma+1) \tag{3-5}$$

With Eq. (3-5) it is clear that in this limiting case either γ or ϵ may be specified interchangeably as a parameter of the problem.

In the viscous layer problem the location of the shock wave relative to the body is unknown. Because of the free boundary nature of this problem, one additional boundary condition will in general be required. This point will be discussed further in connection with each of the various models of the flow field to be considered.

(4) Symmetric Solutions

Subject to the boundary conditions stated previously we now seek cylindrically and spherically symmetric solutions of the complete Navier-Stokes equations which are given in Appendix (A). We assume that the dependent variables have the functional forms

$$\rho = \rho_0(R) \tag{4-1a}$$

$$q_\theta = u(R)\sin\theta \tag{4-1b}$$

$$q_R = -v(R)\cos\theta \tag{4-1c}$$

$$\mu = \mu_0(R)\cos\theta \tag{4-1d}$$

$$\mu^* = \mu_0^*(R)\cos\theta \tag{4-1e}$$

$$p = p_0(R)\cos^2\theta + p_2(R)\sin^2\theta \tag{4-1f}$$

$$h = h_0(R)\cos^2\theta + h_2(R)\sin^2\theta \tag{4-1g}$$

Here μ^* is the dilational or bulk coefficient of viscosity. For simplicity we replace $c_p dT$ by dh in the energy equation and take the Prandtl number $Pr = c_p\mu/k$ to be constant.

With the forms given above substituted into the Navier-Stokes equations, we find on equating like terms in θ that they reduce to the six simultaneous ordinary differential equations

$$(\rho_0 v)' - (1 + j)\rho_0(u - v)/R = 0 \quad (4\text{-}2)$$

$$p_0' + \rho_0 v v' = 2[-\mu_0 v' + (\mu_0^* - \mu_0/3)v\rho_0'/\rho_0]' + (1 + j)\mu_0[u' - 2v' - 3(u - v)/R]/R \quad (4\text{-}3)$$

$$p_2' - \rho_0 u[(u - v)/R] = -(\mu_0/R)\{u' - [(u - v)/R]\} \quad (4\text{-}4)$$

$$[2(p_2 - p_0)/R] + \rho_0\{-vu' + u[(u - v)/R]\} = (\mu_0\{u' - [(u - v)/R]\})' - (4/R)(\rho_0'/\rho_0)v[\mu_0^* - (1/3)\mu_0] + (\mu_0/R)\{(2 + j)u' - (6 + j)[(u - v)/R]\} \quad (4\text{-}5)$$

$$-\rho_0 v h_0' = (1/Pr)\{(\mu_0 h_0')' + [(1 + j)/R]\mu_0 h_0' + 2[(1 + j)/R^2]\mu_0(h_2 - h_0)\} - vp_0' + (4/3)\mu_0(\{v' + [(u - v)/R]\}^2 - (1 - j)v'[(u - v)/R]) - \mu_0^*[(v\rho_0')/\rho_0]^2 \quad (4\text{-}6)$$

$$-\rho_0 v h_2' + 2\rho_0(u/R)(h_2 - h_0) = (1/Pr)\{(\mu_0 h_2')' + [(1 + j)/R]\mu_0 h_2' - (4/R^2)\mu_0(h_2 - h_0)\} - vp_2' + 2(u/R)(p_2 - p_0) + \mu_0\{u' - [(u - v)/R]\}^2 \quad (4\text{-}7)$$

Here a prime denotes differentiation with respect to R, $j = 0$ for two-dimensional flow, and $j = 1$ in axisymmetric flow. We note that Eq. (4-2) derives from the continuity equation, Eqs. (4-3)–(4-5) from the two momentum equations, and Eqs. (4-6) and (4-7) from the energy equation.

We now have six equations for nine unknowns. Two more relations are given by the dependence of the viscosity functions on R. For example, these functions may be related to the temperature along the stagnation streamline $\theta = 0$. An additional relation which deals with the state properties of the fluid is necessary to specify the problem. In the illustrative examples presented in the following sections, we assume the flow in the shock layer to be approximated by one of constant density and specify the state properties by $\rho_0 = \text{const}$. The usefulness of this approximation will be discussed later.

If we consider the flow in the shock layer to be one of variable density, we must introduce an equation of state of the form

$$p = p(\rho, h) \quad (4\text{-}8)$$

However, such an equation yields two additional relations. For example, if we were to use the perfect gas law

$$p = \rho h[(\gamma - 1)/\gamma] \quad (4\text{-}9)$$

we would obtain

$$p_0 = \rho_0 h_0[(\gamma - 1)/\gamma] \quad (4\text{-}10)$$

and

$$p_2 = \rho_0 h_2[(\gamma - 1)/\gamma] \quad (4\text{-}11)$$

These two equations lead to an overdetermined problem. The assumed forms of the solution are thus seen to be consistent with a kinematic equation of state, $\rho_0 = \text{const.}$, but are not capable of exactly satisfying the added degree of freedom of a thermodynamic relation such as the perfect gas law. We note that, in the present case where the stagnation region is of principal interest, a useful approximation, for example, may be to drop the thermodynamic function h_2. This then makes the system determinate, since Eqs. (4-7) and (4-11) are also dropped.

We turn now to the question of whether solutions of the form given by Eqs. (4-1) can meet the boundary conditions prescribed by Eqs. (3-1)–(3-3). At the body it is clear that the no-slip conditions, Eqs. (3-1a), can be satisfied. If we consider the specification of surface enthalpy, we see Eq. (3-1b) can satisfy the assumed solution forms for either a constant surface enthalpy or one which varies as $A\cos^2\theta + B\sin^2\theta$, where A and B are constants. We shall not consider the specification of $\partial h/\partial R$ at the surface, except for the insulated case where it is zero. This condition will, of course, agree with Eqs. (4-1). For the merged layer the assumed form of the solutions are compatible with the outer boundary conditions, Eqs. (3-2). On the other hand, for the viscous layer, our solutions can, in general, only be made compatible with the outer boundary conditions specified by Eqs. (3-3) when the density ratio across the shock can be considered constant along the shock. For strong shocks at hypersonic speeds this is a good approximation and will be used in the present paper (cf. reference 2).

We close this section by restating the boundary conditions in terms of our R-dependent variables. At the body Eqs. (3-1) become

$$u(R_b) = 0, \quad v(R_b) = 0 \quad (4\text{-}12)$$

$$h_0(R_b) \equiv h_{0_b} = A, \quad h_2(R_b) \equiv h_{2_b} = B \quad (4\text{-}13)$$

$$h_0'(R_b) = 0, \quad h_2'(R_b) = 0 \quad (4\text{-}14)$$

where Eq. (4-13) is the boundary condition to be used for a specified wall enthalpy, while Eq. (4-14) is to be used for an insulated surface. When the constants h_{0_b} and h_2 are equal, the surface enthalpy (temperature) is constant.

For the merged layer the outer boundary conditions, Eqs. (3-2), become

$$u \to U, \quad v \to U \quad \text{as } R \to \infty \quad (4\text{-}15)$$

$$\rho_0 \to \rho_\infty, \quad p_0 \to p_\infty, \quad p_2 \to p_\infty \quad \text{as } R \to \infty \quad (4\text{-}16)$$

$$h_0 \to h_\infty, \quad h_2 \to h_\infty \quad \text{as } R \to \infty \quad (4\text{-}17)$$

For the viscous layer, the Hugoniot conditions behind an infinitesimally thin circular or spherical shock, Eqs. (3-3), are

$$u(R_s) \equiv u_s = U, \quad v(R_s) \equiv v_s = \epsilon U \quad (4\text{-}18)$$

$$p_0(R_s) \equiv p_{0_s} = p_\infty + \rho_\infty U^2(1 - \epsilon), \quad p_2(R_s) \equiv p_{2_s} = p_\infty \quad (4\text{-}19)$$

$$h_0(R_s) \equiv h_{0_s} = h_\infty + (1/2)U^2(1 - \epsilon^2), \quad h_2(R_s) \equiv h_{2_s} = h_\infty \quad (4\text{-}20)$$

Here again we note that ϵ is expressed as a parameter

of the problem which is to be specified, and for the viscous layer we take it related to γ by Eq. (3-5):

$$\rho_0(R_s) \equiv \rho_{0_s} = \rho_\infty \epsilon = [(\gamma - 1)/(\gamma + 1)]\rho_\infty \qquad (4\text{-}21)$$

As was mentioned earlier, in general, for the viscous layer problem one additional boundary condition is required. This can be seen by noting that the system may be reduced to one of 10th order with ten boundary conditions, for example, by eliminating p_0 through Eq. (4-10). However, because of the unknown location of the shock wave, an 11th boundary condition is needed to determine the solution. For this purpose we may use the inviscid θ momentum equation applied along the downstream side of the shock, in which the Hugoniot values for the velocity and pressure behind the shock are inserted. This yields a specification on the first radial derivative of q_θ. It corresponds to specifying the vorticity behind the shock to be that calculated from the Hugoniot conditions. We will refer to the resulting relation as the "inviscid" boundary condition.

In the special case of the constant-density approximation, this additional boundary condition is not required because the order of the system is reduced by one due to the elimination of ρ_0', while the number of boundary conditions remains unchanged.*

(5) Viscous Layer Solution for Sphere and Cylinder

In this section we shall consider the viscous layer on a sphere and cylinder. In general, the solution of this problem requires the use of the full set of equations given in Section (3). In order to illustrate the nature of the solutions for the viscous layer, while keeping the calculations as simple as possible, we shall restrict our considerations to the approximation that the density in the viscous layer is constant.† This then approximates the case of an insulated body. However, even with cooled surfaces, there is evidence that the constant-density approximation may be a useful one in the stagnation region of blunt bodies at hypersonic flight speeds, if we are interested not in the details of the flow but in mean surface characteristics such as shear stress and heat-transfer rates. An example, for heat-transfer rate, is to be found in the comparison of the compressible highly cooled stagnation-point boundary-layer results of Fay and Riddell[13] with the corresponding constant-density results of, say, Sibulkin.[14] This comparison shows the constant-density results to agree approximately with the compressible ones, provided all temperature dependent flow variables in the constant-density solution are evaluated at an appropriate location in the shock layer.[23]

Further justification for considering first the comparatively simple constant-density case can be found in the information it provides about the relative changes of shear stress and heat-transfer rate as the Reynolds number decreases. We may reasonably expect that the relative changes in these quantities from their high Reynolds number values will not be affected strongly by compressibility.‡

As indicated previously, the results obtained are principally applicable in a region which is not far removed from the stagnation point. Therefore, in general, we shall associate the constant density with that prevailing on the axis of symmetry behind the normal portion of the shock wave, ρ_{0_s}, since at hypersonic speeds in the stagnation region the difference between this density and the one at the stagnation point is small. With this constant-density approximation, only the ordinary viscosity coefficient μ_0 enters, since the dilational viscosity is everywhere multiplied by ρ_0'. Again, for simplicity of calculation, we will take μ_0 to be constant at its value μ_{0_s} behind the normal portion of the shock. Note that $\mu = \mu_{0_s} \cos\theta$ still has a θ dependence.

The basic symmetry equations, Eqs. (4-2) to (4-7), can be written for this case by dropping the ρ_0' terms. The resulting six equations determine the six unknowns u, v, p_0, p_2, h_0, h_2. We may reduce the unknowns to five by introducing a stream function ψ to satisfy the continuity equation. In polar coordinates, ψ is given by

$$q_\theta(R \sin\theta)^j = \partial\psi/\partial R, \qquad q_R(R \sin\theta)^j = -(1/R)(\partial\psi/\partial\theta) \qquad (5\text{-}1)$$

If we write ψ as

$$\psi = \Psi(R)\ (\sin\theta)^{1+j} \qquad (5\text{-}2)$$

and introduce u and v through Eqs. (4-1b) and (4-1c),

$$u = \Psi'/R^j, \quad v = (1 + j)(\Psi/R^{1+j}) \qquad (5\text{-}3)$$

As is usual for a constant-density flow, the momentum equations can be uncoupled from the energy equations by eliminating the pressure and thereby introducing the vorticity. In the present case, this is accomplished by differentiating Eq. (4-5) and eliminating p_0' and p_2' by means of Eqs. (4-3) and (4-4). The result is the vorticity equation in the variables u and v.

The vorticity in the present problem has only one component, Ω_n, normal to the plane of the flow and may be expressed as

$$\left.\begin{aligned}\Omega_n &= (1/R)[(\partial R q_\theta/\partial R) - (\partial q_R/\partial\theta)] = \\ &\qquad \{u' + [(u - v)/R]\} \sin\theta \\ &= (1/R^j)[\Psi'' + (1 - j)(\Psi'/R) - \\ &\qquad (1 + j)(\Psi/R^2)] \sin\theta \equiv G(R) \sin\theta\end{aligned}\right\} \qquad (5\text{-}4)$$

* This fact was first pointed out to the authors by Drs. A. D. Wood and G. D. Waldman of the Avco Research and Advanced Development Division.

† After completion of the present work and the work of reference 3, a constant-density viscous layer analysis by Oguchi[25] came to the authors' attention. His work differs from ours principally in that he only considered a sphere and neglected curvature effects. His numerical results therefore differ somewhat from those given here.

‡ Calculations including the effects of variable density are at present being carried out and will be reported on later.

With this definition of G, the vorticity equation can be written in terms of Ψ as

$$(R^{1+j}G')' - [2(1+j)/R^{1-j}](\Psi'/R^j)' + (1/\nu_s)[(1+j)R^j\Psi(G/R^j)' - (1-j)\Psi'G] = 0 \quad (5\text{-}5)$$

Here, $\nu_s \equiv \mu_{0_s}/\rho_{0_s}$ is the kinematic viscosity evaluated on the axis of symmetry behind the normal portion of the shock.

The appropriate energy equations are Eqs. (4-6) and (4-7) with $\rho_0' = 0$. A discussion of the form of the energy equation to be used with the assumption of constant density can be found in reference 21. The pressure terms may be eliminated by using the constant-density forms of Eqs. (4-3)–(4-5). Inspection of the two constant-density energy equations shows that they are coupled. However, if one is subtracted from the other and the new enthalpy variable $\bar{h}_2 \equiv h_2 - h_0$ is introduced, the resulting equation depends only on $\bar{h}_2$ and Ψ. It, and the constant-density version of Eq. (4-6), become, using the stream function Ψ:

$$\bar{h}_2'' + \frac{1+j}{R}\bar{h}_2'\left[1 + \frac{Pr}{\nu_s}\frac{\Psi}{R^j}\right] - \frac{2}{R^2}\bar{h}_2\left[3 + j + \frac{Pr}{\nu_s}\frac{R\Psi'}{R^j}\right] = -Pr\left\{\left[\left(\frac{\Psi'}{R^j}\right)' - \left(\frac{\Psi}{R^{1+j}}\right)'\right]^2 + (1+j)\frac{\Psi}{R^{2+j}}\left[\left(\frac{\Psi'}{R^j}\right)' - \left(\frac{\Psi}{R^{1+j}}\right)'\left(1 + \frac{R}{\nu_s}\frac{\Psi'}{R^j}\right)\right] + \frac{\Psi'}{R^j}\left[\left(\frac{\Psi'}{R^j}\right)'' + \frac{1+j}{R}\left(\frac{\Psi'}{R^j}\right)'\left(1 + \frac{1}{\nu_s}\frac{\Psi}{R^j}\right) - \frac{1}{R}\left(\frac{\Psi}{R^{1+j}}\right)'\left(4 + \frac{R}{\nu_s}\frac{\Psi'}{R^j}\right)\right] - 4(1+2j)\left[\left(\frac{\Psi}{R^{1+j}}\right)'\right]^2 - (1+j)^2\frac{\Psi}{R^{2+j}}\left[\left(\frac{\Psi}{R^{1+j}}\right)'\left(1 + \frac{1+j}{\nu_s}\frac{\Psi}{R^j}\right) + \left(\frac{\Psi'}{R^j}\right)'\right]\right\} \quad (5\text{-}6)$$

$$h_0'' + \frac{1+j}{R}h_0'\left[1 + \frac{Pr}{\nu_s}\frac{\Psi}{R^j}\right] + \frac{2(1+j)}{R^2}\bar{h}_2 = -Pr\left\{4(1+2j)\left[\left(\frac{\Psi}{R^{1+j}}\right)'\right]^2 + (1+j)^2\frac{\Psi}{R^{2+j}}\left[\left(\frac{\Psi}{R^{1+j}}\right)'\left(1 + \frac{1+j}{\nu_s}\frac{\Psi}{R^j}\right) + \left(\frac{\Psi'}{R^j}\right)'\right]\right\} \quad (5\text{-}7)$$

The three equations for $\Psi(R)$, $\bar{h}_2(R)$, and $h_0(R)$ can be solved successively rather than simultaneously, since one involves only Ψ and another only Ψ and $\bar{h}_2$. The vorticity equation, Eq. (5-5), is fourth-order and nonlinear in Ψ, while the energy equations for $\bar{h}_2$ and h_0 are linear and second order. In fact, Eq. (5-7) can be treated as a linear first-order equation in h_0'. Once Ψ and its derivatives are found by solving Eq. (5-5), $p_0(R)$ and $p_0(R) - p_2(R)$ can be obtained from the constant-density versions of Eqs. (4-3) and (4-5), the former requiring a single quadrature on R.

From Eq. (4-12) the boundary conditions for the vorticity equation at the body are

$$\Psi(R_b) = 0, \quad \Psi'(R_b) = 0 \quad (5\text{-}8)$$

while at the shock, from Eq. (4-18),

$$\Psi(R_s) \equiv \Psi_s = [\epsilon U/(1+j)]R_s^{1+j}, \quad \Psi'(R_s) \equiv \Psi_s' = UR_s^j \quad (5\text{-}9)$$

One more boundary condition in addition to these four is needed for the solution of the differential equation, Eq. (5-5), because of the unknown location of the boundary at R_s. However, it should be noted that this does not represent an additional boundary condition for the basic constant-density differential system, such as is required in the variable-density model. This relation must be introduced here only because the pressure functions p_0 and p_2 are eliminated by cross differentiation, which reduces the order of the differential system by one while resulting in the loss of the two pressure boundary conditions at the shock. This necessitates the introduction of one additional relation. We obtain the appropriate relation by satisfying the θ momemtum equation, Eq. (4-5), along the shock, where $\Psi(R_s)$ and $\Psi'(R_s)$ are given by Eq. (5-9) and where $2(p_2 - p_0) = (\partial p/\partial\theta)/(\sin\theta\cos\theta)$ is obtained from the Hugoniot relation Eq. (3-3b). The resulting relation between $\Psi'''(R_s)$ and $\Psi''(R_s)$ is

$$\Psi_s'''R_s^{2-j}/(U\,Re_s) = -\{[(1-j)/Re_s] + 1\}(\Psi_s''R_s^{1-j}/U) + [j - 3 + 2\epsilon + (1/\epsilon)] + [4(1-\epsilon)/Re_s] \quad (5\text{-}10)$$

We have used the subscript s here to indicate conditions behind the shock. The Reynolds number Re_s is defined by

$$Re_s \equiv \rho_\infty UR_s/\mu_{0_s} \quad (5\text{-}11)$$

and is appropriate for the viscous layer problem as treated here. We shall term Eq. (5-10) the "viscous" boundary condition for Eq. (5-5).

For a constant surface enthalpy the wall boundary conditions on the enthalpy equations, from Eq. (4-13), are

$$h_0(R_b) \equiv h_{0_b}, \quad \bar{h}_2(R_b) \equiv (h_2 - h_0)_b = 0 \quad (5\text{-}12)$$

With the hypersonic strong shock approximation ($M_\infty^2\cos^2\theta \gg 1$) we may neglect h_∞ in comparison with h_s and we may neglect ϵ^2. From Eq. (4-20) this leads to the boundary conditions at the shock

$$h_0(R_s) = (1/2)U^2, \quad \bar{h}_2(R_s) \equiv (h_0 - h_2)_s = -(1/2)U^2 \quad (5\text{-}13)$$

Of course, even at hypersonic speeds for any finite Mach number with sufficiently large θ, the strong shock approximations will break down. However, as already pointed out, our considerations are in general restricted to the stagnation region where the approximation is valid.

For numerical integration, Eqs. (5-5)–(5-7) may be made nondimensional by using U as the unit of velocity, R_s as the unit of length, and $(1/2)U^2$ as the unit of enthalpy. Then, the dimensionless parameters of the vorticity equation and boundary conditions are ϵ and Re_s, while the enthalpy equations and appropriate boundary conditions introduce Pr and $h_{0_b}/(1/2)U^2$ for the constant wall enthalpy case. Once ϵ and Re_s are chosen, the vorticity equation is integrated as a two-point boundary value problem starting at the shock. The stream function variable Ψ_s and its derivative Ψ_s' are known from Eq. (5-9). A value of Ψ_s'' is assumed, and Ψ_s''' is computed from Eq. (5-10). The integration then proceeds toward the body, whose initially unknown location is to be determined by the simultaneous satisfaction of the no-slip conditions at the same value of R. This will occur for only one value of Ψ_s'', so that the integration must be repeated with different assumed values of Ψ_s'' until the correct value is found, thus determining R_b. Once the vorticity equation is solved, the enthalpy equation for $\bar{h}_2/(1/2)U^2$ is integrated starting from the value -1 at the shock. Various values of $\bar{h}_{2_s}'$ are assumed until $\bar{h}_{2_b} = 0$ is satisfied at the now known body location. Finally, the enthalpy equation for $h_0/(1/2)U^2$ is solved in the same way, using the value 1 on the shock and the prescribed value of $h_{0_b}/(1/2)U^2$ on the body.

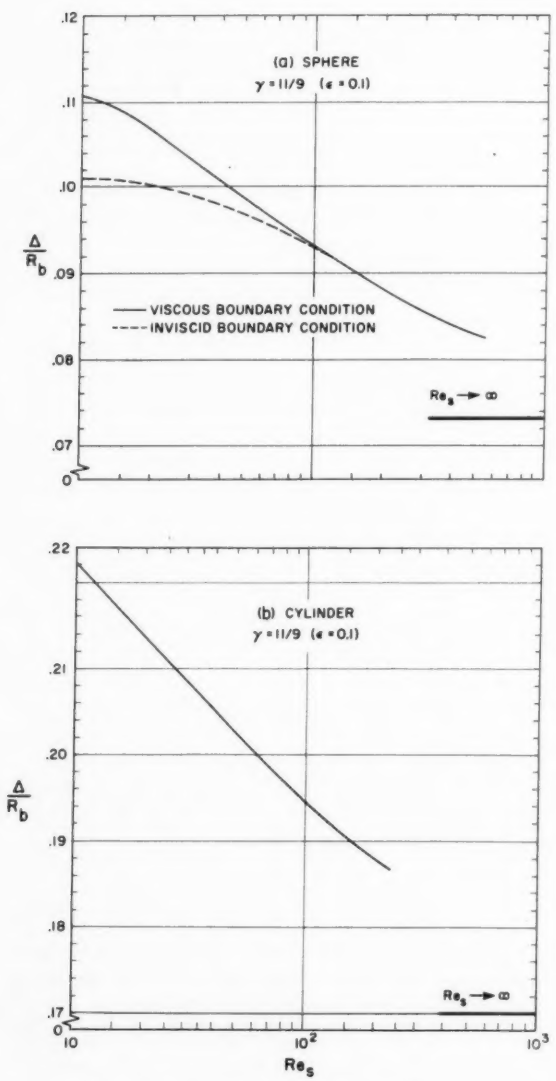

FIG. 3. Viscous layer shock-layer thickness.

The procedure described has been carried out on an IBM 650 digital computer for both the sphere and cylinder cases. The parameters were chosen to correspond to a highly cooled body (surface temperature of the order of the free-stream temperature) in atmospheric hypersonic flight ($h_s \approx U^2/2$). In particular, we took

$$\epsilon = 0.1, \quad Pr = 0.71, \quad h_{0_b}/(1/2)U^2 \to 0 \qquad (5\text{-}14a)$$

For large wall cooling the exact value of $h_{0_b}/(1/2)U^2$ is not important as long as it is sufficiently small. As we pointed out before in Eq. (3-5), for the case of a strong shock wave in a perfect gas where the density ratio approaches its limiting value, we may write this limiting density ratio in terms of the isentropic exponent behind the shock—i.e., $\epsilon = (\gamma - 1)/(\gamma + 1)$. For $\epsilon = 0.1$, the corresponding value of γ is then

$$\gamma = 11/9 \qquad (5\text{-}14b)$$

The use of γ as the parameter rather than ϵ is somewhat more appropriate, since, for the incipient merged layer to be treated in the following section, ϵ is not independent of Reynolds number and we must specify the gas through γ.

The range of Reynolds numbers Re_s for the integration was taken to be between 10 and 1,000 with the upper limit chosen at a point where the viscous layer results could be expected to agree closely with the results of boundary-layer theory. The lower limit was chosen somewhat below the Reynolds number for which the viscous layer theory could be considered valid. According to our estimate of Eq. (2-7), the viscous layer analysis is valid for axisymmetric flow so long as

$$(\epsilon Re_s)^{-1} \ll 1 \qquad (5\text{-}15)$$

In arriving at this form of the inequality, we have used the order-of-magnitude estimates

$$\mu_\infty/\mu_s \sim (T_\infty/T_s)^{1/2} \sim \epsilon^{1/2} M_\infty$$

For a density ratio $\epsilon = 0.1$, Eq. (5-15) implies that the viscous layer model breaks down at a Reynolds number somewhat less than 100.

Fig. 3 shows the calculated shock layer thickness for the sphere and cylinder. For the sphere two values are indicated: one for the "viscous" boundary condition specified by Eq. (5-10) which is correct for our model, and the other for an "inviscid" boundary condition which is the specification of $\Psi''(R_s)$ through Eq. (5-10) by allowing $Re_s \to \infty$. This "inviscid" condition corresponds to that suggested at the end of Section

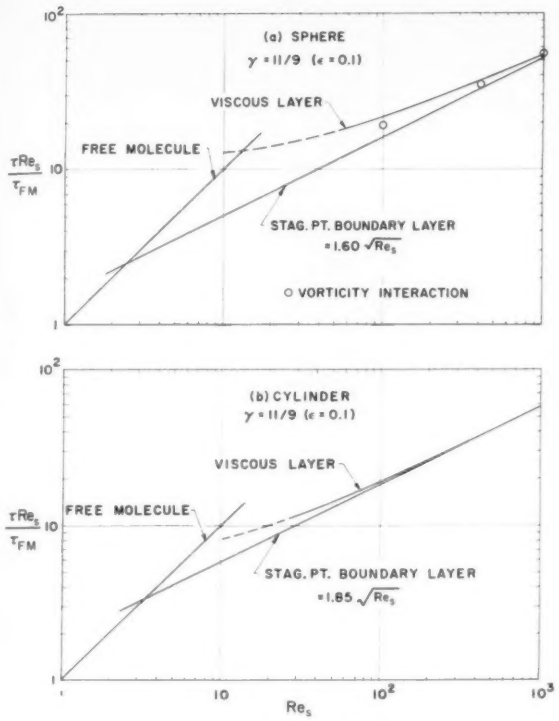

FIG. 4. Viscous layer surface shear stress ($\tau_{FM} = \rho_\infty U^2 \sin\theta \cos\theta$).

(4) to be used as the additional boundary condition in the variable-density case. The use of such an "inviscid" condition in the constant-density case, although not self-consistent, can in part serve to indicate when the viscous layer model itself is breaking down. This follows from the fact that our model is only applicable when the viscous shear and heat conduction immediately behind the shock are negligible. Any appreciable differences in the results found by using the two different conditions would indicate that the assumptions of our model are not being met. It can be seen that divergence between the results begins to occur at a Reynolds number somewhat below 100, which is the approximate value our order-of-magnitude analysis would indicate as a lower bound for the validity of the axisymmetric viscous layer analysis. Similar results are found for the other flow variables. These calculations thus bear out our remarks concerning the use of the viscous or inviscid shock boundary condition. All results presented in the remainder of the paper are for the correct viscous boundary condition. We again caution the reader that the order-of-magnitude estimates must be altered somewhat for the two-dimensional case since Δ/R_b is no longer of order ϵ. Nevertheless, the range of validity of the analysis for the cylinder will be about the same as for the sphere for most of the flow variables.

From Fig. 3 for both the sphere and cylinder, the shock layer thickness may be seen to increase with decreasing Reynolds number. With the present constant-density approximation, this increase results from the increase in the usual displacement thickness, which is included in Δ in a viscous layer analysis, plus the added displacement effect resulting from the inclusion of viscous terms in the shock layer as a whole. (If compressibility with large wall cooling had been taken into account, the ordinary displacement thickness would be negative and so tend to reduce Δ below its inviscid value at high Reynolds numbers where usual boundary-layer theory is valid. However, the inclusion of the viscous terms in the whole shock layer, and not just near the wall, would still tend to make Δ increase with decreasing Reynolds numbers even in the compressible case.) On Fig. 3 we have also shown for reference the infinite Reynolds number stand-off distance corresponding to the calculated result for the Lighthill[11] inviscid sphere solution and the Whitham[12] and Hayes-Probstein[2] inviscid cylinder solution.

On Figs. 4 and 5 are plotted, respectively, the surface shear and heat-transfer rate results for the sphere and cylinder. Both the shear and heat-transfer rate are made dimensionless with respect to the free molecule value for infinite Mach number and completely diffuse reflection (all accommodation coefficients unity). These values are

$$\tau_{FM} = \rho_\infty U^2 \sin\theta \cos\theta \tag{5-16}$$

$$-\dot{q}_{FM} = (1/2)\rho_\infty U^3 \cos\theta \tag{5-17}$$

The viscous layer curves for the shear represent the shear at any point on the body, since τ has only a component proportional to $\sin\theta \cos\theta$, that is

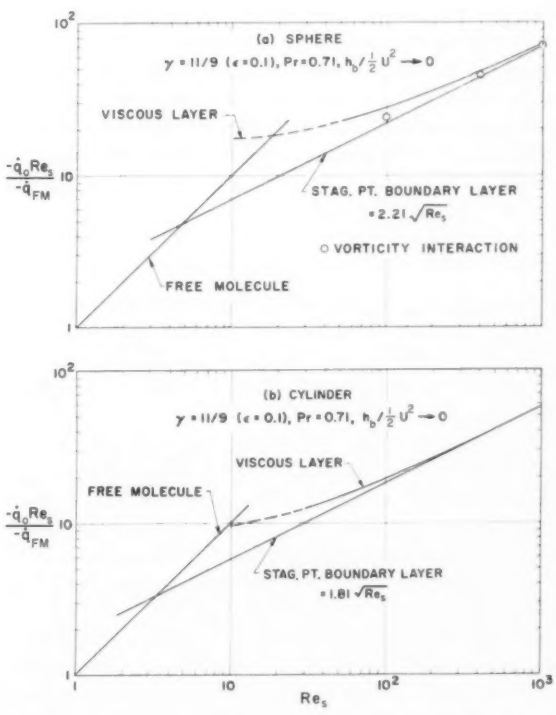

FIG. 5. Viscous layer stagnation-point heat-transfer rate ($-\dot{q}_{FM} = (1/2)\rho_\infty U^3 \cos\theta$).

TABLE 1
Inviscid Flow and Boundary-Layer Constants

	Constant-Density, $\epsilon = 0.1$					
	R_s/R_b		$U^{-1}(dq_\theta/d\theta)_{stag}$			
	Approximate	Complete	Approximate	Complete	f_b''	$(g_b')_{Pr=1}$
Cylinder ($j = 0$)	1.15	1.17	0.548	0.576	1.233	0.570
Sphere ($j = 1$)	1.11	1.07	0.516	0.518	0.928	0.540

$$\tau = [\mu(\partial q_\theta/\partial R)]_b = \mu_{0_s} u_b' \sin\theta\cos\theta \quad (5\text{-}18)$$

On the other hand, the heat transfer is given by the relation

$$-\dot{q} = [k(\partial T/\partial R)]_b = (\mu_{0_s}/Pr)[h_{0_b}' + (h_2 - h_0)_b \sin^2\theta]\cos\theta \equiv -[\dot{q}_0 + \bar{\dot{q}}_2 \sin^2\theta]\cos\theta \quad (5\text{-}19)$$

and we have plotted only the stagnation-point component $-\dot{q}_0$.

For comparison purposes we have also shown the free molecule values from Eqs. (5-16) and (5-17) and the constant-density boundary-layer stagnation-point values. These stagnation-point boundary-layer results may be expressed as

$$\tau Re_s/\tau_{FM} = [(1/U)(dq_\theta/d\theta)]_{stag}^{3/2}(R_s/R_b)^{1/2} \times (Re_s/\epsilon)^{1/2}(1 + j)^{1/2} f_b'' \quad (5\text{-}20)$$

$$-\dot{q}_0 Re_s/-\dot{q}_{FM} = [(1/U)(dq_\theta/d\theta)]_{stag}^{1/2}(R_s/R_b)^{1/2} \times (Re_s/\epsilon)^{1/2}[(1 + j)^{1/2}/Pr]Pr^{0.4}(g_b')_{Pr=1} \quad (5\text{-}21)$$

where f_b'' and $(g_b')_{Pr=1}$ are constants obtained from the appropriate boundary-layer solutions. The inviscid values of the stagnation-point velocity gradient $(dq_\theta \div d\theta)_{stag}$ and R_s/R_b can be found from the complete inviscid constant-density solutions[2,11,12] or can be calculated approximately from the relations (see Chap. 4, reference 2)

$$[(1/U)(dq_\theta/d\theta)]_{stag} = \{[(9 - j)/3]\epsilon\}^{1/2} \quad (5\text{-}22)$$

$$R_b/R_s = 1 - \epsilon[(1/2)\ln(4/3\epsilon)]^{1-j} \quad (5\text{-}23)$$

The approximate relations are given in order to show roughly the ϵ dependence. In Table 1 are presented the values of the velocity gradient and (R_s/R_b) for $\epsilon = 0.1$, as well as the appropriate boundary-layer constants (see, for example, references 14 and 15).

An interesting feature of the viscous layer results shown in Figs. 4 and 5 is that for a given Reynolds number the shear and heat transfer are higher than would be given by an extrapolation of boundary-layer theory to low Reynolds numbers. This result is contrary to previous conjectures by many people, including one of the present authors (see Fig. 2 of reference 1). Shear and heat-transfer values higher than extrapolated boundary-layer theory cannot persist at indefinitely low Reynolds numbers, since they will eventually become higher than free molecule values. Adams and Probstein[1] have shown that using the Navier-Stokes equations it is not physically possible on a cold blunt body to exceed the free molecule shear stress and heat-transfer rate. The fact that the viscous layer results on Figs. 4 and 5 do become higher than the free molecule values near $Re_s = 10$ can be attributed to a breakdown in the viscous layer model at sufficiently low Reynolds numbers. This model does not include curvature, viscous, or heat conductive terms in the conservation equations used across the shock wave. As the Reynolds number decreases these terms within the viscous layer make increasingly larger contributions to the flux of momentum and energy toward the body. We find as a result, because of the discontinuous shock-wave model, that more momentum and energy flow out of the shock toward the body than into the shock from the free stream. This leads eventually to an increase of shear and heat transfer above the free molecule values. At a Reynolds number Re_s somewhat below 100, where curvature, viscous, and conductive terms in the shock conservation laws become important, we expect the viscous layer model to become invalid and a merged layer analysis to become necessary. We may anticipate that such an analysis would provide a drop in the shear and heat-transfer curves relative to the viscous layer values. The results of an analysis which do indicate this drop are presented in the following section.

The fact that the first departure from boundary-layer theory is toward higher shear and heat transfer, as shown by the viscous layer results in Figs. 4 and 5, has been indicated previously by vorticity interaction theory (see reference 2, Section (9.6)), where the outer boundary condition of the momentum equation is modified to account for the strong vorticity present in the inviscid field. Such an analysis is appropriate to the vorticity interaction regime defined in Section (2).

On Figs. 4(a) and 5(a) we have shown for comparison some incompressible, axisymmetric, stagnation-point vorticity interaction results. These results were obtained by using some calculations by Kemp[24] in which the classical constant-density boundary-layer momentum and energy equations were integrated with the vorticity interaction boundary condition $(f')^2 \to 1 + 2\Omega f$ on the momentum equation instead of the usual condition $f' \to 1$ (cf. reference 2, p. 371). Here f is the usual boundary layer reduced stream function and Ω is the vorticity interaction parameter. The results of these integrations for $\Omega < 1$ may be expressed approximately as follows: the usual shear function f_b'' is multiplied by $1 + 0.78\Omega$ and the usual heat-transfer function g_b' is multiplied by $1 + 0.36\Omega$.

For the constant-density case we are considering, Ω is proportional to the constant vorticity in the inviscid flow divided by the average vorticity in the boundary layer and may be written as

$$\Omega = [(1/U)(dq_\theta/d\theta)]_{stag}^{(3/2)}[(R_b/U)(\partial^2 q_\theta/\partial R\partial\theta)]_{stag} \times (\epsilon/Re_s)^{1/2}(R_s/2R_b)^{1/2} \quad (5\text{-}24)$$

The quantities with subscript stag, along with R_s/R_b, are evaluated using the inviscid constant-density sphere

solution of Lighthill.[11] All of these quantities have been given previously for $\epsilon = 0.1$ in Table 1, except

$$[(R_b/U)(\partial^2 q_\theta/\partial R \partial\theta)]_{stag} = (R_b/R_s)^2[(1-\epsilon)^2/\epsilon] - [(1/U)(dq_\theta/d\theta)]_{stag} \quad (5\text{-}25)$$

which is equal to 6.035 for $\epsilon = 0.1$. Using these values we find $\Omega = 3.75/(Re_s)^{1/2}$, which was the result used to obtain the points on Figs. 4(a) and 5(a).

The good agreement between vorticity interaction theory and viscous layer theory down to $Re_s \approx 300$ in the axisymmetric case indicates that it is primarily the strong vorticity in the essentially inviscid part of the flow behind the shock wave which accounts for the initial departures from boundary-layer theory. The viscous layer theory, which includes terms in the Navier-Stokes equations not included in vorticity interaction theory, carries us down about another factor of $3(\approx \epsilon^{-1/2})$ in Reynolds number, in agreement with the order-of-magnitude estimates of Eqs. (2-6) and (2-7). In this regime, the shear and heat transfer are somewhat higher than vorticity interaction predicts.

The agreement of viscous layer and vorticity interaction results for the sphere at the higher Reynolds numbers also leads to a better understanding of the cylinder calculations where the viscous layer effect is seen to be smaller than for axisymmetric flow at a given Re_s. This is perfectly consistent, since it can be shown that for the cylinder, vorticity interaction is a second-order effect (in Reynolds number) as compared to a first-order effect for the sphere. We may put this another way by noting that at the surface of the cylinder, for the inviscid constant-density case, the vorticity is zero. For a sphere under the same conditions the surface vorticity has a relatively large finite value since the velocity profile in the inviscid layer is approximately linear in the radial coordinate. Therefore, equal departures from boundary-layer theory occur at a much lower Reynolds number for a cylinder than for a sphere.

A further confirmation of the ideas we have expressed is found in the calculations of the pressure distribution through the shock layer, which show that for Reynolds numbers greater than 300 the layer is essentially a constant-pressure layer in the neighborhood of the stagnation region. This is immediately recognized as one of the basic boundary-layer assumptions. At these higher Reynolds numbers the calculated behavior of the velocity profiles for both the cylinder and the sphere is also found to be consistent with the vorticity interaction picture just given.

(6) Incipient Merged Layer

In the preceding section we saw that for a Reynolds number Re_s somewhat below 100 the viscous layer model is no longer satisfactory and we may no longer consider the shock as a discontinuity following the classical Hugoniot relations. We can now proceed to solve the fully merged layer problem, including the shock structure. Alternatively, we may consider the shock slightly thickened, though still essentially a discontinuity, but with curvature effects, viscous stresses, and heat conduction taken into account in a manner which satisfies overall energy and momentum conservation laws through the shock wave. Because it is the simpler of the two approaches, we choose the latter course, although we recognize according to our estimate of Eq. (2-8) that such an incipient merged layer solution can at best carry us a factor of three to five lower in Reynolds number. The importance of such a solution, however, is in its alteration of the behavior of the viscous layer solutions so as to bring the shear and heat transfer down in the manner indicated in the preceding section.

Basically this procedure consists of modifying the shock boundary conditions for the viscous layer solution. Determination of these modified boundary conditions involves obtaining integrated conservation laws for a shock wave which include viscous and heat conduction terms as well as curvature terms.* Our method consists of integrating the Navier-Stokes equations from behind the shock, which to some extent is arbitrarily defined, to upstream infinity where it is assumed that all flow gradients vanish. In order to simplify the equations, the orders of magnitude of the remaining terms are estimated using values consistent with the Hugoniot equations, and terms of higher order are dropped. The remaining integrals are then evaluated using the one-dimensional shock-wave solution (including viscosity and heat conduction). With these modified boundary conditions the density ratio can no longer be specified in advance, nor can the tangential velocity component be considered a constant through the shock.

The basic form of the Navier-Stokes equations to be used has already been given in Eqs. (4-2)–(4-6). These equations are repeated in Appendix (B), Eqs. (B-1)–(B-5), in a form more suitable for integration. The dilational viscosity coefficient is taken zero for simplicity, although it could be included in the analysis. These equations are integrated with respect to R from R_s to ∞, and free-stream boundary conditions along with the additional criterion that all gradients vanish are then applied at upstream infinity. The resulting integral relations are given in Appendix (B), Eqs. (B-6)–(B-10). These equations, together with the gas law, replace the Hugoniot relations and are used as the boundary conditions behind the shock for the following quantities: v, ϵ, p_0, p_2, u, u', h_0, h_0', h_2. For the moment we note that Eq. (4-7) for h_2 and its derivative is not considered as it would lead to the boundary con-

* After completion of the present work it was brought to the authors' attention that the idea of modifying the Hugoniot relations in the stagnation region behind a detached shock wave to take into account curvature, viscosity, and heat conduction effects in the flow behind the shock was proposed in reference 26. However, in that work terms dependent on the thickness of the shock wave were neglected, and, since these terms are of the same order as those taken into account, the theory presented is inconsistent; this casts doubt on the results.

ditions for the flow behind the shock wave being overspecified. This is analogous to the overdetermined system discussed in Section (4) in connection with the compressible solutions.

The integrated Eqs. (B-6)–(B-10) contain terms to be evaluated behind the shock wave at R_s, and integrals through the shock wave. The orders of the former terms are estimated using the Hugoniot conditions, Eqs. (4-18)–(4-20), with p_∞ neglected in comparison with $\rho_\infty U^2$ and h_∞ neglected in comparison to $U^2/2$. In addition we take $\mu_0 \sim \mu_{0_s}$, $R \sim R_s$. Where derivatives appear in these terms the operator d/dR is estimated to be of the order of magnitude of Δ^{-1}, with Δ of the order of ϵR_s according to Eq. (2-2). In the integrals in Eqs. (B-6) to (B-10), we note that the integrands all vanish as $R \to \infty$. The range of R over which the integrands have a significant value is taken as the shock thickness δ_s. In the integrands, quantities are estimated by using the largest value they take on. For all quantities but v, which is taken of order U, this leads to the same estimates as were employed above for the integrated terms. Since v and h_0 change rapidly through the shock wave, their derivatives can be large, and for them the operator d/dR must be taken as δ_s^{-1}. On the other hand, because u does not change rapidly, u' may be taken the same as for the integrated terms. After all terms in Eqs. (B-6)–(B-10) have been estimated in this manner, we drop terms which are smaller than Re_s^{-1} or δ_s/R_s times the largest terms in each equation, remembering that ϵ is a small quantity. With $\epsilon = \rho_\infty/\rho_{0_s}$, the resulting conservation equations are:

$$\frac{v_s}{U} = \epsilon\left[1 - (1+j)\int_{R_s}^{\infty} \frac{\rho_0 v}{\rho_\infty U}\left(\frac{u}{v} - 1\right)\frac{dR}{R}\right] \tag{6-1}$$

$$\frac{p_{0_s}}{\rho_\infty U^2} = 1 - \frac{v_s^2}{\epsilon U^2} - (1+j)\int_{R_s}^{\infty} \frac{\rho_0 v}{\rho_\infty U}\frac{u-v}{U}\frac{dR}{R} - \frac{4}{3}\frac{1}{Re_s}\left(\frac{R_s u_s'}{U} + \frac{1+j}{2}\frac{u_s}{U}\right) \tag{6-2}$$

$$\frac{p_{2_s}}{\rho_\infty U^2} = -\int_{R_s}^{\infty} \frac{\rho_0 v u}{\rho_\infty U^2}\left(\frac{u}{v} - 1\right)\frac{dR}{R} \tag{6-3}$$

$$\frac{v_s u_s}{\epsilon U^2} = 1 - (2+j)\int_{R_s}^{\infty} \frac{\rho_0 v u}{\rho_\infty U^2}\left(\frac{u}{v} - 1\right)\frac{dR}{R} + 2\int_{R_s}^{\infty} \frac{p_0}{\rho_\infty U^2}\frac{dR}{R} - \frac{1}{Re_s}\left(\frac{R_s u_s'}{U} - \frac{u_s}{U}\right) - \frac{4}{3}\frac{1}{Re_s}\int_{R_s}^{\infty} \frac{\mu_0}{\mu_{0_s}}\frac{R_s v'}{U}\frac{dR}{R} \tag{6-4}$$

$$\begin{aligned}\frac{v_s}{\epsilon U}\left(\frac{h_{0_s}}{(1/2)U^2} + \frac{v_s^2}{U^2}\right) = 1 &- \frac{1}{Re_s}\frac{R_s h_{0_s}'}{(1/2)U^2 Pr} + \frac{1+j}{Re_s Pr}\int_{R_s}^{\infty} \frac{\mu_0}{\mu_{0_s}}\frac{R_s h_0'}{(1/2)U^2}\frac{dR}{R} + \\ &\frac{4(1+j)}{Re_s}\int_{R_s}^{\infty} \frac{\mu_0}{\mu_{0_s}}\frac{v}{U}\frac{R_s v'}{U}\frac{dR}{R} + \frac{4}{3}\frac{1+j}{Re_s}\int_{R_s}^{\infty} \frac{\mu_0}{\mu_{0_s}}\frac{R_s v'}{U}\frac{u-v}{U}\frac{dR}{R} - \\ &(1+j)\int_{R_s}^{\infty} \frac{\rho_0 v}{\rho_\infty U}\left(\frac{h_0}{(1/2)U^2} + \frac{v_s^2}{U^2}\right)\left(\frac{u}{v} - 1\right)\frac{dR}{R}\end{aligned} \tag{6-5}$$

In these equations the terms remaining are exact as written. We now proceed to approximate them in a manner consistent with the order we are considering. In the integrated terms which are multiplied by Re_s^{-1}, we need only evaluate quantities to zero order, since terms of order higher than Re_s^{-1} have already been dropped. Therefore, we put $u_s = U$ from the inviscid Hugoniot relation, and $R_s v_s'/U = (1+j)$ from the zero order inviscid constant-density continuity equation [Eq. (4.2) with ρ_0 = constant and the v term dropped]. Of course, since we are using these equations to obtain boundary conditions on u_s' and h_{0_s}', these quantities are left undetermined. We note that $v_s/\epsilon U$ which appears in Eqs. (6-4) and (6-5) is to be evaluated using the continuity equation (6-1), since it multiplies a term of order one. On the other hand, in Eq. (6-2), $v_s/\epsilon U$ multiplies v_s/U, which is of order ϵ, so there we must set $v_s/\epsilon U = 1$.

We now approximate the integrals to consistent order by employing the hypersonic one-dimensional shock-wave structure equations, which can, for example, be obtained from the above equations in the limit $R \to \infty$. In particular, we use the results

$$\rho_{0_s} v_s = \rho_\infty U, \quad p_0 + \rho_0 v^2 = \rho_\infty U^2 - (4/3)\mu_0 v'$$

along with the fact that $u = U$. In addition we take $R = R_s$, since R only changes through the shock by δ_s. The resulting equations are

$$v_s/U = \epsilon\left\{1 - (1+j)\int_{R_s}^{\infty} [(U/v) - 1](dR/R_s)\right\} \tag{6-6}$$

$$\frac{p_{0_s}}{\rho_\infty U^2} = 1 - \frac{v_s}{U} - (1+j)\int_{R_s}^{\infty}\left(1 - \frac{v}{U}\right)\frac{dR}{R_s} - \frac{2(1+j)}{Re_s} + \frac{2(1+j)}{Re_s}\int_V^U \frac{\mu_0}{\mu_{0_s}}\frac{dv}{U} \tag{6-7}$$

$$\frac{p_{2_s}}{\rho_\infty U^2} = -\int_{R_s}^{\infty}\left(\frac{U}{v} - 1\right)\frac{dR}{R_s} = -\frac{1}{1+j}\left(1 - \frac{v_s}{\epsilon U}\right) \tag{6-8}$$

$$\frac{u_s}{U} = 1 - \int_{R_s}^{\infty} \left(\frac{U}{v} - 1\right) \frac{dR}{R_s} + 2 \int_{R_s}^{\infty} \left(1 - \frac{v}{U}\right) \frac{dR}{R_s} - \frac{8}{3} \frac{1}{Re_s} \int_V^U \frac{\mu_0}{\mu_{0_s}} \frac{dv}{U} - \frac{1}{Re_s} \left(\frac{R_s u_s'}{U} - 1\right) - \frac{4}{3} \frac{1}{Re_s} \int_V^U \frac{\mu_0}{\mu_{0_s}} \frac{dv}{U} \tag{6-9}$$

$$\frac{h_{0_s}}{(1/2)U^2} + \frac{v_s^2}{U^2} = 1 - \frac{1}{Re_s} \frac{R_s h_{0_s}'}{(1/2)U^2 Pr} + \frac{1+j}{Re_s Pr} \int_{(1/2)U^2}^{0} \frac{\mu_0}{\mu_{0_s}} \frac{dh_0}{(1/2)U^2} + \frac{4}{3} \frac{1+j}{Re_s} \int_V^U \frac{\mu_0}{\mu_{0_s}} \left(1 - \frac{v}{U}\right) \frac{dv}{U} + \frac{4(1+j)}{Re_s} \int_V^U \frac{\mu_0}{\mu_{0_s}} \frac{v}{U} \frac{dv}{U} + (1+j) \left[\left(\frac{h_{0_s}}{(1/2)U^2} + \frac{v_s^2}{U^2} \right) \int_{R_s}^{\infty} \left(\frac{U}{v} - 1\right) \frac{dR}{R_s} - \int_{R_s}^{\infty} \left(\frac{h_0}{(1/2)U^2} + \frac{v^2}{U^2} \right) \left(\frac{U}{v} - 1\right) \frac{dR}{R_s} \right] \tag{6-10}$$

Here the lower limit $V = U(\gamma - 1)/(\gamma + 1)$, the Hugoniot value of v_s.

To evaluate the remaining integrals we must first specify certain fluid properties. In particular, we take $Pr = 3/4$, which leads to Becker's energy integral for a one-dimensional shock,

$$h_0 + (1/2)v^2 = \text{const.} \tag{6-11}$$

In addition we assume the viscosity μ_0 to be proportional to $h_0^{1/2}$, which is consistent with our perfect gas rigid-sphere model. With these fluid property assumptions, we are led to a first-order differential equation for the shock-wave velocity profile. (See, for example, Hayes,[16] p. 456.) In writing this result we again make the hypersonic approximation and drop terms leading to higher order contributions in Re_s. The resulting differential equation is

$$\frac{3}{8} \frac{\gamma}{\gamma + 1} \frac{\rho_\infty U^2}{\mu_{0_s}} dR = \frac{(U^2 - v^2)^{1/2} v dv}{(U - v)(v - V)} \tag{6-12}$$

It is well known that this velocity profile leads to a shock thickness which is logarithmically infinite and so is not suitable for use in approximating the integrals in which v appears in the integrands. We therefore follow the usual practice for defining a shock thickness and use a linear velocity profile whose slope is the maximum value of dv/dR obtained from Eq. (6-12). With $(\gamma - 1)/(\gamma + 1)$ small, this slope is

$$\left(\frac{dv}{dR}\right)_{max} = \frac{3}{8} \frac{\gamma}{\gamma + 1} \frac{U/R_s}{Re_s} \left[1 - 2\left(\frac{\gamma - 1}{\gamma + 1}\right)^{1/2}\right] \tag{6-13}$$

The velocity profile to be used is then written

$$v = (dv/dR)_{max}(R - R_s) + v_s \tag{6-14}$$

From this profile, the shock thickness is defined by setting $v = U$ at $R - R_s = \delta_s$, which yields

$$\delta_s = (U - v_s)/(dv/dR)_{max} \tag{6-15}$$

Using these equations, the following integrations can be performed:

$$\int_{R_s}^{\infty} \left(\frac{U}{v} - 1\right) \frac{dR}{R_s} = \frac{U/R_s}{(dv/dR)_{max}} \left(\ln \frac{U}{v_s} - 1\right) \tag{6-16}$$

$$\int_{R_s}^{\infty} \left(1 - \frac{v}{U}\right) \frac{dR}{R_s} = \frac{1}{2} \frac{U/R_s}{(dv/dR)_{max}} \tag{6-17}$$

Here we have dropped all terms of higher order than Re_s^{-1}.

The remaining integrals are evaluated using Becker's integral Eq. (6-11) and the relation $\mu_0 \sim h_0^{1/2}$. The results are

$$\int_V^U \frac{\mu_0}{\mu_{0_s}} \frac{v}{U} \frac{dv}{U} = \frac{1}{2} \int_V^U \left(1 - \frac{v^2}{U^2}\right)^{1/2} \frac{dv^2}{U^2} = \frac{1}{3} \tag{6-18}$$

$$\int_V^U \frac{\mu_0}{\mu_{0_s}} \frac{dv}{U} = \int_V^U \left(1 - \frac{v^2}{U^2}\right)^{1/2} \frac{dv}{U} = \frac{\pi}{4} \tag{6-19}$$

$$\int_{(1/2)U^2}^{0} \frac{\mu_0}{\mu_{0_s}} \frac{dh_0}{(1/2)U^2} = \int_{(1/2)U^2}^{0} \left(\frac{h_0}{(1/2)U^2}\right)^{1/2} \frac{dh_0}{(1/2)U^2} = -\frac{2}{3} \tag{6-20}$$

where again we have dropped terms of higher order.

Using the preceding results, the modified boundary conditions can be written

$$\frac{v_s}{U} = \epsilon\left\{1 - \frac{8}{3}\frac{\gamma}{\gamma+1}\frac{1+j}{Re_s}\left[1 + 2\left(\frac{\gamma-1}{\gamma+1}\right)^{1/2}\right]\left(\ln\frac{U}{v_s} - 1\right)\right\} \tag{6-21}$$

$$\frac{p_{0_s}}{\rho_\infty U^2} = 1 - \frac{v_s}{U} - \frac{2(1+j)}{Re_s}\left\{1 - \frac{\pi}{4} + \frac{8}{3}\frac{\gamma}{\gamma+1}\left[1 + 2\left(\frac{\gamma-1}{\gamma+1}\right)^{1/2}\right]\right\} \tag{6-22}$$

$$\frac{p_{2_s}}{\rho_\infty U^2} = -\frac{1}{1+j}\left(1 - \frac{v_s}{\epsilon U}\right) \tag{6-23}$$

$$\frac{u_s}{U} = 1 - \frac{1}{1+j}\left(1 - \frac{v_s}{\epsilon U}\right) + \frac{1}{Re_s}\left\{1 - \pi + \frac{8}{3}\frac{\gamma}{\gamma+1}\left[1 + 2\left(\frac{\gamma-1}{\gamma+1}\right)^{1/2}\right] - \frac{R_s u_s'}{U}\right\} \tag{6-24}$$

$$\frac{h_{0_s}}{(1/2)U^2} = 1 - \frac{v_s^2}{U^2} + \frac{1}{Re_s}\left\{(1+j)\frac{\pi}{3} - \frac{4}{3}\frac{R_s h_{0_s}'}{(1/2)U^2}\right\} \tag{6-25}$$

These equations are appropriate shock boundary conditions for the incipient merged layer. They replace the Hugoniot relations with p_∞ and h_∞ negligible and reduce to them for $Re_s \to \infty$. They are not all independent since $p_0(R_s)$, $\rho_0(R_s)$, and $h_0(R_s)$ are assumed related through the perfect gas state equation, which from Eq. (4-10) may be written

$$h_{0_s}/(1/2)U^2 = [2\gamma/(\gamma-1)]\epsilon(p_{0_s}/\rho_\infty U^2) \tag{6-26}$$

Similarly from Eq. (4-11), we can express the corresponding condition on $h_2(R_s)$. We write this condition in terms of our dependent variable $\bar{h}_2$ as

$$\bar{h}_{2_s}/(1/2)U^2 = [2\gamma/(\gamma-1)]\epsilon[(p_{2_s} - p_{0_s})/\rho_\infty U^2] \tag{6-27}$$

To integrate the vorticity equation, an additional condition at R_s, corresponding to Eq. (5-10), is required. This is the momentum relation Eq. (4-5) applied immediately behind the shock wave with ρ_0 and μ_0 taken constant and equal to their values in the shock layer. Consistently we evaluate the pressure difference $p_2(R_s) - p_0(R_s)$ from the modified shock relations, Eqs. (6-22) and (6-23). The result is

$$\frac{R_s^2 u_s''}{Re_s U} = -\left[\frac{1+j}{Re_s} + \frac{v_s}{\epsilon U}\right]\frac{R_s u_s'}{U} + \left[\frac{4}{Re_s} + \frac{u_s}{\epsilon U}\right]\left[\frac{u_s - v_s}{U}\right] - 2\left[1 - \frac{v_s}{U} - \frac{2(1+j)}{Re_s}\left\{1 - \frac{\pi}{4} + \frac{8}{3}\frac{\gamma}{\gamma+1}\left[1 + 2\left(\frac{\gamma-1}{\gamma+1}\right)^{1/2}\right]\right\} + \frac{1}{1+j}\left(1 - \frac{v_s}{\epsilon U}\right)\right] \tag{6-28}$$

We now note that the shock conditions, Eqs. (6-21)–(6-25), when taken together with the boundary conditions at the body, are sufficient to determine a solution to Eqs. (5-5)–(5-7). As already mentioned, in arriving at the shock boundary conditions, we have neglected a conservation equation for h_2 (or $\bar{h}_2$) in order to avoid overspecifying the boundary conditions. Although the viscous correction at the shock involving $h_2'(R_s)$ is of the same order as the other viscous corrections we neglect its influence since $h_2(R_s)$ is by itself small, being of the order of h_∞. Furthermore, the function h_2 is only weakly coupled with h_0 which is the dominant function in the stagnation region where the solution can be considered most significant. These remarks are equivalent to allowing $\bar{h}_2'(R_s)$ to be determined by the integration through the viscous layer itself.

An alternative approach for avoiding overspecification of the modified boundary conditions would have been to drop the function h_2 completely. However, in order to match the incipient merged shock boundary conditions with the already existing constant-density formulation containing h_2, the above approximate approach was chosen. It must be emphasized again that both approximations are equally valid for the stagnation region.

Eqs. (6-21), (6-24), and (6-28), when expressed in terms of Ψ, are the appropriate shock conditions to be used for the integration of the vorticity equation, Eq. (5-5). One method of carrying out the numerical solution of this equation is to choose a value of γ and Re_s and assume a value of ϵ. A value of $u'(R_s)$, say, is then selected and in the same manner as for the viscous layer an iteration of this selected quantity is carried out until the boundary conditions at the body, Eq. (5-8), are both simultaneously satisfied in the integration. For any given γ, Re_s, and ϵ, a body location R_b can be found. We then proceed to the integration of the enthalpy equation for $\bar{h}_2$, Eq. (5-6). This is carried out in the same manner as for the viscous layer with the shock condition on $\bar{h}_2$ expressed through Eq. (6-27). Eq. (5-7) for h_0 is then integrated, with not only the value of $h_0(R_s)$ but also $h_0'(R_s)$ initially specified, Eqs. (6-22), (6-25), and (6-26). Integration of this equation from the shock to the body determines the value of $h_0(R_b)$, which may not agree with the given wall value. We then choose a new value of ϵ, return to the vorticity equation, and repeat the whole procedure until the desired wall condition on the function h_0 is obtained. This coupling between the momentum and energy equations, despite the continued treatment of

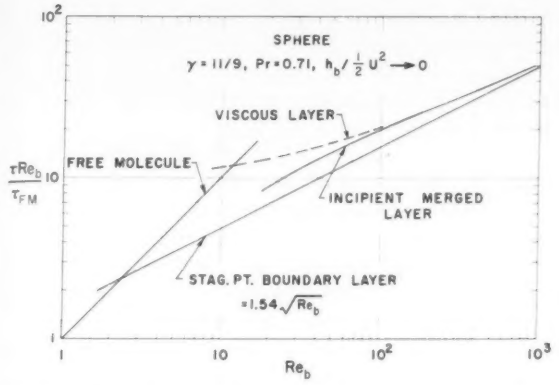

FIG. 6. Incipient merged layer surface shear stress on a sphere ($\tau_{FM} = \rho_\infty U^2 \sin\theta \cos\theta$).

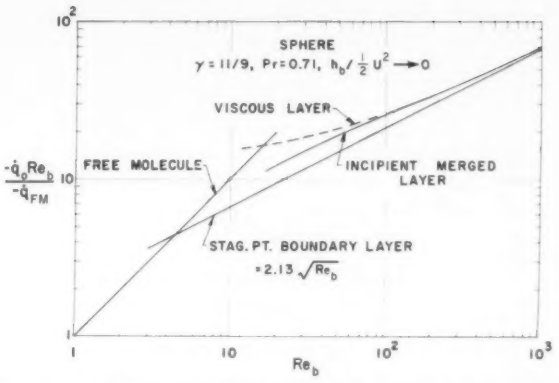

FIG. 7. Incipient merged layer stagnation-point heat-transfer rate on a sphere ($-\dot{q}_{FM} = (1/2)\,\rho_\infty U^3 \cos\theta$).

the shock layer as a constant-density region, is to be expected because of the introduction of gradients into the shock-wave conservation equations. It represents essentially a physical coupling between the strength of the shock-wave (ϵ) and the body geometry (Re_s), determined by the body temperature (h_{0_b}), which is not present when the shock-wave discontinuity is represented by the Hugoniot relations.

Calculations have been carried out in the manner indicated for the incipient merged layer on a highly cooled sphere. The same physical constants were employed as for the viscous layer calculations, with the difference that ϵ could no longer be fixed. Here, however, the gas is specified equivalently through the isentropic exponent γ which was taken equal to 11/9. For Reynolds numbers large enough to be in the viscous layer regime, this corresponds through the perfect gas strong shock relation Eq. (3-5) to a density ratio ϵ of 0.1.

Figs. 6 and 7 show the shear and heat transfer obtained by these calculations. The most significant feature of these results is that, as anticipated, both of these quantities drop off relative to the corresponding viscous layer solutions, beginning at a Reynolds number of about 100. Instead of using Re_s, these results are plotted using a Reynolds number Re_b which is somewhat more appropriate for the incipient merged layer analysis, in which the location of the shock wave is not sharply defined and in which values of the fluid properties in the viscous layer vary with Reynolds number. This Reynolds number Re_b is defined by

$$Re_b \equiv \rho_\infty U R_b/\bar{\mu}_0 \tag{6-29}$$

where R_b is the radius of curvature of the sphere, and $\bar{\mu}_0$ is the viscosity based on the stagnation enthalpy of the free stream, $U^2/2$. All these quantities are specified in a flight situation. The relation between Re_s and Re_b is

$$Re_b = Re_s(R_b/R_s)[h_{0_s}/(1/2)U^2]^{1/2} \tag{6-30}$$

The change from μ_{0_s} to $\bar{\mu}_0$ is made by assuming the viscosity to vary as the square root of the enthalpy on the stagnation streamline. For the viscous layer calculations $\mu_{0_s} = \bar{\mu}_0$ because $h_{0_s} = U^2/2$.

Table 2 shows the comparison between the two Reynolds numbers, the variation in density ratio across the shock wave, and the values of some other important flow quantities behind the shock. An important feature of these results is the decrease in density ratio and enthalpy with decreasing Reynolds number. Note that the dimensionless total enthalpy can be obtained from the static enthalpy given in the table by adding $(v_s/U)^2$.

Calculations have also been carried out in the incipient merged layer regime for an insulated sphere. They were done in the same manner as described above for the highly cooled case, except that the enthalpy boundary conditions on the body were changed to $\bar{h}_2' = h_0' = 0$, in accordance with Eq. (4-14). The same physical constants were employed. Some results are presented in Table 3. In contrast to the highly cooled case, the density ratio and enthalpy behind the shock increase with decreasing Reynolds number. Note also that the stagnation-point enthalpy and the enthalpy

TABLE 2
Incipient Merged Layer Results for Highly Cooled Sphere
$\gamma = 11/9$, $Pr = 0.71$, $h_b/(1/2)U^2 \to 0$

Re_s	ϵ	R_s/R_b	$\frac{h_{e_s}}{(1/2)U^2}$	Re_b	v_s/U	$\frac{p_{e_s}}{\rho_\infty U^2}$
100	0.104*	1.10	0.995	90.9	0.097	0.870
40	0.094	1.10	0.873	34.0	0.076	0.835
25	0.078	1.08	0.710	19.5	0.048	0.827

* This differs slightly from the viscous layer value of 0.1. The difference may well be attributable to the approximations of the theory and small numerical inaccuracies.

TABLE 3
Incipient Merged Layer Results for Insulated Sphere
$\gamma = 11/9$, $Pr = 0.71$, $h_b' = 0$

Re_s	ϵ	R_s/R_b	$\frac{h_{e_s}}{(1/2)U^2}$	Re_b	v_s/U	$\frac{p_{e_s}}{\rho_\infty U^2}$	$\frac{h_{e_b}}{(1/2)U^2}$
40	0.117	1.11	1.05	36.8	0.097	0.816	1.06
25	0.124	1.12	1.05	22.8	0.091	0.770	1.09

behind the shock are higher than the free-stream stagnation value. Although not shown, the stagnation-point pressure behaves similarly.

We may expect these incipient merged layer results to hold down to a Reynolds number of 20 or 30, and possibly somewhat lower. To determine this limit more precisely would entail calculations based on a fully merged layer analysis.

(7) Discussion of Results and Relation to Experiment

The results of the present analysis clearly show that at low Reynolds numbers the usual model of hypersonic blunt-body flow—an infinitesimally thin shock wave, an inviscid region, and a boundary layer—does not give a correct description of the flow quantities, at least in the stagnation region. The thickening, first of the boundary layer and then of the shock wave, as Reynolds number decreases, leads to significant changes in these quantities. In particular, when the shock thickness becomes important, the curvature, viscous, and heat conduction effects have a substantial influence on the conservation of mass, momentum, and energy across the shock wave, as well as in the shock layer. This in turn provides a physical coupling between shock-wave strength and body size and temperature which is not present in the usual flow picture.

Among the stagnation region phenomena predicted by the present theory as the Reynolds number decreases are: an increase in detachment distance for insulated bodies, an altered behavior of surface shear stress and heat-transfer rate relative to extrapolated boundary-layer theory, an increase of stagnation enthalpy and pressure above their free-stream value on insulated bodies, a decrease of normal velocity and enthalpy behind a shock for highly-cooled bodies, an increase or decrease of density behind the shock for highly-cooled or insulated bodies, respectively, and a decrease in pressure behind the shock wave for highly-cooled bodies.

Although some of these effects might seem at first glance to be unexpected, a number of them have been pointed out by other investigators, and in some low Reynolds number experiments certain general features are found which permit qualitative comparison. Moulic[17] has made afterglow tests on insulated spheres at low supersonic speeds. These experiments indicate an increased detachment distance with decreasing Reynolds number, with the order of the increase consistent with the present calculations.

Also of interest are heat-transfer and equilibrium temperature measurements on fine cylindrical wires in a supersonic stream, for example, those of Laufer and McClellan.[18] Although the wires were heated and the total heat transfer was measured rather than the local heat-transfer rate calculated here, the results are nonetheless significant. The change in heat transfer with decreasing Reynolds number, relative to boundary-layer theory, is in the direction indicated by our viscaus layer results (Fig. 5). Also the measured equilibrium temperature shows a rapid increase at low Reynolds numbers, rising above the free-stream stagnation temperature. This effect, caused by the added work done by viscous stresses, is consistent with the results presented in Table 3.

Then there are total pressure measurements, for example, those of Sherman[19] and Enkenhus,[20] in which the pressure is shown to increase with decreasing Reynolds number at an insulated stagnation point. Again, qualitative agreement with the present theory is indicated. For additional experimental results the reader is referred to Schaaf and Chambré.[4]

While some of our results are therefore found to be in qualitative agreement with available experimental data, there are a number of other effects mentioned above, such as the density, pressure, or enthalpy changes, for example, which, if found and measured experimentally, would help to indicate whether the present analysis correctly predicts the physical phenomena. (*Note added in proof:* After the work of references 3 and 25, a report by Hoshizaki[27] appeared in which he also considered the constant-density viscous layer on a sphere. His solutions are not complete symmetric ones in the sense of the present paper, and the additional approximations made are somewhat more restrictive than those used here. However, calculations for several values of ϵ were made, with a lower limit of approximately 500 for Re_s. Where these high Reynolds number calculations overlap ours, there is reasonable agreement.)

Appendix (A)—Navier-Stokes Equations in Polar Coordinates

The Navier-Stokes momentum equations, with variable viscosity, may be found written in both cylindrical and spherical polar coordinates in reference 22, pp. 59–61. The two cases may be combined by the use of a factor j, which is zero for the cylindrical case and one for the spherical case. The energy equation in Cartesian tensor form may be found in the same reference, pp. 15–16, and can easily be converted to the polar coordinates by the use of the strain tensor components given on pp. 59–61.

We use the notation shown in Fig. 2, with the subscript n used to denote the direction normal to the $R - \theta$ plane in either coordinate system. Since we are interested in axisymmetric or two-dimensional flow, all derivatives and velocity components in the direction of n vanish. Then the components of the strain tensor are

$$e_{RR} = 2(\partial q_R/\partial R), \quad e_{\theta\theta} = (2/R)[(\partial q_\theta/\partial\theta) + q_R]$$

$$e_{R\theta} = R(\partial/\partial R)(q_\theta/R) + (1/R)(\partial q_R/\partial\theta),$$

$$e_{nn} = j(2/R)(q_R + q_\theta \cot\theta)$$

The components of the shear stress tensor are related to those of the strain tensor by the viscosity coefficients and are given by

$$\tau_{RR} = \mu e_{RR} + 2[\mu^* - (\mu/3)]\nabla\cdot\mathbf{q}; \quad \tau_{\theta\theta} = \mu e_{\theta\theta} + 2[\mu^* - (\mu/3)]\nabla\cdot\mathbf{q}$$

$$\tau_{nn} = \mu e_{nn} + 2[\mu^* - (\mu/3)]\nabla\cdot\mathbf{q}; \quad \tau_{R\theta} = \mu e_{R\theta}; \quad \tau_{Rn} = \tau_{\theta n} = 0$$

where $$2\nabla\cdot\mathbf{q} \equiv e_{RR} + e_{\theta\theta} + e_{nn} = (2/R)[R(\partial q_R/\partial R) + q_R + (\partial q_\theta/\partial\theta) + j(q_R + q_\theta \cot\theta)]$$

The momentum equations can now be written as

$$\frac{\partial p}{\partial R} + \rho\left[q_R\frac{\partial q_R}{\partial R} + \frac{q_\theta}{R}\frac{\partial q_R}{\partial\theta} - \frac{q_\theta^2}{R}\right] = \frac{\partial}{\partial R}\left[\mu e_{RR} + 2(\mu^* - \mu/3)\nabla\cdot\mathbf{q}\right] + \frac{1}{R}\frac{\partial}{\partial\theta}(\mu e_{R\theta}) + \frac{\mu}{R}(e_{RR} - e_{\theta\theta}) + j\frac{\mu}{R}(e_{RR} - e_{nn} + e_{R\theta}\cot\theta)$$

$$\frac{1}{R}\frac{\partial p}{\partial\theta} + \rho\left[q_R\frac{\partial q_\theta}{\partial R} + \frac{q_\theta}{R}\frac{\partial q_\theta}{\partial\theta} + \frac{q_R q_\theta}{R}\right] = \frac{1}{R}\frac{\partial}{\partial\theta}[\mu e_{\theta\theta} + 2(\mu^* - \mu/3)\nabla\cdot\mathbf{q}] + \frac{\partial}{\partial R}(\mu e_{R\theta}) + 2\frac{\mu}{R}e_{R\theta} + j\frac{\mu}{R}[e_{R\theta} + (e_{\theta\theta} - e_{nn})\cot\theta]$$

The energy equation is

$$\rho\left[q_R\frac{\partial h}{\partial R} + \frac{q_\theta}{R}\frac{\partial h}{\partial\theta}\right] = q_R\frac{\partial p}{\partial R} + \frac{q_\theta}{R}\frac{\partial p}{\partial\theta} + \Phi + \frac{1}{R}\left[\frac{\partial}{\partial R}\left(kR\frac{\partial T}{\partial R}\right) + \frac{\partial}{\partial\theta}\left(\frac{k}{R}\frac{\partial T}{\partial\theta}\right) + jk\left(\frac{\partial T}{\partial R} + \frac{\cot\theta}{R}\frac{\partial T}{\partial\theta}\right)\right]$$

where the dissipation function Φ is defined by

$$\Phi = \frac{1}{2}\mu(e_{RR}^2 + e_{\theta\theta}^2 + e_{nn}^2 + 2e_{R\theta}^2) + \left(\mu^* - \frac{2}{3}\mu\right)(\nabla\cdot\mathbf{q})^2$$

Finally, the continuity equation in these coordinates becomes

$$\nabla\cdot(\rho\mathbf{q}) = \frac{1}{R}\left[R\frac{\partial\rho q_R}{\partial R} + \frac{\partial\rho q_\theta}{\partial\theta} + \rho q_R + j\rho(q_R + q_\theta\cot\theta)\right] = 0$$

Appendix (B)—Shock-Wave Conservation Equations

The compressible symmetry equations, Eqs. (4-2)–(4-7), are rewritten by eliminating p_0', p_2' and $p_2 - p_0$ from the enthalpy equations, Eqs. (4-6) and (4-7), by means of the momentum equations, Eqs. (4-3)–(4-5). Also, the continuity equation, Eq. (4.7), is used for any quantity f to write

$$\rho_0 v f' = (\rho_0 v f)' - f(\rho_0 v)' = (\rho_0 v f)' - (1 + j)\rho_0 f(u - v)/R$$

With these changes and some rearrangement, Eqs. (4-2)–(4-7) become (with $\mu_0{}^*$ ignored)

$$(\rho_0 v)' - (1 + j)\rho_0(u - v)/R = 0 \tag{B-1}$$

$$p_0' + (\rho_0 v^2)' - (1 + j)\rho_0 v\frac{u - v}{R} = -\frac{4}{3}\left[\mu_0\left(v' + \frac{1 + j}{2}\frac{u - v}{R}\right)\right]' + (1 + j)\frac{\mu_0}{R}\left[u' - 2v' - 3\frac{u - v}{R}\right] \tag{B-2}$$

$$p_2' - \rho_0 u\frac{u - v}{R} = -\frac{\mu_0}{R}\left(u' - \frac{u - v}{R}\right) \tag{B-3}$$

$$2\frac{p_2 - p_0}{R} - (\rho_0 v u)' + (2 + j)\rho_0 u\frac{u - v}{R} = \left[\mu_0\left(u' - \frac{u - v}{R}\right)\right]' + \frac{\mu_0}{R}\left[(2 + j)u' - \frac{4}{3}v' - \frac{14 - j}{3}\frac{u - v}{R}\right] \tag{B-4}$$

$$\frac{1}{Pr}\left[(\mu_0 h_0')' + \frac{1 + j}{R}\mu_0 h_0' + \frac{2(1 + j)}{R^2}\mu_0(h_2 - h_0)\right] + \left[\rho_0 v\left(h_0 + \frac{1}{2}v^2\right)\right]' - (1 + j)\rho_0\left(h_0 + \frac{1}{2}v^2\right)\frac{u - v}{R} = -\frac{4}{3}\left[\mu_0 v\left(v' + \frac{1 + j}{2}\frac{u - v}{R}\right)\right]' - \frac{2}{3}(1 + j)\mu_0 v'\frac{u - v}{R} + (1 + j)\frac{\mu_0}{R}v\left(u' - 2v' - 3\frac{u - v}{R}\right) - \frac{4}{3}\mu_0\left(\frac{u - v}{R}\right)^2 \tag{B-5}$$

These equations are integrated on R from R_s to $R \to \infty$, the boundary conditions at ∞, Eqs. (4-15)–(4-17), are inserted, and all gradients are taken to vanish at ∞. The result of the integration is then

$$\rho_\infty U - \rho_{0s} v_s - (1+j)\int_{R_s}^{\infty} \rho_0 \frac{u-v}{R}\,dR = 0 \tag{B-6}$$

$$p_\infty - p_{0s} + \rho_\infty U^2 - \bar{\rho}_{0s} v_s^2 - (1+j)\int_{R_s}^{\infty} \rho_0 v \frac{u-v}{R}\,dR = \frac{4}{3}\mu_{0s}\left(v_s' + \frac{1+j}{2}\frac{u_s - v_s}{R_s}\right) + (1+j)\int_{R_s}^{\infty}\frac{\mu_0}{R}\left(u' - 2v' - 3\frac{u-v}{R}\right)dR \tag{B-7}$$

$$p_\infty - p_{2s} - \int_{R_s}^{\infty}\rho_0 u\frac{u-v}{R}\,dR = -\int_{R_s}^{\infty}\frac{\mu_0}{R}\left(u' - \frac{u-v}{R}\right)dR \tag{B-8}$$

$$2\int_{R_s}^{\infty}\frac{p_2 - p_0}{R}\,dR - \rho_\infty U^2 + \rho_{0s} v_s u_s + (2+j)\int_{R_s}^{\infty}\rho_0 u\frac{u-v}{R}\,dR = -\mu_{0s}\left(u_s' - \frac{u_s - v_s}{R_s}\right) + \int_{R_s}^{\infty}\frac{\mu_0}{R}\left[(2+j)u' - \frac{4}{3}v' - \frac{14-j}{3}\frac{u-v}{R}\right]dR \tag{B-9}$$

$$\frac{1}{Pr}\left[-\mu_{0s}h_{0s}' + \bar{(}1+j)\int_{R_s}^{\infty}\frac{\mu_0}{R}\left(h_0' + \frac{2}{R}\bar{h}_2\right)dR\right] + \rho_\infty U\left(h_\infty + \frac{1}{2}U^2\right) - \rho_{0s}v_s\left(h_{0s} + \frac{1}{2}v_s^2\right) - (1+j)\int_{R_s}^{\infty}\rho_0\left(h_0 + \frac{1}{2}v^2\right)\frac{u-v}{R}\,dR = \frac{4}{3}\mu_{0s}v_s\left(v_s' + \frac{1+j}{2}\frac{u_s - v_s}{R_s}\right) - \frac{2}{3}(1+j)\int_{R_s}^{\infty}\mu_0 v'\frac{u-v}{R}\,dR + (1+j)\int_{R_s}^{\infty}\frac{\mu_0}{R}v\left(u' - 2v' - 3\frac{u-v}{R}\right)dR - \frac{4}{3}\int_{R_s}^{\infty}\mu_0\left(\frac{u-v}{R}\right)^2 dR \tag{B-10}$$

These are the shock-wave conservation equations which are used to obtain the shock-wave boundary conditions in the incipient merged layer model of the flow field.

References

[1] Adams, M. C., and Probstein, R. F., *On the Validity of Continuum Theory for Satellite and Hypersonic Flight Problems at High Altitudes*, Jet Propulsion, Vol. 28, No. 2, pp. 86–89, February, 1958.

[2] Hayes, W. D., and Probstein, R. F., *Hypersonic Flow Theory*, Academic Press, New York, 1959.

[3] Probstein, R. F., *Continuum Theory and Rarefied Hypersonic Aerodynamics*, WADC TN No. 58-145, Div. of Eng., Brown University, Providence, R.I., July, 1958. Also see *Rarefied Gas Dynamics*, Devienne, F. M., (Ed.), Proc. of First Symposium held at Nice, Pergammon Press, London, 1958.

[4] Emmons, H. W., (Ed.), *Fundamentals of Gas Dynamics*, Schaaf, S. A., and Chambré, P. L., "Flow of Rarefied Gases," Sec. H, pp. 687–739, Vol. III, *High Speed Aerodynamics and Jet Propulsion*, Princeton University Press, Princeton, N.J., 1958.

[5] Tsien, H. S., *Superaerodynamics, Mechanics of Rarefied Gases*, Journal of the Aeronautical Sciences, Vol. 13, No. 12, pp. 653–664, December, 1946.

[6] Lunc, M., and Lubonski, J., *Sur une Solution Approcheé du Problème de l'Ecoulement d'un Gaz Raréfié Autour d'un Obstacle*, Arch. Mech. Stos., Vol. 8, pp. 597–616, 1956.

[7] Baker, R. M. L., Jr., and Charwat, A. F., *Transitional Correction to the Drag of a Sphere in Free Molecule Flow*, Phys. Fluids, Vol. 1, No. 2, pp. 73–81, March–April, 1958.

[8] Hammerling, P., and Kivel, B., *Heat Transfer to a Sphere at the Transition from Free Molecule Flow*, Phys. Fluids, Vol. 1, No. 4, pp. 357–358, July–August, 1958.

[9] Liu, V. C., *On Pitot Pressure in an Almost-Free-Molecule Flow—A Physical Theory for Rarefied-Gas Flows*, Journal of the Aero/Space Sciences, Vol. 25, No. 12, pp. 779–785, December, 1958.

[10] Willis, D. R., *On the Flow of Gases Under Nearly Free Molecular Conditions*, Rpt. No. 442, Dept. of Aeronautical Engineering, Princeton University, Princeton, N.J., 1958.

[11] Lighthill, M. J., *Dynamics of a Dissociating Gas. Part I. Equilibrium Flow*, J. Fluid Mech., Vol. 2, pp. 28–31, January, 1957.

[12] Whitham, G. B., *A Note on the Stand-Off Distance of the Shock in High Speed Flow Past a Circular Cylinder*, Comm. on Pure and Applied Math., Vol. X, No. 4, pp. 531–535, November, 1957.

[13] Fay, J. A., and Riddell, F. R., *Theory of Stagnation Point Heat Transfer in Dissociated Air*, Journal of the Aero/Space Sciences, Vol. 25, No. 2, pp. 73–85, February, 1958.

[14] Sibulkin, M., *Heat Transfer Near the Forward Stagnation Point of a Body of Revolution*, Journal of the Aeronautical Sciences, Vol. 19, No. 8, pp. 570–571, August, 1952.

[15] Schlichting, H., *Boundary Layer Theory*, McGraw-Hill Book Co., Inc., New York, 1955.

[16] Emmons, H. W. (Ed.), *Fundamentals of Gas Dynamics*, Hayes, W. D., "The Basic Theory of Gasdynamic Discontinuities," Sec. D, pp. 416–481, Vol. III, *High Speed Aerodynamics and Jet Propulsion*, Princeton University Press, Princeton, N.J., 1958.

[17] Moulic, E. S., *Afterglow Investigations of Shock Detachment Distances at Low Reynolds Numbers*, Tech. Report No. HE-150-148, Inst. of Eng. Res., University of California, Berkeley, Calif., July, 1958. Also, WADC TR 57-643, ASTIA AD 155795, July 15, 1958.

[18] Laufer, J., and McClellan, R., *Measurements of Heat Transfer from Fine Wires in Supersonic Flows*, J. Fluid Mech. Vol., 1, Part 3, pp. 276–289, September, 1956.

[19] Sherman, F. S., *New Experiments on Impact-Pressure Interpretation in Supersonic and Subsonic Rarefied Air Streams*, NACA TN 2995, September, 1953.

[20] Enkenhus, K. R., *Pressure Probes at Very Low Density*, UTIA Rpt. No. 43, Inst. of Aerophys., University of Toronto Toronto, Canada, January, 1957.

[21] Corrsin, S., and Kovasznay, L. S. G., *The Energy Equation for Two Kinds of "Incompressible Flow"*, Journal of the Aeronautical Sciences, Vol. 18, No. 12, pp. 843–844, December, 1951.

[22] Emmons, H. W. (Ed.), *Fundamentals of Gas Dynamics*, Tsien, H. S., "The Equations of Gas Dynamics," Sec. A, pp. 3–

(*Continued on page 218*)

A Study of Vortex Cancellation

ALLAN SCHAFFER*

Space Technology Laboratories, Inc.

Summary

The cancellation of a vortex by means of another concentric vortex of equal strength but opposite spin is investigated. When such a cancellation occurs, there is a recovery of static pressure. The vortices are generated by means of two three-dimensional airfoils cantilevered from the duct wall, one being situated in the wake of the other. The airfoils have opposite effective angles of attack and therefore have trailing vortices of opposite spin, as required.

It is demonstrated experimentally that there exists an optimum angle of attack for the second airfoil which cancels the vortex from the first airfoil and restores uniform flow downstream of the two airfoils. A theoretical solution of this optimum angle of attack is presented, and it is found to depend upon the angle of attack of the first airfoil and upon the geometrical properties of the wings. The pressure recovery accompanying the vortex cancellation is also studied. Theoretical considerations, based on the model of a vortex filament in the center of a circular tube show that a maximum of 62 per cent of the static pressure drop across the first airfoil can be recovered. This maximum is imposed, irrespective of skin friction and separation losses, by the irreversibility associated with establishing a vortex field. Experimental pressure recoveries of 50 per cent are realized.

Perhaps the primary value of the present study is the opportunity it provides to verify certain of the fundamental concepts of fluid mechanics which are brought into play when the trailing vortex system of a lifting wing is cancelled by a second wing.

Symbols

a = radius of vortex core
A = aspect ratio
c = chord
p = pressure
Δp = mean duct pressure upstream of airfoil minus mean duct pressure downstream of airfoil
Δp_i = irreversible portion of Δp
Δp_r = reversible portion of Δp
q = velocity head
r = radial coordinate
R = duct radius
s = half span of the airfoil
s' = half span of the horseshoe vortex
V = velocity
α = angle of attack
β = $(A/2) + (2\alpha/\pi)$
Γ = circulation
η = pressure recovery efficiency
ρ = mass density
$( )_1$ = upstream airfoil
$( )_2$ = downstream airfoil
$( )_*$ = quantity evaluated at airfoil midspan
$( )_0$ = undisturbed flow
$( )_w$ = quantity evaluated at the wall
$( )_\theta$ = tangential component
$(\bar{\ })$ = spatial average value

Received January 19, 1959. Revised and received October 6, 1959.

* Member of the Technical Staff, Physical Research Laboratory.

The author is indebted to Dr. Milton U. Clauser, who suggested the vortex cancellation experiment, to Dr. Lee O. Heflinger for designing the camera to photograph the tuft grid, and to Dr. Rudolf X. Meyer for several helpful discussions.

(1) Introduction

THIS PAPER describes a study of the cancellation of the trailing vortex system of a lifting wing by the use of a second wing situated in the wake of the first.

Three-dimensional half-wings cantilevered from the duct wall are used. A single rolled-up vortex emanates from each. The vortex wake downstream from a half-wing consists of a relatively thin filament, in which to a good approximation the curl of the velocity is constant, surrounded by a flow in which the curl of the velocity is zero. It follows that the tangential velocity varies directly with radius within the filament and inversely with radius outside the filament. Hence, the tangential kinetic energy of the vortex flowfield emanating from the upstream wing is in a highly ordered form and is thus subject to recovery. If the flow can be straightened and the vortex cancelled without appreciable increase in entropy, the tangential kinetic energy can be recovered in the form of increased static pressure.

Pressure recovery by this technique is of interest in the design of rotating compressors; more novel applications are also conceivable. For example, it is possible to mix fluids by means of a vortex, then cancel the vortex and recover a substantial portion of the energy assigned to do the mixing. The net result is a mixing chamber with low overall pressure drop. However, it is not the purpose of this paper to discuss practical applications of vortex cancellation but rather to present the results of some fundamental experiments and theoretical analyses concerning the phenomenon.

Experimental studies of vortex cancellation have been carried out in a conventional low-speed wind tunnel. The technique involves first the generation of a vortex by a half-wing with a given angle of attack; then at a point downstream a similar wing with an opposite effective angle of attack generates a vortex of equal strength but opposite sense of rotation. The wings are aligned so that the two opposite-spinning vortices are concentric, and in this manner vortex cancellation can be achieved.

For maximum cancellation, the angle of attack of the second airfoil must be optimized so that the strength of its trailing vortex is just equal in magnitude to that of the first airfoil. This optimization problem is inves-

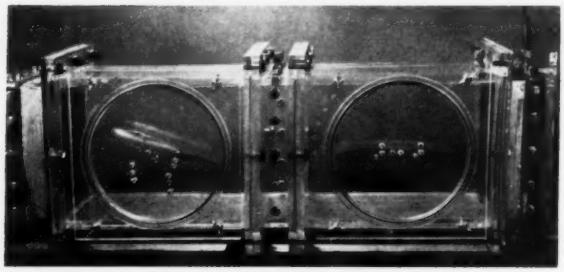

FIG. 1. 6 by 6 in. test section.

tigated experimentally and theoretically in the paper. Similar studies are made of the pressure recovery accomplished by the second airfoil.

(2) Description of Experimental Facilities

The wind tunnel is of conventional low-speed design. It has a maximum test section velocity of 200 ft. per sec. and a 6 by 6 in. square test section, as shown in Figs. 1 and 2. The wings are cantilevered from pivotable discs which form part of the tunnel walls and which can be rotated to any convenient angle of attack. The centers of the two airfoils are 11 in. apart. A tuft grid, located 5 in. past the center of the downstream airfoil, is used to observe the vortices.[1] Static pressure measurements are made by means of both wall taps and spherically ended probes.

(3) Experimental Techniques

The two airfoils are usually geometrically identical. The angle of attack α_1 of the upstream airfoil is generally set just under the stall point so that the strongest possible vortex without separation is produced. All of the airfoils tested are of relatively low aspect ratio (in the range 1 to 4) so that the trailing vortex sheet rolls up into a single vortex in a distance downstream of the order of one chord[2]; for this reason no airfoil pairs have been placed closer together than two chords in the present experimental study.

In order to achieve full vortex cancellation, the filaments from the two airfoils must be coincident. Since the filaments exhibit a neutral stability in that they neither attract nor repel each other, rather careful positioning of the wings is necessary to ensure that the filaments are precisely concentric. As predicted by vortex theory, a slight mismatch still results in cancellation of the irrotational field, but the rotational cores do not then cancel; instead, they translate each other violently.

Once the airfoils have been aligned so that the vortices are concentric, the angle of attack α_2 of the downstream airfoil is optimized by rotating the airfoil mounting disc until the angle is found at which the minimum ordered rotation is visible in the tuft grid pattern. The uncertainty in determining the optimum α_2 by this technique is about $\pm 1°$.

(4) Photographic Results of Vortex Cancellation Experiments

Cancellation tests have been made for three sets of airfoil pairs, the specifications for which are given in Table 1. All are NACA 0012 symmetrical untwisted half-wings of rectangular plan form. Test results are reported for $V_0 = 196$ ft. per sec.; however the phenomenon exhibits negligible Reynolds number dependence within the range of the tests.

Figs. 3 and 4 are typical tuft-grid photographs of the cancellation phenomenon for airfoil pairs (2) and (3) of Table 1, respectively. In Figs. 3(a) and 4(a) only the upstream airfoil is installed, whereas in Figs. 3(b) and 4(b) the downstream airfoil is also installed and α_2 is optimized. Depending upon the illumination, the airfoils are sometimes visible in the photographs. As seen in the figures, the cancellation is virtually complete except for some slight residual core vorticity. The optimized values for α_2 are $-3^1/_2° \pm 1°$ with airfoil pair (2) and $-2^1/_2° \pm 1°$ with airfoil pair (3).

Although only the cancellation phenomenon is shown in the pictures, it is simple to obtain other interactions such as vortex addition merely by varying α_2.

(5) Theoretical Analysis of Vortex Cancellation

The present analysis is intended to be only a first-order description of the phenomenon. The model in Fig. 5 is assumed. The upstream airfoil is represented by a horseshoe vortex with strength Γ_*. The bound portion of the horseshoe vortex has negligible effect and is ignored in the derivation. The discussion is limited to symmetrical untwisted wings with the upstream and downstream airfoils being geometrically identical.

The basis of this analysis is that the optimum α_2 will occur when a trailing vortex from the downstream airfoil has strength of equal magnitude and opposite sign to the corresponding vortex from the upstream

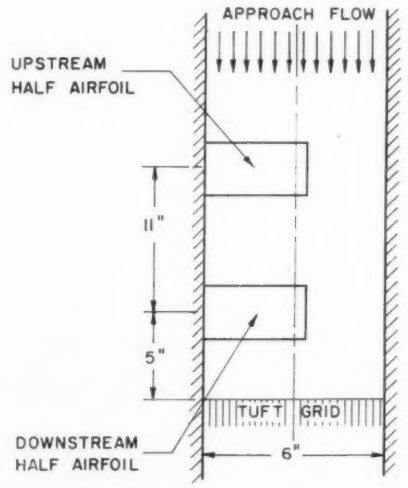

FIG. 2. Plan view of test section.

TABLE 1
Comparison Between Experimental and Theoretical Cancellation Results

Airfoil Pair No.	c	s'	A	α_{stall}	α_1	$\alpha_2)_{exp.}$	$\alpha_2)_{theory}$	$\frac{\alpha_2)_{exp.} - \alpha_2)_{theory}}{\alpha_1}$
(1)	$1^3/_4$ in.	$3^1/_4$ in.	4.00	13°	10°	−5°	−6.2°	0.12
(2)	3 in.	$2^3/_4$ in.	1.94	$15^1/_2$°	14°	$-3^1/_2$°	−4.5°	0.07
(3)	$5^1/_2$ in.	$3^1/_8$ in.	1.16	19°	18°	$-2^1/_2$°	1.0°	−0.19

airfoil. In view of the fact that the circulation Γ_* at the midspan of an airfoil equals the strength of one of its fully rolled-up vortices, the requirement can be formulated as $\Gamma_{*2} = -\Gamma_{*1}$. It is logical that, for this requirement to be met, α_2 should equal the negative of α_1 decreased in magnitude by the induced angle of attack resulting from the upwash† generated by the upstream airfoil. In equation form, one obtains

$$\alpha_2 = -\alpha_1 + (\Gamma_{*1}/\pi s' V_0) \qquad (5.1)$$

Eq. (5.1) can also be derived on a more formal basis by means of elliptical wing theory.

In proceeding with the analysis, the theory for elliptically loaded wings of small span, developed by Weinig,[3] will be used, since the wings employed experimentally have relatively low aspect ratios. The results given by conventional lifting-line theory can always be obtained as a special case by examining the asymptotic limit of the formulas for large aspect ratio.

A useful equation yielded by Weinig's theory is

$$\Gamma_* = \pi c_* V_0 \, [\beta \tan \beta^{-1}/(1 + \tan \beta^{-1})]\alpha \qquad (5.2)$$

where $\beta = (A/2) + (2\alpha/\pi)$. Combining Eq. (5.1) with Eq. (5.2) evaluated for the upstream airfoil, one obtains the desired relationship between α_2 and α_1; viz.,

$$\alpha_2 = \left\{ [c_* \beta \tan \beta^{-1}/s' (1 + \tan \beta^{-1})] - 1 \right\} \alpha_1 \qquad (5.3)$$

As might be expected, no velocity dependence is obtained. For $A \gg 4\alpha_1/\pi$, the formula reduces to that given by conventional lifting-line theory; viz.,

$$\alpha_2 = \left\{ [c_*/s'(1 + 2/A)] - 1 \right\} \alpha_1 \qquad (5.4)$$

Eq. (5.4) shows that for wings with higher aspect ratio, α_2 varies directly with α_1.

In Table 1 the predictions of Eq. (5.3) are compared to the three experimental data points available, all of which are for rectangular wings. The experimental uncertainty in determining α_2 is about ±1°. There appears to be a first-order agreement between theory and experiment; however, no final conclusion as to the accuracy of the theory can be made because insufficient experimental data are available.

(6) Pressure Recovery by Vortex Cancellation

The pressure drop Δp across an airfoil will be defined as the mean duct pressure upstream of the wing minus the mean duct pressure downstream. Moreover, Δp can be divided into a reversible portion Δp_r associated with establishing the ordered vortex field, and an irreversible portion Δp_i, associated with mechanisms producing disordered motion. When the vortex is cancelled, $\Delta p_{r2} = -\Delta p_{r1}$. In view of this relation-

† The term "upwash" is used because the interaction is such as to increase the angle of attack of the downstream airfoil.

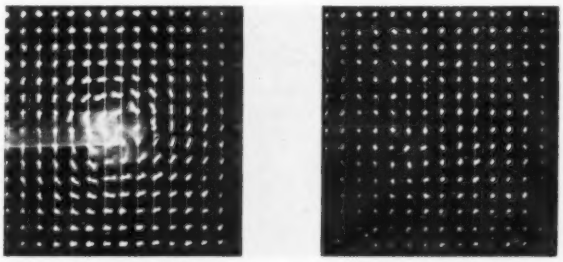

FIG. 3. Cancellation for airfoil pair (2), V_0 = 196 ft. per sec. (a) *Left:* one airfoil $\alpha = +14°$. (b) *Right:* two airfoils, $\alpha_1 = +14°$, $\alpha_2 = -3^1/_2$°.

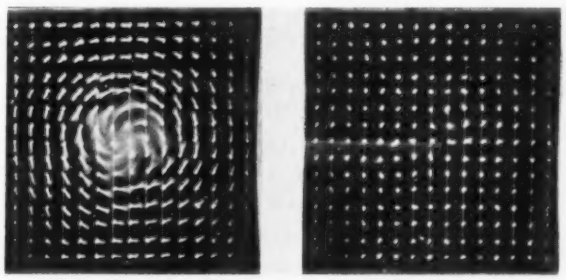

FIG. 4. Cancellation for airfoil pair (3), V_0 = 196 ft. per sec. (a) *Left:* one airfoil, $\alpha = +18°$. (b) *Right:* two airfoils, $\alpha_1 = +18°$, $\alpha_2 = -2^1/_2$°.

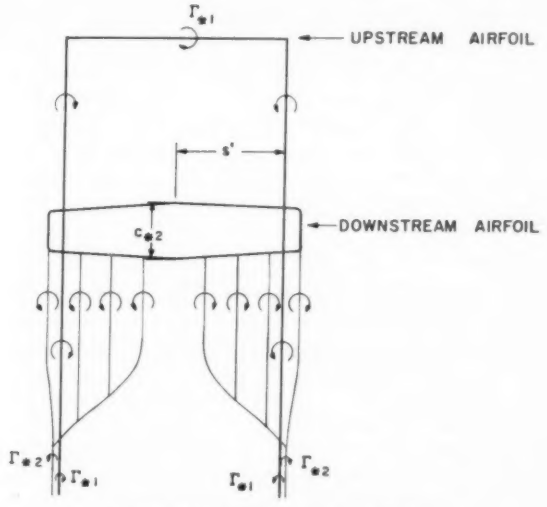

FIG. 5. Model for vortex cancellation.

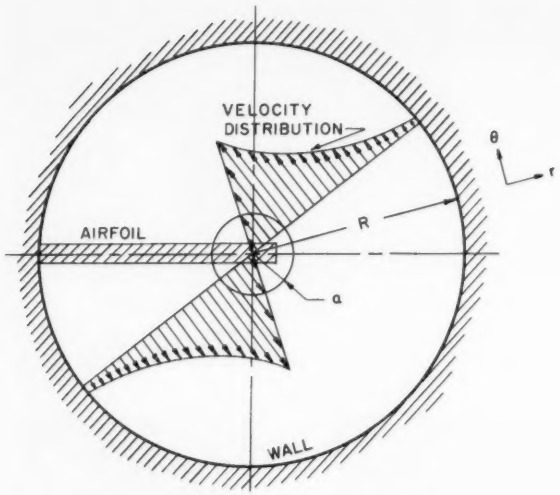

FIG. 6. Tangential velocity distribution.
$V_\theta = r\Gamma_*/2\pi a^2, \quad r \leq a$
$V_\theta = \Gamma_*/2\pi r, \quad a \leq r \leq R$

ship, a recovery efficiency η can be defined as

$$\eta = 1 - [(\Delta p_{t1} + \Delta p_{t2})/\Delta p_1] \tag{6.1}$$

To simplify the computation, the assumption is made that

$$\Delta p_{t1} = \Delta p_{t2} \tag{6.2}$$

This assumption is reasonable since the airfoils are geometrically identical and since for cancellation they experience much the same relative flows. Eq. (6.2), when substituted into Eq. (6.1), together with the identity $\Delta p_1 = \Delta p_{r1} + \Delta p_{t1}$, yields

$$\eta = 1 - \{2/[1 + (\Delta p_{r1}/\Delta p_{t1})]\} \tag{6.3}$$

Eq. (6.3) is useful in determining both the experimental efficiency and the maximum theoretical efficiency. Experimental efficiencies determined this way obviate the tedious task of making pressure traverses in the wake of an airfoil. The procedure is first to ascertain the vortex strength Γ_* and core radius a in the wake from the first airfoil by means of a tuft grid photograph. Assuming the usual velocity distribution for a vortex, Fig. 6, one can compute† Δp_{r1} knowing Γ_* and a. Then Δp_{t1} is found by measuring the total static pressure drop across the two airfoils with vortex cancellation.‡ By Eq. (6.2) Δp_{t1} equals 1/2 this value. Thus, knowing Δp_{r1} and Δp_{t1}, one computes the experimental η from Eq. (6.3). For the airfoils tested, the value obtained by this method is approximately $\eta = 0.5$, and a similar value results when η is determined by means of pressure traverses. Thus, experimental pressure recoveries of approximately 50 per cent have been realized.

† See Eq. (6.6).

‡ Wall taps can be used for this measurement since there is uniform flow upstream of the first airfoil and downstream of the second one.

To determine the maximum theoretical value of η, consider steady incompressible flow over a half airfoil in a circular duct of constant area with no wall friction. We must compute Δp_r and Δp_t in Eq. (6.3). Subscript $(\,)_0$ denotes a station in the undisturbed flow upstream of the first airfoil, no subscript denotes a station in the wake shown in Fig. 6, and subscript $(\,)_\theta$ denotes the tangential component in the wake. From an energy balance together with the relationship $V^2 = V_0^2 + V_\theta^2$ it can easily be shown that, for the upstream airfoil,

$$\Delta p_t = p_0 - \bar{p} - \bar{q}_\theta \tag{6.4}$$

where the notation $(^-)$ means average value over the cross section and $q_\theta = (1/2)\ \rho\ V_\theta^2$ is the tangential velocity head. Δp_r is by definition the value of Δp when Δp_t is zero. Setting $\Delta p_t = 0$ in Eq. (6.4), one obtains

$$p_0 - \bar{p} = \bar{q}_\theta = \Delta p_r \tag{6.5}$$

Eq. (6.5) can be evaluated from the velocity profile equations—namely, $V_\theta = r\Gamma_*/2\pi a^2$ for $r \leq a$ and $V_\theta = \Gamma_*/2\pi r$ for $a \leq r \leq R$. One obtains the final expression for Δp_r as

$$\Delta p_r = 2\ q_{\theta w}[\ln(R/a) + (1/4)] \tag{6.6}$$

where $q_{\theta w}$ is the tangential velocity head at the wall.

It remains to compute Δp_t. The minimum value of Δp_t can be determined by specifying the skin friction and separation losses to be zero. The residual Δp_t, called $\Delta p_t)_{min}$, results from the irreversibility associated with establishing the vortex and is evaluated by means of Eq. (6.4). The value of $\bar{q}_\theta$ to be used in Eq. (6.4) is given by Eq. (6.5) together with Eq. (6.6). The expression for $\bar{p}$ can be deduced by applying Newton's Second Law along the radial direction in Fig. 6; this gives

$$\bar{p} = p_w - 2\ q_{\theta w}[\ln\,(R/a) + (1/4)] \tag{6.7}$$

Combining Eqs. (6.5), (6.6), and (6.7) with Eq. (6.4), one obtains

$$\Delta p_t)_{min} = p_0 - p_w \tag{6.8}$$

But Bernoulli's equation is applicable between points in the undisturbed flow and points in the irrotational region downstream of the airfoil, so that

$$(p_0/\rho) + (V_0^2/2) = (p_w/\rho) + (V_w^2/2) \tag{6.9}$$

and since $V_w^2 = V_0^2 + V_{\theta w}^2$, Eq. (6.8) reduces to

$$\Delta p_t)_{min} = q_{\theta w} \tag{6.10}$$

When Eqs. (6.6) and (6.10) are substituted into Eq. (6.3), the theoretical maximum value of η is obtained as

$$\eta_{max} = [4 \ln (R/a) - 1]/[4 \ln (R/a) + 3] \tag{6.11}$$

It is significant that η_{max} is a function only of R/a and not even a very strong function of it. The numerical results differ little whether R/a or s/a is used in Eq.

(*Continued on page 233*)

Optimization of the Flight-Control, Airframe System†

I. L. ASHKENAS* AND D. T. McRUER**

Systems Technology, Inc.

Summary

The analysis of a system composed of a flight control and an airframe is ordinarily accomplished by using servoanalysis techniques in which the airframe and controller are described in terms of transfer functions. Optimization of such a system at the analytical level involves the selection of desirable relative locations for the poles and zeros of the airframe and controller transfer functions. The appropriate airframe pole and zero locations thus selected are then reflected back into the airframe geometrical characteristics. To achieve such an optimum system thus demands an overall approach which considers both the airframe and flight controller to be alterable system elements. This paper develops the optimization concept and illustrates the procedure with practical examples.

Symbols

a, A = polynomial coefficients

a_y = lateral acceleration at the center of gravity

a_y' = lateral acceleration at a distance l_x from the c.g., $a_y' = a_y + l_x\dot{r}$

a_z = normal acceleration at the center of gravity

a_z' = normal acceleration at a distance l_x from the c.g., $a_z' = a_z - l_x\dot{q}$

AR = amplitude ratio

$A_{y_\delta}(s)$ = transfer function relating lateral acceleration to control-surface deflection, $a_y(s)/\delta(s)$

$A_{y_\delta}'(s)$ = transfer function relating lateral acceleration at a distance l_x from the c.g. to control-surface deflection, $a_y'(s)/\delta(s)$

$A_{z_\delta}(s)$ = transfer function relating normal acceleration to control-surface deflection, $a_z(s)/\delta(s)$

b = wing span

b, B = polynomial coefficients

c, C = polynomial coefficients

C_l = rolling-moment coefficient, (Roll Moment)/$(1/2)\rho U_0^2 Sb$

C_{l_β} = dihedral parameter, variation of rolling-moment coefficient with sideslip, $\partial C_l/\partial\beta$

$C_{l_{\delta_a}}$ = aileron rolling effectiveness, $\partial C_l/\partial\delta_a$

C_{l_p} = roll-damping coefficient, $\partial C_l/\partial(pb/2U_0)$

C_{l_r} = roll coefficient due to yawing velocity, $\partial C_l/\partial(rb/2U_0)$

C_L = lift coefficient, $nW/(1/2)\rho U_0^2 S$

C_n = yawing-moment coefficient, (Yawing Moment)/$(1/2)\rho U_0^2 Sb$

C_{n_β} = static directional stability, $\partial C_n/\partial\beta$

$C_{n_{\delta_a}}$ = aileron yawing effectiveness, $\partial C_n/\partial\delta_a$

C_{n_p} = $\partial C_n/\partial(pb/2U_0)$

C_{n_r} = $\partial C_n/\partial(rb/2U_0)$

C_y = lateral-force coefficient, (Lateral Force)/$(1/2)\rho U_0^2 S$

C_{y_β} = variation of C_y with sideslip angle, $\partial C_y/\partial\beta$

d, D = polynomial coefficients

db = abbreviation for decibels $\equiv 20\log_{10}|\ |$

e, E = polynomial coefficients

E = error

g = acceleration due to gravity

h = altitude

$H_\delta(s)$ = transfer function relating altitude to control-surface deflection, $h(s)/\delta(s)$

I_x, I_y, I_z = moments of inertia referred to stability axes

I_{xz} = product of inertia referred to stability axes

$j\omega$ = the imaginary portion of the complex variable $s = \sigma \pm j\omega$

k_x, k_y, k_z = radii of gyration about X, Y, and Z axis, respectively—e.g., $I_x = mk_x^2$

K_r = transfer function of ideal simplified yaw-rate controller, neglecting servo and sensor dynamics and assuming a linear system, δ_r/r

K_φ = transfer function of ideal, simplified roll controller

$K_{\varphi_{\delta_a}}$ = the zero-frequency value of the transfer function Φ_{δ_a}

l_x = distance along the X axis from the c.g., positive forward

L_β = $\rho SU_0^2 bC_{l_\beta}/2I_x$

L_δ = $\rho SU_0^2 bC_{l_\delta}/2I_x$

L_p = $\rho SU_0 b^2 C_{l_p}/4I_x$

L_r = $\rho SU_0 b^2 C_{l_r}/4I_x$

L_v = L_β/U_0; $\rho SU_0 bC_{l_\beta}/2I_x$

L_i' = $[L_i + (I_{xz}/I_x)N_i]/[1 - (I_{xz}^2/I_xI_z)]$ where i refers to any motion, or input, quantity

$\mathcal{L}$ = Laplace transform of

m = mass

M_α = $U_0 M_w$

$M_{\dot\alpha}$ = $U_0 M_{\dot w}$

M_δ = $\rho SU_0^2 cC_{M_\delta}/2I_y$

M_q = $\rho SU_0 c^2 C_{M_q}/4I_y$

M_u = $\rho SU_0 cC_{M_u}/I_y$

M_w = $\rho SU_0 cC_{M_\alpha}/2I_y$

$M_{\dot w}$ = $\rho Sc^2 C_{M_{\dot\alpha}}/4I_y$

M_i' = $M_i - Z_iM_\delta/Z_\delta$, where i refers to any motion, or input, quantity

$Na_y(s)$ = numerator of transfer function relating c.g. lateral acceleration to control deflection

$Na_y'(s)$ = numerator of transfer function relating lateral acceleration (at point l_x) to control deflection

N_β = $\rho SU_0^2 bC_{n_\beta}/2I_z$

$N_\beta(s)$ = numerator of transfer function relating side lip angle to control deflection

N_δ = $\rho SU_0^2 bC_{n_\delta}/2I_z$

Presented at the Aerodynamics—III Session, IAS 27th Annual Meeting, N.Y., Jan. 26–29, 1959. Revised and received July 20, 1959.

† This research was supported in whole or in part by the United States Air Force under Contract No. AF 33(616)-3906, monitored by Mr. R. O. Anderson, Flight Control Laboratory, Wright Air Development Center, Wright-Patterson Air Force Base, Ohio.

* Vice-President.

** President.

$N_{\lambda\mu}(s)$ = numerator of transfer function relating directly controlled airframe-motion quantity to disturbance input

$N_{\lambda\delta}(s)$ = numerator of transfer function relating directly controlled airframe-motion quantity to control deflection

$N_{\xi\delta}(s)$ = numerator of transfer function relating indirectly controlled airframe-motion quantity to control deflection

$N_{\xi\mu}(s)$ = numerator of transfer function relating indirectly controlled airframe-motion quantity to disturbance input

$N_{\theta}(s)$ = numerator of transfer function relating pitch angle to control deflection

$N_{\varphi}(s)$ = numerator of transfer function relating roll angle to control deflection

$N_{\dot{h}}(s)$ = numerator of transfer function relating rate of climb to control deflection

$N_p = \rho S U_0 b^2 C_{n_p}/4I_z$

$N_r = \rho S U_0 b^2 C_{n_r}/4I_z$

$N_r(s)$ = numerator of transfer function relating yaw rate to control deflection

$N_u(s)$ = numerator of transfer function relating airspeed to control deflection

$N_w = N_\beta/U_0$

$N_w(s)$ = numerator of transfer function relating vertical velocity to control deflection

$N_\omega(s)$ = numerator of transfer function relating lateral angular velocity to control deflection

N_i' = $[N_i + (I_{xz}/I_z)L_i]/[1 - (I_{xz}^2/I_xI_z)]$, where i refers to any motion, or input, quantity

p = roll rate, angular velocity about the X axis, positive right wing going down

q = pitch rate, angular velocity about the Y axis, positive nose going up

r = yaw rate, angular velocity about the Z axis, positive nose going right

$R_\delta(s)$ = transfer function relating yaw rate to control-surface deflection $r(s)/\delta(s)$

s = Laplace operator, $\sigma \pm j\omega$

$1/T_i$ = inverse time constant, particularized by the subscript

u = linear, perturbed velocity along the X axis

U_0 = linear, steady-state velocity along the X axis

$U_\delta(s)$ = transfer function relating airspeed to control deflection, $u(s)/\delta(s)$

v = linear, perturbed velocity along the Y axis

w = linear, perturbed velocity along the Z axis

$W_\delta(s)$ = transfer function relating vertical velocity to control deflection, $w(s)/\delta(s)$

$X_\alpha = U_0X_w$; $\rho SU_0^2(C_L - C_{D_\alpha})/2m$

$X_u = \rho SU_0(-C_D - C_{D_u})/m$

$X_w = \rho SU_0(C_L - C_{D_\alpha})/2m$

$Y_a(s)$ = transfer function of controller forward-loop amplification and equalization

$Y_f(s)$ = transfer function of sensor- and feedback-loop equalization

Y_{OL} = open-loop transfer function; the product of all series transfer functions in the control loop

$Y(s)$, $Y(j\omega)$, $Y(-\sigma)$ = transfer functions with $s = s$, $s = j\omega$, and $s = -\sigma$, respectively

$Y_\delta^* = \rho SU_0C_{y_\delta}/2m$

$Y_p^* = \rho SU_0C_{y_p}/4m$

$Y_r^* = \rho SU_0C_{y_r}/4m$

$Y_v = \rho SU_0C_{y_\beta}/2m$

$Z_\alpha = U_0Z_w$

$Z_\delta = \rho SU_0^2(-C_{L_\delta})/2m$

$Z_q = \rho SU_0c(-C_{L_\dot{\alpha}})/4m$

$Z_u = \rho SU_0(-C_L - C_{L_u})/m$

$Z_w = \rho SU_0(-C_{L_\alpha} - C_D)/2m$

$Z_{\dot{w}} = \rho Sc(-C_{L_{\dot{\alpha}}})/4m$

α = instantaneous angle of attack, under no wind conditions, w/U_0

β = sideslip angle, under no wind conditions, v/U_0

$\beta_\delta(s)$ = transfer function relating sideslip to control surface deflection, $\beta(s)/\delta(s)$

γ = perturbed flight-path angle, $\theta - \alpha$

γ_0 = flight-path angle, steady state

δ = control-surface deflection

Δ = increment change

$\Delta(s)$ = denominator of airframe transfer functions; characteristic equation when set equal to zero

$\Delta_{\text{lat.}}$ = denominator of the lateral transfer functions; lateral characteristic equation when set equal to zero

$\Delta_{\text{long.}}$ = denominator of the longitudinal transfer functions; longitudinal characteristic equation when set equal to zero

ζ_i = damping ratio of linear second-order system particularized by the subscript

η = radius of the circle generated by the real poles and zero $(-1/T_\varphi, -1/T_R, -1/T_s)$ on the root-locus plot

θ = pitch angle; $\int q\,dt$ in straight and level flight

θ_T = gyro tilt angle measured from the X axis in the X–Z plane, positive nose up

$\Theta_\delta(s)$ = transfer function relating pitch to control-surface deflection, $\theta(s)/\delta(s)$

λ = the total directly controlled airframe-motion quantity

Λ_δ = transfer function relating general directly controlled airframe-motion quantity to control deflection, $\lambda(s)/\delta(s)$

μ = general disturbance input

ν = distance, on the root locus plot, from the zero, $-1/T_\varphi$, to the nearest complex zero or pole

ξ = the total indirectly controlled airframe-motion quantity

Ξ_δ = transfer function relating indirectly controlled airframe-motion quantity to control deflection, $\xi(s)/\delta(s)$

ρ = mass density of air

σ = the real portion of the complex variable $s = \sigma \pm j\omega$

φ = roll angle; $(\cos\gamma_0 \int p\,dt - \sin\gamma_0 \int r\,dt)$ in straight and level flight

$\Phi_\delta(s)$ = transfer function relating roll to control surface deflection, $\varphi(s)/\delta(s)$

ω_i = undamped natural frequency of a second-order mode, particularized by the subscript

ω = lateral angular velocity sensed by a gyro tilted amount θ_T, $\omega = r\cos\theta_T + p\sin\theta_T$

$\Omega_\delta(s)$ = transfer function relating lateral angular velocity to control-surface deflection, $\omega(s)/\delta(s)$

Special Subscripts

a = aileron

d = Dutch roll

l = lateral long period

p = phugoid

r = rudder

R = roll subsidence

s = spiral

sp = short period

OL = open loop

CL = closed loop

Introduction

OPTIMIZATION, in an engineering sense, involves a selection between alternatives within prescribed

rules. Under a given set of circumstances, the rules or optimizing *criteria* may be subject to individual discretion, judgment, or instinct. The optimization *process*, regardless of the particular rules employed, will be far less subjective since it involves the establishment of several competing systems based on physical reality. The quality of these competing solutions, and the ultimate success of the optimizing effort will depend directly on the degree of understanding which can be brought to bear on the various interactions involved in the physical system.

The objectives of the present paper are to lay some groundwork for a better appreciation of the overall problem of integrating the flight-control, airframe system to allow consideration of the airframe as an alterable element in the system during preliminary design, to discover what is important in the overall system, and finally to determine what can be done to simplify the system. The possibility of realizing substantial benefits in reduced weight or cost, or in increased reliability, is the ultimate goal. The approach makes use of servo techniques because of their power and applicability, but attention is mainly focused on the airframe and its reduction to simplified approximate servo terms. In outline, the paper starts with a presentation of the airframe equations of motion and progresses rapidly through the reduction of these equations to approximate, factored transfer functions. These define the airframe in servo terms and allow a ready synthesis of the complete system. A simplified example is then used to illustrate possible effects of airframe alterations upon the complete airframe-controller system. These results are summarized and interpreted to support the major thesis of this paper that an *overall approach which considers the airframe, as well as the control system, to be alterable* helps substantially in the establishment of the competing systems essential to optimization.

Airframe Transfer Functions

When the airframe is considered as an element in an automatic control system, its properties are defined by a series of transfer functions which relate transformed output quantities (various airframe motions) to input variables (control deflections or external disturbances). The transfer functions are ratios of higher-order polynominals in the Laplace transform variable, s, with coefficients composed of stability derivatives and inertial and gravitational parameters. These forms are all well known (see, for example, reference 1), so their development is simply summarized below.

The conventional linearized rigid-body equations which describe the perturbed lateral and longitudinal airframe motions about straight and level operating conditions are given in Laplace transform style in Eqs. (1) and (2); initial conditions are assumed zero, and inputs due only to control deflections are considered.

Longitudinal Set:

$$\left.\begin{aligned} (s - X_u)u - (X_{\dot{w}}s + X_w)w + \frac{-X_q s + g\cos\gamma_0}{s} q &= X_\delta\delta \\ -Z_u u + (s - Z_{\dot{w}}s - Z_w)w + \frac{-(U_0 + Z_q)s + g\sin\gamma_0}{s} q &= Z_\delta\delta \\ -M_u u - (M_{\dot{w}}s + M_w)w + (s - M_q)\,q &= M_\delta\delta \end{aligned}\right\} \tag{1}$$

Lateral Set:

$$\left.\begin{aligned} (s - Y_v)v - \frac{Y_p^* s + g\cos\gamma_0}{s} p + \frac{(U_0 - Y_r^*)s - g\sin\gamma_0}{s} r &= U_0 Y_\delta^*\delta \\ -L_v' v + (s - L_p')p - L_r' r &= L_\delta'\delta \\ -N_v' v - N_p' p + (s - N_r')r &= N_\delta'\delta \end{aligned}\right\} \tag{2}$$

In these equations, the primed lateral derivatives are such as to eliminate the explicit appearance of product-of-inertia coupling terms between roll and yaw (see, for example, references 2 and 3); and the control-surface deflection, δ, for the longitudinal set is considered to be an elevator and no subscript is used. For the lateral set, subscripts a and r are later used to distinguish between aileron and rudder.

All the above equations have been written in terms of fundamental airframe motion quantities (angular and translational velocities) measured about and along an axis system fixed in the aircraft; the angles Θ and Φ, which orient the gravity vector to the airframe axis system, have been replaced by their equivalents for straight and level flight—i.e.,

$$\left.\begin{aligned} \theta &= \mathfrak{L}\left(\int q dt\right) = q/s \\ \varphi &= \mathfrak{L}\left(\cos\gamma_0 \int p dt - \sin\gamma_0 \int r dt\right) \\ &= \cos\gamma_0 (p/s) - \sin\gamma_0 (r/s) \end{aligned}\right\} \tag{3}$$

The conventional substitutions for angle of attack ($\alpha = w/U_0$) and sideslip ($\beta = v/U_0$) can also be made in Eqs. (1) and (2), since the assumption of zero airmass velocity is implicit in these equations.

In addition to the fundamental motion quantities given above, many flight control problems also require altitude, normal and lateral acceleration (both at the center of gravity and at a location l_x feet in front of the c.g.), and the lateral angular velocity in the X–Z

plane displaced through an angle θ_T from the X axis. These quantities are given below.

$$\left.\begin{aligned}
\dot{h} &= U_0\gamma_0 + \gamma_0 u + U_0\gamma \\
a_z &= \dot{w} - U_0 q + g\sin\gamma_0 \int q dt \\
&= Z_w w + Z_u u + Z_\delta \delta + Z_q q + Z_{\dot{w}}\dot{w} \\
a_z' &= a_z - l_x\dot{q} \\
a_y &= \dot{v} + U_0 r - g\sin\gamma_0 \int r dt - g\cos\gamma_0 \int p dt \\
&= Y_{\delta_r}\delta_r + Y_{\delta a}\delta_a + Y_p p + Y_r r + Y_v v \\
a_y' &= a_y + l_x\dot{r} \\
\omega &= r\cos\theta_T + p\sin\theta_T
\end{aligned}\right\} \quad (4)$$

The values of some derivatives are such that their contributions to transfer function coefficients are usually negligible. These include X_δ, $X_{\dot{w}}$, X_q, $Z_{\dot{w}}$, Z_q, Y_p*, and Y_r*. All of these are assumed to be zero. Finally it should be observed that the detailed discussions in this paper are restricted to horizontal flight ($\gamma_0 = 0$) which is the simplest of the three degrees of freedom straight and level conditions. With these restrictions, the transfer functions of interest become

Longitudinal Set:

$$O_\delta(s) = \frac{\theta(s)}{\delta(s)} = \frac{N_\theta(s)}{\Delta_{\text{long.}}} = \frac{A_\theta s^2 + B_\theta s + C_\theta}{\Delta_{\text{long.}}} \quad (5)$$

$$W_\delta(s) = \frac{w(s)}{\delta(s)} = \frac{N_w(s)}{\Delta_{\text{long.}}} = \frac{A_w s^3 + B_w s^2 + C_w s + D_w}{\Delta_{\text{long.}}} \quad (6)$$

$$U_\delta(s) = \frac{u(s)}{\delta(s)} = \frac{N_u(s)}{\Delta_{\text{long.}}} = \frac{A_u s^2 + B_u s + C_u}{\Delta_{\text{long.}}} \quad (7)$$

$$H_\delta(s) = \frac{h(s)}{\delta(s)} = \frac{N_h(s)}{s\Delta_{\text{long.}}} = \frac{A_h s^3 + B_h s^2 + C_h s + D_h}{s\Delta_{\text{long.}}} \quad (8)$$

$$A_{z\delta}(s) = a_z(s)/\delta(s) = -[sN_h(s)/\Delta_{\text{long.}}] \quad (9)$$

where $\Delta_{\text{long.}} = As^4 + Bs^3 + Cs^2 + Ds + E$ (10)

and

$$\left.\begin{aligned}
A &= 1 \\
B &= -(M_q + X_u + Z_w + M_{\dot{\alpha}}) \\
C &= M_q Z_w - M_\alpha + X_u(M_q + Z_w + M_{\dot{\alpha}}) - X_u Z_u \\
D &= -X_u(M_q Z_w - M_\alpha) - M_u X_\alpha + M_q X_w Z_u + g(M_{\dot{w}} Z_u + M_u) \\
E &= g(M_w Z_u - M_u Z_w)
\end{aligned}\right\} \quad (11)$$

The numerator coefficients are summarized in Table 1. It should be noted that derivatives with respect to both α and w, as well as primed longitudinal derivatives, defined in the Symbols, are used to achieve conciseness.

TABLE 1
Summary of Longitudinal Transfer Function Numerators

	A	B	C	D
Exact θ	$Z_\delta M_{\dot{w}} + M_\delta$	$Z_\delta(M_w - M_{\dot{w}}X_u) - M_\delta(Z_w + X_u)$	$Z_\delta(M_u X_w - M_w X_u) + M_\delta(Z_w X_u - X_w Z_u)$	
Approx.	M_δ	$Z_\delta M_w - M_\delta Z_w$		
w	Z_δ	$-Z_\delta(M_q + X_u) + U_o M_\delta$	$X_u(Z_\delta M_q - U_o M_\delta)$	$g(Z_\delta M_u - M_\delta Z_u)$
Exact u	$Z_\delta X_w$	$-Z_\delta(gM_{\dot{w}} + M_q X_w) + M_\delta(X_\alpha - g)$	$g(Z_w M_\delta - M_w Z_\delta) = -\frac{gZ_\delta M'_\alpha}{U_o}$	
Approx.		$M_\delta(X_\alpha - g)$		
Exact h	$-Z_\delta$	$Z_\delta(M_{\dot{\alpha}} + M_q + X_u)$	$Z_\delta\left[M_\alpha - X_u(M_{\dot{\alpha}} + M_q)\right] - M_\delta Z_\alpha$	$Z_\delta(M_u X_\alpha - gM_u - M_\alpha X_u) - M_\delta(Z_u X_\alpha - gZ_u - Z_\alpha X_u)$
Approx.			$Z_\delta M'_\alpha$	$-Z_\delta\left[X_u M'_\alpha - (X_\alpha - g)M'_u\right]$
Exact a'_z	$Z_\delta - l_x(Z_\delta M_{\dot{w}} + M_\delta)$	$-Z_\delta(M_{\dot{\alpha}} + M_q + X_u) - l_x\left[Z_\delta(M_w - M_{\dot{w}}X_u) - M_\delta(Z_w + X_u)\right]$	$-\left[Z_\delta M_\alpha - M_\delta Z_\alpha - X_u(M_{\dot{\alpha}} + M_q)\right] - l_x\left[Z_\delta(X_w M_u - M_w X_u) + M_\delta(Z_w X_u - X_w Z_u)\right]$	$Z_\delta(M_\alpha X_u - M_u X_\alpha + gM_u) + M_\delta(Z_u X_\alpha - Z_\alpha X_u - gZ_u)$
Approx.	$Z_\delta - l_x M_\delta$	$-Z_\delta(M_{\dot{\alpha}} + M_q + X_u) - l_x\left[Z_\delta M_w - M_\delta(Z_w + X_u)\right]$	$-Z_\delta M'_\alpha - l_x Z_\delta(X_w M'_u - X_u M'_w)$	$Z_\delta\left[X_u M'_\alpha - (X_\alpha - g)M'_u\right]$

TABLE 2
Summary of Basic Lateral Transfer Function Numerators

	A	B	C	D	E
β	$Y^*_\delta\left[1 - \frac{I_{xz}^2}{I_x I_z}\right]$	$-Y^*_\delta\left[L_p + N_r + \frac{I_{xz}}{I_x}N_p + \frac{I_{xz}}{I_z}L_r\right]$ $- \frac{I_{xz}}{I_z}L_\delta - N_\delta$	$Y^*_\delta(L_p N_r - N_p L_r)$ $+ L_\delta\left(\frac{g}{U_o} - N_p\right)$ $+N_\delta\left(\frac{I_{xz}}{I_x}\frac{g}{U_o} + L_p\right)$	$\frac{g}{U_o}(N_\delta L_r - L_\delta N_r)$	
ϕ	$L_\delta + N_\delta\frac{I_{xz}}{I_x}$	$Y^*_\delta(L_\beta + \frac{I_{xz}}{I_x}N_\beta) - L_\delta(N_r + Y_v)$ $+ N_\delta(L_r - \frac{I_{xz}}{I_x}Y_v)$	$Y^*_\delta(L_r N_\beta - L_\beta N_r)$ $+ L_\delta(Y_v N_r + N_\beta)$ $- N_\delta(L_\beta + Y_v L_r)$		
r	$N_\delta + \frac{I_{xz}}{I_z}L_\delta$	$Y^*_\delta(N_\beta + \frac{I_{xz}}{I_z}L_\beta) + L_\delta N_p - \frac{I_{xz}}{I_z}Y_v)$ $- N_\delta(Y_v + L_p)$	$Y^*_\delta(L_\beta N_p - N_\beta L_p) - L_\delta Y_v N_p + N_\delta Y_v L_p$	$\frac{g}{U_o}(L_\delta N_\beta - N_\delta L_\beta)$	
ω	$A_r + A_\phi \tan\theta_T$	$B_r + B_\phi \tan\theta_T$	$C_r + C_\phi \tan\theta_T$	D_r	Note: $\cos\theta_T \doteq 1$
a_y	$U_o Y^*_\delta(1 - \frac{I_{xz}^2}{I_x I_z})$	$- U_o Y^*_\delta(L_p + N_r + \frac{I_{xz}}{I_x}N_p + \frac{I_{xz}}{I_z}L_r)$	$U_o Y^*_\delta(N_\beta + L_p N_r - N_p L_r + \frac{I_{xz}}{I_z}L_\beta)$ $- U_o Y_v(\frac{I_{xz}}{I_z}L_\delta + N_\delta)$	$U_o Y^*_\delta\left[N_p L_\beta - \frac{g}{U_o}L_\beta\right]$ $- N_\beta(L_p + \frac{g I_{xz}}{U_o I_x})$ $+ U_o Y_v\left[L_\delta(\frac{g}{U_o} - N_p)\right.$ $\left. + N_\delta(\frac{g I_{xz}}{I_x U_o} + L_p)\right]$	$g\left\{Y^*_\delta\left[(L_\beta N_r - N_\beta L_r)\right.\right.$ $\left.\left. + Y_v(N_\delta L_r - L_\delta N_r)\right]\right\}$

Lateral Set:

$$\beta_\delta(s) = \frac{\beta(s)}{\delta(s)} = \frac{N_\beta(s)}{\Delta_{\text{lat.}}} = \frac{A_\beta s^3 + B_\beta s^2 + C_\beta s + D_\beta}{\Delta_{\text{lat.}}} \tag{12}$$

$$\Phi_\delta(s) = \frac{\varphi(s)}{\delta(s)} = \frac{N_\varphi(s)}{\Delta_{\text{lat.}}} = \frac{A_\varphi s^2 + B_\varphi s + C_\varphi}{\Delta_{\text{lat.}}} \tag{13}$$

$$R_\delta(s) = \frac{r(s)}{\delta(s)} = \frac{N_r(s)}{\Delta_{\text{lat.}}} = \frac{A_r s^3 + B_r s^2 + C_r s + D_r}{\Delta_{\text{lat.}}} \tag{14}$$

$$A_{y\delta}(s) = \frac{a_y(s)}{\delta(s)} = \frac{N_{a_y}(s)}{\Delta_{\text{lat.}}} = \frac{A_{a_y} s^4 + B_{a_y} s^3 + C_{a_y} s^2 + D_{a_y} s + E_{a_y}}{\Delta_{\text{lat.}}} \tag{15}$$

$$A_{y\delta}'(s) = \frac{a_y'(s)}{\delta(s)} = \frac{N_{a_y}'(s)}{\Delta_{\text{lat.}}} = \frac{A_{a_y}' s^4 + B_{a_y}' s^3 + C_{a_y}' s^2 + D_{a_y}' s + E_{a_y}'}{\Delta_{\text{lat.}}} \tag{16}$$

$$\Omega_\delta(s) = \frac{\omega(s)}{\delta(s)} = \frac{N_\omega(s)}{\Delta_{\text{lat.}}} = \frac{(A_\omega s^2 + B_\omega s^3 + C_\omega s + D_\omega)\cos\theta_T}{\Delta_{\text{lat.}}} \tag{17}$$

where $\Delta_{\text{lat.}} = as^4 + bs^3 + cs^2 + ds + e$ (18)

When the primed derivatives are used, coefficients of $\Delta_{\text{lat.}}$ are given by

$$\left.\begin{aligned} a &= 1 \\ b &= -(Y_v + L_p' + N_r') \\ c &= N_\beta' + L_p'(Y_v + N_r') - N_p' L_r' + Y_v N_r' \\ d &= N_p' L_\beta' - L_p' N_\beta' + Y_v(N_p' L_r' - L_p' N_r') - (g L_\beta'/U_0) \\ e &= (g/U_0)(L_\beta' N_r' - N_\beta' L_r') \end{aligned}\right\} \tag{19}$$

The numerator coefficients are summarized in Table 2. Unprimed derivatives are used in this table since they lead to slightly simpler results for the numerator factors. These can be changed to primed derivative form by the simple process of setting I_{xz} equal to zero and replacing the L_i and N_i by L_i' and N_i'. It should be noted that whereas the *factors* of a given polynomial will be independent of the use of the prime or unprimed derivatives, the transfer-function gain must be computed using the same type in both numerator and denominator.

Airframe Transfer Functions in Approximate Factored Form

For maximum utility it is desirable to have the numerator and denominator polynomials in factored form. Each transfer function will then be made up of a ratio of first- and second-order polynomial products, and a gain constant. The roots of the denominator are the transfer function "poles"; those of the numerator are its "zeros." The gains, poles, and zeros define the fundamental properties of dynamic elements and are essential in most servoanalysis and synthesis methods and in response calculations. The factorization required to find the poles and zeros can be time-consuming since most of the polynomials involved are of third or higher order. More important, however, is the fact that the poles and zeros of these higher order polynomials are difficult to define in terms of literal values of the transfer function coefficients or of the stability parameters. This is unfortunate because a large number of numerical calculations are then required for comprehension of the tie between configuration characteristics (the stability derivatives, etc.), and the airframe transfer and response characteristics.

To alleviate this situation, it is highly desirable to establish approximate expressions for the poles and zeros in terms of the stability derivatives and inertial parameters. This approach has often been used in the past, either directly by decomposing a fairly complete transfer function form, or indirectly by the use of fewer airframe degrees of freedom. Both schemes have been moderately successful in some instances, while in others the results have been severely restricted in application and scope. In most cases approximate factors have been developed in an artistic fashion, with ill-defined conditions under which they are valid. Such pitfalls have been skirted as much as practically possible in the derivation of the approximate factors given in this paper. Where the basic polynomials are of second or third order, the approximate factors are derived by the use of a method which can be made exact. The method is based upon servoanalysis of an "equivalent" closed-loop system, and the degree of approximation in any given case can be readily assessed. The approximations for the roots of either the lateral or longitudinal characteristic equations, which are both fourth order, are not established in such a formal manner. Instead, they are based upon simplifying assumptions regarding the relative magnitudes of various combinations of stability derivatives. The validity of these simplifying assumptions has been demonstrated, in that the resulting approximations have been applied successfully to a large number of actual configurations.

Table 3 summarizes all the approximate factors for the longitudinal case. Table 4 presents the lateral denominator factors, Table 5 presents the numerator terms for aileron inputs, and Table 6 presents the rudder numerators. Conditions of validity are shown for all cases. The details underlying the derivations presented in these summary tables are given in reference 3.

The ready availability of the relationships given in Tables 3–6 is essential to the optimization thesis advanced here. They are especially helpful in (1) developing the insight required for the determination of airframe-autopilot combinations which offer possible reductions in overall system complexity, (2) assessing the effects of configuration changes on aircraft response and on airframe-autopilot system response, and (3) showing the detailed effects of particular stability derivatives (and their estimated accuracies) upon the poles and zeros, and hence upon aircraft and airframe-

TABLE 3
Summary of Longitudinal Approximate Factors

Factored Forms	Approximate Factors	Conditions of Validity
$\Delta(s) = \underbrace{(s^2 + 2\zeta_p\omega_p s + \omega_p^2)}_{\text{or}}(s^2 + 2\zeta_{sp}\omega_{sp}s + \omega_{sp}^2)$ $\left(s + \frac{1}{T_{p_1}}\right)\left(s + \frac{1}{T_{p_2}}\right)$	$\omega_{sp}^2 \doteq Z_w M_q - M_\alpha$ $2\zeta_{sp}\omega_{sp} \doteq -(Z_w + M_q + M_{\dot\alpha})$ $\omega_p^2 \text{ or } \frac{1}{T_{p_1}T_{p_2}} \doteq \frac{g(M_w Z_u - M_u Z_w)}{Z_w M_q - M_\alpha}$ $2\zeta_p\omega_p \text{ or } \left(\frac{1}{T_{p_1}} + \frac{1}{T_{p_2}}\right) \doteq -X_u - \frac{M_u(X_\alpha - g)}{Z_w M_q - M_\alpha}$	
$N_\theta(s) = A_\theta\left(s + \frac{1}{T_{\theta_1}}\right)\left(s + \frac{1}{T_{\theta_2}}\right)$	$A_\theta \doteq M_\delta$ $\frac{1}{T_{\theta_1}} \doteq -X_u + X_w\frac{M'_u}{M'_w}$ $\frac{1}{T_{\theta_2}} \doteq \frac{Z_\delta}{M_\delta}M'_w - X_u$	$\lvert Z_\delta M_{\dot w}\rvert \ll \lvert M_\delta\rvert$ $\lvert X_u\rvert \ll \lvert Z_w\rvert$
$N_u(s) = A_u\left(s + \frac{1}{T_{u_1}}\right)\left(s + \frac{1}{T_{u_2}}\right)$	$A_u \doteq Z_\delta X_w$ $\frac{1}{T_{u_1}} \doteq \frac{-Z_\delta g M'_\alpha}{U_o M_\delta (X_\alpha - g)}$ $\frac{1}{T_{u_2}} \doteq \frac{M_\delta(X_\alpha - g)}{Z_\delta X_w}$	$\lvert Z_\delta(gM_{\dot w} + M_q X_w)\rvert \ll \lvert M_\delta(X_\alpha - g)\rvert$
$N_w(s) = A_w\left(s + \frac{1}{T_{w_1}}\right)\left(s^2 + 2\zeta_w\omega_w s + \omega_w^2\right)$	$A_w \doteq Z_\delta$ $\frac{1}{T_{w_1}} \doteq \frac{U_o M_\delta}{Z_\delta}$ $\omega_w^2 \doteq \frac{gZ_\delta M'_u}{U_o M_\delta}$ $2\zeta_w\omega_w \doteq -X_u$	$\lvert Z_\delta(M_q + X_u)\rvert \ll \lvert U_o M_\delta\rvert$
$N_h(s)^* = A_h\underbrace{\left(s + \frac{1}{T_{h_1}}\right)\left(s + \frac{1}{T_{h_2}}\right)\left(s - \frac{1}{T_{h_3}}\right)}_{\text{or}}$ Aft Control $(s^2 + 2\zeta_h\omega_h s + \omega_h^2)$ Fwd Control	$A_h \doteq -Z_\delta$ $\frac{1}{T_{h_1}} \doteq -X_u + (X_\alpha - g)\frac{M'_u}{M'_\alpha}$ $\frac{1}{T_{h_2}} = \frac{1}{T_{h_3}} \doteq \sqrt{M'_\alpha}$ $\omega_h^2 \doteq -M'_\alpha$ $2\zeta_h\omega_h \doteq -\left[M_{\dot\alpha} + M_q + (X_\alpha - g)\frac{M'_u}{M'_\alpha}\right]$	$\lvert X_u(M_{\dot\alpha} + M_q)\rvert \ll \lvert Z_\delta M'_\alpha\rvert$

* $\frac{h}{\delta} = \frac{N_h(s)}{s\,\Delta(s)}$; $\frac{\gamma}{\delta} = \frac{N_h(s)}{U_o\,\Delta(s)}$; $\frac{a_z}{\delta} = \frac{sN_h(s)}{\Delta(s)}$

autopilot responses. The factors are also useful in dealing with problems involving the airframe alone, such as obtaining stability derivatives from flight test data.

The Controller as an Equivalent-Airframe Element

The foregoing discussion and the approximations presented in the tables show that a close tie exists between given airframe stability derivatives and their net dynamic effect. From this point of departure it is natural to examine the influence of a control loop by considering its role as an "augmentor" of existing stability derivatives or a "creator" of new ones. This technique, which is in airframe terms rather than in those of servoanalysis, is called the "equivalent-derivative" approach. It is the simplest method to utilize for exploring the motion characteristics of three degree of freedom airframe-autopilot systems, and was the first approach to airframe-autopilot system analysis.[4, 5] Its utility stems from the fact that all automatic control systems involve control deflections which are made functions of airframe motions. These control deflections impose forces and/or moments upon the craft which are proportional to airframe motion quantities. The action of the control system in producing such forces and moments can then be thought of as modifying or creating aircraft stability derivatives. When automatic control systems which effectively create new derivatives are considered, the equivalent-derivative

TABLE 4
Lateral Denominator Approximate Factors

Factored Forms	Approximate Factors	Conditions of Validity
$\Delta(s) = \underbrace{\left(s + \frac{1}{T_s}\right)\left(s + \frac{1}{T_R}\right)}(s^2 + 2\zeta_d\omega_d s + \omega_d^2)$ or	$\omega_{d_1}^2 \doteq N'_\beta$ $2(\zeta\omega)_{d_1} \doteq -(Y_v + N'_r) - \frac{L'_\beta}{N'_\beta}(N'_p - \frac{g}{U_o})$ $\frac{1}{T_{R_1}} \doteq -L'_p + \frac{L'_\beta}{N'_\beta}(N'_p - \frac{g}{U_o})$ $\frac{1}{T_s} \doteq T_{R_1}\frac{g}{U_o}\left(\frac{L'_\beta}{N'_\beta}N'_r - L'_r\right)$ $\omega_d^2 \doteq \omega_{d_1}^2 F_c$ $\frac{1}{T_R} = \frac{1}{T_{R_1}}\frac{1}{F_c}$ $2(\zeta\omega)_d = 2(\zeta\omega)_{d_1} + \frac{1}{T_{R_1}}\left(1 - \frac{1}{F_c}\right)$	$\begin{bmatrix} Y_r = Y_p \doteq 0 \\ \left\|Y_v N'_r - N'_p L'_r\right\| \ll \left\|N'_\beta\right\| \\ \left\|\frac{g}{U_o}\sin\Upsilon_o\right\| \ll \left\|L'_p\right\| \\ \left\|Y_v L'_r\right\| \ll \left\|L'_\beta\right\| \end{bmatrix}^*$ $\left\|\frac{L'_p}{N'_\beta}(Y_v + N'_r)\right\| < 0.3$ $\left\|\frac{L'_\beta}{L'_p N'_\beta}(N'_p - \frac{g}{U_o})\right\| < 0.4$ $\left\|\zeta_{d_1}\right\| < 0.2 \quad , \quad F_c = 1$ $\left\|\zeta_{d_1}\right\| > 0.2 \quad , \quad F_c = \frac{1 + T_{R_1}^2\omega_{d_1}^2}{1 + T_{R_1}^2\omega_{d_1}^2 + 2\zeta_{d_1}\omega_{d_1}T_{R_1}}$
$(s^2 + 2\zeta_1\omega_1 s + \omega_1^2)$	$\omega_1^2 \doteq \frac{\frac{g}{U_o}\left(\frac{L'_\beta N'_r}{N'_\beta} - L'_r\right)}{1 + \frac{L'_p}{N'_\beta}(Y_v + N'_r)}$ $2(\zeta\omega)_1 \doteq \frac{-L'_p + \frac{L'_\beta}{N'_\beta}(N'_p - \frac{g}{U_o})}{1 + \frac{L'_p}{N'_\beta}(Y_v + N'_r)}$ $2(\zeta\omega)_d \doteq -(Y_v + N'_r) - \left\{\frac{L'^2_p(Y_v + N'_r) + L'_\beta(N'_p - \frac{g}{U_o})}{N'_\beta\left[1 + \frac{L'_p}{N'_\beta}(Y_v + N'_r)\right]}\right\}$ $\omega_d^2 \doteq N'_\beta\left[1 + \frac{L'_p}{N'_\beta}(Y_v + N'_r)\right] - \omega_1^2 - 4(\zeta\omega)_1(\zeta\omega)_d$	* Same conditions applicable $\left\|\frac{\frac{g}{U_o}(L'_\beta N'_r - N'_\beta L'_r)}{N'^2_\beta\left[1 + \frac{L'_p}{N'_\beta}(Y_v + N'_r)\right]^2}\right\| \ll 1$ $\left\|\frac{-(Y_v + L'_p + N'_r)\left[-L'_p N'_\beta + L'_\beta(N'_p - \frac{g}{U_o})\right]}{N'^2_\beta\left[1 + \frac{L'_p}{N'_\beta}(Y_v + N'_r)\right]^2}\right\| < 0.25$ $.005 < \frac{\left[-L'_p + \frac{L'_\beta}{N'_\beta}(N'_p - \frac{g}{U_o})\right]^2}{4\frac{g}{U_o}(\frac{L'_\beta N'_r}{N'_\beta} - L'_r)\left[1 + \frac{L'_p}{N'_\beta}(Y_v + N'_r)\right]} < 1$

approach tends to be less useful. One can, of course, derive new approximate factors for different and higher order "equivalent airframes," but the labor becomes excessive. Also for situations where the dynamics of the control-sensor combination greatly modify the simple proportional relationship between the sensed motion and the output control deflection, the equivalent-derivative approach becomes invalid. In such instances, servoanalysis techniques are eminently more suitable, and the application of these methods will be treated later in this paper.

As an example of the equivalent-derivative approach, consider a control system consisting of a rate gyro, properly oriented to measure the yawing velocity, feeding a signal to servo actuators which move the rudder in response to the gyro signal. If the servo and sensor dynamics are neglected and the system assumed linear, the controller transfer function is

TABLE 5
Lateral Numerator Approximate Factors—Aileron

Factored Forms	Approximate Factors	Conditions of Validity
$N_\phi(s) = A_\phi(s^2 + 2\zeta_\phi\omega_\phi s + \omega_\phi^2)$	$A_\phi \doteq L_{\delta_a}$ $\omega_\phi^2 \doteq N_\beta\left(1 - \frac{N_{\delta_a} L_\beta}{L_{\delta_a} N_\beta}\right)$ $2\zeta_\phi\omega_\phi \doteq -(Y_v + N_r) + \frac{N_{\delta_a}}{L_{\delta_a}} L_r$	$Y^*_{\delta_a} \doteq 0$ $\lvert Y_v N_r \rvert \ll \lvert N_\beta \rvert$ $\lvert Y_v L_r \rvert \ll \lvert L_\beta \rvert$ $\left\lvert \frac{I_{xz} N_{\delta_a}}{I_x L_{\delta_a}} \right\rvert \ll 1$
$N_r(s) = A_r\left(s + \frac{1}{T_{r_1}}\right)(s^2 + 2\zeta_r\omega_r s + \omega_r^2)$	$A_r \doteq \frac{I_{xz}}{I_z} L_{\delta_a}$ $\frac{1}{T_{r_1}} \doteq \omega_r \doteq \left(\frac{I_z}{I_{xz}} \frac{g}{U_o} N_\beta\right)^{1/3}$ $2\zeta_r\omega_r \doteq \frac{I_z}{I_x} N_p - Y_v - \frac{1}{T_{r_1}}$	$N_{\delta_a} = Y^*_{\delta_a} \doteq 0$ $B - AC^{1/3} \ll C^{2/3}$ $B = -\frac{I_z}{I_{xz}} Y_v N_p$ $A = \frac{I_z}{I_{xz}} N_p - Y_v$ $C = \frac{I_z}{I_{xz}} \frac{g}{U_o} N_\beta$
$N_\omega(s) = A_\omega\left(s + \frac{1}{T_{\omega_1}}\right)\left(s^2 + 2\zeta_\omega\omega_\omega s + \omega_\omega^2\right)\cos\theta_T$	$A_\omega \doteq N_{\delta_a} + L_{\delta_a}\left(\tan\theta_T + \frac{I_{xz}}{I_z}\right)$ $\frac{1}{T_{\omega_1}} \doteq \frac{g}{U_o \tan\theta_T}$ $\omega_\omega^2 \doteq \frac{\left(L_{\delta_a} N_\beta - N_{\delta_a} L_\beta\right)\tan\theta_T}{N_{\delta_a} + L_{\delta_a}\left(\tan\theta_T + \frac{I_{xz}}{I_z}\right)}$ $2\zeta_\omega\omega_\omega \doteq -Y_v + \frac{L_{\delta_a}\left(N_p - N_r\tan\theta_T\right) - N_{\delta_a} L_p}{N_{\delta_a} + L_{\delta_a}\left(\tan\theta_T + \frac{I_{xz}}{I_z}\right)} - \frac{g}{U\tan\theta_T}$	$Y^*_{\delta_a} \doteq 0$ $\lvert N_p \rvert \ll \lvert N_r \rvert$ $\lvert Y_v N_p \rvert \ll \lvert N_\beta \tan\theta_T \rvert$ $\lvert Y_v L_p \rvert \ll \lvert L_\beta \tan\theta_T \rvert$ $\left\lvert \frac{N_{\delta_a} L_r}{L_{\delta_a} N_r} \right\rvert \ll 1$ $\left\lvert \frac{I_{xz} N_{\delta_a}}{I_x L_{\delta_a}} \right\rvert \ll 1$ $\left.\begin{array}{l} \left\lvert \frac{4g}{U_o\theta_T}(N_r + 2Y_v) \right\rvert \\ \text{and} \\ \left\lvert \delta\left(\frac{g}{U_o\theta_T}\right)^2 \right\rvert \end{array}\right\} < \lvert N_\beta \rvert$

TABLE 6
Lateral Numerator Approximate Factors—Rudder

Factored Forms	Approximate Factors	Conditions of Validity
$N_\phi(s) = A_\phi \underbrace{(s^2 + 2\zeta_\phi\omega_\phi s + \omega_\phi^2)}_{\text{or}} \left(s + \frac{1}{\tau_{\phi_1}}\right)\left(s + \frac{1}{\tau_{\phi_2}}\right)$	$A_\phi \doteq L'_{\delta_r}$ $\omega_\phi^2 \text{ or } \frac{1}{\tau_{\phi_1}\tau_{\phi_2}} \doteq N'_\beta\left[1 - \frac{L'_\beta N'_{\delta_r}}{N'_\beta L'_{\delta_r}} + \frac{Y^v_{\delta_r} L'_r}{L'_{\delta_r}}\left(1 - \frac{L'_r N'_\beta}{N'_r L'_\beta}\right)\right]$ $2(\zeta\omega)_\phi \text{ or } \frac{1}{\tau_{\phi_1}} + \frac{1}{\tau_{\phi_2}} \doteq -(Y_v + N'_r) + \frac{Y^v_{\delta_r} L'_\beta + N'_{\delta_r} L'_r}{L'_{\delta_r}}$	
$N_r(s) = A_r\left(s + \frac{1}{\tau_{r_1}}\right)\underbrace{(s^2 + 2\zeta_r\omega_r s + \omega_r^2)}_{\text{or}} \left(s + \frac{1}{\tau_{r_2}}\right)\left(s + \frac{1}{\tau_{r_3}}\right)$	$A_r \doteq N_{\delta_r}$ $\frac{1}{\tau_{r_1}} \doteq -L_p$ $\frac{1}{\tau_{r_2}} \doteq -\left(Y_v - \frac{Y^v_{\delta_r}}{N_{\delta_r}} N_\beta\right)$ $\frac{1}{\tau_{r_3}} \doteq -\frac{gL_\beta}{U_o L'_p\left(Y_v - \frac{Y^v_{\delta_r}}{N_{\delta_r}} N_\beta\right)}$ $\omega_r^2 \doteq \frac{g}{U_o}\frac{L_\beta}{L_p}$ $2\zeta_r\omega_r \doteq -\left(Y_v - \frac{Y^v_{\delta_r} N_\beta}{N_{\delta_r}} - \frac{g}{U_o}\frac{L_\beta}{L_p}\right)$	$L_{\delta_r} \neq 0$ $\frac{Y^v_{\delta_r} L_\beta I_{xz}}{N_{\delta_r} L_\beta I_z} \ll 1$ $\frac{L_r N_\beta}{N_r L_\beta} \ll 1$ $\left\lvert\frac{g}{U_o}\frac{L_\beta}{L_p}\right\rvert < \left\lvert\frac{\left(Y_v - \frac{Y^v_{\delta_r}}{N_{\delta_r}} N_\beta\right)^2}{4}\right\rvert$ $\left\lvert\frac{\left(Y_v - \frac{Y^v_{\delta_r}}{N_{\delta_r}} N_\beta\right)^2}{4} - \frac{\left(Y_v - \frac{Y^v_{\delta_r}}{N_{\delta_r}} N_\beta\right)}{2}\right\rvert < \left\lvert\frac{g}{U_o}\frac{L_\beta}{L_p}\right\rvert < \left\lvert\frac{\left(Y_v - \frac{Y^v_{\delta_r}}{N_{\delta_r}} N_\beta\right)^2}{4}\right\rvert$
General: $N_{a'_y}(s) = A_{a'_y}\left(s + \frac{1}{\tau_{y'_1}}\right)\left(s + \frac{1}{\tau_{y'_2}}\right)\underbrace{(s^2 + 2\zeta_{y'}\omega_{y'}s + \omega_{y'}^2)}_{\text{or}} \left(s + \frac{1}{\tau_{y'_3}}\right)\left(s + \frac{1}{\tau_{y'_4}}\right)$	$A_{a'_y} = U_o Y^v_{\delta_r} + Y_x N'_{\delta_r}$ $\frac{1}{\tau_{y'_1}} \doteq \frac{g}{U_o}\left[\frac{L_r}{L_p} - \frac{N_r(Y_v L_{\delta_r} - Y^v_{\delta_r} L_\beta)}{L_p(Y_v N_{\delta_r} - Y^v_{\delta_r} N_\beta)}\right]$ $\frac{1}{\tau_{y'_2}} \doteq -L_p$ $\omega_{y'}^2 \text{ or } \frac{1}{\tau_{y'_3}\tau_{y'_4}} \doteq \frac{U_o}{Y_x N'_{\delta_r}}(Y^v_{\delta_r} N_\beta - Y_v N_{\delta_r})$ $2\zeta_{y'}\omega_{y'} \text{ or } \frac{1}{\tau_{y'_3}} + \frac{1}{\tau_{y'_4}} \doteq -\frac{U_o Y^v_{\delta_r}}{Y_x(N'_{\delta_r})^2}(Y^v_{\delta_r} N_\beta - Y_v N_{\delta_r})$	$N'_{\delta_r} L'_p \doteq N_{\delta_r} L_p$ $\left\lvert Y_{\delta_r} N_\beta\right\rvert < \left\lvert Y^v_{\delta_r} N'_\beta\right\rvert$ $\left\lvert\frac{L_r N_\beta}{N_r L_\beta}\right\rvert \ll 1$ $\left\lvert N_{\delta_r} L_\beta\right\rvert \gg \left\lvert Y^v_{\delta_r} N'_\beta - Y_v N'_{\delta_r}\right\rvert$ $\left\lvert\frac{L_p Y^v_{\delta_r}}{N_{\delta_r}}\right\rvert \ll 1$ $\left\lvert L_{\delta_r} N_\beta\right\rvert \ll \left\lvert N_{\delta_r} L_\beta\right\rvert$ $\frac{g}{U_o}$ and $\lvert N_\beta\rvert \ll \lvert L_\beta\rvert$ $Y_v N'_{\delta_r} - Y^v_{\delta_r} N'_\beta \doteq Y_v N_{\delta_r} - Y^v_{\delta_r} N_\beta$
At center of percussion: $N_{a'_y}(s) = 3_{a'_y}\left(s + \frac{1}{\tau_{y'_1}}\right)\left(s + \frac{1}{\tau_{y'_2}}\right)\left(s + \frac{1}{\tau_{y'_3}}\right)$	$3_{a'_y} \doteq -\frac{U_o Y^v_{\delta_r}}{N'_{\delta_r}}(Y^v_{\delta_r} N'_\beta - Y_v N'_{\delta_r})$ $\frac{1}{\tau_{y'_3}} \doteq -\frac{N'_{\delta_r}}{Y^v_{\delta_r}}$	

TABLE 6 (Cont.)

TABLE 6 (Cont.)
Lateral Numerator Approximate Factors—Rudder

Factored Forms	Approximate Factors	Conditions of Validity
	$\left\|\frac{1}{T_{\omega_1}}\right\| \doteq \left\|\frac{D_\omega}{C_\omega}\right\|$, $\left\|\frac{1}{T_{\omega_2}}\right\| \doteq \left\|\frac{B_\omega}{A_\omega}\right\|$, $\left\|\frac{1}{T_{\omega_3}}\right\| \doteq \left\|\frac{C_\omega}{B_\omega}\right\|$	
	$\omega_\omega^2 \doteq \frac{C_\omega}{A_\omega}$	
	$2\zeta_{\omega_\omega}\omega_\omega \doteq \frac{B_\omega}{A_\omega} - \frac{D_\omega}{C_\omega}$	
	$A_\omega \doteq N_{\delta_r} + L_{\delta_r} \tan \Theta_T$	
	$B_\omega \doteq -N_{\delta_r}(Y_v + L_p) + Y_{\delta_r}(N_\beta + L_\beta \tan \Theta_T)$ $-L_{\delta_r}(N_r + Y_v) \tan \Theta_T$	
	$C_\omega \doteq Y_v L_p N_{\delta_r} - Y_{\delta_r} N_\beta L_p$ $+ (L_{\delta_r} N_\beta - N_{\delta_r} L_\beta) \tan \Theta_T$	
	$D_\omega \doteq \frac{g}{U_o}(L_{\delta_r} N_\beta - N_{\delta_r} L_\beta)$	
		$\left\|\frac{L_{\delta_r} N_p}{N_{\delta_r} L_p}\right\}$, $\left\|\frac{L_\beta N_p}{N_\beta L_p}\right\|$ $\left\|\frac{Y_v L_r}{L_\beta}\right\}$, $\left\|\frac{Y_{\delta_r} N_\beta}{Y_v N_{\delta_r}}\right\|$ $\left\|\frac{Y_v N_r}{N_\beta}\right\}$, $\left\|\frac{L_r \tan \Theta_T}{L_p}\right\|$ $\left\|\frac{Y_v L_p}{L_\beta \tan \Theta_T}\right\|$ } ≪ 1
		$D_\omega/B_\omega > 0$, , and:
$\frac{N_\omega(s)}{A_\omega \cos \Theta_T} = \left(s - \frac{1}{T_{\omega_1}}\right)\left(s + \frac{1}{T_{\omega_2}}\right)\left(s - \frac{1}{T_{\omega_3}}\right)$		→ $D_\omega/C_\omega < 0$
$\left(s + \frac{1}{T_{\omega_1}}\right)\left(s + \frac{1}{T_{\omega_2}}\right)\left(s + \frac{1}{T_{\omega_3}}\right)$		→ $D_\omega/C_\omega > 0$, $\frac{B_\omega C_\omega^2}{4 D_\omega} > B_\omega^2 > 4 A_\omega C_\omega$
$\left(s + \frac{1}{T_{\omega_1}}\right)\left(s^2 + 2\zeta_{\omega_\omega}\omega_\omega s + \omega_\omega^2\right)$		→ $D_\omega/C_\omega > 0$, $B_\omega^2 < 4 A_\omega C_\omega$
		For $D_\omega/B_\omega < 0$, and:
$\left(s + \frac{1}{T_{\omega_1}}\right)\left(s + \frac{1}{T_{\omega_2}}\right)\left(s - \frac{1}{T_{\omega_3}}\right)$		→ $D_\omega/C_\omega > 0$
$\left(s - \frac{1}{T_{\omega_1}}\right)\left(s + \frac{1}{T_{\omega_2}}\right)\left(s + \frac{1}{T_{\omega_3}}\right)$		→ $D_\omega/C_\omega < 0$, $B_\omega^2 \geq 4 A_\omega C_\omega$
$\left(s - \frac{1}{T_{\omega_1}}\right)\left(s^2 + 2\zeta_{\omega_\omega}\omega_\omega s + \omega_\omega^2\right)$		→ $D_\omega/C_\omega < 0$, $B_\omega^2 < 4 A_\omega C_\omega$

$\delta_r/r = K_r$. Then all three lateral equations of motion will be modified by the control system—viz.,

$$\left.\begin{aligned} (s - Y_v)\beta - \quad (g/U_0)\varphi + \quad (1 - Y_{\delta_r}{}^*K_r)r \quad &= 0 \\ -L_\beta'\beta + (s - L_p')p - \quad (L_r' + L_{\delta_r}'K_r)r \quad &= 0 \\ -N_\beta'\beta - \quad N_p'p + [s - (N_r' + N_{\delta_r}'K_r)]r \quad &= 0 \end{aligned}\right\} \tag{20}$$

The total effect of the control system is to augment L_r' and N_r' and to modify the side-acceleration term which originally came from the centripetal force mU_0r. In most practical cases, however, the principal effect of the r to δ_r feedback is to augment N_r'. Referring to Table 4, which gives the lateral-denominator approximate factors, it is seen that an increase in $-N_r'$ by an increment, $-\Delta N_r'$, will (1) increase the Dutch roll damping by the amount of $-\Delta N_r'$; i.e.,

$$\Delta 2(\zeta\omega)_{d_1} = -\Delta N_r'$$

(2) make the spiral mode more stable (assuming that L_β'/N_β' is negative) by adding an increment

$$\Delta 1/T_s = -T_{R_1}(g/U_0)(L_\beta'/N_\beta')\Delta N_r'$$

These changes to the denominator factors are equivalent to those which would be found by closing the control system loop using servoanalysis methods. Therefore, the closed r to δ_r system is characterized by an increased Dutch roll damping and a more stable spiral mode when the sign of K_r is properly taken. The converse will occur for an opposite sign of K_r.

Besides the changes to the poles of the lateral transfer functions given above, an increase in $-N_r'$ will also modify many transfer function zeros. For instance, from Tables 5 and 6 it can be seen that the numerators of the control deflection transfer functions are affected as follows: (1) the roll-numerator damping, $2\zeta_{\varphi a}\omega_{\varphi a}$, will be increased for the aileron case by that increment ΔN_r of $\Delta N_r'$; i.e.,

$$\Delta 2\zeta_{\varphi a}\omega_{\varphi a} = -\Delta N_r$$

and for the rudder case by the increment $\Delta N_r'$; i.e.,

$$\Delta 2\zeta_{\varphi r}\omega_{\varphi r} = -\Delta N_r'$$

(2) the damping of the quadratic numerator for $N_\omega(s)$ is increased almost directly by an incremental change in $-\Delta N_r$.

All yaw-rate numerators are unaffected by changes in $-N_r'$ since no subscript r derivatives can be present in the numerator determinant $N_r(s)$.

The above example demonstrates the application of the approximate-factor formulas to the assessment of relatively low-gain feedback in an r to δ_r control system. Similar examples could have covered p, q, r, u, v, or w signals fed to appropriate surfaces. While the example given was for a single-sensor control loop, the equivalent-stability-derivative method is not restricted to such single feedbacks. Indeed, in practice, the method is probably most valuable when several feedbacks are used, since these system types are simply handled by the equivalent-stability-derivative procedure but become a complex multiloop analysis problem when servo techniques are employed. Applied in preliminary analysis of multiloop problems, the practical utility of this method is sufficiently great to justify the development of airframe approximate factors for use in it alone.

Closed-Loop Servo Implications of the Airframe

Precise analysis of airframe-controller systems requires the use of servo methods; the optimization process requires consideration of the airframe as an alterable element. In practice, the determination of the closed-loop effects due to variation in the airframe element demands a separate analysis for each of several sets of relative pole, zero locations consistent with varying combinations of airframe and control systems. The results of these analyses provide the foundation required to develop an appreciation for the potentialities of tailoring the airframe-controller system. The relative roles to be played by each of the system elements can then be determined on a rational basis by considering competing possibilities.

The series of servoanalyses referred to above is straightforward as far as procedure is concerned, but complicated in detail. Therefore, in considering the servoanalysis approach, a "single-sensor control loop system" will be used here to provide a simple example. The types of systems classified under this title have the distinguishing characteristic that their functional operation can be described by single-loop block diagrams composed of analytically simple transfer function blocks. Such a system is shown in Fig. 1. The forward-loop transfer function, $Y_a(s)$, may include closed-loop transfer functions of simple inner loops such as a positional servo. Also, the feedback transfer function, $Y_f(s)$, may be a combined representation of two or more sensors and additional simple closed-loop transfer functions. In both of these cases the transfer functions resulting from the sensor combination or the inner loop closure are simple, and the overall outer control loop, or "sensor loop," is a "single control loop." In other words, while each of the single series blocks in the block diagram of Fig. 1 may involve more than one loop and/or more than one sensor, the system is still a "single-sensor control-loop system."

Further restrictions are desirable because of the complex form of airframe transfer functions and the nature of closed-loop studies. In particular, both actuator and sensor dynamics are assumed to be ideal. These assumptions are made for two reasons: first, to simplify the analytical treatment, and second, to focus attention upon the airframe rather than the control system. In a practical flight-control design

problem such simplification, of course, would not be employed.

In the diagram of Fig. 1, the two disturbance blocks essentially convert the disturbance input, μ, into equivalent surface deflections appropriately "scaled" for ultimate conversion of μ into components of the airframe motion quantities ξ and λ. The total directly controlled airframe-motion quantity, λ, is given by

$$\left.\begin{aligned}\lambda &= \frac{Y_a\Lambda_\delta}{1 + Y_aY_f\Lambda_\delta}\left\{\lambda_c + \frac{1}{Y_a}\frac{N_{\lambda_\mu}}{N_{\lambda_\delta}}\mu\right\} \\ &= \left[\frac{Y_{OL}}{1 + Y_{OL}}\right]\left\{\frac{\lambda_c}{Y_f} + \frac{1}{Y_aY_f}\left[\frac{N_{\lambda_\mu}}{N_{\lambda_\delta}}\right]\mu\right\} \\ &\qquad \text{where } Y_{OL} = Y_aY_f\Lambda_\delta\end{aligned}\right\} \quad (21)$$

The components entering into the calculation of λ† are seen to be (1) the "closed-loop" transfer function, $Y_{OL}/(1 + Y_{OL})$ (this term contains all of the *system* (as opposed to input) dynamic and static characteristics), (2) the command input, λ_c, modified to system-output units by dividing by the feedback transfer function Y_f, and (3) the disturbance, μ, with units changed to output terms by a suitable factor.

The transfer functions Y_f and Y_aY_f are ordinarily relatively simple. In the discussion to follow they are further idealized. Also, the disturbance numerators, N_{λ_μ}, are given in terms that are simplified, but sufficiently precise for most purposes, in reference 3, and the control numerators N_{λ_δ} have been presented in Tables 1 through 6 in various forms. Therefore the contribution of the terms listed as items 2 and 3 above is easily computed with the formulas already available. The closed-loop transfer function, on the other hand, has not yet been considered. Therefore the following discussion will be devoted to investigations of the *influence of possible forms of specific airframe transfer functions upon the closed-loop transfer functions.* The closed-loop characteristics will be simply and concisely shown in terms of the airframe transfer function by using standard methods of servoanalysis.

When all of the component elements listed above are known, one can readily determine the response of the directly controlled airframe-motion quantity, λ, to the various inputs. Further, the influence of possible air-

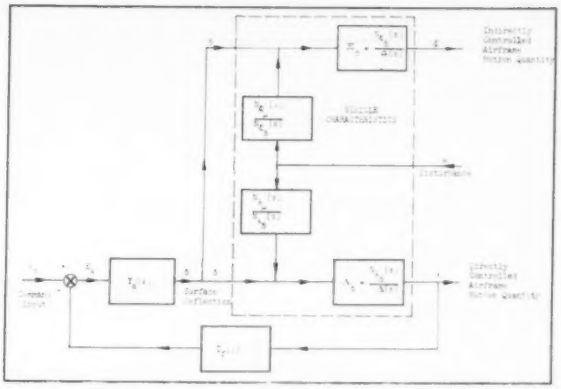

FIG. 1. Single-sensor control system with command and disturbance inputs.

frame changes upon the component elements can be assessed through the medium of the airframe transfer function approximate factors. In actual practice, these pieces of knowledge allow the evolution of a rapid, cut-and-try, airframe-optimization procedure for single-sensor control-loop systems (as far as the directly controlled airframe-motion quantity is concerned).

As the single-sensor control-loop example, consider a lateral control system in which roll angle and roll rate are both fed to the aileron. In terms of the block diagram of Fig. 1 and the expressions given in Eq. (21), this is equivalent to defining

$$Y_a \equiv K_\varphi(1 + T_\varphi s) \quad \text{and} \quad Y_f \equiv 1$$

Actually the basic roll and roll-rate system can incorporate the $1 + T_\varphi s$ term in either Y_a or Y_f and systems have been built both ways. However, the location of the lead within the block diagram will be of no further concern here since the major interest is centered upon the closed-loop transfer function $Y_{OL}/(1 + Y_{OL})$.

(I) *Closed-Loop Transfer Function Considerations Using Simplified Airframe Representation*

To introduce some of the concepts, it is advantageous to consider first a simplified roll transfer function, derivable from the basic equations of motion by setting the $(s - Y_v)\beta$ term equal to zero. Reference 3 shows that such a simplification yields the roll-subsidence and spiral modes given in Table 4. For such a simplification, and letting $Y_{\delta_a}{}^* = 0$,

$$\left.\begin{aligned}\Phi_{\delta_a} &= \frac{L_{\delta_a}'[1 - (N_{\delta_a}'L_\beta'/L_{\delta_a}'N_\beta')]}{s^2 + \{[N_p' - (g/U_0)](L_\beta'/N_\beta') - L_p'\}\, s + (g/U_0)\,[N_r'(L_\beta'/N_\beta') - L_r']} \\ &= \frac{K_{\varphi\delta_a}}{(T_s s + 1)(T_R s + 1)} \text{ or } \frac{K_{\varphi\delta_a}}{(s/\omega_1)^2 + (2\zeta_1 s/\omega_1) + 1}\end{aligned}\right\} \quad (22)$$

where $$K_{\varphi\delta_a} = \frac{U_0L_{\delta_a}'}{gN_r'}\,\frac{N_\beta'}{L_\beta'}\,\frac{[1 - (N_{\delta_a}'L_\beta'/L_{\delta_a}'N_\beta')]}{[1 - (N_\beta'L_r'/L_\beta'N_r')]}$$

$$(1/T_s) + (1/T_R) = 2\zeta_1\omega_1 = -L_p' + [N_p' - (g/U_0)](L_\beta'/N_\beta')$$

$$1/T_sT_R = \omega_1{}^2 = (g/U_0)[N_r'(L_\beta'/N_\beta') - L_r']$$

† A corresponding development for the indirectly-controlled airframe-motion quantities, such as ξ in Fig. 1, leads to the same implications.

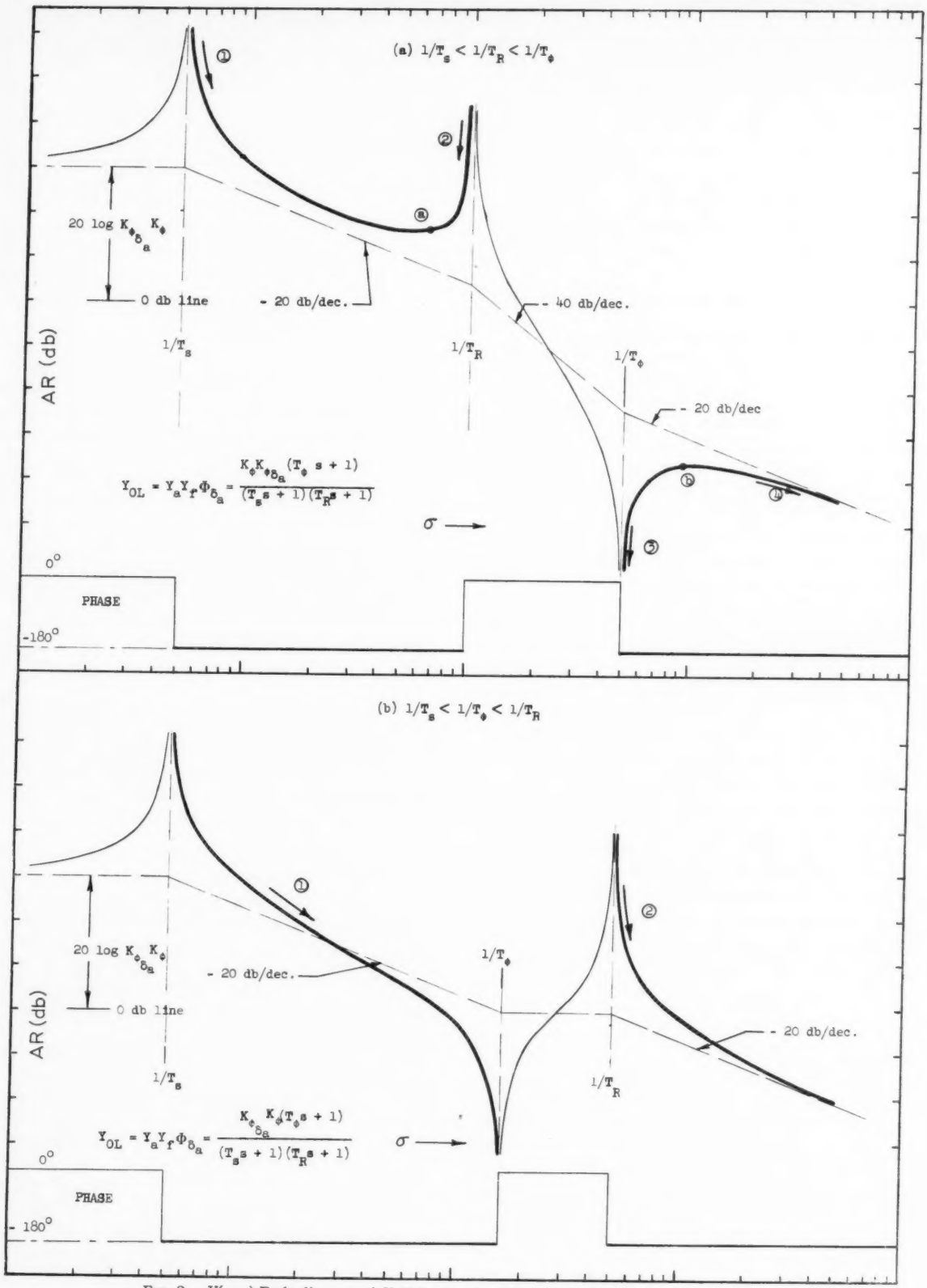

FIG. 2. $Y(-\sigma)$ Bode diagram of $Y_a Y_f \Phi_{\delta a}$ for simplified roll case with lead equalization.

Since the case with two real roots is the more common, it will be used here.

The open-loop transfer function is formed by taking the product of the airplane and controller transfer functions—viz.,

$$Y_{OL} = \frac{K_\varphi K_{\varphi b_a}(T_\varphi s + 1)}{(T_s s + 1)(T_R s + 1)} \tag{23}$$

Since the roll subsidence is always greater than the spiral root, the simplified system characteristics will be strongly dependent upon the relative location of $1/T_\varphi$ and $1/T_R$. Fig. 2 shows generic open-loop $Y(-\sigma)$ Bode diagrams[6] for the two possible cases (excluding the trivial one when $1/T_\varphi = 1/T_R$). Root locus plots[7] corresponding to the Bodes are shown in Fig. 3. Although $Y(j\omega)$ Bode diagrams are also useful representations in the analysis procedure, they add little to the present discussion.

Each one of the three diagrams mentioned contains *all* the information available concerning the control system and its open- and closed-loop transfer functions —i.e., the closed-loop transfer function poles and zeros can be obtained from, or are presented on, each of the plots. The reason for using al three forms in normal generic analyses is that each plot emphasizes certain features of interest more than the others. The plots are supplementary in that they each yield the closed-loop secrets with various degrees of difficulty in various regions. While it is not within the scope of this paper to describe the use and interpretation of these plots in detail, the two most applicable to the present situation will be discussed rather fully for illustrative purposes.

(a) The root locus plot, Fig. 3, consists of loci which are paths defining all possible closed-loop transfer function poles. The plot uses a linear scale, and the roots are shown as complex numbers with the abscissa giving the real part and the ordinate the imaginary part of a closed-loop root. Gain is a parameter on the loci (the arrows are drawn in the direction of increasing open-loop gain).

(1) At zero gain, the poles (X's) of the closed-loop transfer function are simply the poles of the airframe transfer function alone. In other words, with the control system gain turned down to zero, the airframe motions are those of the airframe itself. In Fig. 3, these airframe dynamics are defined by the spiral root ($-1/T_s$) and by the roll subsidence root ($-1/T_R$).

(2) At very large controller gain, the roots defining the airframe's motions fall along the high-gain, straight-line asymptotes to the locus, or tend to approach the zeros ($\odot$) of the open-loop transfer function. For the simplified situation of Fig. 3(a) there is one transfer function zero, and the high-gain asymptote, ④, is actually part of the locus throughout its entire extent. This portion of the locus, and the other real root proceeding along the path ③, result from a decoupling at the encircled b point of the coupled spiral and roll-subsidence modes.

(3) At intermediate values of gain, the closed-loop roots defining the airframe motions are somewhere on

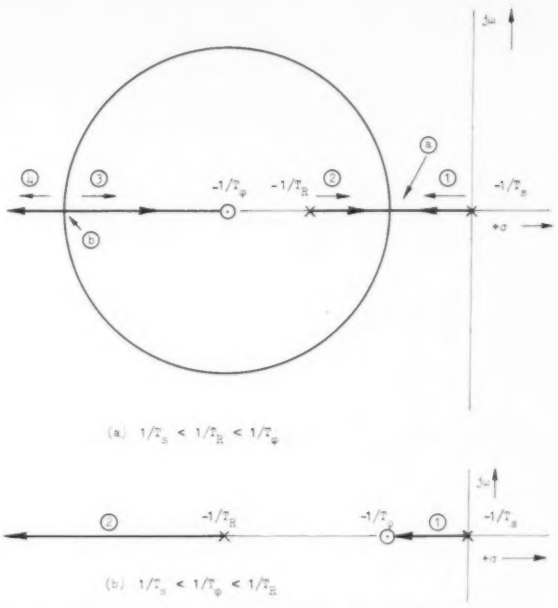

FIG. 3. Root locus for simplified roll case with lead equalization.

the locus between the airframe-alone poles and the zero and asymptote. In Fig. 3(a), the "effective" closed-loop spiral root becomes a larger negative number (path ①) and the modified roll-subsidence root becomes smaller (path ②) until the two couple (at the encircled a point) to form an oscillatory pair. The locus of roots between the encircled points a and b is a circle. If the imaginary axis is y and the real axis x, the equations for the locus can be shown to be[8]

$$[x + (1/T_\varphi)]^2 + y^2 = (1/T_\varphi)^2 + (1/T_R T_s) - (1/T_\varphi)[(1/T_R) + (1/T_s)] \tag{24}$$

$$y = 0 \tag{25}$$

The circle described by Eq. (24) has its center at $(-1/T_\varphi, 0)$ and has a radius which is approximately $\sqrt{1/T_\varphi}\,\sqrt{1/T_\varphi - 1/T_R}$ (if $1/T_R \gg 1/T_s$). When $1/T_\varphi < 1/T_R$, the radius is imaginary, and the situation corresponds to Fig. 3(b). Eq. (25) has regions of validity regardless of the relative orientation of $1/T_\varphi$, $1/T_R$, and $1/T_s$; it is therefore a companion to Eq. (24) when the circle exists, or the sole locus equation if the radius is imaginary.

(b) The amplitude ratio portion of the $Y(-\sigma)$ Bode plot of Fig. 2 is obtained by (1) substituting the real variable, $-\sigma$, for the complex variable, s, in the open-loop transfer function; and then (2) plotting 20 log $|Y(-\sigma)|$ versus log σ. The amplitude-ratio asymptotes are identical to those of a $Y(j\omega)$ Bode diagram. The phase angle is either zero or -180 degrees, depending upon the sign of $Y(-\sigma)$. The portions of the plot where the phase angle is $-180°$ satisfy the angle criterion for a closed-loop root—i.e., for a closed-loop root to exist, $Y(s) + 1$ must equal zero, so $Y(s) = -1$ or $\angle Y(s) = -180°$. The amplitude ratio in the regions where the phase is $-180°$ is therefore a locus

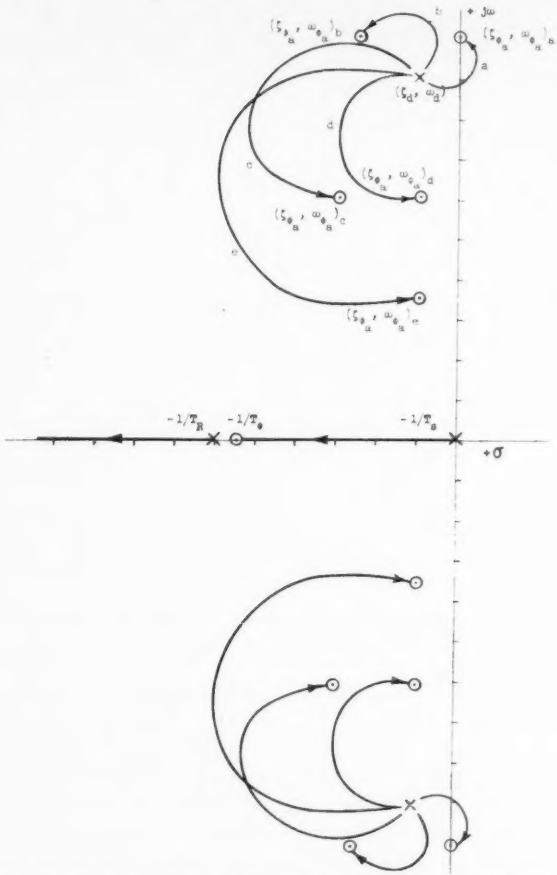

FIG. 4. Root loci of $\delta_a = K_\varphi(T_\varphi s + 1)\varphi$ system for Condition I. $1/T_s < 1/T_\varphi < 1/T_R$.

of the negatives of real roots versus gain. The $Y(-\sigma)$ Bode is both an open-loop plot and a locus of all real closed-loop roots.

(1) When $1/T_\varphi > 1/T_R$ [Fig. (2a)], as gain is increased the modified spiral and roll-subsidence proceed down paths ① and ② until the zero *db* line reaches the encircled *a* point. At higher gains the roots become complex. At still higher gains the presence of $1/T_\varphi$ becomes a more emphatic factor in the character of the system. For the zero *db* line at the encircled *b* point or lower—i.e., higher gains—the two oscillatory roots have returned to the real axis: one goes into $(-1/T_\varphi)$ while the other increases (negatively) with increased gain.

(2) In Fig. 2(b), the presence of the zero, $-1/T_\varphi$, between the $-1/T_s$ and $-1/T_R$ poles leads to a system which exhibits considerable differences from the above. The behavior of the closed-loop roots as gain is increased is straightforward—i.e., the modified spiral goes down path ① to the lead term $1/T_\varphi$, and the modified roll subsidence proceeds along path ②.

Paths ① and ② and encircled points *a* and *b* are correlated directly with the same paths and points on the root loci of Fig. 3. As can be appreciated from the above discussion, the airframe approximate factors are as useful in the servo techniques as they are for the equivalent-stability-derivative approach. In the root locus, for instance, they define the starting and end points of the locus; and the intermediate points are completely determined by a weighted effect of each pole and zero. For example, in the case discussed here (with $1/T_R \gg 1/T_s$), it is apparent that the response time, total system damping, etc., are direct functions of $1/T_R$. Since $1/T_R$ is known approximately in terms of airframe parameters, the influence of these upon the closed-loop system can be readily assessed.

(2) *Closed-Loop Transfer Function Considerations With the Complete Airframe Representation*

If the complete three degree of freedom airframe characteristics are used, the $\Phi_{\delta a}$ transfer function, with $Y_{\delta a}{}^* = 0$, has the form

$$\Phi_{\delta a} = \frac{K_{\varphi\delta a}[(s/\omega_{\varphi a})^2 + (2\zeta_{\varphi a}/\omega_{\varphi a})s + 1]}{(T_s s + 1)(T_R s + 1)[(s/\omega_d)^2 + (2\zeta_d s/\omega_d) + 1]} \tag{26}$$

The approximate values of T_s, T_R, and $K_{\varphi\delta a}$ for this complete case are the same as those previously used in the simplified roll-control situation. The primary change in going from the simplified case to the more complex one is, then, a multiplication of the simplified airframe transfer function by a ratio of quadratics.

As noted in reference 3, the values of $\zeta_d\omega_d$ and $\zeta_{\varphi a}\omega_{\varphi a}$ are ordinarily about the same; the ratio of $\omega_{\varphi a}$ and ω_d can be either greater or less than unity; and $1/T_R$ may be either greater or less than ω_d (or $\omega_{\varphi a}$). Most of these relative pole and zero locations are amenable to fairly simple changes by modifying the airframe parameters. The various possible combinations and permutations of these parameters, as well as the value of $1/T_\varphi$, are therefore of interest.

As one might suspect from the discussion of Figs. 2 and 3, the relative location of $1/T_R$, $1/T_\varphi$, and $1/T_s$ can be used as a principal classifying device. Roman numerals will be used for this basic division—i.e.,

Condition I $\quad 1/T_s < 1/T_\varphi < 1/T_R$

Condition II $\quad 1/T_s < 1/T_R < 1/T_\varphi$

The practical single-sensor control-loop cases for Condition I, for all types of $\omega_{\varphi a}/\omega_d$ ratios, are shown in the root loci of Fig. 4. As gain is increased, the spiral root always goes toward the lead-equalization zero, the roll-subsidence root goes out the real axis, and the Dutch roll roots move into the roll-numerator quadratic zeros. In the latter portion of the locus, the modified Dutch roll roots always approach the roll-numerator quadratic along counterclockwise paths which resemble a sector of a circle. It is clear from this behavior that situations corresponding to $\omega_{\varphi a}/\omega_d > 1$ can become unstable (as in Fig. 4, curve a), while the converse is true when $\omega_{\varphi a}/\omega_d < 1$. For the modified Dutch roll to actually become unstable, a phase dip in a $Y(j\omega)$ Bode diagram exceeding $-180°$ is required. The presence of such a dip depends, of course, upon the actual relative values of ζ_d, $\zeta_{\varphi a}$, $\omega_{\varphi a}$, ω_d, $1/T_R$, and $1/T_\varphi$.

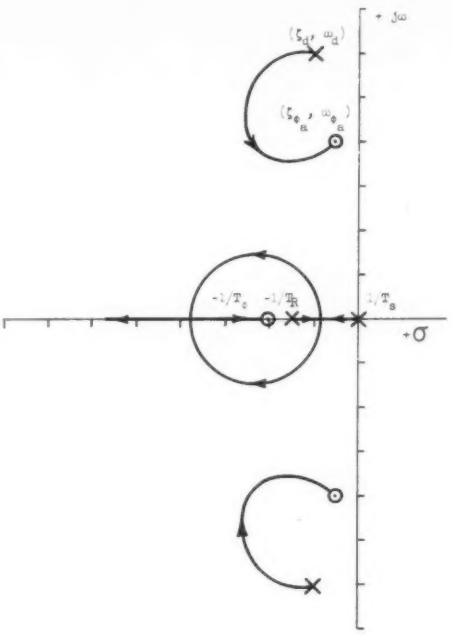

Case 1. $\omega_{\phi_a}/\omega_d < 1\ ;\ \eta < \nu$

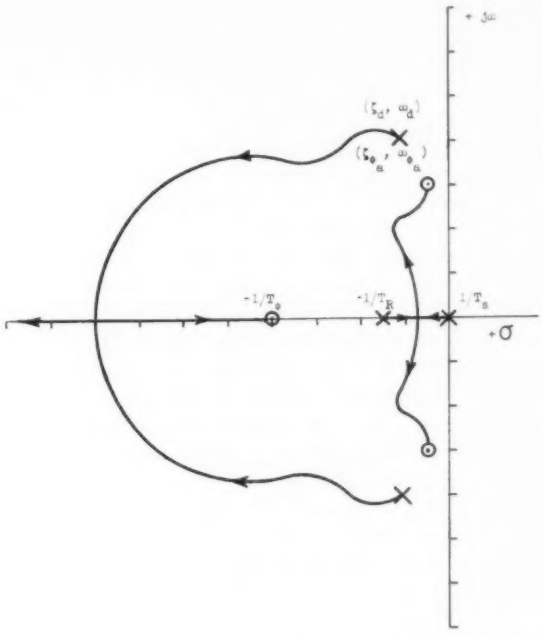

Case 2. $\omega_{\phi_a}/\omega_d < 1\ ,\ \eta \doteq \nu$

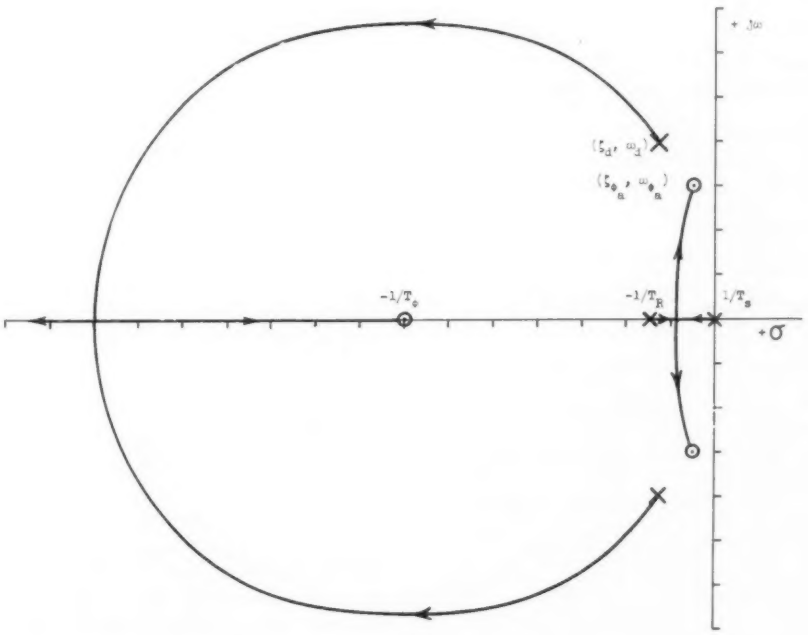

Case 3. $\omega_{\phi_a}/\omega_d < 1\ ;\ \eta > \nu$

FIG. 5. Root loci of $\delta_a = K_\varphi(T_\varphi s + 1)\varphi$ for Condition II $(1/T_s < 1/T_R < 1/T_\varphi)$ when $\omega_{\varphi_a}/\omega_d < 1$.

Condition II situations can be much more varied than those of Condition I. The chief reason for this is the mutual influence and interaction of the coupled roll-subsidence and spiral mode with the $\omega_{\varphi a}$, $\zeta_{\varphi a}$ and ω_d, ζ_d pair. In the discussion of the simplified case, it was noted that the coupled spiral and roll-subsidence mode was a circle. The addition of the ratio of quadratics to the airframe transfer function modifies this somewhat, but a large part of the root locus is still quasi-circular. Now if the radius, η, of the circle generated by the real poles and zeros ($-1/T_\varphi$, $-1/T_R$, $-1/T_s$) is about the same as the distance, ν, from $-1/T_\varphi$ to the ω_d zero (if $\omega_{\varphi a}/\omega_d > 1$) or the $\omega_{\varphi a}$ pole (if $\omega_{\varphi a}/\omega_d < 1$), then one would expect strong interactions between the quasi-circle due to $-1/T_\varphi$, etc., and the loci which in Condition I departed from the Dutch roll roots and arrived at the numerator quadratic zeros. Just such interactions do exist; and so the relative magnitudes of η and ν become an appropriate classifying characteristic.

The distance ν, from $-1/T_\varphi$ to a point $-\zeta\omega_n$, $\omega_n\sqrt{1-\zeta^2}$ (where ω_n and ζ can refer to either the $\omega_{\varphi a}$ zeros or ω_d poles, whichever is physically closer to $1/T_\varphi$) is

$$\left.\begin{aligned}\nu^2 &= [(1/T_\varphi) - \zeta\omega_n]^2 + (\omega_n\sqrt{1-\zeta^2})^2 \\ &= (1/T_\varphi)^2 - 2\zeta\omega_n/T_\varphi + \omega_n^2\end{aligned}\right\} \quad (27)$$

The approximate radius of the circle, η, is

$$\eta^2 = (1/T_\varphi)^2 - (1/T_\varphi T_R) \quad (28)$$

By combining Eqs. (27) and (28), the classifying criteria become

$$\left.\begin{aligned}&\eta^2 > \nu^2, \quad \text{or} \quad (1/T_\varphi\omega_n)[(1/T_R\omega_n) - 2\zeta] < 1 \\ &\eta^2 < \nu^2, \quad \text{or} \quad (1/T_\varphi\omega_n)[(1/T_R\omega_n) - 2\zeta] > 1\end{aligned}\right\} \quad (29)$$

Besides the "influence" parameter discussed above, the $\omega_{\varphi a}/\omega_d$ ratio is also of consequence. Therefore, the total cases of some practical interest for Condition II include

$\omega_{\varphi a}/\omega_d < 1$	$\omega_{\varphi a}/\omega_d > 1$
Case 1: $\eta < \nu$	Case 1′: $\eta < \nu$
Case 2: $\eta \doteq \nu$	Case 2′: $\eta \doteq \nu$
Case 3: $\eta > \nu$	Case 3′: $\eta > \nu$

The unprimed cases ($\omega_{\varphi a}/\omega_d < 1$) are shown in Fig. 5. In Case 1, the circle centered approximately on $-1/T_\varphi$ has little influence on the shape of the other loci. In essence this case is similar to that shown in Fig. 3 with the addition of a quadratic pair which are widely separated from the other roots.

Case 2 is a transition configuration. The circle is still largely present, but is broken up in the neighborhood of the $\omega_{\varphi a}$, ω_d pair. The coupled roll-subsidence and spiral mode starts along the circle, and then takes off in a different direction toward the roll-numerator zeros. The modified Dutch roll roots, as one proceeds along the locus from low to higher gains, seem to be starting toward $\omega_{\varphi a}$ as in Case 1, and then change direction to go into orbit about $-1/T_\varphi$.

Case 3 shows the situation after transition. The Dutch roll is now the basis of the circular segment, and the coupled spiral and roll-subsidence mode advances directly into the roll numerator.

The primed situations ($\omega_{\varphi a}/\omega_d > 1$) are surveyed in Fig. 6. An example of Case 1′ is not shown since it would be similar to Case 1 except that the locus starting at ω_d and moving toward $\omega_{\varphi a}$, while still counterclockwise, would be rotated roughly 180° (since $\omega_{\varphi a} > \omega_d$) thus bringing portions of it into the right half (unstable) plane.

The example shown for Case 2′ is not as interesting as its counterpart, Case 2, since no apparent transition effects are evident. The locus shown does provide a good illustration of how close one can come to a transitional situation with little apparent effect upon the locus.

The Case 3′ example is similar to that for the unprimed case with the notable addition that instability of the coupled roll-subsidence and spiral mode can conceivably exist. In these primed cases, as with the previous instances where $\omega_{\varphi a}/\omega_d > 1$, the simplest quantitative picture of the stability problem is given by the phase dip on the $Y(j\omega)$ Bode representation.

For all the Condition I and II cases discussed, the high-gain behavior of the closed-loop transfer function will be essentially the same—i.e.,

$$\frac{Y_{OL}}{1+Y_{OL}} = \left[\frac{K_\varphi K_{\varphi\delta a}}{1+K_\varphi K_{\varphi\delta a}}\right] \frac{(T_\varphi s+1)\,[(s/\omega_{\varphi a})^2 + (2\zeta_{\varphi a}s/\omega_{\varphi a}) + 1]}{(T_{CL}s+1)(T_{\varphi CL}s+1)[(s/\omega_{CL})^2 + (2\zeta_{CL}s/\omega_{CL}) + 1]} \quad (30)$$

which, as $K_\varphi K_{\varphi\delta a}$ becomes much larger than unity, approaches

$$[Y_{OL}/(1+Y_{OL})]_{K_\varphi K_{\varphi\delta a}\text{large}} \doteq 1/(T_{CL}s+1) \quad (31)$$

since, then, $T_{\varphi CL} \doteq T_\varphi$, $\omega_{CL} \doteq \omega_{\varphi a}$, and $\zeta_{CL} \doteq \zeta_{\varphi a}$ The value of $1/T_{CL}$ at high gain is simply the intersection of the zero *db* line and the high-frequency asymptote of the $Y(j\omega)$ or $Y(-\sigma)$ Bode diagrams.

The cases presented above as examples are also useful for other purposes. For instance, an important objective in the design of a simple and reliable control system is to avoid changes in the equalization, $1/T_\varphi$, throughout the flight regime. As the flight condition is changed, the airplane characteristics also change; as a result, the relative location of the controller-airframe system poles and zeros may be altered drastically. In Fig. 5, for instance, Case 1 could be a high-speed condition, Case 2 could represent intermediate or cruise conditions, and Case 3 a post-launch or low-

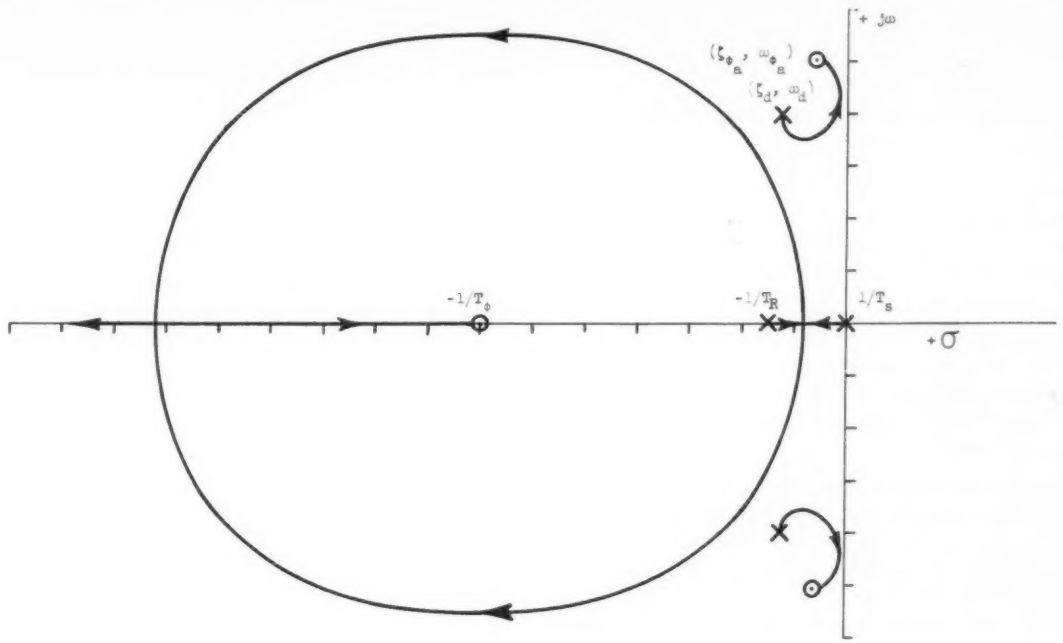

Case 2′. $\omega_{\phi_a}/\omega_d > 1$; $\eta \doteq \nu$

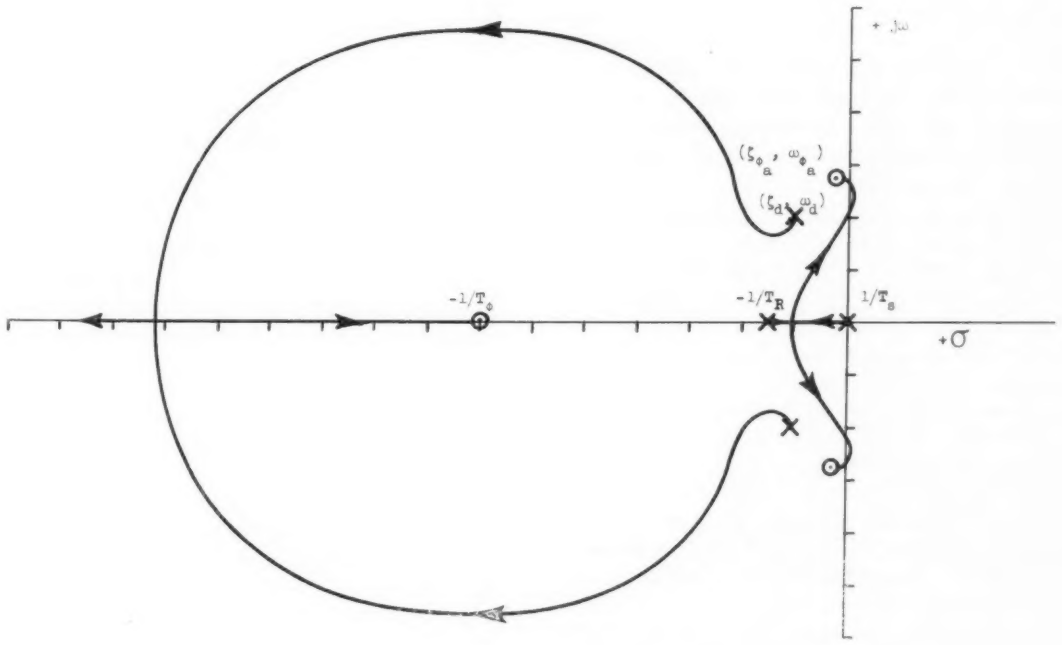

Case 3′. $\omega_{\phi_a}/\omega_d > 1$; $\eta > \nu$

FIG. 6. Root loci of $\delta_a = K_\varphi(T_\varphi s + 1)\varphi$ system for Condition II $(1/T_s < 1/T_R < 1/T_\varphi)$ when $\omega_{\varphi_a}/\omega_d > 1$.

speed condition, with the control system $1/T_\varphi$ held constant. As can be seen from this sequence, the character of the closed-loop response could change drastically as a function of the actual flight condition.

(3) *Summary of Significant Closed-Loop Considerations,* $\varphi(T_\varphi s + 1) \rightarrow \delta_a$

Pertinent points developed in the text above are summarized below. One should realize that $1/T_s$, ζ_d, ω_d, $\zeta_{\varphi a}$, and $\omega_{\varphi a}$ are airframe parameters that are relatively variable (although not necessarily independently variable).

(a) *Spiral,* $1/T_s$—The spiral mode has little effect upon the lead-equalized roll system studied for physically reasonable gain values, although a divergent spiral places a lower limit on suitable gain values if it is to be stabilized.

(b) *The Ratio of Lead Equalization to Roll Subsidence,* T_φ/T_R—The ratio of the lead-equalization time constant, T_φ, to that for the roll-subsidence, T_R, is a suitable classification parameter for lead-equalized roll control systems.

For $T_\varphi/T_R < 1$, (a) all systems examined have real-axis root loci in which $-1/T_s$ goes to $-1/T_\varphi$, and $-1/T_R$ advances toward $-\infty$ as K_φ increases (the roll-subsidence and spiral modes do not couple), and (b) the Dutch roll roots proceed in a counterclockwise direction into the roll-numerator zeros.

For $T_\varphi/T_R > 1$, (a) the roll-subsidence and spiral modes couple and break off the real axis, sometimes in a quasi-circular path back to the real axis and thence to $-\infty$ and $-1/T_\varphi$, and sometimes to the roll-numerator zeros, and (b) the Dutch roll roots either go into the roll-numerator zeros along a counterclockwise path or form a quasi-circular segment to the real axis (and then to $-\infty$ and $-1/T_\varphi$).

(c) *The* $(1/T_\varphi\omega_n)[(1/T_R\omega_n) - 2\zeta]$ *Influence Parameter*—This "influence" parameter is of some consequence when $T_\varphi/T_R > 1$. The ω_n and ζ refer to either $\omega_{\varphi a}$ and $\zeta_{\varphi a}$ or ω_d and ζ_d, whichever set represents the point closest to $1/T_\varphi$. The relative magnitude of the parameter compared with unity offers a crude and approximate classification device to separate the detailed locus interaction forms appearing at intermediate gains. When $T_\varphi/T_R > 1$, and

(1) $(1/T_\varphi\omega_n)[(1/T_R\omega_n) - 2\zeta] < 1$, (i.e., $\eta^2 > \nu^2$)

the Dutch roll roots will ordinarily go toward the real axis along a quasi-circular segment; the coupled spiral and roll-subsidence roots proceed to the roll-numerator zeros;

(2) $(1/T_\varphi\omega_n)[(1/T_R\omega_n) - 2\zeta] > 1$, (i.e., $\eta^2 < \nu^2$)

the Dutch roll roots will ordinarily move to the roll-numerator zeros and the coupled spiral and roll-subsidence will form a quasi-circular locus.

(d) *The Ratio of Roll-Numerator Frequency to Dutch Roll Frequency,* $\omega_{\varphi a}/\omega_d$—A ratio of $\omega_{\varphi a}/\omega_d$ less than unity is preferable in all cases and mandatory in some to retain stability at intermediate gains.

Examples of Competing Systems

The various forms of the controller-airframe transfer function given in the foregoing discussion indicate the possibility of setting up a number of competing systems. This possibility can best be demonstrated with a hypothetical example considering an airframe which initially has characteristics with certain common deficiencies from a single-sensor control viewpoint. By relating these shortcomings to the airframe configuration, certain changes in geometry can be investigated to determine their influence on the required controller. The competing systems can then be compared to determine possible advantages.

Consider the roll control of an airframe having very lightly damped Dutch roll and numerator modes, and having all other dynamic characteristics quite similar to those shown for Condition Ia of Fig. 4. Such a situation frequently arises in practical cases for flight conditions corresponding to high-altitude cruise operations. Since the assumed poor Dutch roll damping is lower than that shown in Fig. 4 (which corresponds to a $\zeta \doteq 0.1$), the root locus connecting the Dutch roll pole with the numerator zero will pass into the right half plane (negative damping) at fairly low open-loop gains. Closure of the roll loop at any gain whatever will *decrease* the damping of the Dutch roll mode which is already too low.

A conventional solution to such a problem is to add a yaw-rate-to-rudder loop to the controller, which, so far, consists of only the roll loop. With this auxiliary control, certain of the "augmented airframe" poles and zeros will shift to the left, as already noted in the discussion of the equivalent-derivative approach. The important displacements in this case are those for $\zeta_d\omega_d$ and $\zeta_\varphi\omega_\varphi$ (respectively, the Dutch roll and numerator dampings) which, for rudders with low rolling moments, will be about equal. If these roughly equal shifts are made sufficiently large, the resulting root locus loop shown for Condition Ia of Fig. 4 will always be in the left half plane. The complete closed-loop Dutch roll will then always be positively damped, even though the presence of the roll-numerator zero will reduce this damping somewhat depending on the roll gain employed.

As competition for the foregoing solution, it is pertinent to investigate the airframe configuration changes required to achieve a pole, zero relationship corresponding roughly to Condition Id of Fig. 4. If this could be simply accomplished, then as indicated by the root locus plot, the system would be stable for all roll-loop gains without requiring the auxiliary rudder loop. Furthermore, the Dutch roll damping could be considerably increased by proper choice of gain. The basic change required to achieve the desired approximate pole, zero configuration involves reducing, to less than unity, the ratio of

$$\left(\frac{\omega_\varphi}{\omega_d}\right)^2 \doteq 1 - \frac{N_{\delta_a}' L_\beta'}{L_{\delta_a}' N_\beta'} \doteq 1 - \frac{[(C_{n_{\delta_a}}/C_{l_{\delta_a}}) + (I_{xz}/I_x)][(C_{l_\beta}/C_{n_\beta}) + (I_{xz}/I_z)]}{[1 + (I_{xz}/I_x)(C_{l_\beta}/C_{n_\beta})]} \tag{32}$$

In the root locus plot of Fig. 4, the value of $(\omega_\varphi/\omega_d)^2$ corresponding to Condition (a), the original configuration, is about 1.25, whereas a more desirable value, corresponding to Condition (d), is approximately 0.6. In setting up the airframe characteristics for the original example, factors which contributed strongly to the resulting poorly damped Dutch roll were a highly effective dihedral (large negative C_{l_β}) and a moderately low (but negative) value of I_{xz}. The influence of these parameters on the Dutch roll damping can be appreciated by converting the approximate expression of $2\zeta_d\omega_d$ given in Table 4 to basic terms—viz.,

$$2\zeta_d\omega_d \doteq -\frac{\rho S U_0}{2m}\left\{C_{y_\beta} + \frac{1}{2}\left(\frac{b}{k_z}\right)^2\left(C_{n_r} + \frac{I_{xz}}{I_x}C_{l_r}\right) - \frac{(I_z/I_x)(C_{l_\beta}/C_{n_\beta}) + (I_{xz}/I_x)}{1 + (I_{xz}/I_x)(C_{l_\beta}/C_{n_\beta})} \times \left[C_L - \frac{1}{2}\left(\frac{b}{k_z}\right)^2\left(C_{n_p} + \frac{I_{xz}}{I_x}C_{l_p}\right)\right]\right\} \tag{33}$$

With C_{n_β} positive (which is normally the case and is indicated by the moderately large value of ω_d) and referring to Eq. (32), the last numerator bracket will be negative and the denominator bracket positive. Since $\omega_\varphi/\omega_d > 1$ for this example, it follows that the term $(C_{n_{\delta_a}}/C_{l_{\delta_a}} + I_{xz}/I_x)$ must be positive. Since I_{xz}/I_x is negative, this means that $C_{n_{\delta_a}}/C_{l_{\delta_a}}$ must be positive and larger numerically than I_{xz}/I_x. The original configuration is thus seen to involve favorable aileron yawing moments (e.g., corresponding to inboard ailerons),† high effective dihedral, and a low positive inclination of the principal axis (low negative I_{xz}) for the given flight situation.

To reduce ω_φ/ω_d to the desired value it is clear that a change in sign must be effected for the term, $C_{n_{\delta_a}}/C_{l_{\delta_a}} + I_{xz}/I_x$. Decreasing, but maintaining positive, dihedral would not accomplish the desired reduction since, as $C_{l_\beta} \to 0$, $\omega_\varphi/\omega_d \to 1$. Also a reduction in effective dihedral may not be actually possible since a major portion of C_{l_β} may be due to effects other than those associated with geometric dihedral. There are then two possible basic configuration changes which can be made. These are associated with either (1) increasing the negative value of I_{xz}, or (2) making $C_{n_{\delta_a}}$ more negative. The first involves raising the principal axis of inertia; the second involves either moving ailerons outboard or coupling them to the rudder.

† Inboard ailerons tend to violate one of the conditions of validity required for Eq. (32) since such an arrangement usually creates $Y_{\delta a}$* terms due to sidewash effects. The errors involved can be checked in detail on the basis of the rudder approximation (Table 6) which includes all effectiveness terms (L_δ, N_δ, and Y_δ*). In the specific numerical case later considered these errors are small, so Eq. (32) is retained for simplicity.

TABLE 7
Variation of $(\omega_\varphi/\omega_d)^2$ With Stability Parameters for a Hypothetical Case

Basic Configuration	$\frac{I_z}{I_x} = 9$; $\frac{C_{l_\beta}}{C_{n_\beta}} = -5$; $\frac{I_{xz}}{I_x} = \left(1 - \frac{I_z}{I_x}\right)\alpha + 0.40$		
Case	1	2	3
$\left(\frac{\omega_\varphi}{\omega_d}\right)^2$	1.25	.60	.60
α-rad.	.071	.121	.071
$\frac{I_{xz}}{I_x}$	-.17	-.57	-.17
$\frac{C_{n_{\delta_a}}}{C_{l_{\delta_a}}}$	+.26	+.26	+.02

To give a better appreciation for the magnitude of the changes involved, consider the numerical values given in Table 7. As indicated by the table, the desired change in the character of the root locus for the hypothetical example can be accomplished by either (1) increasing the principal axis flight attitude by 0.05 radian (about 3°) (a) through a decrease in wing incidence, or (b) through a mass redistribution effort; or (2) decreasing the favorable aileron yaw to approximately zero (or less) by (a) shifting ailerons outboard, or (b) cross-feeding aileron signal to rudder.

The elements for optimizing the airframe and roll-control system are now present in that a total of five competing arrangements have been set up as possible solutions to the basic problem. These all involve the basic equalized-roll-to-aileron loop and (1) the original airframe plus a yaw-rate-to-rudder loop, (2) the original airframe plus an aileron cross-feed to rudder, (3) the original airframe with modified mass distribution to achieve $\Delta I_{xz}/I_z = -0.40$, (4) the original airframe with wing incidence reduced approximately 3° to achieve $\Delta I_{xz}/I_z = -0.40$, and (5) the original airframe with ailerons shifted to an outboard position.

Since, in this crude example, no attention has been paid to considerations other than the improvement of closed-loop Dutch roll damping, the competing systems may not be equivalent when all modes of dynamic performance are considered. This reservation applies particularly to the possible adverse effects of sensor and actuator dynamics, which have been completely neglected, and to various steady-state problems. Despite these reservations, the competition appears to be valid from a system-synthesis standpoint. The basic choice of one or the other of the foregoing solutions must then depend on the optimization criteria employed and the physical implications of the various possibilities in regard to performance, weight, reliability, cost, etc. For example, if weight, reliability, complexity, maintainability, or cost were the most important optimiz-

ation criteria for the example noted, the two competing systems requiring a rudder axis of control would almost certainly be put into an unfavorable position relative to the three possibilities where control by aileron alone could be sufficient.

Preliminary Design Implications

The case outlined above is, of course, intended to serve only as an example of the advantages acquired in problems concerning the airframe-controller system simply by considering possible airframe alterations. Many other considerations leading to potential system simplification and optimization can be deduced by carrying out procedures similar to that used above for other system types, and then combining the analytical operations with detailed examination of the airframe transfer functions. For example, possibilities for tailoring the airframe element include:

(1) Airframe basic geometry changes to modify such parameters as N_β', L_β', and M_a, thereby influencing controller static and dynamic requirements as well as affecting numerator characteristics such as the ω_φ/ω_d ratio discussed previously.

(2) Selection of appropriate control-application points and magnitudes—i.e., the various control arms (both positive and negative) and effectiveness—to obtain favorable airframe transfer characteristics from the standpoint of control.

(3) Attempts to attain favorable airframe mass-distribution characteristics, particularly in I_{zz}, which has a profound effect on both numerator and denominator terms.

(4) Selection of sensor orientation and location within the structure to obtain favorable effects that would otherwise require complex controller-equalization procedures—e.g., use of tilt in lateral gyros—or placement of accelerometers near the center of percussion.

Full utilization of these and other possibilities requires the basic understanding sought, and hopefully advanced, by the work reported here. In addition it requires concerted, systematic teamwork between the stability and control aerodynamicist and the flight control designer at the earliest possible stage of preliminary design.

References

[1] *Dynamics of the Airframe*, Northrop Aircraft, Inc., BuAer Report AE-61-4 II, September, 1952.

[2] Tsu, C. N., *A Note about the Effects of Product of Inertia on Lateral Stability*, Journal of the Aeronautical Sciences, Vol. 21, No. 7, p. 496, July, 1954.

[3] Ashkenas, I. L., and McRuer, D. T., *Approximate Airframe Transfer Functions and Application to Single Sensor Control Systems*, WADC Technical Report 58-82, ASTIA Document No. AD 151 025, June, 1958.

[4] Klemin, A., Pepper, P. A., and Wittner, H. A., *Longitudinal Stability in Relation to the Use of an Automatic Pilot*, NACA TN 666, 1938.

[5] Imlay, F. H., *A Theoretical Study of Lateral Stability with an Automatic Pilot*, NACA Report No. 693, 1940.

[6] Kusters, N. L., and Moore, W. J. M., *A Generalization of the Frequency Response Method for the Study of Feedback Control Systems*, Tustin, A., "Automatic and Manual Control"; Academic Press, Inc., New York, 1952.

[7] Evans, W. R., *Control-System Dynamics*, McGraw-Hill Book Co., Inc., New York, 1954.

[8] Banerjee, H., and Higgins, T. J., *Root Locus Delineations for Higher-Order Servomechanisms*, Proceedings of the National Electronic Conference, Vol. 13, pp. 520–536, 1957.

Viscous Aerodynamic Characteristics in Hypersonic Rarefied Gas Flow

(*Continued from page 192*)

63, Vol. III, *High Speed Aerodynamics and Jet Propulsion*, Princeton University Press, Princeton, N.J., 1958.

[23] Fay, J. A., Riddell, F. R., and Kemp, N. H., *Stagnation Point Heat Transfer in Dissociated Air Flow*, Jet Propulsion, Vol. 27, No. 6, pp. 672–674, June, 1957.

[24] Kemp, N. H., *Vorticity Interaction at an Axisymmetric Stagnation Point in a Viscous Incompressible Fluid*, Journal of the Aero/Space Sciences, Vol. 26, No. 8, pp. 543–544, August, 1959.

[25] Oguchi, H., *Hypersonic Flow Near the Forward Stagnation Point of a Blunt Body of Revolution*, Journal of the Aero/Space Sciences, Vol. 25, No. 12, pp. 789–790, December, 1958. Also see Rpt. No. 337, Aeronautical Research Institute, Univ. of Tokyo, Tokyo, Japan, November, 1958.

[26] Sedov, L. I., Michailova, M. P., and Chernyi, G. G., *On the Influence of Viscosity and Heat Conduction on the Gas Flow Behind a Strong Shock Wave*, Vestnik Moskovskovo Universiteta, No. 3, 1953, pp. 95–100, translated by R. F. Probstein as WADC TN No. 59-349, Div. of Eng., Brown University, Providence, R. I., October, 1959.

[27] Hoshizaki, H., *Shock-Generated Vorticity Effects at Low Reynolds Numbers*, Report No. LMSD-48381, Vol. I, pp. 9–43, Lockheed Aircraft Corp., Missiles and Space Div., January, 1959.

Heat Conduction in a Melting Slab†

STEPHEN J. CITRON*
Columbia University

Summary

The behavior, after the initiation of melting, of a slab insulated on one side and subjected to a heat input varying arbitrarily with time on the other is studied. A method of successive approximations is developed which requires the solution of an ordinary nonlinear differential equation; this equation is readily solved numerically on a desk calculator. Since any heat input is permitted, solutions by this method may be used to match conditions resulting from the aerodynamic heating problem. Curves of melt-thickness versus time are presented for a constant heat input and for a typical heat input incurred by a body descending through the atmosphere.

Symbols

x	= space variable
t	= time variable
k	= thermal conductivity
c	= specific heat
ρ	= density
κ	= $k/\rho c$, thermal diffusivity
L	= latent heat of melting
l	= slab length
$Q(t)$	= heat flux
Q_0	= reference value of the heat flux
$T_0(x, t)$	= premelting slab temperature distribution
$T(x, t)$	= slab temperature distribution after melting has begun
T^*	= melting temperature
t^*	= time at which melting begins
t_l	= time for slab to melt completely
$s(t)$	= position of solid boundary after melting has begun (amount of material melted)
S	= s/l, nondimensional form of s
z	= $(x - s)/l$, nondimensional space variable
τ	= $\kappa(t - t^*)/l^2$, nondimensional time variable
τ_l	= nondimensional time after melting has begun at which slab is completely melted
$(\tau_l)_a$	= approximate value of τ_l obtained from solution
θ	= T/T^*, nondimensional temperature variable
$2M/\pi^{1/2}$	= cT^*/L, ratio of heat content at melting temperature to latent heat of melting
r	= kT^*/lQ_0, ratio of heat flux kT^*/l to reference value of the heat input flux Q_0.
$'$	= $\partial/\partial z$
$\dot{S}$	= $\partial S/\partial_\tau$
$\dot{s}$	= $\partial s/\partial t$

Presented at the Thermal Stress Session, IAS 27th Annual Meeting, N.Y., Jan. 26–29, 1959. Revised and received September 8, 1959.

† This paper is based on a thesis submitted in partial fulfillment of the requirements for the degree of Doctor of Philosophy, in the Faculty of Pure Science, Columbia University. The author would like to express his appreciation to Professor Bruno A. Boley, his thesis adviser, for the advice and assistance received during the course of this investigation. The work is part of a project supported by the Office of Naval Research.

* Formerly, Research Assistant, Institute of Flight Structures, Columbia University. Now, Assistant Professor, Division of Engineering Sciences, Purdue University.

Introduction

In recent years, since the advent of hypersonic missile flight, the so-called "re-entry" problem has been given an increasing amount of study, among the most important aspects of which has been that concerned with the reduction of structural damage caused by aerodynamic heating. To accomplish this protection a variety of design methods have been discussed in the literature and used in practice; these include, for example, the use of heat sinks,[1] of transpiration cooling[2] and of mass-transfer cooling.[3] An accurate analysis of the latter two methods would treat the interaction of a gaseous region, a liquid region, and a finite solid region. Since the rate at which the liquid is formed is not necessarily equal to the rate at which it is swept away by the flowing gas, the dimensions of these regions will vary with time and, thus, ablation of the melt formed is an important part of the total problem. The question of ablation will occupy our attention in this investigation.

The classical work in heat conduction contains many references[4–10] to moving (free) boundary problems, often called Stefan problems. It should be noticed that in all these examples the overall dimensions of the material under consideration remained constant while a phase-change front moved through the material—that is, no ablation was assumed to occur. In addition, in the solutions of the above problems the methods used do not permit arbitrary initial temperature distributions prior to melting; this must, however, be allowed in the ablation problem to account for the heating history before melting begins.

The earliest work relating to ablation which overcomes these difficulties is that of Landau[11] who studied in detail the case of a melting or sublimating semi-infinite solid under constant heat input. Under the assumption of total instantaneous removal of the liquid or gas formed, curves of thickness melted and melting rate versus time were obtained numerically by digital computer over a complete range of physical parameters. The assumption of total ablation implies that the protective effect of the actual liquid region adjoining the solid body will be small—i.e., the heat input to the body will not have been reduced in passing through the liquid.

The conditions under which this assumption is valid have been studied by Goodman[12] who discusses ana-

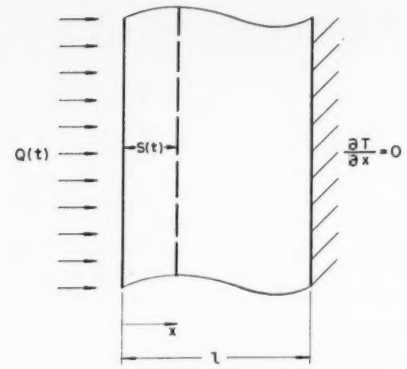

FIG. 1. Slab geometry.

lytically, under certain restrictions, the ablation due to aerodynamic heating. The major restrictions introduced are that the liquid have a Prandtl number which is small compared to unity, that the ratio of melt thickness to boundary-layer thickness be small compared to unity, that the solid region be semi-infinite in extent and that its temperature be held constant at its melting value.

In reference 13, Sutton solves a similar problem, by use of a REAC differential analyzer, without some of the restrictions which were required in the analytical work of Goodman; the solid is, however, still semi-infinite in extent. A solution is obtained for a glass of high Prandtl number and the results are compared with those of Landau. For the particular example solved it is shown that only 70 per cent of the energy arriving at the gas-liquid interface reaches the solid body. Conversely, it is indicated that, for liquids with low Prandtl numbers, the shielding effect of the molten film is much smaller and may therefore be usually neglected in general. In the latter case the assumption made by Landau of instantaneous ablation is thus justified.

As has been mentioned, in the work on ablation of Landau and the related work of Goodman and Sutton it was assumed that the solid material was semi-infinite in extent. This assumption, however, will lead to melting rates that are too slow—i.e., not conservative—because of the finite dimensions of the actual structure. The present investigation concerns itself with heat conduction in a melting slab. The behavior, after the initiation of melting, of a slab insulated on one side and subjected to a heat input varying arbitrarily with time on the other is studied. A method of successive approximations is developed and solutions are obtained through use of a desk calculator which permit an arbitrary initial temperature distribution (to account for the heating history prior to melting) and an arbitrary heat input (to match conditions arising from the aerodynamic problem). Solutions for a constant heat input and for a typical heat input incurred by a body descending through the atmosphere are obtained.

Formulation and General Properties of the Solution

Consider the slab of thickness l shown in Fig. 1, insulated at $x = l$ and subjected to a net heat input $Q(t)$ at $x = 0$. We will let $t = t^*$ be the time at which the temperature at $x = 0$ reaches the melting value T^*, while the interior temperature at this time will be $T_0(x, t^*)$. $T_0(x, t)$ denotes the solution to the heat conduction problem in the slab prior to melting ($0 < t < t^*$) obtained from the heat conduction equation:

$$\kappa\, \partial^2 T_0(x, t)/\partial x^2 = \partial T_0(x, t)/\partial t, \quad 0 < x < l \qquad (1)$$

under the conditions

$$\left.\begin{aligned} &\text{(a)} \quad Q(t) = -\left.\frac{k\partial T_0}{\partial x}\right|_{x=0} \\ &\text{(b)} \quad \left.\frac{\partial T_0}{\partial x}\right|_{x=l} = 0 \\ &\text{(c)} \quad T_0(x, 0) = 0 \end{aligned}\right\} \qquad (2)$$

The first condition gives the heat input to the slab at $x = 0$, the second requires the slab to be insulated at $x = l$, while the third condition prescribes the initial temperature distribution, taken here to be zero.

Since one face of the slab is insulated the addition of more and more heat will eventually cause the slab to melt. After melting has begun, the position of the hot face is no longer fixed but will be an unknown function of time which must be determined and, hence, gives rise to a floating boundary value problem. The position of the solid boundary after melting has begun will be denoted by $x = s(t)$ while the temperature at this boundary is held fixed at the melting temperature T^*.

Mathematically the problem may be formulated in the following manner for the post-melting period, $t > t^*$, $s > 0$:

$$\kappa\, \partial^2 T(x, t)/\partial x^2 = \partial T_0(x, t)/\partial t, \quad s(t) < x < l \qquad (3)$$

with conditions

$$\left.\begin{aligned} &\left.\begin{aligned} &\text{(a)}\ Q(t) = -(k\partial T/\partial x) + \rho L\dot{s} \\ &(b)\ T(x, t) = T^* \end{aligned}\right\} \quad x = s(t) \\ &(c)\ \partial T(x, t)/\partial x|_{x=l} = 0 \\ &\text{(d)}\ T(x, t^*) = T_0(x, t^*) \\ &\text{(e)}\ s(t^*) = 0 \end{aligned}\right\} \qquad (4)$$

The first three are boundary conditions which provide (a) that a part of the incoming heat at the melting boundary enter the solid while the remainder go toward overcoming the latent heat of melting L, (*b*) that the melting temperature exist at the melting face, and (c) that the slab be insulated at the other face. The last two are initial conditions which provide (d) that the temperature be continuous when melting begins, and (e) that the solid be of length l at this time.

The presence of the moving boundary $s(t)$ thus introduces an additional unknown which necessitates three boundary conditions (4a, b, c) and two initial conditions (4d, e) in place of the two boundary conditions (2a, b) and one initial condition (2c) of the premelting

problem. Certain general results can be immediately obtained from Eqs. (3) and (4a–e), and will now be discussed.

(a) We see from (4a) that if $Q(t)$ is to be continuous at $t = t^*$ the melting rate $s(t^*)$ must, in general, vanish — i.e., $s(t^*) = 0$; $L \neq 0$. In the special case, however, where the latent heat is identically zero, a finite initial melting rate will not disturb the continuity of $Q(t)$ at $t = t^*$.

(b) As the surface at $x = l$ is insulated the addition of heat to the slab will eventually cause it to melt completely; the time† (t_l) at which this occurs may be derived from the set of Eqs. (3) and (4a–e) as follows. We proceed by integrating both sides of (4a) between t^* and t, with the result

$$\int_{t^*}^{t} Q(\beta)d\beta = -\int_{t^*}^{t} k\ \partial T(s,\beta)/\partial x d\beta + \rho L s(t)$$

The first term on the right may be rewritten using the fact that

$$-k\ \partial T(s,t)/\partial x = (\partial/\partial t)\left[\int_{s(t)}^{l} \rho c T(x,t)dx + \rho c\ T^*\ s(t)\right]$$

obtained by integrating Eq. (3) between $s(t)$ and l, taking the derivative with respect to time outside the integral and using conditions (4b, c, e).

One then has

$$\int_{t^*}^{t} Q(\beta)\ d\beta = \int_{t^*}^{t} (\partial/\partial\beta)\left[\int_{s(\beta)}^{l} \rho c\ T(x,\beta)dx + \rho c\ T^* s(\beta)\right]d\beta + \rho L\, s(t)$$

which upon integration yields

$$\int_{t^*}^{t} Q(\beta)\ d\beta = \rho\ s(t)[L + cT^*] + \int_{s(t)}^{l} \rho c\ T(x,t)\ dx - \int_{0}^{l} \rho c\ T_0(x,t^*)\ dx \quad (5)$$

As $s \to l$; i.e., complete melting of the slab is approached; we obtain

$$\int_{t^*}^{t_l} Q(\beta)\ d\beta = \rho l\ [L + cT^*] - \int_{0}^{l} \rho c\ T_0(\zeta, t^*)\ d\zeta \quad (6)$$

from which, for any $Q(t)$ the melting time may be computed. For the particular case in which $Q(t) = Q_0$, a constant, Eq. (6) reduces to

$$t_l = t^* + \rho l\{[L + cT^*]/Q_0\} - (1/Q_0)\int_{0}^{l} \rho c\ T_0(\zeta, t^*)\ d\zeta \quad (7)$$

An expression for t^* may be derived in a similar manner from a heat balance for the premelting period $0 < t < t^*$ resulting in

$$\int_{0}^{t^*} Q(\beta)\ d\beta = \int_{0}^{l} \rho c\ T_0(\zeta, t^*)\ d\zeta$$

for arbitrary heat inputs and

$$t^* = (1/Q_0)\int_{0}^{l} \rho c\ T_0(\zeta, t^*)\ d\zeta$$

for a constant heat input, Q_0. Hence, the total time required for a slab to melt completely under a constant heat input is given by

$$t_l = \rho l\{[L + cT^*]/Q_0\} \quad (8)$$

(c) To ensure that the temperature in the interior nowhere exceeds T^* the temperature gradient at $x = s(t)$ must be negative or at most zero, $\partial T(s,t)/\partial x \leqslant 0$. From Eq. (4a) we see that this implies for a positive heat input the relation

$$\dot{s} \leqslant Q(t)/\rho L \quad (9)$$

Since the gradient at the front face approaches zero as $s \to l$ we see that the equality holds at $t = t_l$. Further, if $Q(t) > 0$, the melting rate will have its maximum value at $t = t_l$.

(d) The solution of the postmelting problem for the limiting case $M = 0$; i.e., an infinite latent heat of melting; has not been presented here because of space limitations but could be obtained in a manner analogous to that of reference 11. For the other limiting case $M = \infty$; i.e., no latent heat of melting; the initial melting rate has been found to be not zero but

$$S(0) = r\left.\frac{\partial^2\theta}{\partial z^2}\right|_{x=0}$$

where the symbols are defined below.

We will now present the problem in a nondimensional form. For the postmelting period it is convenient to change the independent variables from x and t to z and τ.

$$z = [x - s(t)]/l, \quad \tau = (\kappa/l^2)(t - t^*) \quad (10a)$$

We thus see that when $x = s(t)$, $z = 0$, and, hence, this transformation fixes the melting boundary. The transformation in time is used to shift the time scale so that it is zero when melting starts, therefore $\tau > 0$ after melting has begun. The nondimensional temperature and the nondimensional melt parameter are defined to be

$$\theta(z,\tau) = T(z,\tau)/T^*, \quad S(\tau) = s(\tau)/l \quad (10b)$$

respectively. The only physical parameters which will appear in the solution of the problem are the quantities M and r given here.

$$M = (\pi^{1/2}/2)(cT^*/L), \quad r = kT^*/lQ_0 \quad (11)$$

The parameter M may be interpreted physically as the ratio of the heat per unit volume required to raise the solid to the melting temperature to the latent heat of melting. The numerical constant $\pi^{1/2}/2$ in M was included for consistency with reference 11. The quantity Q_0 in r is a reference value of the heat input.† In

† This was first obtained by Landau[11] using Gauss' theorem on the heat conduction equation in the x, t plane.

† If $Q(\tau)|_{t=0} = 0$ some other reference value may be taken without affecting the discussion.

what follows it will be convenient to take

$$Q_0 = Q(\tau)\big|_{\tau=0} \neq 0$$

Our problem then requires the determination of the temperature $\theta(z, \tau)$ in the solid and the position of the moving free boundary $S(\tau)$.

In terms of these quantities, Eqs. (3) and (4a–e) become by direct substitution Eqs. (12) and (13a–e), respectively, with corresponding physical interpretations.

$$\partial^2\theta(z, \tau)/\partial z^2 + \dot{S}\,\partial\theta(z, \tau)/\partial z = \partial\theta(z, \tau)/\partial\tau, \quad 0 < z < 1 - S \tag{12}$$

with conditions

$$\left.\begin{array}{ll} \text{(a)} & \dfrac{Q(\tau)}{Q_0} = -r\left.\dfrac{\partial\theta}{\partial z}\right|_{z=0} + \dfrac{\pi^{1/2}}{2}\dfrac{r}{M}\dot{S} \\ \text{(b)} & \theta(0, \tau) = 1 \\ \text{(c)} & \partial\theta(1 - S, \tau)/\partial z = 0 \\ \text{(d)} & \theta(z, 0) = T_0(x, t^*)/T^* \\ \text{(e)} & S(0) = 0 \end{array}\right\} \tag{13}$$

The nondimensional equivalent of Eq. (9) is then

$$\dot{S} \leqslant (2M/\pi^{1/2}r)[Q(\tau)/Q_0] \tag{14}$$

We shall denote by $\tau_l = (\kappa/l^2)(t_l - t^*)$ the dimensionless time after melting has begun at which the slab has been completely melted away. In the case where $Q(\tau) = Q_0$, a constant, for $\tau > 0$ we obtain

$$\tau_l = r + (\pi^{1/2}/2)(r/M) - \int_0^1 [T_0(\zeta, t^*)/T^*]\,d\zeta \tag{15}$$

by putting Eq. (7) in nondimensional form.

Method of Solution

To obtain the general solution it is useful to represent our nondimensional temperature $\theta(z, \tau)$ in the following form:

$$\theta(z, \tau) = [T_0(z, t^*)/T^*] - [T_0'(1 - S, t^*)/T^*]\varphi(z, \tau) \tag{16}$$

where prime indicates $\partial/\partial z$ and $\varphi(z, \tau)$ is now a new dependent variable. The reason for this change will become apparent as we proceed. Substituting Eq. (16) into Eqs. (12) and (13a–e) we obtain the equation and conditions which must be satisfied to determine $\varphi(z, \tau)$, hence the temperature, and $S(\tau)$, hence the amount of material melted. They are given below, each one corresponding in physical interpretation to that of Eq. (3) and conditions (4a–e) which are listed in the same order and from which they stem:

$$\frac{\partial^2\varphi}{\partial z^2} + \dot{S}\frac{\partial\varphi}{\partial z} - \frac{(\partial/\partial\tau)T_0'(1 - S, t^*)\,\varphi}{T_0'(1 - S, t^*)} = \frac{\partial\varphi}{\partial\tau} + \frac{T_0''(z, t^*)}{T_0'(1 - S, t^*)} + \frac{\dot{S}T_0'(z, t^*)}{T_0'(1 - S, t^*)} \tag{17}$$

and

$$\left.\begin{array}{ll} \text{(a)} & Q(\tau)/Q_0 = (\pi^{1/2}/2)(r/M)\dot{S} - (r/T^*)[T_0'(0, t^*) - T_0'(1 - S, t^*)\varphi'(0, \tau)] \\ \text{(b)} & \varphi(0, t) = 0 \\ \text{(c)} & \partial\varphi(1 - S, \tau)/\partial z = 1 \\ \text{(d)} & \lim_{\tau\to 0} T_0'(1 - S, t^*)\varphi(z, \tau) = 0 \\ \text{(e)} & S(0) = 0 \end{array}\right\} \tag{18}$$

Eqs. (17) and (18a–e) represent a nonlinear problem which we are unable to treat in an exact analytical manner. The alternatives exist of using either high-speed computers or of finding an approximate solution; the latter course was chosen here. The problem is particularly suited to finding an approximate solution since certain relations (14), (15) have already been derived which the exact solution must obey; the degree to which they are satisfied by the approximate solution can then serve as a check on its accuracy. To review, relation (14) gives the melting rate which occurs when $s = l$ (complete melting of the slab) while relation (15) gives the time after melting begins at which the slab is completely melted away.

On examining Eqs. (17) and (18) we note that at $z = 0$ the function φ does not vary and hence $\partial\varphi/\partial\tau\big|_{z=0} = 0$. Since at the critical surface where melting actually takes place $\partial\varphi/\partial\tau$ is identically zero, an examination of Eq. (17) suggests that we neglect this term in the equation during a first attempt at an approximate solution. If this is done τ will no longer appear as an independent variable in the equation but will then only occur implicitly as a parameter. Consistent with this, we note further that on the boundaries of the region $0 < z < 1 - S$ the function φ satisfies two time independent conditions (18b, c). By neglecting $\partial\varphi/\partial\tau$ in Eq. (17) a linear second-order equation in z results which may be used to satisfy these conditions. The equation in question is

$$\frac{\partial^2\varphi}{\partial z^2} + \dot{S}\frac{\partial\varphi}{\partial z} - \frac{(\partial/\partial\tau)T_0'(1 - S, t^*)\varphi}{T_0'(1 - S, t^*)} = \frac{T_0''(z, \tau)}{T_0'(1 - S, t^*)} + \frac{\dot{S}T_0'(z, t^*)}{T_0'(1 - S, t^*)} \equiv F_0(z, \tau), \quad 0 < z < 1 - S, \quad \tau > 0 \tag{19}$$

The solution [satisfying conditions (18b, c)] of this linear second-order differential equation may be obtained in general using the method of variation of parameters and is shown next. It will usually prove easier, however, to solve particular cases directly rather than to substitute into this general solution.

$$\varphi(z, \tau) = G[e^{\lambda_1 z} - e^{\lambda_2 z}] - e^{\lambda_1 z}\int_0^z \frac{F_0(\alpha, \tau)\,e^{-\lambda_1\alpha}}{(\lambda_2 - \lambda_1)}\,d\alpha + e^{\lambda_2 z}\int_0^z \frac{F_0(\alpha, \tau)e^{-\lambda_2\alpha}}{(\lambda_2 - \lambda_1)}\,d\alpha \tag{20}$$

where

$$\lambda_{1,2} = -\frac{\dot{S}}{2} \pm \left\{\frac{\dot{S}^2}{4} + \frac{(\partial/\partial\tau)T_0'(1 - S, t^*)}{T_0'(1 - S, t^*)}\right\}^{1/2} \tag{21}$$

and

$$G = \frac{1}{[1 - (\lambda_2/\lambda_1)e^{(\lambda_2-\lambda_1)(1-S)}]} \times \left\{\int_0^{1-S} \frac{F_0(\alpha, \tau)e^{-\lambda_1\alpha}}{(\lambda_2 - \lambda_1)}\, d\alpha - \frac{\lambda_2}{\lambda_1} e^{(\lambda_2-\lambda_1)(1-S)} \times \int_0^{1-S} \frac{F_0(\alpha, \tau)e^{-\lambda_2\alpha}}{(\lambda_2 - \lambda_1)}\, d\alpha + \frac{e^{-\lambda_1(1-S)}}{\lambda_1}\right\} \quad (22)$$

We shall denote by φ_1 the first approximation given above by the solution of Eq. (19), to the function φ. An improved solution may be obtained by forming $\partial\varphi_1/\partial\tau$, now a known function of $(z, S, \dot{S})$, and placing it in the inhomogeneous right-hand side of Eq. (17). In general, the ith approximation to the function φ will be obtained by solving the equation

$$\frac{\partial^2\varphi_i}{\partial z^2} + \dot{S}\frac{\partial\varphi_i}{\partial z} - \frac{(\partial/\partial\tau)T_0'(1 - S, t^*)}{T_0'(1 - S, t^*)}\varphi_i \times \frac{\partial\varphi_{i-1}}{\partial\tau} + \frac{T_0''(z, \tau)}{T_0'(1 - S, t^*)} + \frac{\dot{S}T_0'(z, t^*)}{T_0'(1 - S, t^*)} \equiv F_{i-1}(z, \tau), \quad i = 2, 3, \ldots \quad (23)$$

satisfying conditions (18b, c). This solution could again be written in general by the method of variation of parameters and would correspond in form to Eqs. (20)–(22).

The process for approximating φ may be carried as far as is desirable. Note that the function φ_i determined in this manner is still expressed in terms of $S(\tau)$ and its derivatives and that one boundary condition (18a) remains to be satisfied. When the desired approximation has been obtained the remaining boundary condition (18a) yields a nonlinear ordinary differential equation for the determination of $S(\tau)$.

To summarize, instead of solving the original nonlinear partial differential Eq. (17) our problem for determining the temperature in the solid and the amount of material melted at any time has been reduced to finding the solution of two ordinary differential equations as follows: (1) the determination of $\varphi_i(z, \tau)$ in terms of $S(\tau)$ and its derivatives to the desired degree of accuracy from a linear ordinary second-order differential equation in z, and (2) the determination of $S(\tau)$ from the nonlinear ordinary differential equation resulting from satisfying the third and last boundary condition (18a). It should be emphasized that in finding the solution of Eq. (23) the aid of high-speed computers is not needed. The method developed in this paper has the utility of readily providing accurate approximate solutions using only a desk computer.

We will use this method to find $S(\tau)$ for two heat inputs, the first constant and the second corresponding to that which might be encountered by a body descending through the atmosphere. The constant heat input example will first be used to discuss the accuracy of the method by comparing several approximations with each other and with the exact relations (14) and (15).

Example I—Constant Heat Input

The premelting $(0 < t < t^*)$ temperature distribution in a slab $(0 < x < l)$ under a constant heat input Q_0 at $x = 0$ and insulated at $x = l$ is[14]

$$T_0(x, t) = \frac{Q_0 l}{k}\left\{\frac{\kappa t}{l^2} + \frac{3x^2 - 6xl + 2l^2}{6l^2} - \frac{2}{\pi^2}\sum_{1,2}^{\infty}\frac{e^{(-n^2\pi^2\kappa t)/l^2}}{n^2}\cos\frac{n\pi x}{l}\right\}$$

To obtain the postmelting solution we proceed in the manner shown in the previous section. However, for simplicity of illustration we shall assume that quasi-steady conditions have been achieved before the initiation of melting in which case the exponential terms may be neglected, though clearly this assumption is by no means essential to the use of the method. Expressed in the nondimensional variables of Eqs. (10) and (11), we then have at $t = t^*$

$$T_0(z, t^*)/T^* = 1 + [(z^2 - 2z)/2r] \quad (24)$$

Corresponding to Eq. (15) we find the nondimensional time after melting has begun at which the slab has been completely melted away to be

$$\tau_l = (1/3) + (\pi^{1/2}/2)(r/M) \quad (25)$$

First Approximation

We will now find the first approximation for the general case of arbitrary M. We obtain from Eq. (24)

$$\frac{T_0'(1 - S, t^*)}{T^*} = -\frac{S}{r}, \quad \frac{(\partial/\partial\tau)T_0'(1 - S, t^*)}{T^*} = -\frac{\dot{S}}{r}$$

$$\frac{T_0'(z, t^*)}{T^*} = \frac{z - 1}{r}, \quad \frac{T_0''(z, t^*)}{T^*} = \frac{1}{r}$$

Using these relations in Eq. (16) our expression for the temperature then becomes

$$\theta(z, \tau) = 1 + [(z^2 - 2z)/2r] + (S/r)\varphi(z, \tau) \quad (26)$$

where the governing equation (19) for the first approximation to the function φ is

$$(\partial^2\varphi_1/\partial z^2) + \dot{S}(\partial\varphi_1/\partial z) - (\dot{S}/S)\varphi_1 = [(\dot{S} - 1)/S] - (\dot{S}/S)z \quad (27)$$

The solution of this equation for $\varphi_1(z, \tau)$ satisfying conditions (18b, c) is given by Eq. (20) or may be obtained directly as

$$\varphi_1(z, \tau) = A + z + C_1e^{\lambda_1 z} + C_2^{\lambda_2 z} \quad (28)$$

where

$$\left.\begin{aligned} \lambda_{1,2} &= -(\dot{S}/2) \pm \{(\dot{S}^2/4) + (\dot{S}/S)\}^{1/2} \\ A &= S - 1 + (1/\dot{S}) \\ C_1 &= \frac{(\lambda_2/\lambda_1)Ae^{(\lambda_2-\lambda_1)(1-S)}}{[1 - (\lambda_2/\lambda_1)e^{(\lambda_2-\lambda_1)(1-S)}]} \\ C_2 &= \frac{-A}{[1 - (\lambda_2/\lambda_1)e^{(\lambda_2-\lambda_1)(1-S)}]} \end{aligned}\right\} \quad (28a)$$

The equation resulting from substituting Eq. (28) into the remaining boundary condition (18a) for the

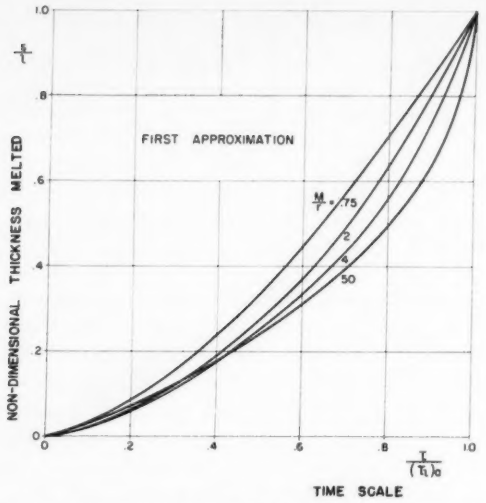

FIG. 2. Nondimensional curves of thickness melted versus time for a constant heat input. Normalized scales.

determination of $S(\tau)$ is

$$\frac{Q(\tau)}{Q_0} = 1 + \frac{\pi^{1/2}\tau}{2M}\dot{S} - S\left\{1 - \frac{\lambda_2 A[1 - e^{(\lambda_2-\lambda_1)(1-S)}]}{[1 - (\lambda_2/\lambda_1)e^{(\lambda_2-\lambda_1)(1-S)}]}\right\} \quad (29)$$

We can already verify at this state that one of the derived, auxiliary relations, Eq. (14), which must be satisfied by the exact solution is obeyed by the approximate one. Remembering that we are treating the case $Q(\tau) = Q_0$, it is evident that at $S = 1$ we obtain from Eq. (29) the velocity of melting

$$\dot{S}|_{s=1} = 2M/\pi^{1/2}\tau$$

which is the melting velocity required in the exact solution by relation (14).

Eq. (29) is easily solved numerically by desk computer. The procedure used was the following: if S is known at some time τ_i, the value of $\dot{S}(\tau_i)$ can be obtained from Eq. (29) with $Q(\tau_i) \equiv Q_0$; once the melting velocity $\dot{S}(\tau_i)$ has been obtained the value of S at a later time τ_{i+1} can be calculated using central differences—i.e., from

$$S(\tau_{i+1}) = S(\tau_{i-1}) + 2\Delta\tau\dot{S}(\tau_i) \quad (30)$$

The process is then continued until $S = 1$—i.e., complete melting has occurred.

This procedure is satisfactory everywhere except at $\tau = 0$ where it fails for the following reason. We note first that setting $S(\tau_i) = 0$ in Eq. (29) requires that $\dot{S}(\tau_i) = 0$ (for all $L \neq 0$) and hence, if $S(\tau_{i-1})$ also is zero, we find that $S(\tau) = 0$ for all $\tau \geq \tau_i$. Now since $S(\tau) = 0$ for $\tau \leq 0$ we have $\dot{S}(0) = 0$ [cf. Eq. (4)]; hence $S(\tau_i)$ will also equal zero, and therefore the result $S(\tau) = 0$ for $\tau \geq 0$ would follow. We must therefore start the numerical solution of this equation in a different way—namely, by finding an analytic solution which is valid in the neighborhood of $\tau = 0$. In this region it can be expected[11] that $S \leq \dot{S} \leq 1$. Under these assumptions Eq. (29) reduces to

$$Q(\tau)/Q_0 = 1 + (\pi^{1/2}/2)(\tau/M)\dot{S} - \{S/\dot{S}\}^{1/2}$$

which has as its solution for $Q(\tau) = Q_0$

$$S(\tau) = (2/\pi^{1/2})(M/\tau)[\tau^{3/2}/(3/2)^{3/2}] \quad (31)$$

a function which satisfies the assumptions just made on its behavior and that of its derivative in the neighborhood of the origin.

We can now see that the initial condition (18d) will be satisfied—i.e.,

$$\lim_{\tau\to 0} T_0'(1 - S, t^*)\varphi_1(z, \tau) = \lim_{\tau\to 0} S\varphi_1(z, \tau) = 0 \quad (32)$$

Eq. (31) can be taken to be the solution for $S(\tau)$ in the region $0 \leq \tau \leq \tau_1$. For $\tau \geq \tau_1$ the numerical procedure outlined above was employed.

The solutions obtained in this way from Eq. (29) for $S(\tau)$ are presented in Fig. 2 by curves of $S(\tau)$ versus $\tau/(\tau_l)a$ for $M/\tau = 0.75$, 2, 4, and 50; $(\tau_l)a$ denotes the approximate value of τ_l (nondimensional time after melting at which the slab is completely melted away) obtained by solving Eq. (29). A comparison is given in Fig. 3 between $(\tau_l)a$ and the exact value of τ_l [Eq. (25)] as a function of M/τ. The amount by which these differ is a measure of the accuracy of the approximate solution. It may be seen to be everywhere less than 15 per cent; in the range of greatest physical interest, namely, that of large M—i.e., a small latent heat of melting—the error is much less.

Second Approximation

The second approximation $\varphi_2(z, \tau)$ is obtained in the manner previously indicated. First,

$$\partial\varphi_1/\partial\tau = A + [\dot{C}_1 + \dot{\lambda}_1 C_1 z]e^{\lambda_1 z} + [\dot{C}_2 + \dot{\lambda}_2 C_2 z]e^{\lambda_2 z}$$

is obtained from Eq. (28) and substituted into Eq. (23). The resulting equation

$$(\partial^2\varphi_2/\partial z^2) + \dot{S}(\partial\varphi_2/\partial z) - (\dot{S}/S)\varphi_2 = [(\dot{S} - 1)/S] - (\dot{S}/S)z + \dot{A} + [\dot{C}_1 + \dot{\lambda}_1 C_1 z]e^{\lambda_1 z} + [\dot{C}_2 + \dot{\lambda}_2 C_2 z]e^{\lambda_2 z} \quad (33)$$

is then solved for $\varphi_2(z, \tau)$ yielding

$$\varphi_2(z, \tau) = \bar{A} + z + \bar{C}_1 e^{\lambda_1 z} + \bar{C}_2 e^{\lambda_2 z} + D_1 z^2 e^{\lambda_1 z} + D_2 z^2 e^{\lambda_2 z} + F_1 z e^{\lambda_1 z} + F_2 z e^{\lambda_2 z} \quad (34)$$

where

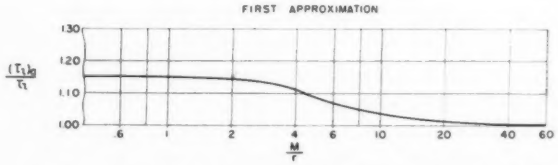

FIG. 3. The ratio of the approximate to the exact value of the nondimensional time after melting begins at which the slab is completely melted away versus the physical parameters occurring. Constant heat input.

$$\left.\begin{aligned}
\bar{C}_1 &= -(\lambda_2/\lambda_1)\bar{C}_2 e^{(\lambda_2-\lambda_1)(1-S)} - [(1-S)/\lambda_1]\{D_1[2+\lambda_1(1-S)] + \\
&\quad D_2[2+\lambda_2(1-S)]e^{(\lambda_2-\lambda_1)(1-S)}\} - (1/\lambda_1)\{F_1[1+\lambda_1(1-S)] + F_2[1+\lambda_2(1-S)]e^{(\lambda_2-\lambda_1)(1-S)}\} \\
\bar{C}_2 &= \frac{-1}{[1-(\lambda_2/\lambda_1)e^{(\lambda_2-\lambda_1)(1-S)}]}\left[\bar{A} + \frac{(1-S)}{\lambda_1}\{D_1[2+\lambda_1(1-S)] + D_2[2+\lambda_2(1-S)]\} + \right. \\
&\quad \left. \frac{1}{\lambda_1}\{F_1[1+\lambda_1(1-S)] + F_2[1+\lambda_2(1-S)]e^{(\lambda_2-\lambda_1)(1-S)}\}\right]
\end{aligned}\right\} \quad (35)$$

$$\begin{aligned}
D_1 &= -\lambda_1 C_1/2(\lambda_2-\lambda_1), \quad D_2 = \lambda_2 C_2/2(\lambda_2-\lambda_1) \\
F_1 &= -[\dot{C}_1/(\lambda_2-\lambda_1)] - [\lambda_1 C_1/(\lambda_2-\lambda_1)^2] \\
F_2 &= [\dot{C}_2/(\lambda_2-\lambda_1)] - [\lambda_2 C_2/(\lambda_2-\lambda_1)] \\
\bar{A} &= (S\ddot{S}/\dot{S}^3) - 1 + (1/\dot{S})
\end{aligned}$$

Corresponding to Eq. (29) for the first approximation, the equation for the determination of $S(\tau)$ is obtained by substituting Eq. (34) into Eq. (18a), resulting in

$$\begin{aligned}
\frac{Q(\tau)}{Q_0} &= 1 + \frac{\pi^{1/2}}{2}\frac{\tau}{M}\dot{S} - S + \frac{S[1-e^{(\lambda_2-\lambda_1)(1-S)}]}{[1-(\lambda_2/\lambda_1)e^{(\lambda_2-\lambda_1)(1-S)}]} \times \\
&\quad \{\lambda_2 A - (\lambda_2/\lambda_1)S(1-S)[D_1\{2+\lambda_1(1-S)\} + D_2\{2+\lambda_2(1-S)\}e^{(\lambda_2-\lambda_1)(1-S)}] - \\
&\quad (\lambda_2/\lambda_1)S[F_1\{1+\lambda_1(1-S)\} + F_2\{1+\lambda_2(1-S)\}e^{(\lambda_2-\lambda_1)(1-S)}]\} + S(1-S)[D_1\{2+\lambda_1(1-S)\} + \\
&\quad D_2\{2+\lambda_2(1-S)\}e^{(\lambda_2-\lambda_1)(1-S)}] + S[F_1\{1+\lambda_1(1-S)\} + F_2\{1+\lambda_2(1-S)\}e^{(\lambda_2-\lambda_1)(1-S)}] - S[F_1+F_2]
\end{aligned} \quad (36)$$

It is seen that at $S = 1$ the second approximation also results in the correct melting velocity

$$\dot{S}\big|_{s=1} = (2/\pi^{1/2})(M/\tau)$$

given in Eq. (14) for the exact solution.

We shall solve Eq. (36) numerically in the same general manner as Eq. (29) was solved. The only difference results from the fact that $\ddot{S}$ now appears in the equation along with S and $\dot{S}$ which occurred in the first approximation equation. We proceed as follows: knowing the value of S and $\dot{S}$ at some time τ_i the value of $\ddot{S}(\tau_i)$ was obtained by trial and error so as to satisfy Eq. (36) with $Q(\tau) = Q_0$. Once $\ddot{S}(\tau_i)$ had been obtained the value of S and $\dot{S}$ at some later time τ_{i+1} were calculated using central differences from

$$\left.\begin{aligned}
\dot{S}(\tau_{i+1}) &= \dot{S}(\tau_{i-1}) + 2\Delta\tau\,\ddot{S}(\tau_i) \\
S(\tau_{i+1}) &= S(\tau_{i-1}) + 2\Delta\tau\,\dot{S}(\tau_i)
\end{aligned}\right\} \quad (37)$$

and the process continued until $S = 1$; i.e., complete melting.

To start the solution to Eq. (36) it is still necessary to find an analytic solution which is valid in the neighborhood of $\tau = 0$ since $\ddot{S}(0) = \infty$. For $S \ll \dot{S} \ll 1$ about $\tau = 0$, Eq. (36) becomes

$$\begin{aligned}
Q(\tau)/Q_0 = 1 &+ (\pi^{1/2}/2)(\tau/M)\dot{S} - \\
&(9/8)\{S/\dot{S}\}^{1/2} - (S^2\ddot{S}/\dot{S}_3)\{\dot{S}/S\}^{1/2} + \\
&(\ddot{S}/2\dot{S})\{S/\dot{S}\}^{3/2} + (\ddot{S}/8S)\{S/\dot{S}\}^{5/2}
\end{aligned}$$

which has as its solution for $Q(\tau) = Q_0$.

$$S(\tau) = (2/\pi^{1/2})(M/\tau)[(5/4)/(3/2)^{3/2}]\tau^{3/2} \quad (38)$$

and is of the same form as the starting solution (31) for the first approximation.

We can again see that the initial condition (18d) is satisfied—i.e.,

$$\lim_{\tau\to 0} T_0\,(1-S, t^*)\varphi_2(z,\tau) = \lim_{\tau\to 0} S\varphi_2(z,\tau) = 0 \quad (39)$$

Using Eq. (38) to start the solution we obtain curves of S versus τ which are plotted in Fig. 4 for $M/\tau = 4.89$ and 50 and compared with the corresponding first approximation curves. We note that the two approximations for $M/\tau = 50$ are almost identical and that for $M/\tau = 4.89$ the approximations are nearly the same over a major portion of the melting time. Further we see that the error in $(\tau_i)a$ for $M/\tau = 50$ is negligible and that for $M/\tau = 4.89$ it has been reduced from 9 per cent to 3 per cent from the first to the second approximation.

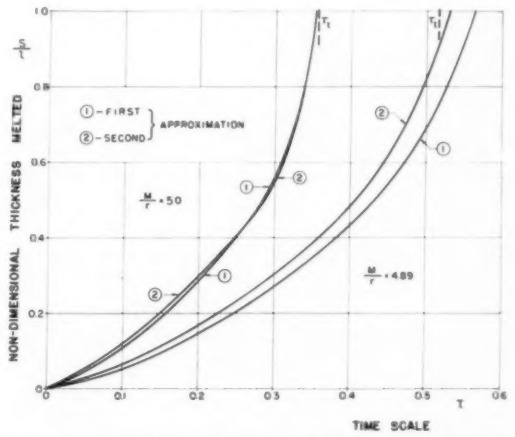

FIG. 4. Nondimensional curves of thickness melted versus time for a constant heat input.

In addition, curves of S versus $\tau/(\tau_i)a$ are shown for each approximation in Fig. 5 and Fig. 6. It can be seen that when normalized in this manner the two approximations fall very close to each other over the total melting period. This suggests that a good approximation to the exact solution for the amount of material melted at any time may be obtained from the first approximation for S versus τ by multiplying the ordinate by $\tau/(\tau_i)a$.

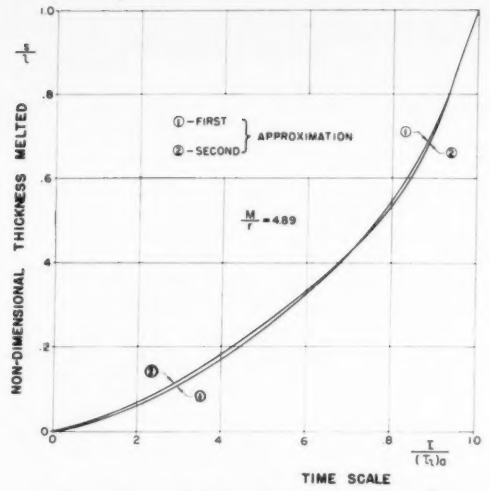

FIG. 5. Comparison of first and second approximations of the nondimensional thickness melted versus time for a constant heat input. Normalized scales.

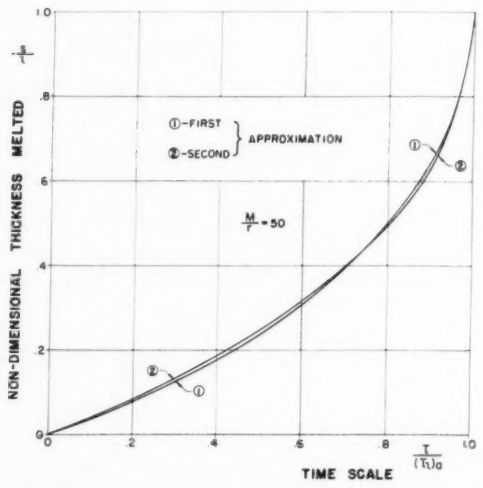

FIG. 6. Comparison of first and second approximations of the nondimensional thickness melted versus time for a constant heat input. Normalized scales.

The temperature in the slab at $x = l/2$ and l ($z = (1/2) - S$ and $1 - S$) can be obtained from Eq. (26). For the particular case of $M/r = 4.89$, $r = 0.75$, both the first and second approximations are shown in Fig. 7 as a function of $\tau/(\tau_l)a$. One sees that, as was the case for the thickness melted, there is little difference between the first and second approximations for the temperature in the slab.

Example II—Atmospheric Heating

In this section we will calculate the first approximation for the problem of a slab insulated at $x = l$ but now subjected to a time varying heat input $Q(t)$ on the other face. The particular heat input used is meant to correspond to one that which might be incurred by a body descending through the atmosphere and is given in Fig. 8. The maximum rate of heat input was taken as 200 cal./cm.^{2}-sec., (736 B.t.u./ft.^{2}-sec.) with a total heat input of 2,244 cal./cm.^{2}, (8,258 B.t.u./ft.^{2}). The form of $Q(t)$ was arrived at in the manner shown in reference 15.

To obtain an analytic representation of the temperature in the slab a function of the form $\tilde{Q}(t) = R(e^{\alpha t} - 1)$ was used to approximate the actual heat input $Q(t)$ over the first portion of the descent time. Once melting begins the actual heat input can be used since the procedure is then numerical. The agreement between this simple representation of the heat input $\tilde{Q}(t)$ and the actual function $Q(t)$ is also shown in Fig. 8 for the numerical values given in reference 16 and with

$$\tilde{Q} = 11.776(e^{0.152t} - 1) \tag{40}$$

Using the expression for $\tilde{Q}(t)$ the temperature distribution within the slab for $0 \leq t \leq t^*$ (i.e., before melting starts) is derived in reference 16. It is

$$T_0(x, t) = \frac{Rl}{2k}\left\{2e^{\alpha t}\,\gamma^{1/2}\,\frac{\cosh\,\gamma^{-(1/2)}(1 - x/l)}{\sinh\,\gamma^{-(1/2)}} + \frac{1}{3} - \frac{(x-l)^2}{l^2} - 2\gamma(1 + \alpha t) + \sum_{1,2}^{\infty}\frac{4e^{-n^2\pi^2 Kt/l^2}}{n^2\pi^2 + n^4\pi^4\gamma}\cos\frac{n\pi x}{l}\right\} \tag{41}$$

where $\gamma = K/\alpha l^2$

Consider a steel slab with the following physical properties:

$$\left.\begin{aligned} l &= 2\text{ cm.}, \quad \kappa = 0.0986\text{ cm.}^2/\text{sec.}, \quad \rho = 7.8\text{ gm./cm.}^3 \\ L &= 8\text{ cal./gm.}, \quad T^* = 1{,}500°\text{C.}, \quad c = 0.13\text{ cal./gm.-°C.} \end{aligned}\right\} \tag{42}$$

From this we may calculate that

$$M = (\pi^{1/2}/2)(cT^*/L) = 21.6, \quad r = kT^*/lQ_0 = 0.375$$

where the reference value of the heat input was taken to be 200 cal./cm.^{2}-sec.

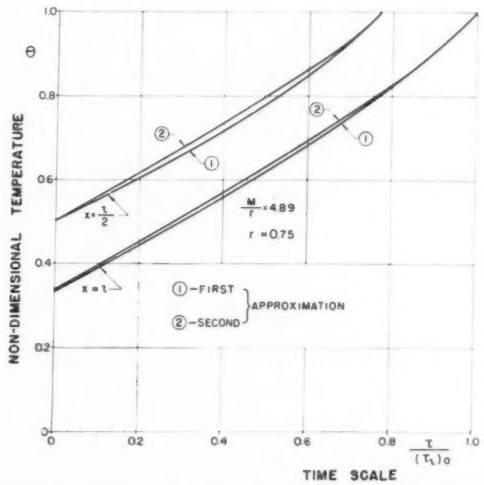

FIG. 7. Comparison of first and second approximations for the nondimensional temperature versus time for a constant heat input. Normalized scales.

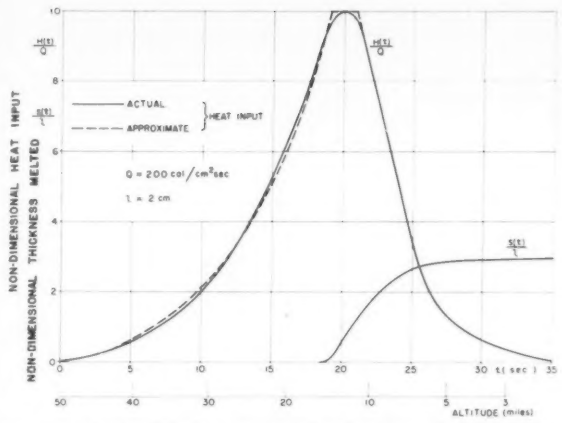

FIG. 8. Melting due to a heat input incurred by a body descending through the atmosphere.

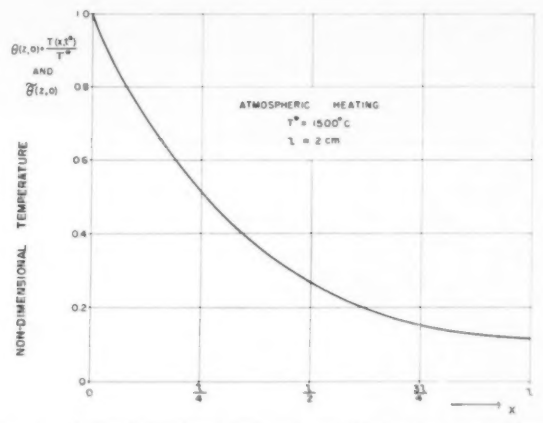

FIG. 9. A nondimensional temperature distribution at the time melting begins in a slab undergoing atmospheric heating.

It can be shown from Eq. (41) using these properties and the heat input given by Eq. (40) that at $t = 19$ sec. the temperature at $x = 0$ will be 1,500°C. and melting will begin—i.e., $T_0(0, 19) = T_0(0, t^*) = T^*$. To facilitate computations we express the nondimensional temperature at this time,

$$\theta(z, 0) = T_0(x, t^*)/T^*$$

in terms of a polynomial. The temperature $\theta(z, 0)$ is accurately given by

$$T_0(x, t^*)/T^* \cong \tilde{\theta}(z, 0) = 1 - 2.6667z + 3.3267z^2 - 2.1809z^3 + 0.6394z^4 \quad (43)$$

where $\tilde{\theta}(z, 0)$ has the same value and slope at $x = 0, l$ and the same value at $x = l/2$ as $\theta(z, 0)$. A comparison of $\tilde{\theta}(z, 0)$ and $\theta(z, 0)$ in Fig. 9 shows them to be indistinguishable for the scale used.

Using Eq. (43) we obtain from Eq. (16)

$$\theta(z, \tau) = 1 - 2.6667z + 3.3267z^2 - 2.1809z^3 + 0.6394z^4 + 1.236S(1 - 0.9104S + 2.068S^2)\varphi_1(z, \tau) \quad (44)$$

The function $\varphi_1(z, \tau)$ is then the solution of Eq. (19) containing the inhomogeneous terms obtained from Eq. (43). Eq. (19) becomes

$$(\partial^2\varphi_1/\partial z^2) + \dot{S}(\partial\varphi_1/\partial z) - (\dot{S}/S)q\varphi_1 = a - bz + cz^2 - dz^3 \quad (45)$$

where

$$q = \frac{1 - 1.8209S + 6.2039S^2}{1 - 0.9104S + 2.068S^2}$$

$$a = \frac{(2.1575\dot{S} - 5.383)}{S(1 - 0.9104S + 2.068S^2)}, \quad b = \frac{(5.383\dot{S} - 10.5869)}{S(1 - 0.9104S + 2.068S^2)}$$

$$c = \frac{(5.2934\dot{S} - 6.2039)}{S(1 - 0.9104S + 2.068S^2)}, \quad d = \frac{(2.068\dot{S})}{S(1 - 0.9104S + 2.068S^2)}$$

The solution of this equation satisfying conditions (18b, c) is

$$\varphi_1(z, \tau) = A_1e^{\lambda_1\tau} + A_2e^{\lambda_2\tau} + B_0 + B_1z + B_2z^2 + B_3z^3 \quad (46)$$

where

$$\lambda_{1,2} = -(\dot{S}/2) + \{(\dot{S}^2/4) + (\dot{S}/S)q\}^{1/2}$$

$$A_1 = -B_0 - A_2$$

$$A_2 = \frac{e^{-\lambda_1(1-S)}}{\lambda_1}\left\{\frac{\lambda_1B_0e^{\lambda_1(1-S)} + 1 - B_1 - 2B_2(1 - S) - 3B_3(1 - S)^2}{1 - (\lambda_2/\lambda_1)e^{(\lambda_2-\lambda_1)(1-S)}}\right\}$$

and

$$B_3 = dS/q\dot{S}, \quad B_2 = -(cS/q\dot{S}) + (3SB_3/q)$$

$$B_1 = (bS/q\dot{s}) + (S/q)[(6B_3/\dot{S}) + B_2]$$

$$B_0 = -(aS/q\dot{S}) + (S/q)[(2B_2/\dot{S}) + B_1]$$

The third and last boundary condition for the determination of $S(\tau)$ is given by Eq. (18a). In our present problem this becomes

$$\frac{Q(\tau)}{Q_0} = 1 + \frac{\dot{S}}{65} - \frac{0.463S[1 - 0.9104S + 2.068S^2]}{[1 - (\lambda_2/\lambda_1)e^{(\lambda_2-\lambda_1)(1-S)}]} \{-\lambda_2 B_0[1 - e^{(\lambda_2-\lambda_1)(1-S)}] + (1 - B_1) \times$$

$$[1 - (\lambda_2/\lambda_1)]e^{-\lambda_1(1-S)} + B_1[1 - (\lambda_2/\lambda_1)e^{(\lambda_2-\lambda_1)(1-S)}] - (1 - S)[1 - (\lambda_2/\lambda_1)][2B_2 + 3B_3(1 - S)]e^{-\lambda_1(1-S)}\} \quad (47)$$

Notice that at $S = 1$, the melting velocity is

$$\dot{S}\Big|_{s=1} = \frac{2}{\pi^{1/2}} \frac{M}{r} \frac{Q(\tau)}{Q_0}\Big|_{s=1} = 65 \frac{Q(\tau)}{Q_0}\Big|_{s=1}$$

which is once more the condition the exact solution must satisfy [cf. Eq. (14)].

To start the numerical solution of Eq. (47) we must again obtain an analytic solution which is valid in the neighborhood of zero. Assuming that $S < \dot{S} < 1$ we obtain the equation

$$Q(\tau)/Q_0 = 1 + (\dot{S}/65) - 2.495\{S/\dot{S}\}^{1/2}$$

for this region. Since $Q(\tau)/Q_0 - 1 = 0$ over the small region needed to start the solution we find that the remaining terms are satisfied by

$$S = 88.277\ \tau^{3/2}, \quad \dot{S} = 132.42\tau^{1/2} \qquad (48)$$

functions which agree with the assumptions made on their behavior about $\tau = 0$.

The solution for $S(\tau)$ obtained from Eq. (47) and the heat input $Q(\tau)$ it corresponds to is shown in Fig. 8. For the particular choice of variables used approximately 3/10 of the slab was melted away.

References

[1] Stalder, J. R., *The Useful Heat Capacity of Several Materials for Ballistic Nose-Cone Construction*, NACA TN 4141, November, 1957.

[2] Masson, D. J., and Gazley, C., Jr., *Surface-Protection and Cooling Systems for High Speed Flight*, Rand Corporation Memorandum RM-1735, March, 1956.

[3] Roberts, L., *A Theoretical Study of Stagnation Point Ablation*, NACA TN 4392, September, 1958.

[4] Stefan, J., *Uber die Theorie der Eisbildung, inbesondere uber die Eisbildung im Polarmere*, Annalen der Physik und Chemie, Vol. 42, p. 269, 1891.

[5] Evans, G. W., Isaacson, E., and MacDonald, J. K. L., *Stefan-Like Problems*, Quart. Appl. Math., Vol. 8, pp. 312–319, 1950.

[6] Ruoff, A. L., *An Alternate Solution of Stefan's Problem*, Quart. of Appl. Math., Vol. 16, pp. 197–201, July, 1958.

[7] Weber, H., *Partiellen Differential-Gleichungen*, Vol. 2, pp. 117–121; Friedr. Vieweg and Sohn, Braunschweig, Germany, 1912.

[8] Ingersoll, L. R., and Zobel, O. J., *An Introduction to the Mathematical Theory of Heat Conduction*, pp. 149–159; Ginn and Co., New York, 1913.

[9] Neumann, F., Konigsberger Vorlesungen, unpublished, circa 1835–1840.

[10] Lightfoot, N. M. H., *The Solidification of Molten Steel*, Proceedings of the London Mathematical Society, Series 2, Vol. 31, pp. 97–116, 1930.

[11] Landau, H. G., *Heat Conduction in a Melting Solid*, Quart. Appl. Math., Vol. 8, pp. 81–94, April, 1950.

[12] Goodman, T. R., *Aerodynamic Ablation of Melting Bodies*, Proceedings of the third U.S. National Congress of Applied Mechanics, Brown University, 1958.

[13] Sutton, G. W., *The Hydrodynamics and Heat Conduction of a Melting Surface*, Journal of the Aeronautical Sciences, Vol. 25, No. 1, pp. 29–32, 36, January 1958.

[14] Carslaw, H. S., and Jaeger, J. C., *Conduction of Heat in Solids*, 1st Ed., Oxford at the Clarendon Press, 1947.

[15] Allen, J. H., and Eggers, A. J., Jr., *A Study of the Motion and Aerodynamic Heating of Missiles Entering the Earth's Atmosphere at High Supersonic Speeds*, NACA TN 4047, October, 1957.

[16] Citron, S. J., *Heat Conduction in a Melting Slab*, Contract No. Nonr-266(20), Technical Report No. 15, Columbia University, January, 1959.

Microcards for Volumes 1–5 Available

Microcards for Volumes 3–5 of the JOURNAL are now available (Vols. 1 and 2 were republished in this form earlier). All five volumes are priced at $5.50 each, and are obtainable through:

J. S. Canner & Company, Inc.
Boston, Roxbury 20, Mass.

An Authorized Binding for Journal of the Aero/Space Sciences

Arrangements have been made by the Institute of the Aeronautical Sciences for members and subscribers to have their Journals bound carefully and economically. Simply write for details to:

Publisher's Authorized Bindery Service, 5809 West Division St., Chicago 51, Ill.

Electrogasdynamic Motion of a Charged Body in a Plasma†

L. KRAUS* AND H. YOSHIHARA**

Convair, A Division of General Dynamics Corporation

(1) Introduction

GASDYNAMICS has generally been concerned with the motion of bodies through compressible fluids. In recent years there has been renewed interest in a fluid which differs in so many of its properties from an ordinary gas that it has been called a "fourth state of matter." We refer, of course, to a plasma which is an electrically neutral gas containing ions and electrons. Plasmas now occur in many situations which are of aeronautical or astronautical interest—e.g., the ionosphere, interplanetary space, jet exhausts, hypersonic shock layers, etc. The possibility of affecting the properties of plasma flows by means of external magnetic fields has stimulated an extensive literature in aeronautical magnetohydrodynamics. We wish now to consider the motion of a body through a plasma where electrostatic phenomena are significant.

The motion of body in a plasma will in general induce a negative charge on the body due to the fact that the relative flux of the electrons to the body is greater than that of the ions. This charge will then affect the flow through the Coulomb interaction with the plasma. A charge may also be induced on a body by entirely different or even artificial mechanisms. The motion of charged bodies in a plasma is what we have called "electrohydrodynamics," or since a plasma is generally a compressible fluid. "electrogasdynamics."

The effect of an electric charge on the motion of a body through a plasma was discussed by Jastrow and Pearse[1] in connection with satellite motion through the ionosphere. They considered the effect of charged particle interaction with the static potential field of the charged body, assuming that the electrostatic field is undisturbed by the flow. However, a plasma flow interacts with an electrostatic field on the body, and the dynamic modifications of both the field and the flow must be considered. This was done by Kraus and Watson.[2] The modifications are considerable when the flow velocity is greater than the velocity of sound in the (ion) fluid, as is the situation for satellite or meteorite motion.

Presented at the Aerodynamics—I Session, IAS 27th Annual Meeting, N.Y., Jan. 26–29, 1959.

† This work was performed under the Convair-sponsored Applied Research Program, directed by Mr. C. W. Frick. The authors wish to express their appreciation to Professors H. Grad and K. Watson for helpful discussions.

* Physics Section, Convair, San Diego.

** Chief of Theoretical Aerodynamics, Convair, San Diego.

It is our purpose in this paper to review briefly the basis for treating a plasma as a fluid to which hydrodynamic considerations may be applied. We will then describe briefly the basic equations and illustrate the theory by treating the very simple case of the supersonic flow of a plasma past a two-dimensional slender dielectric body.

(2) The Plasma as a Fluid

A plasma differs from a gas of neutral particles in certain important respects. In a neutral gas, local properties are determined by collisions between particles. The free path for such collisions is given by

$$l = 1/\pi n q^2$$

where n is the number density of particles and πq^2 is the effective cross section of the particle where q, for example, will simply be the radius of neutral particles when considered as rigid elastic spheres. In general, q is the distance of closest approach under the influence of the force exerted by one particle on another, the force here being so short in range that only two particles are involved in any encounter.

In a plasma, however, the influence of the inverse square Coulomb force between charged particles is effective at considerable distances; thus, the motion of a given particle influences the motion of many particles. Alternatively, each charged particle moves under the influence of all the charged particles in the plasma. With respect to a particular test particle, the plasma may be separated into two regions. First, there is a region in the neighborhood of the test particle in which the effect of the Coulomb force is similar to that of short range forces, the interactions here being of a random thermal character. Second, there is the region exterior to this neighborhood, in which the individuality of the particle charges need not be considered and the overall effects of the Coulomb forces, due to these particles, can be considered as a body force on the test particle. The size of the region in which the random thermal motion can occur may be characterized by the Debye radius,

$$R_D^2 = kT/4\pi n_e e^2$$

where T is the plasma temperature in degrees Kelvin, n_e is the number density of electrons, e is the electron charge, and k is the Boltzmann constant. The Debye distance may also be characterized as the distance in

which electric charges can be separated by the thermal motion in the plasma. Since the test particle in a plasma is affected by all the particles in the Debye region, an "effective cross section," πq^2, may be defined, as well as an "effective free path." These are similar to the quantities defined above for the interaction of two neutral particles, except for a factor which takes into account the effects of all particles in the region.[3, 4] We may then define a distribution function which satisfies Boltzmann's equation, and the collision integral now refers to interactions in the modified sense just described. By taking moments of the Boltzmann's equation, we arrive at the usual macroscopic equations of motion. These equations can be reduced to the ordinary equations of gasdynamics when a *scalar* pressure can be introduced.[5] This can be done if the "effective free path" is less than a characteristic length of interest in the problem. We note now that this is possible in the case of a plasma when the characteristic length is much less than with neutral particles. The effective cross section for charged particles may be several orders of magnitude greater than for neutral particles in a gas at the same density and temperature.*

For the ionosphere and in interplanetary space, the ionization density is very low and the "effective free paths" are very long. It may not, therefore, be possible to reduce the pressure tensor to a scalar. If, however, there is a charged body in this thin plasma, there will be a macroscopic electric field. There will now be a collective effect similar to that produced by a point charge. This effect now appears in the Boltzmann equation as a macroscopic body force. By introducing the directed particle velocity resulting from the electric force and an approximate linearization based on the difference between the directed and random velocity, the equations describing the flow can be reduced to a form (at least when dissipative effects are neglected) which is analogous to those for the linearized continuum flow.[2] The physical basis for treating a rarefied gas with an impressed electric field is similar to that encountered in the magnetohydrodynamics of rarefied high temperature plasmas, but there is considerable simplification in the former because the complicated electromagnetic effects are absent.

(3) Basic Equations

To exhibit some of the phenomena of electrogasdynamics, we consider the flow equations which, in view of the above discussion for the high plasma density case, may be written in the steady case as

$$Mn_i\mathbf{V}\cdot\nabla\mathbf{V} + \nabla p_i - n_i e\mathbf{E} = 0 \tag{1}$$

$$\nabla\cdot(n_i\mathbf{V}) = 0 \tag{2}$$

$$p_i n_i^{-\gamma} = \text{const.} \tag{3}$$

where M is the ion mass, n_i the number density of ions, p_i the ion fluid pressure, γ the adiabatic constant, $\mathbf{V}$ the velocity vector of a fluid particle, and $\mathbf{E}$ the electrostatic force field. A similar set of equations governs the motion of electrons. Here, it has been assumed that the plasma is composed of electrons and singly ionized atoms of one chemical species. The electric field is determined by Poisson's equation:

$$\nabla\cdot\mathbf{E} = 4\pi e(n_i - n_e) \tag{4}$$

If the electrons are in local thermodynamic equilibrium, it is readily shown from the equation of state and the electron equation of motion with the inertia term neglected that[5]

$$n_e = n_o \exp(e\Phi/kT) \tag{5}$$

where $\nabla\Phi = -\mathbf{E}$ defines the electrostatic potential and n_o is the equilibrium ionization density. Furthermore, the electron pressure p_e may be found from the electron equation of state, $p_e = n_e kT$, or using Eq. (5), we obtain

$$p_e = n_o kT \exp(e\Phi/kT) \tag{5a}$$

(Note that the equilibrium electron temperature T will be constant throughout the flow.)

If we now define the usual small disturbance variables by the formulas

$$n_i = n_o + n', \quad p_i = p_o + p_i,$$

$$n_e = n_o(1 + e\Phi/kT), \quad \mathbf{V} = \mathbf{V}_0 + \mathbf{v}$$

(where n_o, p_o, and $\mathbf{V}_0$ refer to the undisturbed free stream plasma, and n', p_i', and $\mathbf{v}$ are small perturbations), and we introduce a velocity potential P by

$$\nabla P = \mathbf{v} \tag{6}$$

we obtain the coupled linear equations

$$-V_o^2 P_{xx} + a_i^2\nabla^2 P = (eV_o/M)\Phi_x \tag{7}$$

$$[\nabla^2 - (A^2/R_D^2 a_i^2)]\Phi = (\omega_{pi}^2/a_i^2)(V_o M/e)P_x \tag{8}$$

Here, we have defined the sound speed in the ion fluid, a_i, by

$$a_i^2 = \gamma p_o/n_o M \tag{9}$$

x is the coordinate in the direction of the free stream, R_D is the Debye distance defined previously, and

$$A^2 = a_i^2 + \omega_{pi}^2 R_D^2 \tag{10}$$

where the quantity

$$\omega_{pi}^2 = 4\pi e^2 n_o/M$$

will be recognized as the ion plasma frequency.

Let us next introduce the following scale transformation in Eqs. (7) and (8).

$$\xi = x/c, \quad \eta = y/c, \quad \zeta = z/c$$

$$P(x, y, z) = cV_o p(\xi, \eta, \zeta)\ \Phi(x, y, z) = (MV_o^2/e)\phi(\xi, \eta, \zeta) \tag{11}$$

where c is a characteristic length of the problem, and (x, y, z) are Cartesian coordinates.

* For a more detailed discussion, see reference 3, Chap. 5.

The basic Eqs. (7) and (8) now become

$$-V_o^2 p_{\xi\xi} + a_i^2 \nabla^2 p = V_o^2 \phi_\xi \tag{12}$$

$$[\nabla^2 - (A^2 c^2 / R_D^2 a_i^2)]\phi = c^2(\omega_{pi}^2/a_i^2) p_\xi \tag{13}$$

Eqs. (12) and (13) may be decoupled to obtain, for example, for p, the fourth-order equation

$$[\nabla^2 - (A^2 c^2/\omega_{pi}^2 R_D^2)] \times (-V_o^2 p_{\xi\xi} + a_i^2 \nabla^2 p) - (c^2 V_o^2 \omega_{pi}^2/a_i^2) p_{\xi\xi} = 0 \tag{14}$$

A similar fourth-order equation may be obtained for ϕ.

The equation of the characteristics of Eq. (14) is a fourth-order polynomial. If the free stream velocity V_o is less than the ion sound speed, all the roots are imaginary, and the equation is completely elliptic. If the V_o is greater than the ion sound speed, we have two real and two imaginary roots. That is, the equation is twofold elliptic and twofold hyperbolic. The latter case is of particular interest, since here one expects many of the effects of supersonic aerodynamics.

For an electrostatic point source, a solution of this equation has been obtained.[2] The solution shows that for the velocity of the source less than the ion sound speed, no significant effects are obtained, except that the electrostatic equipotential lines are distorted from their usual spherical shape to ellipsoids. For a source velocity greater than ion sound speed, these equipotentials extend to infinity along the characteristics. A "bunching up" of equipotentials occurs near the Mach cone; upstream, the potential decays exponentially. Downstream of the Mach cone, the equipotentials decay algebraically, and there is an important transition region where the ionization density shows a marked increase. In addition, there is a supersonic drag phenomenon. It should be noted that essentially the same solution was also obtained for the case of very low density plasmas.

The Debye radius is usually very small in comparison with other lengths of interest in the problem, so that

$$\nabla^2\phi/\phi << A^2 c^2/a_i^2 R_D^2 \tag{15}$$

Eq. (13) now reduces to

$$\phi = -(1/V_o^2) M_p^2 R_D^2 \omega_{pi}^2 p_\xi \tag{16}$$

where $M_p = V_o/A$ is the "plasma" Mach Number. Eq. (12) with (16) now becomes

$$-M_p^2 p_{\xi\xi} + \nabla^2 p = 0 \tag{17}$$

The reduction of the order of the equation by this singular perturbation has important consequences. The second-order equation will be valid throughout the flow, with the possible exception of certain regions such as the neighborhood of the body where boundary conditions are required. In these regions where the inequality, Eq. (15), does not hold, there appears a type of boundary layer phenomenon. It will also be noted that the Mach angle is altered from the exact case with the acoustic velocity increased to

$$A = (a_i^2 + \omega_{pi}^2 R_D^2)^{1/2}$$

from the exact value a_i. The resulting steepening of the Mach waves may be interpreted in the following way. The twofold ellipticity of the fourth-order equations implies that perturbations of the flow at a given point will propagate upstream to infinity, the intensity of the perturbation attenuating as it propagates upstream. In the reduced system, this upstream propagation will, however, be confined between the region formed by the two Mach cones resulting from the two acoustic velocities. The elliptic character of the flow in this region assumes a modified hyperbolic character. In the exact case, there is, of course, additionally a weak effect upstream of the steeper Mach cone. We have essentially then an "electrostatic Mach cone."

To define a unique solution to the problem, we must supplement the above differential equations by boundary and Cauchy type conditions. The number and type of conditions required to yield a well-posed problem follows from the purely fluid or electrostatic problems. These include the following. At the surface of the body, the direction of the velocity vector must be parallel with the slope of the body. For the electrostatic potential ϕ, we have different conditions at the body depending upon the nature of the body material. We shall consider it composed of either a conductor or an isotropic dielectric. For the conductor, the potential must be a constant at the body surface; this constant is related to the total charge on the conductor, since the normal derivative of the potential at the body surface is essentially the local surface charge density. For the dielectric, the potential or its normal derivative may be arbitrarily prescribed. The surface charge accumulation may be determined in this case from the plasma flow problem, together with the purely electrostatic problem in the interior of the dielectric body. This will be illustrated in a subsequent example.

Far from the body, the function p and the potential ϕ must either vanish identically or be composed of "outgoing waves," as in the usual sense of supersonic flows.

For the decoupled fourth-order equations such as Eq. (14), clearly all of the above conditions, expressed, of course, in terms of the decoupled dependent variable, must be used.

Lastly, we obtain from the linearized equations of motion of the ions the "Bernoulli equation"

$$p_i' = -n_o M V_o^2 (p_\xi + \Phi) \tag{18a}$$

For the electrons, we obtain from Eq. (5a) the expression

$$p_e' = n_o M V_o^2 \Phi \tag{18b}$$

where $p_e' = p_e - p_o$.

(4) Plasma Flow Over a Thin Dielectric Body

As an example, we shall consider the two-dimensional flow over a thin profile at zero angle of attack. To

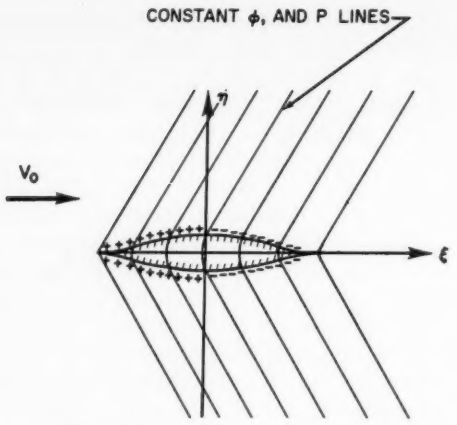

FIG. 1. Electrogasdynamic motion over a dielectric body.

simplify the mathematics, we shall choose an example for which the approximation, as given in Eq. (15), is valid throughout the domain of the problem. This will mean that "boundary-layer effects" must be minimized. The body selected must thus have cusped leading and trailing edges to avoid the "boundary layers" along the nose and tail Mach waves. Additionally, no condition on ϕ will be directly imposed at the body. Instead, ϕ will be so selected that no boundary layer arises along the body.

The symmetric profile to be considered is given in the upper half plane by the equation

$$\eta = (\tau_o/4)(1 + \cos 2\pi\xi) \quad -(1/2) \leq \xi \leq (1/2) \tag{19}$$

where τ_o is the thickness ratio. The profile is qualitatively sketched in Fig. 1 where also the orientation of the coordinate system is given. Our basic flow equation can now be written as

$$\lambda^2 p_{\xi\xi} - p_{\eta\eta} = 0 \tag{20}$$

where $\lambda^2 = M_p^2 - 1$. This decoupled equation for p, together with the conditions on p as given previously, will be sufficient to determine a unique solution. This will be analogous to the Ackeret solution. The resulting p will be inserted in Eq. (16) to obtain ϕ. We obtain to this order of approximation

$$\left.\begin{aligned} p &= -(\tau_o/4\lambda)\cos 2\pi\,(\xi - \lambda\eta), \quad -\tfrac{1}{2} < \xi - \lambda\eta < \tfrac{1}{2} \\ \phi &= \{[\pi(\lambda^2+1)]/2\lambda V_o^2\} R_D^2 \omega_{pi}^2 \tau_o \times \\ &\qquad \sin 2\pi(\xi - \lambda\eta) \end{aligned}\right\}$$

$$\left.\begin{aligned} p &= 0, \quad \xi - \lambda\eta < -\tfrac{1}{2}, \quad \xi - \lambda\eta > \tfrac{1}{2} \\ \phi &= 0 \end{aligned}\right\} \tag{21}$$

Note that p and ϕ are symmetric with respect to η.

From Eq. (21), the drag may now be computed. It will be composed of the fluid pressure drag (wave drag) D_F and the electrostatic body force drag, D_E. The calculation of the wave drag may be calculated by integrating the pressure, as given by Eq. (18), over the contour. The result is

$$D_F = (\pi^2/4)(n_0 M V_o^2 \tau_o^2 c/\lambda) \tag{22}$$

or

$$C_{DF} = (\pi^2/2)(\tau_o^2/\lambda) \tag{23}$$

Here and in the following, we have assumed that the electron and ion temperatures are equal.

The electrostatic drag D_E is given by

$$D_E = 2(M/e)\int_{-(1/2)}^{+(1/2)} \omega(\xi)(\partial\phi/\partial\xi)d\xi \tag{24}$$

where $\omega(\xi)$ is the induced surface charge density given by[6]

$$\epsilon_o(\partial\phi/\partial n) - \epsilon_B(\partial\phi_B/\partial n) = -(ec/MV_o^2)\omega\,(\xi) \tag{25}$$

Here, ϵ_o and ϵ_B are the dielectric constants for the fluid and the body, respectively; ϕ_B is the potential in the interior of the body, and the normal derivative to the body surface is to be taken as positive in an outward direction from the body.

The function ϕ_B is now determined from the purely electrostatic problem in the interior of the dielectric body. In the absence of volume charges, ϕ_B is defined by the Dirichlet problem where the boundary values are given by Eq. (21) with η set equal to zero.

Assuming a slender body, one may solve this problem approximately with the result

$$\phi_B = -\{[\pi(\lambda^2+1)]/2\lambda V_o^2\}\tau_o R_D^2 \omega_{pi}^2 \times \sin 2\pi\xi \cosh 2\pi\eta \tag{26}$$

This expression, together with Eq. (21) for ϕ, may now be used in Eq. (25) to compute the surface charge density. Integrating the charge density over the body now gives the total charge on the body. In the present case, the net charge is zero. The electrostatic drag is next found from Eq. (24) and is given by

$$D_E = (\pi^4/\lambda)(M/e)^2(\epsilon_o/c)V_o^4\tau_o^2[1/(\gamma+1)^2] \tag{27}$$

The total drag coefficient is now given essentially by the sum of Eqs. (27) and (23), that is

$$C_D = C_{DF}\,(1 + r) \tag{28}$$

where

$$r = D_E/D_F = (16\pi^3/\lambda)M_p^2(R_D/c)^2[1/(\gamma+1)]$$

Here we have set $\epsilon_o = 1$, and we have assumed equal electron and ion temperatures, so that

$$a_i^2 = \gamma\omega_{pi}^2 R_D^2$$

Since for a dense plasma, $R_D/c \ll 1$, we see therefore that the electrostatic body force is negligible in comparison to the wave drag.

On the other hand, it is seen that the wave drag in the plasma is significantly different as compared to the neutral gas case at the same thermodynamic state. The ratio R of the plasma and neutral gas wave drags being given by

$$R = \sqrt{M_o^2 - 1}/\sqrt{M_p^2 - 1}$$

where M_p, the "plasma Mach Number" (with A^2 =

$a_i^2 + \omega_{p_i}{}^2 R_D{}^2$ used as the square of the acoustic speed), is $\sqrt{\gamma/(\gamma+1)}$ times the Mach Number M_o based on the ion thermal speed.

(5) Final Remarks

In the present paper, a simple example has been examined which indicated some of the aspects of the coupling between the fluid motion and the electrostatic properties of a plasma. The simplication required that "boundary layer" effects be absent. Here, "boundary layers" are defined as narrow regions in which the electrostatic potential and the flow properties change rapidly. In a more general case, important modification must therefore arise near the body. The precise analysis of these effects would require the use of the complete fourth-order system of differential equations. As noted previously, these equations are twofold hyperbolic and twofold elliptic when the motion of the body is supersonic with respect to the ion thermal velocity. This property manifests itself, for example, by an upstream effect ahead of the leading edge Mach wave which damps exponentially. Electrical effects, instead of influencing the entire medium, are confined essentially to a region downstream of an electrostatic Mach envelope. Along these Mach envelopes, charge separation takes place which provides an interesting modification of the flow that may be observed experimentally.

The dense plasma case treated in the present paper is, of course, not directly applicable to the motion of a charged body in the rarefied ionosphere. In the latter case, "fluid type" equations also arise when the molecular collisions due to short range forces are neglected, and a treatment similar to the dense case may be carried out.

References

[1] Jastrow, R., and Pearse, E., *Atmospheric Drag on the Satellite*, J. Geophysical Res., Vol. 62, p. 413, 1957.

[2] Kraus, L., and Watson, K., *Plasma Motions Induced by Satellites in the Ionosphere*, Convair-San Diego Technical Report ZPh-016, May, 1958, and Physics of Fluids, Vol. 1, No. 2, pp. 480–488, November-December, 1958.

[3] Spitzer, L., *Physics of Fully Ionized Gas*, Interscience Publishers, New York, 1956.

[4] Pines, D., and Bohm, D., *A Collective Description of Electron Interactions*, Phys. Rev., Vol. 85, No. 2, p. 338–353, January, 1952.

[5] Chapman, S., and Cowling, T. G., *The Mathematical Theory of Nonuniform Gases*, Cambridge University Press, Cambridge, 1953.

[6] Stratton, J. A., *Electromagnetic Theory*, p. 164, McGraw-Hill Book Co., Inc., New York, 1941.

A Study of Vortex Cancellation

(*Continued from page 196*)

(6.11). Moreover, the value of s/a is given by elliptic wing theory[2] as $s/a = 6.45$. Combining this result with Eq. (6.11), one finds $\eta_{max} = 0.62$ for vortex cancellation in a circular duct. Thus, the analysis indicates that for the geometry considered only 62 per cent of the pressure drop across the first airfoil can be recovered even if there are no skin-friction and separation losses in the system. This value can be compared to the experimental recovery efficiencies of 50 per cent that have been realized.

In concluding the discussion, mention will be made of two interesting side calculations that can be performed using the results of this study. The first calculation involves the ratio $\Delta p_r/\Delta p_i$. If one uses the experimental value $\eta = 0.5$ and solves Eq. (6.3) for the above ratio, there results $\Delta p_r/\Delta p_i = 3$. This implies that the induced drag comprises 3/4 of the total drag on the airfoil. The second calculation involves the ratio $\Delta p_i)_{min}/\Delta p_i$. Since, by Eq. (6.10), $\Delta p_i)_{min} = q_{0w}$, one can evaluate $\Delta p_i)_{min}$ experimentally from tuft grid pictures. Moreover, Δp_i can be measured in the manner previously described in the discussion concerning the experimental determination of η. It is found that for the tests performed $\Delta p_i)_{min}/\Delta p_i \approx 0.8$. This implies that 4/5 of the irreversible pressure drop across the airfoil comes from establishing the vortex field and 1/5 comes from skin-friction and separation losses.

References

[1] Bird, J. D., and Riley, D. R., *Some Experiments on Visualization of Flow Fields Behind Low-Aspect-Ratio Wings by Means of a Tuft Grid*, NACA TN 2674, May, 1952.

[2] Spreiter, J. R., and Sacks, A. H., *The Rolling Up of the Trailing Vortex Sheet and Its Effect on the Downwash Behind Wings*, Journal of the Aeronautical Sciences, Vol. 18, No. 1, p. 21, January, 1951.

[3] Weinig, F., *Lift and Drag of Wings with Small Span*, NACA TM 1151, August, 1947.

Readers' Forum

BRIEF REPORTS of investigations in the aerospace sciences and discussions of papers published in the JOURNAL are presented in this special department. Entries must be restricted to a maximum of 1,300 words or the equivalent of one JOURNAL page including formulas and illustrations. Publication is completed as soon as possible after receipt of the material. The Editorial Committee does not hold itself responsible for the opinions expressed by the correspondents.

Contents

On Maximum Pressure Rise With Turbulent Boundary Layer.....A. MAGER AND A. W. GOLDSTEIN 234

Pitot-Probe Measurement of Local Skin-Friction Reduction Due to Transpiration in a Low-Speed, Turbulent Boundary Layer.....BERNARD M. LEADON AND E. ROY BARTLE 235

Limit Analysis of Multicell Boxes Submitted to Pure Torque.....FERNANDO VENANCIO FILHO 236

Inertia Effects on Some Static Aeroelastic Problems.....D. J. JOHNS 237

Formulas for the Determination of Thermal Stresses in Rings.....MARVIN FORRAY 238

Stress Functions for Plates Bounded by Piecewise Analytic Curves.....MING M. CHEN AND P. T. HSU 240

On Maximum Pressure Rise With Turbulent Boundary Layer

A. Mager and A. W. Goldstein

Research Consultant, ASTRO, The Marquardt Corporation, Van Nuys, Calif., and Aeronautical Research Engineer, NASA, Lewis Research Center, Cleveland, Ohio, Respectively

November 5, 1959

RECENTLY, B. S. Stratford published[1, 2] the results of an analytical and experimental investigation concerning the maximum attainable pressure rise in the presence of incompressible turbulent boundary layer. The examination of his experimental data reveals that it is also in essential agreement with some of our work,[3] in which the allowable turbulent boundary-layer pressure rise was used as a criterion for the prescription of cascade blade velocity distribution. A comparison between the analytical results of reference 3 (computed, however, for the diffusion coefficient $D_T = -0.017$) and the Stratford experimental data is shown in Figs. 1, 2, and 3.

As may be seen from Fig. 1, the agreement of the analytically predicted surface velocity distribution is not too good initially, but, for $(U/U_0)^2 < 0.65$, the data are very close to the results of our calculation method. This initial discrepancy stems probably from the fact that the turbulent boundary layer can withstand some suddenly applied pressure rise (such as produced by shocks, for example) without separation, while our calculation scheme did not allow for such happenings. In this respect, the analytical method suggested by Stratford is somewhat better in this region (see Fig. 4 of reference 2). It should be noted, however, that, from the practical standpoint, this difference in the velocity distribution in the initial region is rather unimportant, since it occurs for only very small surface length ($1.0 \leq x/x_0 \leq 1.15$) and, thus, should not affect substantially the aerodynamic design.

Turning now to Fig. 2, the predicted behavior of the momentum thickness (θ/θ_0) as a function of the pressure coefficient C_p

Contributors Please Note

Readers' Forum items must be confined to the equivalent of one page in the *Journal*. Contributions that exceed this limit will be returned to the authors for condensation and rewrite. To avoid inconvenience and delay, please adhere to the following specifications:

(1) Five, double-spaced, typewritten, manuscript pages ($8\frac{1}{2}$ by 11 in.), including wide margins, formulas, and headings, equal one printed page.

(2) For every illustration, deduct at least one-half or as much as one manuscript page, depending on the size of the illustration.

$[= 1 - (U/U_0)^2]$ shows good agreement initially but tends to overestimate somewhat the boundary-layer momentum deficiency for very high pressure coefficients. As will be mentioned later, this probably is the effect of an outmoded friction law which our early method has employed. On the other hand, the development of the form factor H, shown in Fig. 3, while initially slower by calculations, rises more rapidly later on to reach ultimately nearly the same final values as the experimental data indicates ($H = 2.6$). This behavior of the form factor H reflects, of course, the somewhat steeper initial experimental pressure gradient, which may be expected to affect primarily the shape of the boundary layer velocity profile. Even so, the predicted values of H are never too far off from those obtained experimentally and are certainly considerably better than those resulting from Stratford's analysis (see Fig. 6 of reference 2) which underestimates the final value of H by a rather substantial amount ($H = 2.0$).

It may be worthwhile to point out that this reasonably good agreement between the experiments of Stratford and the analysis of reference 3 is even more remarkable when one considers the fact that the analysis of reference 3 was based on a now outdated correlation of Garner,[4] which was obtained from only limited amount of data, all measured with pressure distributions radically different from those suggested here. Furthermore,

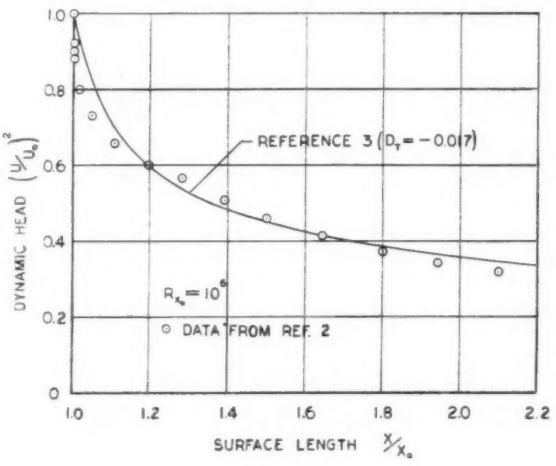

FIG. 1.

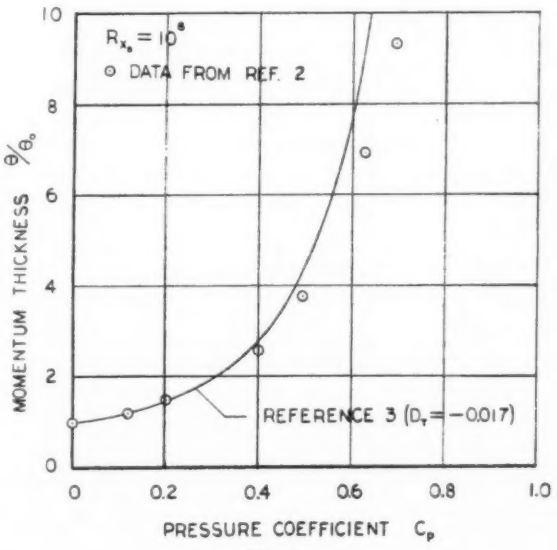

FIG. 2.

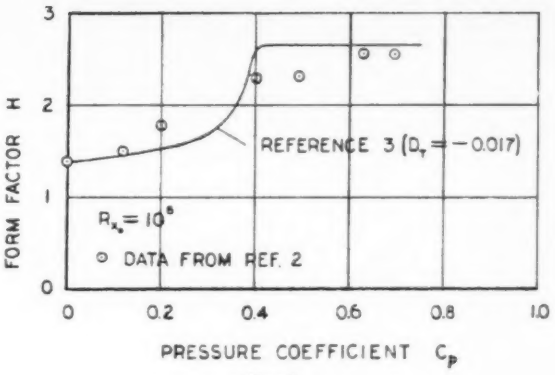

FIG. 3.

Garner's correlation resulted in a single analytical statement valid for all unfavorable pressure gradients and employed a zero pressure gradient friction law, both of which are thought today to be totally unacceptable for turbulent boundary-layer analysis. One cannot help but wonder, therefore, whether the agreement shown here indicates that the modern turbulent boundary-layer solution refinements are only a small perturbation on the essential features already conceived by Garner and other early investigators.

REFERENCES

[1] Stratford, B. S., *The Prediction of Separation of the Turbulent Boundary Layer*, J. Fluid Mech. Vol., 5, Part 1, pp. 1–16, 1959.

[2] Stratford, B. S., *An Experimental Flow With Zero Skin Friction Throughout its Region of Pressure Rise*, J. Fluid Mech., Vol. 5, Part I, pp. 17–35, 1959.

[3] Goldstein, A. W., and Mager, A., *Attainable Circulation of Airfoils in Cascade*, NACA TN 1941, September, 1949.

[4] Garner, H. C., *The Development of Turbulent Boundary Layers*, R&M No. 2133, Brit. ARC, June, 1944.

Pitot-Probe Measurement of Local Skin-Friction Reduction Due to Transpiration in a Low-Speed, Turbulent Boundary Layer

Bernard M. Leadon and E. Roy Bartle

Senior Staff Scientist and Staff Scientist, Respectively, Convair Scientific Research Laboratory, San Diego, Calif.

October 13, 1959

IT IS perhaps unnecessary to mention that a fixed pitot probe set at about

$$y_0^+ = y u_1 \sqrt{C_{f_0}/2} / \nu = 100$$

is capable of providing the value of the local skin-friction coefficient for zero blowing, C_{f_0}, by means of the usual law of the wall (see Table IV of reference 1). This well-known possibility has not been particularly recommended because, for most solid-wall situations, a simple round probe set firmly against the surface may be used equally as well.[2, 3, 7] However, the addition of a rigid foot to the probe will probably often be a permissable complication, and one may then freely use the law of the wall for C_{f_0} and seek to extend the idea of such measurements to the transpiration case.

Recently, one of us observed that the logarithmic portion of the low-speed velocity profile when expressed in certain coordinates has a slope which varies but little, if at all, with transpiration rate.[4] As long as this is true, an exceedingly simple measurement of the local turbulent skin friction, with blowing or without, can be made.

The logarithmic portion of the mean velocity profile for a low-speed, turbulent boundary layer on a porous flat plate may be represented by the equation

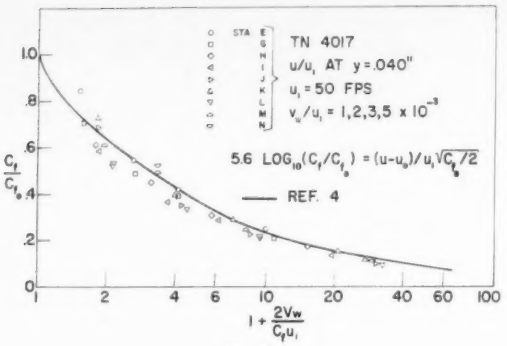

FIG. 1.

$$u^+/C = A \log (y^+/C) + B \tag{1}$$

where

$$u^+ = u/u_1\sqrt{C_f/2}, \quad y^+ = yu_1\sqrt{C_f/2}\,/\,\nu$$

subscript 1 indicates the free-stream value, C is a function of the blowing rate having the value unity for zero blowing, and A and B are constants which may be taken as 5.6 and 4.9, respectively. When the available experimental data[6] are plotted in the coordinates u/u_1 vs. log $(y\,u_1/\nu)$, it is found that the blowing rate does not noticeably alter the slope of the logarithmic portion. Hence,

$$1/C^2 = C_f/C_{f0} \tag{2}$$

and, for any fixed value of y in the logarithmic region,

$$A \log_{10}(C_f/C_{f0}) = (u - u_0)/u_1\sqrt{C_{f0}/2} \tag{3}$$

where subscript 0 indicates zero blowing values. The tendency of the logarithmic region is to expand with blowing, so that, for a fixed probe centered in the zero-blowing logarithmic region, Eq. (1) will probably remain valid up to quite high blowing rates.

Alternatively, the probe may be moved so as to hold u/u_1 constant, in which case

$$C_f/C_{f0} = y_0/y \tag{4}$$

but there is some danger that, in moving the probe to larger distances from the wall as blowing is increased, it may leave the logarithmic region and thus invalidate Eq. (1).

The data of Mickley and Davis for the probe positioned at y = 0.040 in. and for u_1 = 50 ft./per/sec. were used in Eq. (3) with A = 5.6 to compute the ratio C_f/C_{f0}. These results are plotted in Fig. 1, together with an empirical curve which well represents the results of a similarity analysis of the complete velocity profiles.[4] The blowing parameter log $(1 + 2v_w/C_f u_1)$ most smoothly correlates such data, after which the results may readily be converted to the more practical parameter $2v_w/C_{f0}u_1$.

It should be noted that some of the data scatter of Fig. 1 is surely due to the fact that the probe was repositioned for each reading, whereas, in an experiment planned for the use of Eq. (3), the probe would remain fixed. The contents of this note have been included orally with a related presentation.[5]

REFERENCES

[1] Coles, D., *Measurements in the Boundary Layer on a Smooth Flat Plate in Supersonic Flow. I. The Problem of the Turbulent Boundary Layer*, Rpt. No. 20-69, Jet Propulsion Laboratory, Pasadena, Calif., June 1, 1953.

[2] Fenter, F. W., and Stalmach, C. L., Jr., *The Measurement of Turbulent-Boundary-Layer Shear Stress by Means of Surface Impact-Pressure Probes*, Readers' Forum, Journal of the Aero/Space Sciences, Vol. 25, No. 12, pp. 793–4, December, 1958.

[3] Hsu, E. Y., *The Measurement of Local Turbulent Skin Friction by Means of Surface Pitot Tubes*, Rpt. No. 957, David Taylor Model Basin, Washington, D.C., August, 1955.

[4] Leadon, B. M., *Mass Transfer in a Turbulent Boundary Layer*, ARS Preprint 857-59, presented at the ARS Semiannual Meeting, San Diego, June 8–11, 1959.

[5] Leadon, B. M., and Bartle, E. R., *On the Measurement of Local Skin Friction by Means of a Surface Probe in the Case of Low Speed Turbulent Flow Over a Porous Flat Plate With Mass Injection*, Midwestern Conference on Fluid and Solid Mechanics, Univ. of Texas, September 9–11, 1959.

[6] Mickley, H. S., and Davis, R. S., *Momentum Transfer for Flow over a Flat Plate with Blowing*, NACA TN 4017, November, 1957.

[7] Preston, J. H., *The Determination of Turbulent Skin Friction by Means of Pitot Tubes*, J. RAeS., Vol. 58, No. 110, February, 1954.

Limit Analysis of Multicell Boxes Submitted to Pure Torque

Fernando Venancio Filho
Instituto Tecnológico de Aeronáutica, São Paulo, Brazil

October 9, 1959

ASSUMING an ideal elasto-plastic material, expressions for the collapse torque of two types of two- and three-cell boxes are derived. Results show that the collapse torque is, at most, of the order of 10 per cent higher than the torque at which yield begins.

Consider the box of Fig. 1(a), submitted to pure torque. The three following assumptions are made: (a) the thickness t of the walls is constant; (b) the material has an ideal elasto-plastic diagram in shear, Fig. 2; and (c) the walls yield before buckling can occur. A purely elastic analysis furnishes the following values for the shear flows q_1 and q_2, taking into account that $\lambda = b/a$:

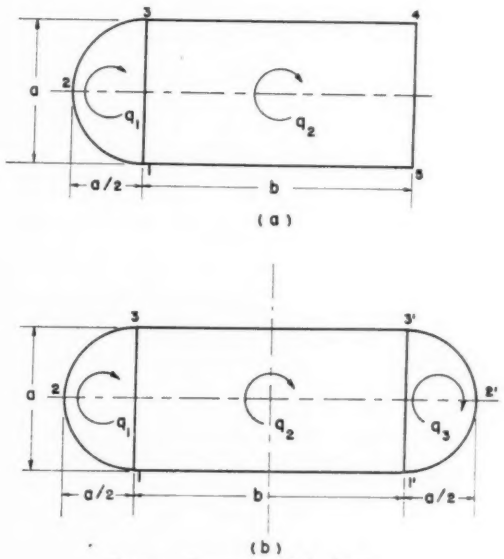

FIG. 1. Geometry of the boxes.

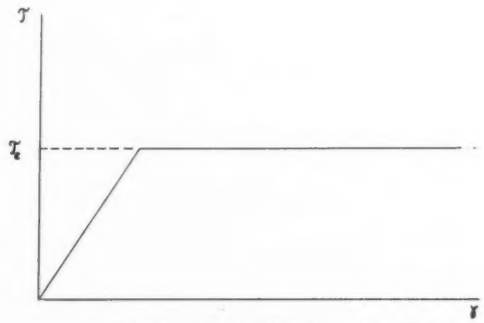

FIG. 2. Ideal elasto-plastic diagram in shear.

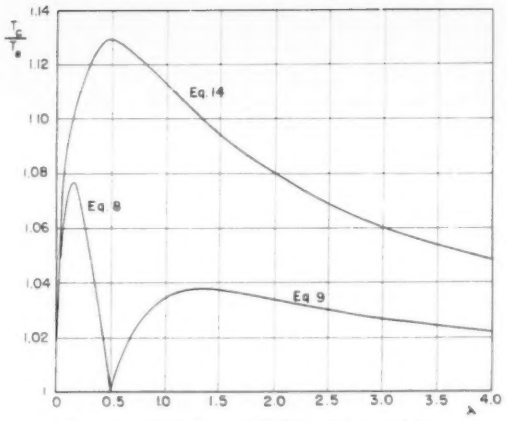

FIG. 3. Variation of T_c/T_e with $\lambda = b/a$.

$$q_1 = \frac{2 + 4.54\lambda}{1.57 + 5.56\lambda + 13.06\lambda^2} \frac{T}{a^2} \tag{1}$$

$$q_2 = \frac{1 + 6.53\lambda}{1.57 + 5.56\lambda + 13.06\lambda^2} \frac{T}{a^2} \tag{2}$$

In comparing Eqs. (1) and (2), it is seen that $q_1 > q_2$ for $0 < \lambda \leq 0.5$, and $q_2 > q_1$ for $\lambda \geq 0.5$. For the first of the above conditions, yield will start in wall 123 when

$$q_1 = q_e = 3_s t \tag{3}$$

where 3_s is the shear yield stress of the material, Fig. 2. Substituting Eq. (1) in Eq. (3), one finds T_e, the torque which first causes yielding:

$$T_e = \frac{1.57 + 5.56\lambda + 13.06\lambda^2}{2 + 4.54\lambda} q_e a^2 \tag{4}$$

Under this torque shear flow in cell 2 is, from Eqs. (2) and (4),

$$q_{2e} = [(1 + 6.53\lambda)/(2 + 4.54\lambda)]q_e \tag{5}$$

For torques T greater than T_e, the difference $T - T_e$ will be resisted only by cell 2 until, for a torque T_c, the outer walls from this cell will yield, causing collapse of the whole box. Then T_c can be calculated by

$$[(T_c - T_e)/2ab] + q_{2e} = q_e \tag{6}$$

Inserting Eqs. (4) and (5) in Eq. (6) and noting that $\lambda = b/a$,

$$T_c = (0{,}78 + 2\lambda)q_e a^2 \tag{7}$$

Finally, dividing Eq. (7) by Eq. (4),

$$\frac{T_c}{T_e} = \frac{1.6 + 7.6\lambda + 9.1\lambda^2}{1.6 + 5.6\lambda + 13.1\lambda^2} \tag{8}$$

For the second condition, yielding begins in walls 34, 45, and 51. The counterparts of Eqs. (3)—(8), respectively, are

$$q_2 = q_e$$

$$T_e = \frac{1.57 + 5.56\lambda + 13.06\lambda^2}{1 + 6.53\lambda} q_e a^2$$

$$q_{1e} = [(2 + 4.54\lambda)/(1 + 6.53\lambda)]q_e$$

$$[(T_c - T_e)/0.25\pi a^2] + q_{1e} = q_e$$

$$T_c = (0{,}78 + 2\lambda)q_e a^2$$

and

$$\frac{T_c}{T_e} = \frac{0.8 + 7.1\lambda + 13.1\lambda^2}{1.6 + 5.6\lambda + 13.1\lambda^2} \tag{9}$$

The results obtained from Eqs. (8) and (9) are presented in Fig. 3.

For the doubly symmetrical box of Fig. 1(b), the purely elastic analysis gives, taking into account that by symmetry the shear flows in walls 123 and 1′2′3 are equal and noting that $\lambda = b/a$,

$$q_1 = \frac{2 + 4.54\lambda}{3.14 + 11.15\lambda + 13.06\lambda^2} \frac{T}{a^2} \tag{10}$$

$$q_2 = \frac{2 + 6.53\lambda}{3.14 + 11.15\lambda + 13.06\lambda^2} \frac{T}{a^2} \tag{11}$$

Eqs. (10) and (11) show that $q_2 > q_1$ for $\lambda > 0$. Thus, yielding first starts at walls 11′ and 33′ at a torque given by

$$T_e = \frac{3.14 + 11.15\lambda + 13.06\lambda^2}{2 + 6.53\lambda} q_e a^2 \tag{12}$$

For torques greater than T, the box will behave like two separate boxes 123 and 1′2′3′ until it collapses at a torque T_c, given by

$$T_c = \frac{3.14 + 14.33\lambda + 13.06\lambda^2}{2 + 6.53\lambda} q_e a^2 \tag{13}$$

Dividing Eq. (13) by Eq. (12),

$$\frac{T_c}{T_e} = \frac{3.1 + 14.3\lambda + 13.1\lambda^2}{3.1 + 11.2\lambda + 13.1\lambda^2} \tag{14}$$

The values from Eq. (14) are plotted in Fig. 3.

Inertia Effects on Some Static Aeroelastic Problems

D. J. Johns
Lecturer in Aeroelasticity, College of Aeronautics, Cranfield, England
October 20, 1959

SYMBOLS

a	=	normal acceleration
B	=	moment of inertia about center of gravity
c	=	wing chord
d	=	longitudinal acceleration
D	=	total drag
e	=	distance of body centers of pressure from datum (Fig. 1)
E	=	Young's modulus
f	=	fraction of chord of wing center of pressure forward of elastic axis
g	=	distance of body centers of gravity from datum (Fig. 1)
G	=	shear modulus
h	=	fraction of chord of inertia axis forward of wing elastic axis
I	=	second moment of area
J	=	polar moment of area
k	=	stability parameter
$K\theta$, $\overline{K\theta}$	=	joint stiffness, critical value of $K\theta$
l	=	wing semispan, body length
L	=	lift/unit incidence
m	=	mass/unit length of body
M	=	total mass
q	=	pitching acceleration
s	=	rigid static margin
T	=	thrust
x	=	streamwise coordinate (Fig. 1)
Z	=	normal offset distance of deformed body center of gravity from body datum
α	=	rigid incidence
θ	=	twist deformation

Subscripts

W	=	wing
T	=	concentrated mass
1, 2, c	=	body (1), body (2), rigid combination, respectively
A	=	aerodynamic
I	=	inertial

DISCUSSION

STATIC aeroelastic problems are defined as those in which frequency-dependent air and inertia forces are not considered, but inertia forces due to overall body motions may be included. It is with these latter forces that this note is concerned.

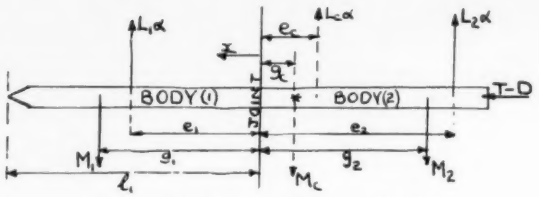

FIG. 1. Schematic of rigid combination.

For unswept wings where the section flexural axis and center of gravity are nearly coincident, it has been the usual practice to ignore the lateral and longitudinal inertia forces in the analysis of wing torsional divergence. While this has been justified for the lateral forces—i.e., those normal to the wing plane, the neglect of the longitudinal forces has not been justified. The main phenomenon that can occur is flexure-torsion instability, in which loads applied in the plane of a slender beam can cause deformations out of that plane if the flexural stiffness in the normal direction is low. One deduces from reference 1 that for a thin, unswept, uniform cantilever beam—e.g., a wing, with the flexural axis and center of gravity coincident, the inertia instability parameter, for a uniformly distributed and a concentrated tip inertia force, is

$$k_I = (dl^2/\sqrt{GJEI})(M_W + 3.225M_T) = 12.9 \quad (1)$$

For wings with, say, the center of gravity well forward of the flexural axis, both lateral and longitudinal inertia forces should be more significant in the torsional sense, being stabilizing and destabilizing, respectively. The aerodynamic torsional-divergence parameter for a uniform unswept wing is given by[2]

$$k_A = L_W(fcl/GJ) = 2.47 \quad (2)$$

The corresponding criterion when lateral and longitudinal inertia effects due to uniformly distributed and concentrated tip masses are considered is easily shown to be

$$k_{AI} = (cl/GJ)\{L_W f - [(2L_W/M_c) - d] \times (M_W h_W + 2.47M_T h_T)\} = 2.47 \quad (3)$$

The inertia effects on most practical aircraft designs should be small, but, for highly swept wings, lateral effects might be significant.

The problem of aerodynamic chordwise divergence in supersonic flow is well known and need not be discussed further here. In the corresponding problem, due to longitudinal inertia, the longitudinal buckling parameter for a semichord of a uniform wing due to a uniform mass distribution and a concentrated mass at the leading edge is[3, 4]

$$k_I = (dc^2/4EI)(M_W + 6.33M_T) = 15.68 \quad (4)$$

Because most wings have low mass/stiffness ratios, this problem should not be critical for practical wing designs.

Although longitudinal inertia effects would appear to be negligible for practical wing designs, these effects might be more significant for slender fuselages. Only a simple solution is presented here, using the assumptions that only one body region is flexible, all rigid incidences and deformations are small, drag of body acts along the thrust axis, and changes in aerodynamic coefficients, etc., due to deformation are not explicitly considered. The notation used is explained by Fig. 1.

The equations of motion for the configuration simplify to

$$B_c\dot{q} = L_2(e_2 - g_c)\alpha - L_1(\alpha + \theta)(e_1 + g_c) - (T - D)Z \quad (5)$$

$$M_c a = L_2\alpha + L_1(\alpha + \theta) + (T - D)\sigma \quad (6)$$

$$M_c d = (T - D) \quad (7)$$

where θ is the angular deformation between the two rigid sections 1 and 2.

The deformation equation is

$$K_\theta\theta = L_1(\alpha + \theta)e_1 + \int_0^{l_1} [m_1\dot{q}(x + g_c) - m_1 a + m_1 d(\alpha + \theta)]x\,dx \quad (8)$$

Static instability would occur at some positive value of θ/α and K_θ at which $\dot{q} = 0$. Therefore, by rearranging Eqs. (5)–(8) and using the result

$$Z = M_1 g_1 \theta/M_c \quad (9)$$

the critical joint stiffness $\bar{K}_\theta$ is obtained.

$$\bar{K}_\theta L_c s_c = (L_1 L_2/M_c)[M_2 s_2 e_1 - M_1 s_1 e_2] + (M_1 g_1 d/M_c)[M_c L_2 s_2 + g_2(M_1 L_2 - M_2 L_1)] \quad (10)$$

To assess the effect of longitudinal acceleration d, consider the simple example in which $L_2/L_1 = M_2/M_1 = 1$ and $e_1 = g_1$, i.e., $s_1 = 0$. Therefore, the second expression on the right hand side of Eq. (10) equals the first when

$$d = L_1/2M_1 = L_c/2M_c \quad (11)$$

Thus, it is seen that longitudinal acceleration has the same effect, in this example, as the lateral aerodynamic and inertia forces when the longitudinal acceleration is one half the possible lateral acceleration of the rigid body for one radian incidence.

The condition from Eq. (10) that longitudinal inertia effects be negligible is given by

$$M_c L_2 s_2 = g_2(M_2 L_1 - M_1 L_2) \quad (12)$$

or

$$M_c L_2 e_2 = M_2 L_c g_2 \quad (13)$$

Also, the further condition from Eq. (10) which, with Eq. (13), makes the critical joint stiffness zero is

$$M_2 s_2 e_1 = M_1 s_1 e_2 \quad (14)$$

but the satisfaction of both Eqs. (13) and (14) may be difficult in practice.

CONCLUSIONS

Longitudinal inertia forces should have no significant effect on static aeroelastic problems of wings but can have a pronounced effect on similar problems for aircraft bodies. This is because the latter have larger values than the former of the ratios mass/stiffness and mass/lift.

Lateral inertia forces can modify the results of static aeroelastic analyses for unconventional wings and should then be considered, as they are already in the problems of entire bodies.

REFERENCES

[1] Case, J., *The Strength of Materials*, pp. 375–380, Edward Arnold and Co., Ltd., London, 1930.

[2] Fung, Y. C., *Introduction to the Theory of Aeroelasticity*, pp. 81–99, John Wiley and Sons Inc., New York.

[3] Timoshenko, S., *Strength of Materials*, pp. 586–590, McMillan and Co. Ltd., 1930.

[4] Case, J., loc. cit., pp. 289.

Formulas for the Determination of Thermal Stresses in Rings

Marvin Forray
Design Specialist, Structures, Applied Research and Development, Republic Aviation Corporation, Farmingdale, L.I., N.Y.
October 21, 1959

THE PLANE-STRESS, linear elastic solution of a traction-free circular ring of inner radius a and outer radius b subjected to a general two-dimensional temperature distribution was considered in a previous note.[1] Design equations will now be presented for the determination of the polar-coordinate stress components corresponding to

$$E\alpha T = A_{K,n} r^K \cos n\theta, \qquad (K = 0, 1, 2, \ldots, n = 0, 1, 2, \ldots) \quad (1)$$

Case A: $K + 2 - n \neq 0$. The stress components are given by

$$\left.\begin{aligned}
\sigma_{rr} &= (a_0/r^2) + 2b_0 + [2b_1 r - (2a_1'/r^3)] \cos\theta + \sum_{n=2}^{\infty} [(n - n^2)a_n r^{n-2} + (n + 2 - n^2)b_n r^n - (n + n^2)a_n' r^{n-2} + (2 - n - n^2)b_n' r^{-n}] \cos n\theta - \{[A_{K,n}(K + 2 - n^2)r^K \cos n\theta] \div [(K + 2 + n)(K + 2 - n)]\} \\
\sigma_{r\theta} &= [2b_1 r - 2(a_1'/r^3)] \sin\theta + \sum_{n=2,3\ldots}^{\infty} [+n(n-1)a_n r^{n-2} + n(n+1)b_n r^n - n(n+1)a_n' r^{-n-2} + n(1-n) \times b_n' r^{-n}] \sin n\theta - \{[n(K+1)A_{K,n} r^K \sin n\theta] \div [(K+2+n)(K+2-n)]\} \\
\sigma_{\theta\theta} &= (-a_0/r^2) + 2b_0 + [6b_1 r + (2a_1'/r^3)] \cos\theta + \sum_{n=2,3\ldots}^{\infty} [n(n-1)a_n r^{n-2} + (n+2)(n+1)b_n r^n + n(n+1)a_n' r^{-n-2} + (2-n)(1-n)b_n' r^{-n}] \cos n\theta - A_{K,n}\{[(K+2)(K+1)r^K \cos n\theta]/[(K+2+n) \times (K+2-n)]\}
\end{aligned}\right\} \quad (2)$$

where the coefficients a_0, b_0, b_1, a_1', a_n, b_n, a_n', and b_n' are determined from the boundary conditions

$$\sigma_{rr} = \sigma_{r\theta} = 0 \text{ on } r = a,\ r = b \quad (3)$$

Case A_1: $n = 0$ ($K + 2 - n \neq 0$ is automatically satisfied.) This is the axisymmetric case. Substitution of Eqs. (2) into (3) yields

$$\begin{aligned}
a_0 &= [-A_{K,0}/(K+2)]\{[(b^K - a^K)a^2b^2]/[b^2 - a^2)]\} \\
2b_0 &= [A_{K,0}/(K+2)][(b^{K+2} - a^{K+2})/(b^2 - a^2)] \quad (4)
\end{aligned}$$

$$a_1' = b_1 = 0, \quad a_n = b_n = a_n' = b_n' = 0 \text{ for } n = 2, 3, 4, \ldots$$

If $T = T_0(r/b)^K$, the stress components in nondimensional form become

$$\left.\begin{aligned}
\sigma_{rr}/E\alpha T_0 &= -[(a/b)^K/(K+2)] \times \left((b^2/r^2)\{[(b/a)^K - 1]/[(b/a)^2 - 1]\} - \{[(b/a)^{K+2} - 1]/[(b/a)^2 - 1]\} + (r/a)^K\right) \\
\sigma_{r\theta}/E\alpha T_0 &= 0 \\
\sigma_{\theta\theta}/E\alpha T_0 &= -[(a/b)^K/(K+2)] \times \left((-b^2/r^2)\{[(b/a)^K - 1]/[(b/a)^2 - 1]\} - \{[(b/a)^{K+2} - 1]/[(b/a)^2 - 1]\} + (K+1)(r/a)^K\right)
\end{aligned}\right\} \quad (5)$$

Case A_2: $n = 1$. ($K + 2 - n \neq 0$ is automatically satisfied.) If $T = T_0(r/b)^K \cos\theta$, the stress components are

$$\left.\begin{aligned}
\sigma_{rr}/E\alpha T_0 &= [1/(K+3)]\left(\{[1 - (a/b)^{K+3}]/[1 - (a/b)^4]\}^{r/b} + \{[(a/b)^{K+3} - (a/b)^4]/[1 - (a/b)^4](r/b)^3\} - (r/b)^K\right)\cos\theta \\
\sigma_{r\theta}/E\alpha T_0 &= [1/(K+3)]\left(\{[1 - (a/b)^{K+3}]/[1 - (a/b)^4]\}^{r/b} + \{[(a/b)^{K+3} - (a/b)^4]/[1 - (a/b)^4](r/b)^3\} - (r/b)^K\right)\sin\theta \\
\sigma_{\theta\theta}/E\alpha T_0 &= [1/(K+3)]\left(\{3[1 - (a/b)^{K+3}]/[1 - (a/b)^4]\}^{r/b} + \{[(a/b)^4 - (a/b)^{K+3}]/[1 - (a/b)^4](r/b)^3\} - (K+2)(r/b)^K\right)\cos\theta
\end{aligned}\right\} \quad (6)$$

Case A_3: $n > 1$. ($K + 2 - n \neq 0$.) With the substitution

$$x = b^{n-K-2}a_n/A_{K,n} \qquad y = b^{n-K}b_n/A_{K,n}$$
$$z = b^{-n-K-2}a_n'/A_{K,n} \qquad w = b^{-n-K}b_n'/A_{K,n}$$

there results

$$\left.\begin{aligned}
\sigma_{rr}/E\alpha T_0 &= \{x(n - n^2)(r/b)^{n-2} + y(n + 2 - n^2) \times (r/b)^n + z(-n - n^2)(r/b)^{-n-2} + w(2 - n - n^2) \times (r/b)^{-n} - [(K + 2 - n^2)(r/b)^K]/[(K + 2 + n) \times (K + 2 - n)]\} \cos n\theta \\
\sigma_{r\theta}/E\alpha T_0 &= \{x(n)(n-1)(r/b)^{n-2} + y(n)(n+1)(r/b)^n - z(n)(n+1)(r/b)^{-n-2} + w(n)(1-n)(r/b)^{-n} - [n(K+1)(r/b)^K]/[(K+2+n)(K+2-n)]\} \sin n\theta \\
\sigma_{\theta\theta}/E\alpha T_0 &= \{x(n)(n-1)(r/b)^{n-2} + y(n+2)(n+1) \times (r/b)^n + z(n)(n+1)(r/b)^{-n-2} + w(2-n)(1-n) \times (r/b)^{-n} - [(K+2)(K+1)(r/b)^K]/[(K+2+n) \times (K+2-n)]\} \cos n\theta
\end{aligned}\right\} \quad (7)$$

where x, y, z, and w are determined from

$$\left.\begin{aligned}
&(n - n^2)(a/b)^{n-K-2}x + (n + 2 - n^2)(a/b)^{n-K}y + (-n - n^2)(a/b)^{-n-K-2}z + (2 - n - n^2)(a/b)^{-n-K}w = \{(K + 2 - n^2)/[(K + 2 + n)(K + 2 - n)]\} \\
&(n - n^2)x + (n + 2 - n^2)y + (-n - n^2)z + (2 - n - n^2)w = \{(K + 2 - n^2)/[(K + 2 + n) \times (K + 2 - n)]\} \\
&n(n-1)(a/b)^{n-K-2}x + n(n+1)(a/b)^{n-K}y - n(n+1)(a/b)^{-n-K-2}z + n(1-n)(a/b)^{-n-K}w = \{n(K+1)/[(K+2+n)(K+2-n)]\} \\
&n(n-1)x + n(n+1)y - n(n+1)z + n(1-n)w = \{n(K+1)/[(K+2+n)(K+2-n)]\}
\end{aligned}\right\} \quad (8)$$

Case B: $K + 2 - n = 0$. The components of stress are

$$\left.\begin{aligned}
\sigma_{rr}/E\alpha T_0 &= \left(x'(n - n^2)(r/b)^{n-2} + y'(n + 2 - n^2) \times (r/b)^n + z'(-n - n^2)(b/r)^{n+2} + w'(2 - n - n^2) \times (r/b)^{-n} - (r/b)^{n-2}\{[(1 - n)/2] \log_e(r/a) + (1/4)[(1/n) + 1]\}\right)\cos n\theta \\
\sigma_{r\theta}/E\alpha T_0 &= \left(x'(n^2 - n)(r/b)^{n-2} + y'(n)(n+1)(r/b)^n + z'(-n - n^2)(b/r)^{n+2} + w'n(1-n)(r/b)^{-n} - (r/b)^{n-2} \times \{[(n - 1)/2] \log_e(r/a) + (1/4)[(1/n) + 1]\}\right)\sin n_\theta \\
\sigma_{\theta\theta}/E\alpha T_0 &= \left(x'(n)(n-1)(r/b)^{n-2} + y'(n+2)(n+1) \times (r/b)^n + z'n(n+1)(b/r)^{n+2} + w'(n-2)(n-1) \times (r/b)^{-n} - (r/b)^{n-2}\{[(n - 1)/2] \log_e(r/a) + (1/4)[3 - (1/n)]\}\right)\cos n^\theta
\end{aligned}\right\} \quad (9)$$

where x', y', z', and w' are determined from

$$\left.\begin{aligned}
&(n - n^2)x' + (n + 2 - n^2)(a/b)^2y' - (n + n^2) \times (a/b)^{-2n}z' + (2 - n - n^2)(a/b)^{2-2n}w' = (1/4)[(1/n) + 1] \\
&(n - n^2)x' + (n + 2 - n^2)y' - (n + n^2)z' + (2 - n - n^2)w' = \{[(1 - n)\log_e(b/a)]/2\} + (1/4)[(1/n) + 1] \\
&(n^2 - n)x' + n(n + 1)(a/b)^2y' - (n + n^2)(a/b)^{-2n}z' + n(1 - n)(a/b)^{2-2n}w' = (1/4)[(1/n) + 1] \\
&(n^2 - n)x' + n(n + 1)y' - (n + n^2)z' + n(1 - n)w' = \{[(n - 1)\log_e(b/a)]/2\} + (1/4)[(1/n) + 1]
\end{aligned}\right\} \quad (10)$$

Remarks

(1) All stress components are identically zero when $K = n$, i.e., $T = T_0(r/b)^n \cos n\theta$ because $r^n \cos n\theta$ is the real part of the analytic function z^n and must satisfy Laplace's equation $\nabla^2 T = 0$.

(2) When the temperature distribution is expressed as a series of terms of the form (1), the stress components corresponding to the individual terms may be superposed to obtain the resultant.

(3) The prescribed temperature can always be expressed as the sum of symmetrical and antisymmetrical terms in θ. The expression (1) represents the symmetrical component, while the antisymmetrical components will be made up of terms of the form $E\alpha T = \sum_{Kn} B_{Kn} r^K \sin n\theta$.

The above formulas remain valid if $\cos n\theta$ and $\sin n\theta$, respectively, are replaced by $\sin n\theta$ and $-\cos n\theta$, respectively.

References

[1] Forray, M. J., *Thermal Stresses in Rings*, Readers' Forum, Journal of the Aero/Space Sciences, Vol. 26, No. 5, pp. 310–311, May, 1959.

Stress Functions for Plates Bounded by Piecewise Analytic Curves

Ming M. Chen and P. T. Hsu
Research Staff Members,
Aeroelastic and Structures Research Laboratory,
Massachusetts Institute of Technology, Cambridge, Mass.
October 15, 1959

In a recent note, Balmer[1] has shown that the stress function for a plate of polygonal shape fulfilling the stress-free boundary conditions can be derived from the generalization of the standard expression for the Airy stress function for rectangular plates. It appears that this generalization can be carried out further to include planforms which are bounded by piecewise analytic curves, Fig. 1.

Suppose the plate is bounded by m analytic curves which can be expressed as

$$g_i(x, y) = 0, \quad i = 1, 2, \ldots . m \tag{1}$$

The stress function whichful fills the stress-free boundary conditions on each curve can then be expressed in the following form

$$\phi(x, y) = \prod_{i=1}^{m} [g_i(x, y)]^2 P(x, y) \tag{2}$$

where $P(x, y)$ is an arbitrary function which is nonvanishing over

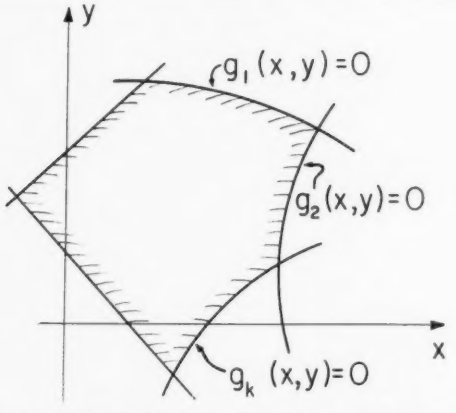

Fig. 1. Arbitrary planform bounded by analytic curves.

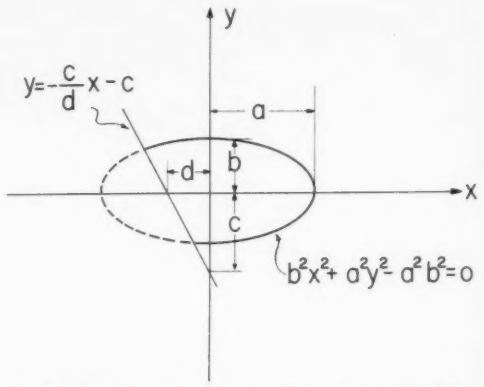

Fig. 2. Planform bounded by an ellipse and a straight line.

the planform. The stress-free boundary conditions require that

$$\left.\begin{aligned} (N_n)_i &= \frac{\partial^2 \phi}{\partial t_i^2} = 0 \\ (N_{nt})_i &= -\frac{\partial^2 \phi}{\partial n_i \partial t_i} = 0 \end{aligned}\right\} \quad \begin{array}{l} \text{on } g_i(x, y) = 0 \\ i = 1, 2, \ldots . m \end{array} \tag{3}$$

where $(N_n)_i$ and $(N_{nt})_i$ are the normal and shear stress resultants and n_i and t_i are the normal and tangent on the ith boundary, respectively.

In order to show that Eq. (2) satisfies the condition of Eq. (3), it suffices to consider only one edge. For the ith edge, we write

$$\phi(x, y) = [g_i(x, y)]^2 Q(x, y) \tag{4}$$

where $Q(x, y)$ includes $P(x, y)$ and the remaining functions. The second derivatives in directions of n and t are

$$\begin{aligned} N_n &= \phi_{,tt} = \phi_{,xx}(\partial x/\partial t)^2 + \phi_{,yy}(\partial y/\partial t)^2 + 2\phi_{,xy}(\partial x/\partial t)(\partial y/\partial t) \\ N_t &= \phi_{,nn} = \phi_{,xx}(\partial x/\partial n)^2 + \\ &\qquad \phi_{,yy}(\partial y/\partial n)^2 + 2\phi_{,xy}(\partial x/\partial n)(\partial y/\partial n) \\ -N_{nt} &= \phi_{,nt} = \phi_{,xx}(\partial x/\partial t)(\partial x/\partial n) + \phi_{,yy}(\partial y/\partial t)(\partial y/\partial n) + \\ &\qquad \phi_{,xy}(\partial x/\partial t)\,(\partial y/\partial n) + (\partial y/\partial t)\,(\partial x/\partial n) \end{aligned} \tag{5}$$

Differentiating ϕ of Eq. (4) with respect to x and y and noting that $g_i(x, y) = 0$ on curve i, one obtains

$$\begin{aligned} \phi_{,xx} &= 2Q[\partial g_i(x, y)/\partial x]^2 \\ \phi_{,yy} &= 2Q[\partial g_i(x, y)/\partial y]^2 \\ \phi_{,xy} &= 2Q\{[\partial g_i(x, y)/\partial x][\partial g_i(x, y)/\partial y]\} \end{aligned} \tag{6}$$

Substituting Eq. (6) into Eq. (5), one obtains

$$\begin{aligned} (N_n)_i &= 2Q\{[\partial g_i(x, y)/\partial x]\,(\partial x/\partial t_i) + [\partial g_i(x, y)/\partial y](\partial y/\partial t_i)\} \\ &\equiv 2Q[\partial g_i/\partial t_i]^2 \\ (N_t)_i &= 2Q[\partial g_i/\partial n_i]^2 \\ (N_{nt})_i &= -2Q[(\partial g_i/\partial n_i)(\partial g_i/\partial t_i)] \end{aligned} \tag{7}$$

Since $g_i(x, y) = 0$ on curve i, it is obvious that $\partial g_i/\partial t_i$ vanishes. Consequently the free-stress boundary conditions

$$(N_n)_i = 0, \quad (N_{nt})_i = 0$$

are satisfied.

As a simple example, the stress function for a plate shown in Fig. 2 can be expressed as:

$$\phi(x, y) = [y + (c/d)x + c]^2(b^2x^2 + a^2y^2 - a^2b^2)^2 P(x, y) \tag{8}$$

Aside from the stress-free boundaries, there can be boundaries on which either the stresses or the displacements are prescribed. These boundary conditions can be satisfied on the average through the use of a variational principle. However, for the case of prescribed stresses, it is sometimes possible to satisfy these conditions by proper choice of the function $P(x, y)$.

Reference

[1] Balmer, Hans A., *Stress Functions for Plates of Convex Polygonal Shape*, Readers' Forum, Journal of the Aero/Space Sciences, Vol. 26, No. 10, p. 675, October, 1959.

REQUIREMENTS *for* CONTRIBUTIONS

to the publications of the

INSTITUTE *of the* AERONAUTICAL SCIENCES

The Institute of the Aeronautical Sciences invites both members and nonmembers from any country to submit papers for publication in the JOURNAL OF THE AERO/SPACE SCIENCES and AERO/SPACE ENGINEERING. The Institute, following the practice of other societies, does not pay for contributions.

The following directions for the preparation of papers, if followed by authors, will save correspondence, avoid the return of papers for changes, minimize the work of preparation for the printer, and save the expense due to the charges made for "author's corrections."

MANUSCRIPTS: The original typewritten copy of the paper is desired. **To expedite review, an additional copy of both the manuscript and figures should be submitted.** The manuscript must be double or triple spaced on one side of white paper sheets, consecutively numbered. There should be wide margins to allow for the marking of directions to the printer. Correcting, changing, or adding to papers after they are in type is costly. It is, therefore, imperative that papers submitted be in final form. Typographical errors may be corrected on proofs, but if authors wish to add material, they may do so at their own expense. In mailing, drawings may be rolled, but manuscripts should be sent flat. Send by first-class mail (register if you wish for your own protection) to the Editorial Office, Institute of the Aeronautical Sciences, 2 East 64th Street, New York 21, N.Y. All manuscripts will be examined by the Editorial Committee and by the Editor. Authors will be advised as promptly as possible whether the paper is acceptable for publication.

TITLES: The title of the paper should be brief. The name and initials of the author should be written as he prefers. The use of the full name of an author is advocated because of the frequent duplication of initials and surnames which sometimes makes it difficult to establish the identity of the author. This is particularly important for large annual indexing and abstracting services. All titles and degrees or honors are omitted. The name of the organization with which the author is associated should be placed after his name on a separate line. The date on which the paper is received will be inserted by the Editor. The author's title or position should be indicated in a footnote.

SUMMARIES OR ABSTRACTS: An abstract to be printed at the beginning should accompany each article. It should be adequate as an *index* and as a *summary*. It should contain a statement of major conclusions reached, since summaries in many cases constitute the only source of information used in compiling scientific reference indexes. Abstracts printed in other journals, especially foreign, in most cases consist of summaries from printed papers. The summary should explain as adequately as possible the major conclusions to a nonspecialist in the subject and should contain from 100 to 300 words, depending on the length of the paper.

SUBHEADINGS: Subheadings should be inserted by the author at frequent intervals. The work of editorial preparation will be simplified by the author's provision of many subheadings.

MATTER USUALLY DELETED: Photographs or illustrations of little technical interest and not showing advances in general practice. Too detailed tabular matter (general results of such tables may be included in the text). Lengthy descriptions of materials or processes or of preliminary experiments or theories that preceded final results; salient features only are of interest.

REFERENCES: References should be numbered consecutively and grouped together at the end of the manuscript, with only the corresponding number being mentioned in the text. The arrangement should be as follows. For books: [1] Durand, W. F., *Aerodynamic Theory*, 1st Ed., Vol. 1, p. 23; Julius Springer, Berlin, 1934. For magazines: [1] England, C. R., Crawford, A. B., and Mumford, W. W., *Some Results of a Study of Ultra-Short-Wave Transmission Phenomenon*, Proc. IRE, Vol. 20, No. 12, pp. 481–482, March, 1933. Please give author, title, edition, volume, number, page, publisher, and place and date of publication as indicated. Omission of one required fact causes much extra editorial work and possible inaccuracies.

ILLUSTRATIONS: Illustrations should accompany manuscripts, and each should always be referred to in the text by number. Drawings or graphs should not be larger than 12 × 16 inches, and must be made with jet black India ink on white paper or tracing cloth, the latter being preferred. *Do not use typewriter for lettering.* The smallest lettering on 8 × 10 inch figures should be no less than $^1/_4$ inch high. Cross-section paper (white with black lines) may be used, but it should not have more than 4 lines per inch. If finer ruled paper is used, the major division lines should be drawn in with black ink, omitting the finer divisions. In the case of finely ruled paper, only blue-lined paper can be accepted. *Tracing paper and blueprints* are not acceptable. Lettering and all markings must be large enough to be readable after reduction to single-column width ($3^5/_{16}$ in.). Mail rolled or flat; never fold. Drawings that cannot be reproduced (including pencil drawings) will be returned to the author for redrawing, thus delaying publication of the paper. Photographs should be distinct and show clear black and white contrasts. They must be on glossy white paper. Avoid round or oval photographs.

CAPTIONS AND LEGENDS: Legends or captions must accompany each drawing or photograph submitted. If written on the drawing or photograph, they should be placed below and well outside the part to be reproduced. Each table should have a caption such as Table 1, Table 2, Table 3, etc. Captions should be complete in themselves so as to make the data intelligible to the reader without reference to the text. A duplicate list of captions for figures should be included as the last page of the manuscript. Use "Fig. 1" (not Figure 1), "Figs. 3 and 4," etc., in both the text and the numbering of illustrations. In the text, "Eq. (1)" or "Eqs. (1) and (2)" is used, not "Equation (1)." In captions, legends, and in table headings, write all words in full; do not abbreviate, except for "Fig." and "Eq."

MATHEMATICAL WORK: Formulas may be typewritten or carefully written in pen and ink, the writing to be large enough so that it can be marked for the printer. Considerable space for marking should be allowed above and below all equations. All complicated equations should be repeated on separate sheets with plenty of space left for marking. The solidus should be used for simple fractions appearing within the text. Make all expressions clear to the typesetter. Greek letters used in formulas should be clearly designated by name in the margin of the manuscript. The difference between capital and lower-case letters should be clearly distinguished and care taken to avoid confusion between zero (0) and the letter (o), between the numeral (one) and the letter (ell) and the prime (′), between alpha and a, kappa and k, u and mu, v and nu, n and eta. All subscripts and exponents should be clearly distinguished. Avoid complicated exponents and subscripts. Dots and bars over letters or mathematical expressions should also be avoided. When it is necessary to repeat a complicated expression, it should be represented by some convenient symbol.

SYMBOLS AND ABBREVIATIONS: The symbols recommended in the American Standard Association "Letter Symbols for Aeronautical Sciences," ASA Y10.7—1954, should be used wherever practicable. All symbols should be clearly written and carefully checked. Standard abbreviations should be used, and it should be noted that most abbreviations are lower case, such as m.p.h., b.m.e.p., i.h.p. b.hp., hp., etc.

CORPORATE MEMBERS

OF THE

INSTITUTE OF THE AERONAUTICAL SCIENCES

AC SPARK PLUG DIVISION, GENERAL MOTORS CORPORATION

ACADEMY OF AERONAUTICS

AEROJET-GENERAL CORPORATION

AEROLAB DEVELOPMENT COMPANY

AERONCA MANUFACTURING CORPORATION

AERONUTRONIC SYSTEMS, INC.

AEROQUIP CORPORATION

AGAWAM AIRCRAFT PRODUCTS, INC.

ALLIED RESEARCH ASSOCIATES, INC.

ALLISON DIVISION, GENERAL MOTORS CORPORATION

ALUMINUM COMPANY OF AMERICA

AMERICAN AIRLINES, INC.

AMERICAN BOSCH ARMA CORPORATION

AMERICAN STEEL & WIRE DIVISION, UNITED STATES STEEL CORPORATION

AMOCO CHEMICALS CORPORATION

AMPHENOL-BORG ELECTRONICS CORPORATION

ANDERSON, GREENWOOD & CO.

ARDE ASSOCIATES

ASSOCIATED AVIATION UNDERWRITERS

AUTOMATION INDUSTRIES, INCORPORATED

AVCO RESEARCH LABORATORY

AVIEN, INC.

BEECH AIRCRAFT CORPORATION

BELL AIRCRAFT CORPORATION

BENDIX AVIATION CORPORATION

BOEING AIRPLANE COMPANY

BOOZ, ALLEN & HAMILTON

THE BRISTOL AEROPLANE COMPANY (U.S.A.) INC.

BULOVA RESEARCH AND DEVELOPMENT LABORATORIES, INC.

CANADAIR, LTD.

THE CESSNA AIRCRAFT COMPANY

CHANCE VOUGHT AIRCRAFT, INCORPORATED

THE CHASE MANHATTAN BANK

CHICAGO AERIAL INDUSTRIES, INC.

THE CLEVELAND PNEUMATIC INDUSTRIES, INC.

CONSOLIDATED CONTROLS CORPORATION

CONTINENTAL MOTORS CORPORATION

CORNELL AERONAUTICAL LABORATORY, INC.

CURTISS-WRIGHT CORPORATION

DANIEL, MANN, JOHNSON, & MENDENHALL

THE DECKER CORPORATION

DEL MAR ENGINEERING LABORATORIES

DELCO-REMY DIVISION, GENERAL MOTORS CORPORATION

DOAK AIRCRAFT COMPANY, INC.

DOUGLAS AIRCRAFT COMPANY, INC.

DZUS FASTENER COMPANY, INC.

EASTERN AIR LINES, INC.

EATON MANUFACTURING COMPANY

EDO CORPORATION

ELASTIC STOP NUT CORPORATION OF AMERICA

ENGINEERING SUPERVISION COMPANY

FAIRCHILD CAMERA AND INSTRUMENT CORPORATION

FAIRCHILD ENGINE AND AIRPLANE CORPORATION

THE GARRETT CORPORATION

GENERAL APPLIED SCIENCE LABORATORIES, INC.

GENERAL DYNAMICS CORPORATION

GENERAL ELECTRIC COMPANY

GENERAL PRECISION EQUIPMENT CORPORATION

G. M. GIANNINI & CO., INC.

GIANNINI PLASMADYNE CORPORATION

THE B. F. GOODRICH COMPANY

GOODYEAR AIRCRAFT CORPORATION

GRUMMAN AIRCRAFT ENGINEERING CORPORATION

HYDRO-AIRE CO.

INSURANCE COMPANY OF NORTH AMERICA COMPANIES

INTERNATIONAL BUSINESS MACHINES CORPORATION

THE INTERNATIONAL NICKEL COMPANY, INC.

ITT LABORATORIES, DIVISION OF INTERNATIONAL TELEPHONE AND TELEGRAPH CORPORATION

JANITROL AIRCRAFT, A DIVISION OF MIDLAND-ROSS CORPORATION

JOHNS-MANVILLE SALES CORPORATION

WALTER KIDDE & COMPANY, INC.

KOLLSMAN INSTRUMENT CORPORATION

LAVELLE AIRCRAFT CORPORATION

LEAR, INCORPORATED

C. W. LEMMERMAN, INC.

LIBRASCOPE DIVISION OF GENERAL PRECISION, INC.

THE LIQUIDOMETER CORPORATION

LOCKHEED AIRCRAFT CORPORATION

LOEWY-HYDROPRESS DIVISION OF BALDWIN-LIMA-HAMILTON CORPORATION

THE MARQUARDT CORPORATION

THE MARTIN COMPANY

McDONNELL AIRCRAFT CORPORATION

MELETRON CORPORATION

MINNEAPOLIS-HONEYWELL REGULATOR COMPANY

NATIONAL CREDIT OFFICE, INC.

NORTH AMERICAN AVIATION, INC.

NORTHROP CORPORATION

NUCLEAR DEVELOPMENT CORPORATION OF AMERICA

PAN AMERICAN WORLD AIRWAYS, INC.

THE RALPH M. PARSONS COMPANY

PESCO PRODUCTS DIVISION, BORG-WARNER CORPORATION

PHILLIPS PETROLEUM COMPANY

PIASECKI AIRCRAFT CORPORATION

RADIO CORPORATION OF AMERICA
ASTRO-ELECTRONIC PRODUCTS DIVISION
DEFENSE ELECTRONIC PRODUCTS

RAMO-WOOLDRIDGE DIVISION, THOMPSON RAMO WOOLDRIDGE INC.

REPUBLIC AVIATION CORPORATION

ROHR AIRCRAFT CORPORATION

PAUL ROSENBERG ASSOCIATES

RYAN AERONAUTICAL COMPANY

SANDBERG-SERRELL CORPORATION

SHAFER BEARING DIVISION, CHAIN BELT COMPANY

SHELL OIL COMPANY

SIMMONDS AEROCESSORIES, INC.

SOCONY MOBIL OIL COMPANY, INC.

SOLAR AIRCRAFT COMPANY

SOUTHWEST PRODUCTS CO.

SPACE TECHNOLOGY LABORATORIES, INC.

R. DIXON SPEAS ASSOCIATES

SPERRY GYROSCOPE COMPANY DIVISION OF SPERRY RAND CORPORATION

STANDARD OIL COMPANY OF CALIFORNIA

STANDARD OIL COMPANY (INDIANA)

STANDARD-THOMSON CORPORATION
CLIFFORD MANUFACTURING DIVISION

STANLEY AVIATION CORPORATION

THIOKOL CHEMICAL CORPORATION

THOMPSON RAMO WOOLDRIDGE INC.

TRANS WORLD AIRLINES, INC.

TURBO PRODUCTS, INC.

UNION CARBIDE CORPORATION

UNITED AIR LINES, INC.

UNITED AIRCRAFT CORPORATION

UNITED STATES AVIATION UNDERWRITERS, INC.

VERTOL AIRCRAFT CORPORATION

VITRO CORPORATION OF AMERICA

WESTERN GEAR CORPORATION

WESTINGHOUSE ELECTRIC CORPORATION

WYMAN-GORDON COMPANY

YOUNG RADIATOR COMPANY